WWU
MÜNSTER

Inelastic electron scattering in tritium gas and ppm-precise energy scale at the KATRIN experiment

Caroline Rodenbeck, Dissertation 2023

wissen.leben

Institut für Kernphysik

Westfälische Wilhelms-
Universität Münster

Experimentelle Physik

Inelastic electron scattering in tritium gas and ppm-precise energy scale at the KATRIN experiment

Inaugural-Dissertation
zur Erlangung des Doktorgrades der Naturwissenschaften
im Fachbereich Physik
der Mathematisch-Naturwissenschaftlichen Fakultät
der Westfälischen Wilhelms-Universität Münster

vorgelegt von
Caroline Rodenbeck
aus Bremervörde

— 2023 —

WWU
MÜNSTER

Überarbeitete Fassung, Dezember 2023

Es wurden folgende Fehler korrigiert: ¶ Einige Gleichungen in Kapitel 1 hatten verdrehte Indizes oder ein fehlendes Minuszeichen. ¶ Gleichungen (3.8) und (4.9) enthielten Tippfehler; ebenfalls durch einen Tippfehler zustandegekommen war ein falscher Wert für a' in Bildunterschrift 4.21. Nach Korrektur sind diese Stellen nun konsistent mit dem Rest der Arbeit. ¶ Bildunterschrift 3.1 war fehlerhaft. ¶ Die „grobe Schätzung“ der Streuwahrscheinlichkeiten auf S. 73 verwendet nun sinnigerweise die integrierten Raten. ¶ Die Beschreibung von δU_{dep} auf S. 127 war irreführend.

Außerdem wurden einige Kleinigkeiten überarbeitet: ¶ Der exakte Wert von M_{20} ist nun in Bildunterschrift 4.20 vermerkt. ¶ Einige Verweise auf veraltete Plot-Layouts wurden ausgebessert: oben/unten statt links/rechts u.Ä. ¶ Sprache: Rechtschreib- und Grammatikfehler verbessert; und einige Bildunterschriften wurden klarer formuliert. ¶ Darstellung der Bibliografie wurde aufgeräumt und um Kollaborationsnamen ergänzt. Einige Kürzel haben sich dadurch geändert. ¶ Diverse kleine typografische Korrekturen und an Plots und Tabellen oberflächliche Verbesserungen. ¶ Die ergänzenden internen URLs in den Randnotizen wurden zu klickbaren Links gekürzt und aktualisiert.

Dekan:	Prof. Dr. Michael Rohlfing
Erster Gutachter:	Prof. Dr. Christian Weinheimer
Zweiter Gutachter:	Prof. Dr. Anton Andronic
Tag der mündlichen Prüfung:	11. Juli 2023
Tag der Promotion:	11. Juli 2023

Abstract

One of the open questions in particle physics is the mass of neutrinos. It is multiple orders of magnitude smaller than the mass of any other known particle and the mechanism behind it has not been established yet. And even though the mass differences between the mass eigenstates are known, the absolute mass scale is not.

To determine the absolute mass scale, the Karlsruhe Tritium Neutrino (KATRIN) experiment measures the tritium beta-decay spectrum around its endpoint at 18.6 keV. The KATRIN experiment has set the current best limit of 0.8 eV/c^2 (90 % confidence level, C.L.) and is currently accumulating more statistics while also attempting to reduce systematics in order to reach a sensitivity of 0.2 eV/c^2 (90 % C.L.).

Fundamentally, KATRIN operates by performing high-precision electron spectroscopy. It uses a high-luminosity gaseous tritium source and an integrating spectrometer that combines magnetic collimation with an electrostatic filter.

Any imprecision in measuring an electron's energy distorts the beta-decay spectrum, which leads to a bias in the measured neutrino mass. In this thesis, characteristics that can result in such distortions, namely the energy loss inside the source, the spectrometer's retarding potential, and the overall energy scale, are investigated and their effects are reduced successfully.

Within the source, beta-decay electrons can scatter inelastically on tritium. The scattering processes include electronic excitations and ionization of tritium molecules. The energy loss that results from this scattering needs to be determined precisely so that it can be accounted for in the spectrum analysis. Measurements using a time-of-flight method to measure the energy loss in a differential way are presented in this thesis. Using these measurements, a semi-empirical description of the energy-loss function is determined which is used as input for the neutrino mass analysis.

At the spectrometer, instabilities of the retarding potential affect the transmission conditions and alter the measured spectrum. For example, a Gaussian broadening of the retarding potential of 60 mV ($3\times10^{-6} = 3$ ppm at 18.6 kV) would distort the spectrum in a way that results in a 7×10^{-3} eV$^2/c^4$ shift of the measured squared neutrino mass value. To reduce this, a precision stabilization for the retarding potential is in place which is combined with calibration procedures to trace the measured retarding potential value to a metrological standard. Its implementation for routine use at KATRIN's spectrometer and further improvements are presented within this thesis. Overall, the retarding potential is shown to have sub-ppm precision and ppm trueness on time scales from microseconds up to years.

The energy scale of KATRIN also includes other components besides the retarding potential, such as work functions of various surfaces or the plasma potential inside the source. To calibrate the full energy scale, conversion electrons from the 32.2-keV transition of the nuclear isomer ^{83m}Kr are used. Comparing the measured energies to the appropriate literature values allows for an independent evaluation of the energy scale, but the uncertainties in some of the literature values obtained by gamma spectroscopy are a limiting factor. Building upon the already excellent linearity of KATRIN's energy scale, a novel method for determining the ^{83m}Kr transition energies via high-precision electron spectroscopy is proposed. Notably, the method makes use of conversion electrons from the 41.6-keV direct transition of ^{83m}Kr to its ground state in addition to conversion electrons from the much more frequent cascade of a 32.2-keV and a 9.4-keV transition. By implementing this method, KATRIN may be able to deliver order-of-magnitude improvements in precision over current ^{83m}Kr transition energy literature values.

Zusammenfassung

Eine der offenen Fragen in der Teilchenphysik ist die Neutrinomasse. Sie ist mehrere Größenordnungen kleiner als die Masse jedes anderen bekannten Teilchens und der genaue Mechanismus, wie das Neutrino seine Masse erhält, ist bisher noch ungeklärt. Obwohl die Massendifferenzen zwischen den Masseneigenzuständen bekannt sind, ist die absolute Massenskala bisher noch unbekannt.

Zur Bestimmung der absoluten Massenskala misst das Karlsruhe Tritium Neutrino (KATRIN) Experiment das Tritiumspektrum an seinem Endpunkt (bei 18,6 keV). Das KATRIN-Experiment hat das bisher beste Limit von $0{,}8\,\mathrm{eV}/c^2$ (90 % Konfidenzniveau, C.L.) gesetzt und aktuell wird mehr Statistik gesammelt und gleichzeitig versucht, die Systematiken zu verringern, um eine Sensitivität von $0{,}2\,\mathrm{eV}/c^2$ (90 % C.L.) erreichen zu können.

KATRINs grundlegendes Funktionsprinzip ist hochpräzise Elektronenspektroskopie. Verwendet wird dabei eine gasförmige Tritiumquelle mit hoher Luminosität und ein integrierendes Spektrometer, welches magnetische Kollimation und einen elektrostatischen Filter vereint.

Jegliche Ungenauigkeit bei der Messung der Elektronenenergien verzerrt das aufgenommene Betazerfallsspektrum und führt somit zu einem systematischen Fehler in der gemessenen Neutrinomasse. Innerhalb dieser Doktorarbeit werden Eigenschaften des KATRIN-Aufbaus, welche genau solche Verzerrungen verusachen, untersucht und ihre Auswirkungen reduziert. Hierzu zählen Energieverluste innerhalb der Quelle, das Retardierungspotential des Spektrometers und die gesamte Energieskala des Experiments.

Innerhalb der Quelle können Betazerfallselektronen inelastisch an Tritium streuen. Zu den Streuprozessen gehören elektronische Anregungen und Ionisation der Tritiummoleküle. Energieverluste, die von Streuungen verursacht werden, müssen sehr genau bestimmt und dann in der Spektrumsanalyse berücksichtigt werden. Messungen, die eine Flugzeitmethode anwenden, mit der die Energieverluste auf differentielle Weise bestimmt werden können, werden in der vorliegenden Arbeit vorgestellt. Unter Verwendung dieser Messungen wird eine semi-empirische Beschreibung der Energieverlustfunktion bestimmt, welche dann einen grundlegenden Baustein in der Neutrinomassenanalyse bildet.

Am Spektrometer beeinflussen Instabilitäten des Retardierungspotentials die Transmissionsbedingungen und verfälschen das gemessene Spektrum. Zum Beispiel kann eine Gaußsche Verbreiterung des Retardierungspotentials von 60 mV ($3 \cdot 10^{-6} = 3\,\mathrm{ppm}$ bei 18,6 kV) das Spektrum so verfälschen, dass die gemessene quadrierte Neutrinomasse um $7 \cdot 10^{-3}\,\mathrm{eV}^2/c^4$ verschoben wird. Um diesen Effekt zu verringern, existiert eine Präzisionsstabilisierung des Retardierungspotentials, welche ergänzt ist mit Kalibrierungsprozeduren, die das gemessene Retardierungspotential auf einen messtechnischen Standard zurückführen. Ihre Implementierung für den regulären Messbetrieb an KATRINs Spektrometer und weitere Verbesserungen werden in der vorliegenden Arbeit vorgestellt. Insgesamt konnte gezeigt werden, dass das Retardierungspotential auf Zeitskalen von Mikrosekunden bis zu Jahren eine Präzision besser als 1 ppm und eine Genauigkeit im einstelligen ppm-Bereich aufweist.

Neben dem Retardierungspotential beinhaltet die Energieskala von KATRIN noch weitere Komponenten. Dazu zählen Austrittsarbeiten von verschiedenen Oberflächen und das Plasmapotential innerhalb der Quelle. Um die gesamte Energieskala zu kalibrieren, werden Konversionselektronen von dem 32,2-keV-Übergang des Isomers $^{83\mathrm{m}}$Kr verwendet. Der Vergleich der gemessenen Energien mit zugehörigen Literaturwerten ermöglicht eine unabhängige Bestimmung der Energieskala, die jedoch durch die Unsicherheiten in den aus Gammaspektroskopie bestimmten Literaturwerten limitiert ist. Ausgehend von der bereits exzellenten Linearität von KATRINs Energieskala wurde eine neue Methode entwickelt, um die $^{83\mathrm{m}}$Kr-Übergangsenergien mithilfe von Hochpräzisionselektronenspek-

troskopie zu bestimmen. Die Methode verwendet sowohl Konversionselektronen des direkten 41,6-keV-Übergangs von ^{83m}Kr zu seinem Grundzustand als auch Konversionselektronen der sehr viel häufigeren 32,2-keV–9,4-keV-Übergangskaskade. Falls diese Methode bei KATRIN implementiert wird, sind Präzisionsverbesserungen um eine Größenordnung gegenüber den aktuellen ^{83m}Kr-Übergangsenergieliteraturwerten erreichbar.

Contents

Introduction

Almost seventy years after their detection and over ninety years after their postulation, the mass of the neutrinos remains an unsolved puzzle in particle physics. Neutrinos are electrically neutral particles and come in three known flavors, more precisely three weak interaction states, called electron, muon, and tauon neutrinos. Each weak interaction state is a linear superposition of mass eigenstates, and as the neutrinos propagate through space they can oscillate from one flavor into another. The oscillation parameters such as the differences between the mass eigenstates are known nowadays to a precision of a few percent but the absolute mass of the neutrino mass eigenstates is not known yet.

Already before their first direct observation [Cow+56], measurements of the tritium beta-decay spectrum limited the neutrino mass to values below 1000 eV/c^2 [HP49; CAC49]. Today, many years and many different experimental setups later, the neutrino mass value is known to be smaller than 0.8 eV/c^2 [Kat22]. Neutrinos are the lightest known particles and their mass is at least 6×10^5 times smaller than the mass of the second lightest particle (the electron), raising questions about the mechanism behind their small mass.

On the experimental side, efforts are ongoing to further improve the upper limit on the absolute mass value. The best limit to date (0.8 eV/c^2) has been set by the Karlsruhe tritium neutrino (KATRIN) experiment, but KATRIN aims to achieve an even higher sensitivity of 0.2 eV/c^2 (at 90 % confidence level) [Kat05].

The KATRIN setup consists of a high-luminosity gaseous tritium source from which beta-decay electrons are magnetically guided into a high-precision spectrometer that combines magnetic collimation and an electrostatic filter. The electrostatic filter transmits only electrons with energies above a certain threshold, controlled by the retarding potential. After transmission, the remaining electrons are guided to the detector where they are counted. In order to accumulate an integral electron spectrum, the retarding potential is adjusted repeatedly in a step-wise manner. For the neutrino mass analysis, the beta-decay spectrum is measured close to the endpoint at 18.6 keV where the effect of the neutrino mass is most pronounced.

Inside KATRIN's gaseous tritium source, beta-decay electrons can inelastically scatter on tritium gas. Neglecting the energy loss caused by scattering distorts the measured beta-decay spectrum, and thus distorts the extracted neutrino mass value. To reduce this systematic effect, in-situ energy-loss measurements are performed. Monoenergetic electrons from an electron gun are shot into the tritium source from the end opposite of the detector, and from there they travel the same way to the spectrometer as the beta-decay electrons. At the spectrometer, the electrons' energy relative to their energy before entering the source is precisely measured and thus the energy loss inside the source is evaluated. The resulting energy-loss function is used as an input for the neutrino mass analysis.

Another important parameter for the neutrino mass analysis is KATRIN's energy scale. It needs to be linear and stable during the measurements. For example, a Gaussian broadening of 60 meV shifts the measured squared neutrino mass value by $7 \times 10^{-3}\,\mathrm{eV}^2/c^4$ [Kat05].

A key component of the energy scale is the retarding potential. Any instability it exhibits incurs a broadening of the energy scale. To achieve KATRIN's sensitivity goal, the standard deviation of the retarding potential should be below 60 mV which translates to a stability requirement of 3 ppm (3×10^{-6}) on a wide range of time scales (from microseconds up to months). A measurement chain with two precision high-voltage dividers [TMW09; Bau+13] is in place and it is combined with a custom-made MHz-bandwidth regulation loop, called "post-regulation" [Rod+22]. The high-voltage setup stabilizes, sets, and measures the retarding potential with the required precision.

Other components influencing KATRIN's energy scale are work functions of spectrometer and source surfaces, and the plasma potential inside the tritium source. All individual components combined lead to a systematic shift of the fitted effective tritium endpoint. As long as the shift is stable over time or its drift is known from external measurements, the neutrino mass analysis is not affected.

In the neutrino mass fit, the effective endpoint and the squared neutrino mass value are strongly correlated parameters with a correlation coefficient of 0.97 [Kat19]. Therefore, any systematic that leads to a shift in the fitted effective endpoint also biases the measured neutrino mass. In turn, this effect can be used to check for hidden systematics in the neutrino mass by translating the effective endpoint into the Q-value [OW08] and comparing it with the Q-value obtained by independent measurements of the tritium–helium-3 mass difference [Str+14; Mye+15]. For such a cross-check the absolute energy scale needs to be determined. Measuring the energies of $^{83\mathrm{m}}$Kr conversion electrons and comparing them to appropriate literature values allows for an independent evaluation of the energy scale, limited by the uncertainties of the $^{83\mathrm{m}}$Kr transition energies.

This thesis is outlined as follows:

Chapter 1 gives a general introduction to neutrino physics.

Chapter 2 introduces the KATRIN experiment.

Chapter 3 explains how the energy-loss function for electron scattering on tritium is determined using a time-of-flight measurement technique.

Chapter 4 details the stabilization and calibration of the retarding potential.

Chapter 5 describes a novel method for determining the ^{83m}Kr transition energies with KATRIN's high-precision electron spectroscopy.

1 Neutrino physics

In the early 20th century, the discovery of radioactivity by Becquerel [Bec96] inspired many investigations on this new phenomenon. Soon, the discovered radiation was classified into three types: alpha, beta and gamma radiation. Their naming reflects the thickness of shielding needed (alpha rays need the least amount of shielding). Due to their interaction with magnetic fields, alpha rays were identified as positively charged "particles", the beta rays as negatively charged, and the gamma rays as neutral particles. [Rut99; Rut03]

Throughout this work, a citation after a full stop always concerns the entirety of the paragraph preceding it.

Contrary to the expectations from experience with mono-energetic alpha and gamma radiation, Chadwick [Cha14] measured a continuous beta-ray spectrum. Additional measurements by Ellis et al. [EWR27] and Meitner et al. [MO30] have since confirmed the – at that time – unexpected and puzzling result. Furthermore, these measurements proved that the beta decay is not characterized by a definite beta-ray energy, unlike alpha and gamma decay. And they excluded the possibility of a continuous gamma-ray emission to compensate the missing energy of the beta rays. [MO30]

Retrospectively, the continuous nature of the beta-rays was already visible in the absorption measurements by Wilson [Wil09]. Instead of varying exponentially with the thickness of the material, the ionization varied linearly, with the exception of "a small portion at the end of the curve" [Wil09].

In a "desperate attempt" to explain the observations, Pauli [Pau30] proposed to introduce an additional particle. The particle should be electrically neutral, with a spin of $1/2$, not traveling with the speed of light, and "in any event not larger than 0.01 proton mass". [Pau30] With this particle, the beta decay becomes a three-body process allowing for the beta rays to vary in energy. Building on the experimental results, including the discovery of the neutron [Cha32] and Pauli's suggestion, Fermi [Fer34] developed a theory to explain the beta decay and named the new particle "neutrino".

Continuing on the historical path, the next section gives a brief overview on observations on weak interactions and neutrinos, leading to the description of the neutrino in the Standard Model. With the discovery of the neutrino oscillations, described in section 1.2, an extension of the Standard Model which covers the generation of neutrino masses is inevitable and two of such possible extensions are presented in section 1.3. In section 1.4, methods to determine the neutrino mass are presented.

1.1 Neutrino observations and their integration into the Standard Model

Twenty years after the neutrino hypothesis, Reines et al. [RC53a] set out for a definite proof. Even though the neutrino is the ideal explanation for the observed beta-decay spectra, observing a neutrino's effect remote from its origin point would resolve any doubts for its existence and might uncover more of its properties [RC53a].

Antineutrinos emitted in the beta decay of nuclear fission progenies in a reactor were chosen as source. For their detection, the antineutrino capture reaction (inverse beta-decay)

$$\bar{\nu}_e + p \longrightarrow e^+ + n\,. \tag{1.1}$$

was employed with a water solution of cadmium chloride as target. Both reaction products, the positron and neutron can be revealed via detection of photons. For this, the target is surrounded by scintillation detector. The positron annihilation produces a prompt photon signal, which is followed by the delayed photon signal created by the capture of the neutron by the cadmium. An antineutrino signal was then identified by the time-coincidence of both signals and their energies. [Cow+56]

After the first hints for a detection [RC53b], the setup was improved, including among other things an increased target volume and improved background shielding. At the new setup, the first distinct neutrino signature, from an electron antineutrino, was observed [Cow+56].

Later, two other neutrino flavors were observed. First the muon neutrino [Dan+62] and then almost forty years later the tauon neutrino [Kod+01]. The direct neutrino detection validated Fermi's theory for the beta decay, but it was missing one important characteristic of weak interactions: parity violation. At present, parity violation is included in Fermi's theory and in this form still valid to describe most of the low-energy weak interactions [Zub20].

If parity is conserved in a process, its mirrored process has the same probability as the original. Wu et al. [Wu+57] investigated parity by measuring beta decay in nuclear spin polarized cobalt-60. The decay is given by

$$^{60}\mathrm{Co} \longrightarrow {}^{60}\mathrm{Ni}^* + e^- + \bar{\nu}_e\,. \tag{1.2}$$

The mirrored configuration was achieved by reversing the magnetic field and with it switching the polarization of cobalt-60. The emitted electrons showed a clear preferred spin direction opposite to the spin of the cobalt-60 nucleus and therefore violating parity. [Wu+57] In all other known fundamental forces: the strong force, electromagnetic force and gravity, parity is conserved.

One year later, Goldhaber et al. [GGS58] published results of an experiment measuring the helicity of the neutrinos. A particle has positive helicity if the directions of spin and momentum align and negative helicity if they are opposite. The experiment used the elec-

tron capture of europium-152

$$\underset{J=0}{e^- + {}^{152}\mathrm{Eu}} \longrightarrow \underset{J=1}{\nu_e + {}^{152}\mathrm{Sm}^*} \longrightarrow \underset{J=0}{\gamma + {}^{152}\mathrm{Sm}}\,. \tag{1.3}$$

Due to the nuclear spin $J = 0$ of ^{152}Eu, the spin of the initial state is characterized by the spin of the electron $J_z = \pm 1/2$. The spin of the initial state together with the premise that $J = 1$ for ^{152}Sm* and $J = 0$ for ^{152}Sm implies that the spins of photon and neutrino can only be opposite. Their helicity matches if they are emitted in opposite directions (opposite momenta). Using resonant absorption on samarium-152 for the photon detection restricts the detected photons to only those emitted in opposite direction to the neutrinos. [GGS58]

For photons, the helicity is equivalent to its circular polarization, which was measured via Compton scattering inside a magnetized iron block [Zub20]. From the photon measurement, Goldhaber et al. [GGS58] showed that only electron neutrinos with negative helicity take part in the weak interaction reaction (1.3).

Negative helicity is often linked to "left-handed" and positive helicity to "right-handed". Helicity is not Lorentz invariant, which implies that a transformation into a frame where a particle with mass has a reversed direction is always possible. Chirality, a related Lorentz-invariant concept, is introduced via the γ_5 matrix. The two eigenstates of γ_5 are defined as left- and right-handed chiral states. Only for the case of massless particles, chirality and helicity coincide and the eigenstates of helicity are identical to eigenstates of the γ_5 matrix. [Tho13]

The observations of parity violation and the three neutrino flavors are incorporated in the Glashow-Weinberg-Salam model [Gla61; Wei67; Sal68] (GSW), describing the electroweak section within the Standard Model. The Standard Model group is a direct product of the three symmetry groups SU(3)⊗SU(2)⊗SU(1). SU(3) is the color group of quantum chromodynamics, SU(2) the weak isospin and U(1) the hypercharge. The elementary fermions within the Standard Model can be grouped into doublets for the left-handed fields and singlets for right-handed fields. [Zub20]

Omitting the quarks, the left-handed fields of the remaining elementary fermions (leptons) are

$$\begin{pmatrix} e \\ \nu_e \end{pmatrix}_L \quad \begin{pmatrix} \mu \\ \nu_\mu \end{pmatrix}_L \quad \begin{pmatrix} \tau \\ \nu_\tau \end{pmatrix}_L \tag{1.4}$$

and the singlets

$$(e)_R, (\mu)_R, (\tau)_R\,. \tag{1.5}$$

Matching the experimental observations (for example the experiment by Goldhaber et al. [GGS58]), no right-handed neutrinos are included.

Within the Standard Model, all particles are considered massless to guarantee gauge invariance. By spontaneous symmetry breaking, fermions obtain their mass via the *Higgs mechanism* [Hig64; EB64; Kib67]. The left- and right-handed fields couple via a *Yukawa coupling* to the Higgs field. After symmetry breaking, the Higgs field develops

its vacuum expectation value and forms a mass term together with the Yukawa coupling. [Zub20]

Since the Yukawa coupling is not possible without the right-handed component, the neutrinos are massless within this description. Without experimental evidence for non-vanishing neutrino masses, a well justified description at that time.

1.2 Discovery of neutrino flavor oscillations

Early on, neutrinos were discovered as ideal messenger particles. Since they are neutral particles, similar to photons, they travel in a direct path from their origin point to the detector, without deflection by electromagnetic fields. Unlike photons, their interaction is limited to the weak interaction, a double-edged property. They can travel over long distances undisturbed, but large volumes are needed for detection.

One application for neutrinos as messenger particles is the investigation of fusion reactions inside the Sun. As stated by Bahcall [Bah64b], "only neutrinos, with their extremely small interaction cross sections, can enable us to see into the interior of a star".

1.2.1 *Solar neutrinos*

Inside the Sun, helium is produced by fusion of hydrogen via

$$4\,\mathrm{p} \longrightarrow {}^{4}\mathrm{He} + 2\,\mathrm{e}^{+} + 2\,\nu_{\mathrm{e}} + 26.2\,\mathrm{MeV}. \tag{1.6}$$

Behind this net reaction are two fundamental fusion cycles; the pp-cycle and the CNO-cycle. [Zub20]

Bahcall [Bah64a] compiled the expected energy spectrum for neutrinos to be tested with a neutrino detection experiment. The expected spectrum consists of multiple continuous and mono-energetic spectra with endpoint and line energies ranging from about 0.4 MeV up to about 17 MeV [Bah64a]. Over time, the predictions for the fusion process inside the Sun were further refined and summarized in the *standard solar model*.

Solar neutrinos can be captured by the endothermic inverse beta-decay reaction

$${}^{37}\mathrm{Cl} + \nu_{\mathrm{e}} \longrightarrow {}^{37}\mathrm{Ar} + \mathrm{e}^{-} \tag{1.7}$$

with an energy threshold of 0.81 MeV [Bah64b]. The produced ^{37}Ar has a half-life of 35 days. Extracting it and observing its electron capture decay via x-rays and 2.8-keV Auger electrons gives a measure of the neutrino flux. In the experiment conducted by Davis [Dav64], Perchloroethylene C_2Cl_4, also known as "dry-cleaning fluid", was filled into large tanks as a chlorine-37 source. To minimize the production of argon-37 by background processes, the experiment was located deep underground (4000 meters of water-equivalent shielding, m.w.e.).

After increasing the detector volume from about 3.8 m^3 to about 1500 m^3 and moving even deeper underground (4400 m.w.e.), a significant amount of argon-37 above the expected background was measured. However, the measured rate did not match the expectation by the standard solar model but was significantly lower. [DHH68]

The experiment was located in the Homestake gold mine in Lead, South Dakota [DHH68].

The experiment, also referred to as the *Homestake experiment*, was further improved and repeatedly conducted over twenty years. Still, the observed rate was reproducibly only about a third of the prediction by the standard solar model. [Cle+98] The discrepancy was dubbed the *solar neutrino problem*.

The experiments have different energy thresholds and are therefore sensitive to different parts of the solar neutrino spectrum. As introduced later in section 1.2.3, the neutrino oscillation probability is energy dependent, explaining the different reduction factors.

Other experiments have confirmed the existence of a solar neutrino shortage, although they have observed different reduction factors. For example, Super-Kamiokande and also its predecessor experiment Kamiokande. In contrast to the Homestake experiment, it is a real-time measurement, including directional information of the neutrinos via an imaging water Cherenkov detector. [SK98b]

The later built Sudbury Neutrino Observatory (SNO) experiment, solved the solar neutrino problem. Analogous to Kamiokande and Super Kamiokande, SNO is a real-time Cherenkov detector. Neutrinos are detected via elastic scattering (ES) on electrons

$$\nu_x + e^- \longrightarrow \nu_x + e^- . \tag{1.8}$$

Here, ν_x represents all three flavors. For ν_μ and ν_τ, ES only works via neutral currents, resulting in a reduced detection sensitivity. SNO used heavy water (D_2O) instead of water. The deuterium allows for a neutrino flavor independent detection via the neutral current (NC) reaction

$$\nu_x + d \longrightarrow p + n + \nu_x . \tag{1.9}$$

Combined with the charged current (CC) reaction

$$\nu_e + d \longrightarrow p + p + e^- \tag{1.10}$$

which is exclusive for the electron neutrino, the electron and non-electron solar neutrino flux can be measured. The total flux measured via NC is in agreement with the prediction of the solar model. The flux measured via CC and ES is again lower than the prediction, compatible to the other experiments only sensitive to electron neutrinos. The SNO measurement proved that the overall solar neutrino flux predicted by the solar model was correct, but the neutrinos changed their flavor on their way to Earth. [Sno02]

1.2.2 *Atmospheric neutrinos*

Cosmic rays hitting nuclei in the Earth's atmosphere create pions which in turn decay mainly into muons and muon neutrinos. On their way to Earth, the muons decay into electrons, electron neutrinos, and muon neutrinos. Therefore, the number of muon neutrinos arriving on Earth is about double the number of electron neutrinos. [Hir+88]

Water Cherenkov detectors measure not only solar neutrinos but also atmospheric neutrinos which normally have higher energies than the solar neutrinos. Atmospheric muon neutrinos produce muons via CC reactions inside the water and the electron neutrinos produce electromagnetic showers. The showers result in a broader Cherenkov light pattern compared to the sharper light pattern of the muon. Using the light pattern, the events are classified into muon-neutrino-like events and electron-neutrino-like events. [Zub20]

The atmospheric neutrino flux was measured at Kamiokande. Instead of a muon neutrino flux double the electron neutrino flux, a significantly lower muon neutrino flux was measured [Hir+88]. The successor experiment Super-Kamiokande, with higher statistics and improved resolution, reproduced the lower flux and found a spatial asymmetry [SK98a].

Atmospheric neutrinos entering the Super-Kamiokande detector at the top (downward-going) have a much shorter travel length (about 15 km) than the ones entering at the bottom (upward-going) which first need to pass through the Earth (about 13 000 km). The muon neutrino flux deviance showed a dependence on the neutrinos flight path; the longer the flight path, the higher the deviation. Additionally, an energy dependency was measured. The observations can be explained by a two-neutrino flavor oscillation from muon neutrinos into tauon neutrinos. [SK98a]

The discovery of flavor change for atmospheric neutrinos at Super-Kamiokande, and the discovery at SNO that solar neutrinos do not disappear but also change their flavor on their way to earth was rewarded with the Nobel Prize in physics: "for the discovery of neutrino oscillations, which shows that neutrinos have mass". [Nob15]

1.2.3 *Framework for neutrino oscillations*

Flavor change is well-known from the quark sector. Here, the weak and mass eigenstates are not identical but connected via the CKM matrix. Since quarks interact dominantly via the strong interaction, the mass eigenstates are more familiar than the weak eigenstates and therefore they define the flavor of the particles. For neutrinos it is the other way around. Their weak eigenstates are the ones observed in the measurement and therefore it is natural to connect their different flavors to the weak eigenstates. [Gri08]

For neutrinos, three flavor eigenstates $|\nu_\alpha\rangle$ are known with $\alpha = e, \tau, \mu$. With the Pontecorvo Maki Nakagawa Sakata (PMNS) mixing matrix U, the flavor eigenstates can be expressed in terms of the three mass eigenstates $|\nu_i\rangle$ with $i = 1, 2, 3$:

The naming reflects the important contributors Pontecorvo [Pon58] and Maki et al. [MNS62].

$$|\nu_\alpha\rangle = \sum_i U_{\alpha i} |\nu_i\rangle \,. \tag{1.11}$$

Or the other way around,

$$|\nu_i\rangle = \sum_\alpha U^*_{\alpha i} |\nu_\alpha\rangle \,, \tag{1.12}$$

using that U is unitary and $\left(U^{-1}\right)_{kl} = \left(U^\dagger\right)_{kl} = \left((U^*)^T\right)_{kl} = (U^*)_{lk}$, with $U^\dagger$ the complex conjugate transpose of U and U^* the complex conjugate of U. The complex conjugate of (1.11) and (1.12), gives the relation between the eigenstates for antineutrinos. [Zub20; Tho13]

The unitary condition $UU^\dagger = \mathbb{1}$, with $\mathbb{1}$ the identity matrix, in Kronecker delta notation: $(I)_{ij} = \delta_{ij}$ also implies that

$$\sum_i U_{\alpha i} U^*_{\beta i} = \delta_{\alpha\beta} \,. \tag{1.13}$$

In other words, the eighteen independent parameters (nine complex numbers) are constrained by nine fixed relations. A basic, real, 3×3 orthogonal rotation matrix is described by three rotation angles θ_{12}, θ_{23}, and θ_{13}. Since the PMNS matrix is complex, six complex phases are additional degrees of freedom. However, five of them can be absorbed into the definitions of the particles without physical consequences. Leaving the three mixing angles and a single complex phase δ. [Tho13]

The full PMNS matrix can be written as [Tho13]

$$\begin{aligned} U = &\begin{pmatrix} 1 & 0 & 0 \\ 0 & \cos\theta_{23} & \sin\theta_{23} \\ 0 & -\sin\theta_{23} & \cos\theta_{23} \end{pmatrix} \times \begin{pmatrix} \cos\theta_{13} & 0 & \sin\theta_{13}e^{-i\delta} \\ 0 & 1 & 0 \\ -\sin\theta_{13}e^{-i\delta} & 0 & \cos\theta_{13} \end{pmatrix} \\ &\times \begin{pmatrix} \cos\theta_{12} & \sin\theta_{12} & 0 \\ -\sin\theta_{12} & \cos\theta_{12} & 0 \\ 0 & & 1 \end{pmatrix}. \end{aligned} \tag{1.14}$$

The wave function of a neutrino with flavor α produced at $t = 0$ is a coherent linear superposition of mass eigenstates (1.11)

$$|\Psi(0)\rangle = |\nu_\alpha\rangle = \sum_i U_{\alpha i}|\nu_i\rangle\,. \tag{1.15}$$

The time dependency of the mass eigenstates, examined at a fixed point $\vec{x}$, is

$$|\Psi(\vec{x},t)\rangle = \sum_i U_{\alpha i}e^{-i\phi_i}|\nu_i\rangle = \sum_{i,\beta} U_{\alpha i}U^*_{\beta i}e^{-i\phi_i}|\nu_\beta\rangle\,. \tag{1.16}$$

Here, ϕ_i is the phase of the plane wave for each mass eigenstate

$$\phi_i = p_i \cdot x_i = (E_i t - \vec{p}\cdot\vec{x}) \tag{1.17}$$

and $|\Psi(\vec{x},t)\rangle$ is expressed in terms of the flavor states using (1.12). The probability of oscillation from a flavor α into β can be calculated from

$$P(\nu_\alpha \to \nu_\beta) = \left|\langle\nu_\beta|\Psi(\vec{x},t)\rangle\right|^2 = \left|\sum_{i,\beta} U_{\alpha i}U^*_{\beta i}e^{-i\phi_i}\right|^2. \tag{1.18}$$

The explicit form of the oscillation probability is now written for the case of two-flavor oscillation. Even though it is a simplification, the main properties can be illustrated with it. In the case of two-flavor oscillations, the PMNS matrix (1.14) is reduced to

$$U' = \begin{pmatrix} \cos\theta & \sin\theta \\ -\sin\theta & \cos\theta \end{pmatrix}. \tag{1.19}$$

Analogous to the three-flavor case, it is a unitary matrix with four parameters. One rotation angle θ and three complex phases. The phases are again absorbed in the definitions of the particles and only θ remains. In particular, without a complex phase, charge-parity (CP) violation is not possible. It occurs only for three or more eigenstates. [Tho13]

With the two-flavor mixing matrix (1.19), the oscillation probability (1.18) for the two flavor case is

$$P(\nu_\alpha \to \nu_\beta) = \sin^2(2\theta)\,\sin^2\left(\frac{\Delta\phi_{12}}{2}\right), \tag{1.20}$$

Table 1.1 **Neutrino mixing parameters.** The values are taken from the Particle Data Group [PDG22]. Δm^2_{ij} is defined as $m_i^2 - m_j^2$. The PMNS matrix (1.14) can be obtained with the values for the mixing angles listed in the table together with the CP-violating phase $\delta = 1.36^{+0.20}_{-0.16}\,\pi\,\mathrm{rad}$ [PDG22]. Currently, normal ordering (marked with (n) in the table) is favored over inverted ordering (i) by a $\Delta\chi^2$ within $2\,\sigma$ to $3\,\sigma$, depending on the selected data [PDG22].

ij	$\sin^2(\theta_{ij})$	Δm^2_{ij} in $\mathrm{eV}^2/\mathrm{c}^4$
12	0.307(13)	$-7.53(18) \times 10^{-5}$
23 (n)	0.546(21)	$-2.453(33) \times 10^{-3}$
23 (i)	0.539(22)	$2.536(34) \times 10^{-3}$
13	0.0220(7)	

where $\Delta\phi_{12} = \phi_1 - \phi_2$ is the phase difference. The oscillation probability is zero for the case $\Delta\phi_{12} = 0$. With the definition of the plane wave's phase (1.17), $\Delta\phi_{12}$ can be linked to the masses of ν_1 and ν_2 by assuming $p_1 = p_2 = p$ and using $m \ll E$:

$$\Delta\Phi_{12} \approx \frac{m_1^2 - m_2^2}{2p} L\,. \tag{1.21}$$

Additionally it was assumed that the neutrino velocity is $v/c \approx 1$ and with it $L \approx T$ (natural units), neglecting that the different mass eigenstates will propagate with different velocities. Justification of this simplified approach to avoid a full wave-packet treatment can be done by checking that the same result is obtained by assuming $E_1 = E_2$ or the same velocities $v_1 = v_2$. (1.21) show that oscillation is only possible if the mass eigenstates are different which in turn demands for at least one mass state to be non-zero. [Tho13]

The full two-flavor neutrino oscillation probability in terms of travel distance, mass difference and energy of the neutrino ($p = E_\nu$) follows from (1.20) and (1.21) [Tho13]:

$$P(\nu_\alpha \to \nu_\beta) = \sin^2(2\theta)\,\sin^2\left(\frac{m_1^2 - m_2^2}{4E_\nu} L\right). \tag{1.22}$$

The mixing angle θ and the mass difference $\Delta m^2_{12} = m_1^2 - m_2^2$ are probed via neutrino sources of different energies and at different distances. From the oscillation probability follows that an experiment is the most sensitive at $\Delta m^2_{12} \approx E/L$. Depending on the detector, or the source, E and L are not always very well defined. [Zub20]

A variety of experiments, using solar, atmospheric, accelerator and reactor neutrinos, allows to determine the parameters of the three-neutrino mixing. A list of the most recent results is given in table 1.1.

Flavor oscillation experiments provide access to the mass differences Δm^2_{ij} and the elements of the PMNS matrix. Using the mass differences, possible values for the mass eigenstates can be predicted.

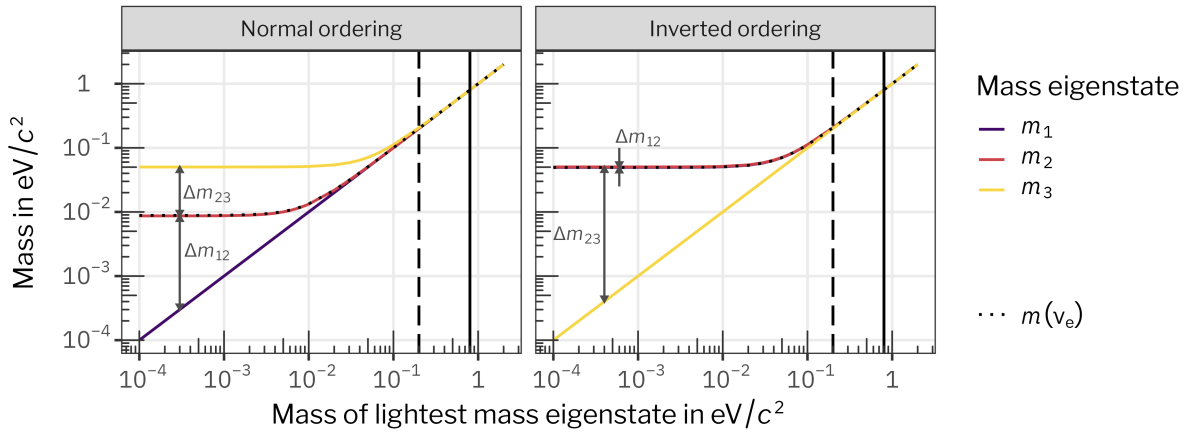

Figure 1.2 **Best-fit values for neutrino masses.** Using the mass differences listed in table 1.1, the values for the mass eigenstates m_1, m_2, m_3 can be calculated in dependence of the lightest one. In normal ordering, the lightest mass state is m_1, and in inverted ordering, it is m_3. The dotted line represents $m(\nu_e)$ which is an average of the mass eigenstates for the electron neutrino, weighted by the PMNS matrix (1.11). The vertical lines show the current limit (solid) and future sensitivity (dashed) on $m(\nu_e)$ from KATRIN (cf. chapter 2).

The figure is based on [OW08].

Two questions are still open; one is the ordering of the mass states. m_1 could be the lightest mass state, this case is commonly known as *normal ordering*, or m_3 could be lightest, known as *inverted ordering*. The ordering of the two closest mass states is known from the Mikheyev-Smirnov-Wolfenstein (MSW) effect [Wol78; MS86].

The second open question is the absolute mass scale for neutrinos. Without a value for the absolute mass scale, the mass of the lightest neutrino mass state is unknown. In fig. 1.2, the possible masses of the mass eigenstates m_i are plotted against the lightest mass eigenstate for normal ordering as well as inverted. If the mass of the lightest mass eigenstate is larger than $0.1\,\mathrm{eV}/c^2$, all three m_i have a similar value. This case is often referred to as *degenerate limit*.

Additionally, the weighted average of mass eigenstates for the electron neutrino $m(\nu_e)$ is plotted in fig. 1.2. For the degenerate limit, $m(\nu_e)$ coincides with m_i, including the lightest mass eigenstate. The value of $m(\nu_e)$ is limited by measurements of the KATRIN experiment which will be presented in chapter 2.

1.3 Neutrino mass generation

As discussed above, neutrino oscillations are only possible if the mass eigenstates are different, requiring at least two out of the three mass eigenstates to be non-zero. Therefore, the Standard Model as introduced in section 1.1 needs to be extended to incorporate non-zero neutrino masses.

Following a short introduction into Dirac and Majorana mass terms, the *seesaw mechanism*, a common textbook approach to explain the experimentally observed small neutrino masses, is presented. Afterwards, the *scotogenic model* is introduced in which the neutrinos acquire their mass at a one-loop level, instead of at tree-level, as in the common seesaw mechanism.

1.3.1 *Dirac and Majorana mass terms*

This section follows the more detailed introduction given in the book [Zub20].

A general Dirac mass term is defined as

$$\mathscr{L} = -m_{\mathrm{D}}\overline{\psi}\psi, \tag{1.23}$$

where ψ are four-component Dirac spinors.

The chirality for ψ is defined via the γ_5 operator. Its two eigenvalues ± 1 reflect the chirality of the particle (+1 right-handed and −1 left-handed). The right- and left-handed components can be defined with two projection operators and the γ_5 matrix in the Dirac basis

$$P_{\mathrm{R}} = \frac{1}{2}(1-\gamma_5), \quad P_{\mathrm{L}} = \frac{1}{2}(1+\gamma_5), \quad \gamma_5 = \begin{pmatrix} 0 & \mathbb{1} \\ \mathbb{1} & 0 \end{pmatrix}. \tag{1.24}$$

Using P_{R} and P_{L}, any spinor can be written in its chiral components as

$$\psi = (P_{\mathrm{R}} + P_{\mathrm{L}})\psi = P_{\mathrm{R}}\psi + P_{\mathrm{L}}\psi = \psi_{\mathrm{R}} + \psi_{\mathrm{L}}\,. \tag{1.25}$$

The Dirac mass term (1.23) expressed in chiral components is

$$\mathscr{L} = -m_{\mathrm{D}}\left(\overline{\psi}_{\mathrm{L}}\psi_{\mathrm{R}} + \overline{\psi}_{\mathrm{R}}\psi_{\mathrm{L}}\right). \tag{1.26}$$

Adding the charge conjugate of ψ (ψ^c), two additional mass terms, namely the Majorana mass terms

$$\mathscr{L}_{\mathrm{M}} = -\frac{1}{2}\left(m_{\mathrm{M}}\overline{\psi}\psi^c + m_{\mathrm{M}}^*\overline{\psi}^c\psi\right) = -\frac{1}{2}m_{\mathrm{M}}\overline{\psi}\psi^c + \mathrm{h.c.} \tag{1.27}$$

are possible (the factor $1/2$ keeps normalization). "h.c." is used as shorthand for hermitian conjugate. Using the notation (analogously for ψ_{L}^c)

$$\psi_{\mathrm{R}}^c = (\psi^c)_{\mathrm{R}} = (\psi_{\mathrm{L}})^c, \tag{1.28}$$

the Majorana mass term is written in chiral components as

$$\mathscr{L}_{\mathrm{M}} = -\frac{1}{2}\left(m_{\mathrm{L}}\overline{\psi}_{\mathrm{L}}\psi_{\mathrm{R}}^c + \mathrm{h.c.} + m_{\mathrm{R}}\overline{\psi}_{\mathrm{L}}^c\psi_{\mathrm{R}} + \mathrm{h.c.}\right). \tag{1.29}$$

It is important to note that the Majorana mass terms are only allowed for the neutrino. For the other fundamental fermions, only Dirac mass terms are allowed due to their electric charge.

To distinguish between fields for neutrinos participating in the weak interaction, called active neutrinos, and the ones not participating, called sterile neutrinos, the following notation is chosen

$$\psi_{\mathrm{L}} = \nu_{\mathrm{L}}, \quad \psi_{\mathrm{R}}^c = \nu_{\mathrm{R}}^c, \quad \psi_{\mathrm{R}} = N_{\mathrm{R}}, \quad \psi_{\mathrm{L}}^c = N_{\mathrm{L}}^c\,. \tag{1.30}$$

The active neutrinos are marked with ν and the sterile ones with N.

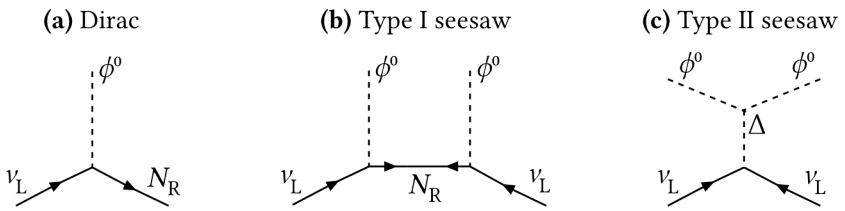

Figure 1.3 **Neutrino mass generation.** The schematic visualizes different possible neutrino mass generations at tree level. The dashed line denotes the neutral Higgs field ϕ^0. The solid black lines depict neutrino fields as defined in (1.30). The arrows of charge-conjugated fields point backward in time (from right to left). Δ is a Higgs triplet.
The schematic is adapted from [OW08].

1.3.2 *Seesaw mechanism*

The most naive approach is to assume that neutrinos acquire their masses analogously to other fermions via a pure Dirac mass term (1.26). For this to work for neutrinos, a right-handed neutrino field N_R and a Yukawa coupling [Kay03]

$$-f_\nu \, \phi^0 \, \bar{\nu}_L \, N_R + \text{h.c.} \tag{1.31}$$

is introduced in addition to the already existing left-handed neutrino field ν_L. f_ν is a coupling constant, ϕ^0 the neutral Higgs field, N_R a right-handed neutrino field. The mechanism is shown in fig. 1.3a. When the Higgs field develops a vacuum expectation value $\langle\phi^0\rangle$, the Yukawa coupling yields a Dirac mass term for the neutrino [Kay03]

$$\mathscr{L}_D = -f_\nu \langle\phi^0\rangle \, \bar{\nu}_L \, N_R + \text{h.c.} = -m_D \, \bar{\nu}_L \, N_R + \text{h.c.}\,. \tag{1.32}$$

For small neutrino masses, for example $m_D < 0.8\,\text{eV}/c^2$, and with $\langle\phi^0\rangle = 246\,\text{GeV}/\sqrt{2}$ [PDG22], the coupling f_ν is smaller than 5×10^{-12}. Therefore, at least six orders of magnitude smaller than for the electron ($\approx 3 \times 10^{-6}$). Such differences in the Yukawa couplings are not excluded but are considered to be rather unnatural [OW08].

Another approach, allowing for more flexibility, is to assume that neutrinos are Majorana particles, implying they are their own antiparticles. Though, if neutrinos were Majorana particles, the lepton number would be violated. [OW08]

Allowing Majorana fields and combining the Dirac (1.26) and Majorana mass terms (1.29) in the notation defined in (1.30), results in a universal Dirac-Majorana mass term [Zub20]:

$$\begin{aligned}\mathscr{L} &= -\frac{1}{2}\left(m_D\left(\bar{\nu}_L \, N_R + \bar{N}_L^c \, N_R^c\right) + m_L \bar{\nu}_L \, N_R^c + m_R \bar{N}_L^c \, N_R\right) + \text{h.c.} \\ &= -\frac{1}{2}\begin{pmatrix}\bar{\nu}_L & \bar{N}_L^c\end{pmatrix}\begin{pmatrix}m_L & m_D \\ m_D & m_R\end{pmatrix}\begin{pmatrix}N_R^c \\ N_R\end{pmatrix} + \text{h.c.}\,.\end{aligned} \tag{1.33}$$

The matrix introduced in the last step is called mass matrix M. Calculating the eigenvalues of M and using their absolute values gives two possible neutrino masses.

For the case of $m_\mathrm{L} = 0$ and $m_\mathrm{D} \ll m_\mathrm{R}$, the two mass values are [Zub20]

$$m_1 = m_\nu = \frac{m_\mathrm{D}^2}{m_\mathrm{R}}, \quad m_2 = m_\mathrm{N} = m_\mathrm{R}\left(1 + \frac{m_\mathrm{D}^2}{m_\mathrm{R}^2}\right) \approx m_\mathrm{R}\,. \tag{1.34}$$

Assuming a sterile neutrino with a mass (m_N) in the order of the grand unification energy (GUT scale), the Dirac mass can be on the same order as for other leptons while still allowing for a sub-eV scale active neutrino. This scenario is referred to as type I seesaw and is illustrated in fig. 1.3b. [OW08]

Another possibility is the type II seesaw, depicted in fig. 1.3c. Here, small neutrino masses are realized with a Higgs triplet Δ. In this case, $m_\mathrm{L} \neq 0$ and the left-handed neutrino and its charge conjugate couple to Δ.

In a generalized approach, the type I and II seesaw are described by an effective dimension-five operator [Wei79]. It contains two Higgs fields, two left-handed fermion doublets and is scaled by a large effective mass in the denominator which generates the small neutrino masses [OW08]. In total, there are only three tree-level realizations of this operator [Ma98] (two of them were discussed here) and all three of them lead to new particles with masses too heavy to be easily observed in the near future [Ma06].

1.3.3 *Scotogenic model*

As a member of the DFG-financed Research Training Group "Strong and weak interactions from hadrons to dark matter" (GRK2149), I had the opportunity to complete a two-month collaborative theory project. Within this project, I participated in investigating the scotogenic model with regard to the neutrino mass and the capabilities of KATRIN, which led to the publication [Boe+20]. My contributions were the inital setup and the validation calculations (benchmarks with comparisons to previous publications). In the rest of this section, I briefly report on the results presented in [Boe+20].

As an alternative to the seesaw mechanism, a radiative seesaw mechanism, later named the *scotogenic model*, was proposed by Ma [Ma06]. The new particles introduced in this model can be light enough to be detected at current experiments [Ma06].

The scotogenic model is only a small extension to the Standard Model (SM). In addition to the three sterile neutrinos N_i already needed for the type I seesaw, one Higgs doublet η is added. N_i and η are odd, whereas the SM neutrinos and Higgs are even under discrete $\mathbb{Z}_2$ symmetry. Analogous to *R-parity* in the supersymmetric standard model, $\mathbb{Z}_2$ is an exact symmetry. With exact $\mathbb{Z}_2$ symmetry, the vacuum expectation value of η^0 is zero, a lightest stable particle (LSP) exists and no Dirac mass links the SM neutrinos to the sterile neutrinos. [Ma06]

The discussion in section 1.3.2 above was restricted to one generation of neutrinos. With three neutrino generations, three sterile neutrinos are needed.

Without Dirac masses linking the neutrinos to the sterile neutrinos, the seesaw mechanism is not operable. The masses of neutrinos are only generated by coupling to the SM Higgs over one loop via η, as depicted in fig. 1.4. The LSP, the lightest among the new particles, is

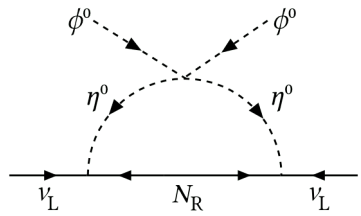

Figure 1.4 **Neutrino mass generation in the scotogenic model.** The neutral component η^0 of the complex Higgs doublet η couples to the Standard Model (SM) neutral Higgs field ϕ^0. Fermion singlets N_R couple to η^0 and SM neutrinos ν, thereby generating neutrino masses within one loop.

an ideal dark matter candidate. Hence, within the scotogenic model, neutrinos acquire their masses only due to their interactions with dark matter. [Ma06]

1.3.3.1 *Model definition*

Representing the fermions with Weyl spinors, the Lagrangian of the scotogenic model is

$$\mathscr{L}_N = -\frac{1}{2} m_{N_i} N_i N_i + y_{i\alpha} (\eta^\dagger L_\alpha) N_i + h.c - V, \tag{1.35}$$

where

N_i are three fermion singlets (sterile neutrinos) and

m_{N_i} are their masses, and the lightest is a LSP (dark matter candidate),

$y_{i\alpha}$ are 3×3 matrices of Yukawa couplings,

η is a complex Higgs doublet, with a charged scalar component η^+ and a neutral component with real and imaginary parts $\eta^0 = (\eta_R + i\eta_I)$,

L_α with $\alpha = 1, 2, 3$ are left-handed doublets (three generations of SM leptons), and

V a scalar potential (Higgs potential).

The Higgs potential is defined as

$$\begin{aligned} V =& m_\phi^2 \phi^\dagger \phi + m_\eta^2 \eta^\dagger \eta \\ &+ \frac{\lambda_1}{2} \left(\phi^\dagger \phi\right)^2 + \frac{\lambda_2}{2} \left(\eta^\dagger \eta\right)^2 \\ &+ \lambda_3 \left(\phi^\dagger \phi\right) \left(\eta^\dagger \eta\right) + \lambda_4 \left(\phi^\dagger \eta\right) \left(\eta^\dagger \phi\right) \\ &+ \frac{\lambda_5}{2} \left(\left(\phi^\dagger \eta\right)^2 + \left(\eta^\dagger \phi\right)^2\right), \end{aligned} \tag{1.36}$$

where ϕ is the SM Higgs doublet. The mass m_ϕ is determined by the Higgs boson mass m_h as $m_\phi^2 = m_h^2/2$. The parameter λ_1 is fixed by the Higgs vacuum expectation value $\langle \phi^0 \rangle$ and m_h to $\lambda_1 = m_h^2/(2\langle \phi^0 \rangle^2)$.

Setting $\lambda_2 = 0.2$ without loss of generality, the masses of η^+ and the real and imaginary parts of η^0 are:

$$\begin{aligned} m_{\eta^+}^2 &= m_\eta^2 + \lambda_3 \langle \phi^0 \rangle^2 \,, \\ m_R^2 &= m_\eta^2 + (\lambda_3 + \lambda_4 + \lambda_5) \langle \phi^0 \rangle^2 \,, \\ m_I^2 &= m_\eta^2 + (\lambda_3 + \lambda_4 - \lambda_5) \langle \phi^0 \rangle^2 \,. \end{aligned} \tag{1.37}$$

Important to note, if $\lambda_5 = 0$ lepton number would be conserved and neutrinos would be massless.

The SM neutrino mass matrix is constructed with the diagonal mass matrix Λ containing the dark sector masses and a Yukawa matrix y describing the coupling

$$(m_\nu)_{\alpha\beta} = (y^T \Lambda y)_{\alpha\beta} \,. \tag{1.38}$$

To incorporate flavor oscillations, the PMNS matrix U is used to diagonalize the mass matrix:

$$U^T m_\nu U = \hat{m}_\nu \equiv \mathrm{diag}(m_1, m_2, m_3) \,. \tag{1.39}$$

The masses, and with it the Yukawa couplings, can be constrained by experimental inputs, such as neutrino oscillation results or investigations of lepton flavor violation (LFV) bounds. For this, the *Casas-Ibarra parametrization*, named after its inventors [CI01] is used. It is a bottom-up approach which starts with existing experimental information and finds compatible Yukawa couplings [CI01]. More precisely, the Yukawa couplings can be expressed in terms of a set of given masses Λ_i and the mixing parameters contained in U as

$$y = \sqrt{\Lambda^{-1}} R \sqrt{\hat{m}_\nu} U^\dagger \,, \tag{1.40}$$

where R is an orthogonal matrix which depends on arbitrary rotation angles $\theta_i \in [0; 2\pi]$.

For the case of $\lambda_5 \ll 1$, $m_R^2 \approx m_I^2$, the neutrino mass matrix (1.38) is approximately

$$\begin{aligned} (m_\nu)_{\alpha\beta} \approx 2\lambda_5 \langle \phi^0 \rangle^2 \sum_{i=1}^{3} & \frac{y_{i\alpha} y_{i\beta} m_{N_i}}{32\pi^2 (m_{R,I}^2 - m_{N_i}^2)} \\ & \times \left(1 + \frac{m_{N_i}^2}{m_{R,I}^2 - m_{N_i}^2} \log\left(\frac{m_{N_i}^2}{m_{R,I}^2} \right) \right) \end{aligned} \tag{1.41}$$

and linear in λ_5.

1.3.3.2 *Numerical inputs*

The masses of the dark sector (m_η, m_{N_i}) are varied within 0.1 – 10 TeV/c^2. For the neutrino mass matrix, the neutrino mixing parameters summarized in [Est+20] are used. They are allowed to vary within their $3\,\sigma$ uncertainties. To fulfill the perturbativity bound, $|\lambda_2, \lambda_3, \lambda_4, \lambda_5| < 4\pi$ and $|y_{i\alpha}|^2 < 4\pi$ is used.

The results are restricted to satisfy current and future LFV bounds, as well as dark matter (DM) relic density. For LFV bounds, the branching ratios (BR) and conversion rates (CR) of the following three processes are considered:

$$
\begin{aligned}
&\mathrm{BR}(\mu \longrightarrow \mathrm{e}\,\gamma) && < 4.2 \times 10^{-13}\ [\mathrm{Meg16}] && (2 \times 10^{-15}\ [\mathrm{Ren18}])\,,\\
&\mathrm{BR}(\mu \longrightarrow 3\,\mathrm{e}) && < 1 \times 10^{-12}\ [\mathrm{Sin88}] && (10^{-16}\ [\mathrm{Blo{+}13}])\,,\\
&\mathrm{CR}(\mu \longrightarrow \mathrm{e}) && < 4.3 \times 10^{-12}\ [\mathrm{Sin93}] && (10^{-18}\ [\mathrm{Pri06}])\,.
\end{aligned}
$$

For the computation of BR and CR from the masses of the charged scalar and sterile neutrinos and their Yukawa couplings, the software SPheno v4.0.3 [PS12] was used.

The Planck measurement of $\Omega h^2 = 0.12$ is used as input for the central value of the DM relic density. Using the software micrOMEGAs v5.0.8 [Bél+18], the results are restricted to the central value, within an uncertainty of 0.02.

1.3.3.3 *Numerical results*

With the above defined input parameters and constraints, the parameter space for the scotogenic model is scanned. Possible points, satisfying either the LFV or dark matter constraints, or both, are investigated further. The linear dependency of the SM neutrino masses on the dark sector Higgs boson coupling λ_5 (1.41) is investigated by plotting λ_5 against the lightest neutrino mass m_{lightest} in fig. 1.5. After applying LFV and DM relic density constraints, a linear fit of λ_5 on $m_{\mathrm{lightest}} \geq 0.052\,\mathrm{eV}/c^2$ results in a slope of

$$
|\lambda_5| = \begin{cases} 3.08(5) \times 10^{-9} m_{\mathrm{lightest}}/(\mathrm{eV}/c^2) & (\mathrm{NO})\,, \\ 3.11(6) \times 10^{-9} m_{\mathrm{lightest}}/(\mathrm{eV}/c^2) & (\mathrm{IO})\,. \end{cases} \tag{1.42}
$$

In both cases, normal ordering (NO) and inverted ordering (IO), m_{lightest} is defined to be the lightest mass eigenstate. For $m_{\mathrm{lightest}} < 0.052\,\mathrm{eV}/c^2$, λ_5 is independent of m_{lightest} and

$$
|\lambda_5| = \begin{cases} 1.6(7) \times 10^{-10} & (\mathrm{NO})\,, \\ 1.7(15) \times 10^{-10} & (\mathrm{IO})\,. \end{cases} \tag{1.43}
$$

Therefore, as soon as the absolute neutrino mass scale is known, also λ_5 is fixed.

Already new experimental constraints on the absolute mass scale and LFV, as displayed in fig. 1.6 can further limit the whole available parameter space of the scotogenic model. Important to note, LFV and the mass scale constrain the parameter space in an orthogonal way.

1.4 Neutrino mass measurement

The implications of the absolute mass scale for the scotogenic model is only one example out of many of the importance of its determination. Another example is the significance of the neutrino mass scale for cosmology. The obvious way forward to understand the origin of neutrino masses and to complete the understanding within neutrino physics is the experimental determination of the absolute neutrino mass scale.

The ongoing pursuit on the mass scale can be categorized in three general paths. The first uses cosmological observations to determine

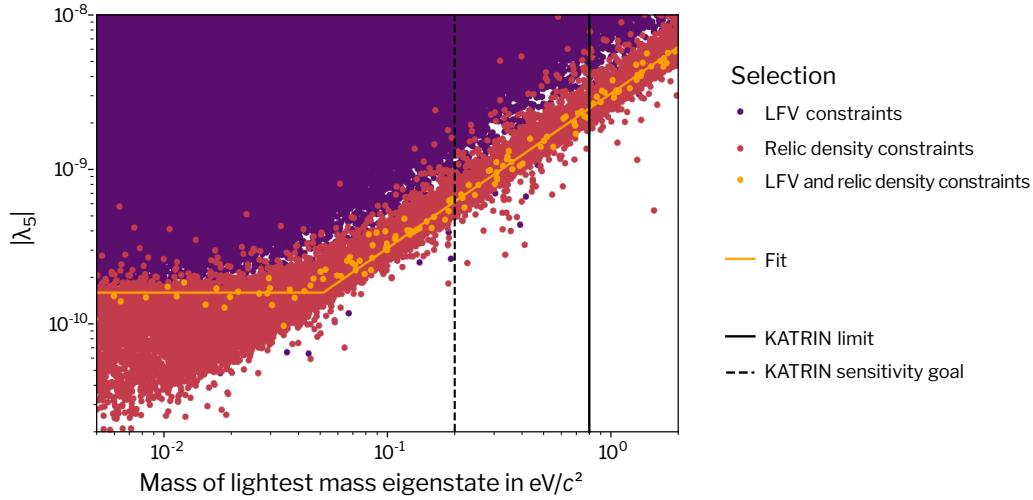

Figure 1.5 **Influence of the lightest neutrino mass on Yukawa couplings within the scotogenic model.** The absolute values of the dark sector Higgs boson coupling λ_5 are shown as a function of the lightest neutrino mass m_{lightest}. The lepton flavor violation (LVF) and dark matter relic density constraints are applied individually as well as together. The vertical lines indicate current (solid) and future (dashed) constraints by the KATRIN experiment (cf. chapter 2).

The plot is adapted from [Boe+20], used under CC BY 4.0.

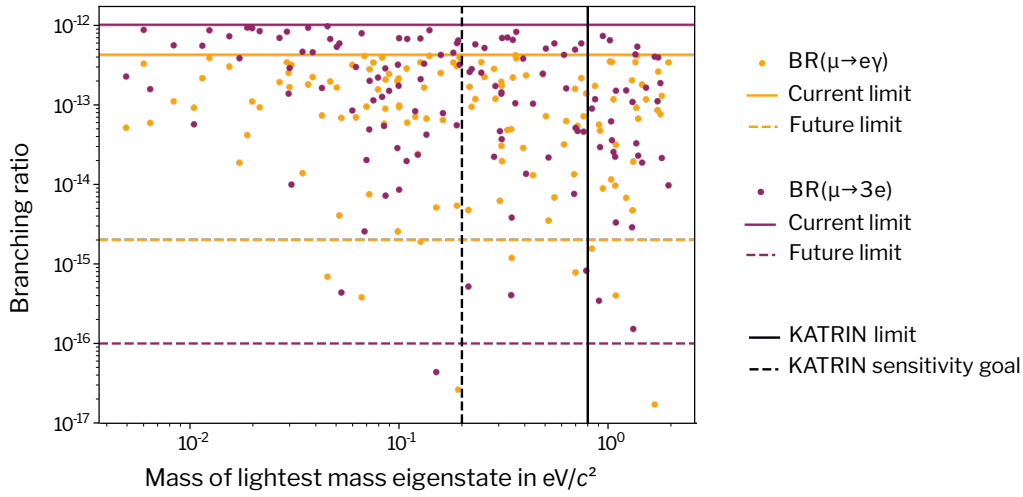

Figure 1.6 **Orthogonal constraints on the scotogenic model.** The lepton flavor violation branching ratios and the lightest neutrino mass of viable scotogenic models are plotted. The parameter space of the model is constrained in an orthogonal way by experimental results, shrinking as new results are obtained.

The plot is adapted from [Boe+20], used under CC BY 4.0.

the neutrino mass. The second is the search for the neutrinoless double beta decay. The third path combines kinematic approaches, including the measurement of electrons from beta decay. All three are introduced in the following section.

1.4.1 *Cosmological observations*

Cosmology is sensitive to the neutrino density, the number of neutrino species and their absolute masses. Within the standard hot Big Bang model, a relic neutrino background (CνB), similar to the cosmic microwave background (CMB) is predicted. After the Big Bang, the neutrinos decoupled from the thermal plasma at temperatures of about 2 MeV, and since cooled down to temperatures of about 1.7×10^{-4} eV corresponding to about 1.9 K. Since the temperature is smaller than $\sqrt{|\Delta m^2_{12}|}$,$\sqrt{|\Delta m^2_{23}|}$, at least two neutrino masses are non-relativistic today (their mass equals their average momentum). [PDG22]

The neutrino energy density for the non-relativistic neutrinos is given by

$$\rho_\nu \approx \sum_i m_i n_i \,, \tag{1.44}$$

with the number density n_i. If the lightest neutrino mass state would be still relativistic today, the expression is slightly incorrect. From neutrino decoupling studies n_i/n_γ is known, and n_γ is predicted from the CMB temperature. Therefore, the total neutrino density can be calculated in terms of the critical density ρ_c:

$$\Omega_\nu = \frac{\rho_\nu}{\rho_c} \approx \frac{\sum_i m_i}{93\,\mathrm{eV}h^2} \,, \tag{1.45}$$

with the Hubble constant h in units of 100 km/(s Mpc). [PDG22]

One example of an imprint of neutrinos on the CMB is the observed non-statistical fluctuations of the CMB. Since the relic neutrinos are not bound to local gravitational fields during structure formation, they can relax the local fluctuations of the mass and energy distribution in a diffusion-like transport in between. Similar to a diffusion process, the relaxation depends on the overall density. [OW08]

By combining multiple cosmological observations, the sum of neutrino masses can be limited. The most robust constraint comes from Planck data with [PDG22; Pla20]

$$\sum_i m_i < 0.26\,\mathrm{eV}/c^2 \quad \text{at } 95\,\% \text{ confidence level (C.L.)} \,. \tag{1.46}$$

The mass limit depends strongly on the selected datasets and ranges from very tight bounds of $\sum_i m_i < 0.1\,\mathrm{eV}/c^2$ already excluding the inverted ordering, up to more relaxed bounds of $\sum_i m_i < 0.5\,\mathrm{eV}/c^2$. [PDG22]

Although the limits set by cosmology are very stringent on the allowed mass range, they are not a direct measurement of the neutrino mass but a result of fitting a model with many parameters. For one of those parameters, the Hubble constant, currently a tension exists between early- and late-universe estimations [Pla20; Rie+19]. A direct measurement of the neutrino mass would allow to remove one

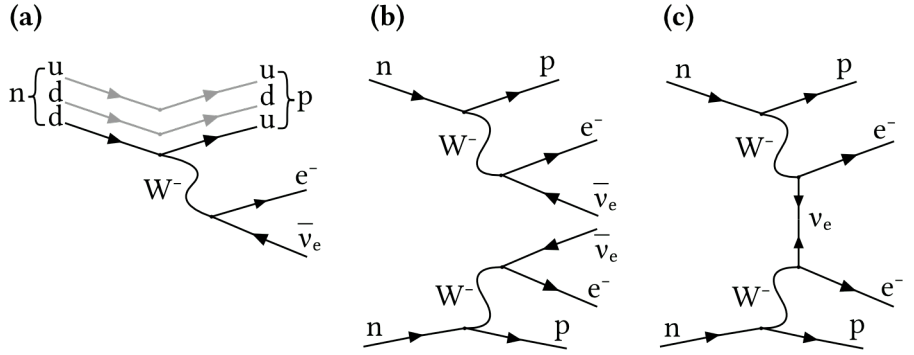

Figure 1.7 **Beta-decay schematic.** Figure (a) shows the schematic for single beta decay, more precisely the β^- decay (1.47), where a neutron is converted into a proton via W^--boson exchange. Figure (b) shows the normal double beta decay and (c) the neutrinoless double beta decay.

degree of freedom in cosmological models and therefore allow a better determination of parameters only accessible via cosmology. [FGR21]

1.4.2 *Search for neutrinoless double beta decay*

If neutrinos are Majorana neutrinos, lepton number would be violated and rare processes such as neutrinoless double beta decay ($0\nu\beta\beta$) are allowed and $0\nu\beta\beta$ can be used to extract information about the neutrino mass.

The single beta decay (see also fig. 1.7) has three possible decay modes: [Zub20]

$$\begin{aligned} {}^{A}_{Z}X &\longrightarrow {}^{A}_{Z+1}X + e^- + \bar{\nu}_e \quad (\beta^- \text{ decay}), \\ {}^{A}_{Z}X &\longrightarrow {}^{A}_{Z-1}X + e^+ + \nu_e \quad (\beta^+ \text{ decay}), \\ e^- + {}^{A}_{Z}X &\longrightarrow {}^{A}_{Z-1}X + \nu_e \quad (\text{electron capture}). \end{aligned} \tag{1.47}$$

Double beta decay is possible for even-even nuclei X (even number of protons and neutrons) and if the single beta decay is not allowed. As illustrated in fig. 1.8, for even-even nuclei the single beta decay would lead to an energetically less favorable state but not two simultaneous decays, the double beta decay (cf. fig. 1.7):

$${}^{A}_{Z}X \longrightarrow {}^{A}_{Z+2}X + e^-_1 + e^-_2 + \bar{\nu}_{e,1} + \bar{\nu}_{e,2}\,. \tag{1.48}$$

The first theoretical calculations of the double beta decay by Goeppert-Mayer [Goe35] predicted a half-life of over 1×10^{17} years. Over fifty years later, the first experimental detection succeeded, measuring double beta decay in selenium-82, with a half-life of $1 \times 10^{20^{+0.8}_{-0.3}}$ years [EHM87].

The neutrinoless double beta decay can be seen as two subsequent steps, happening in the same nucleus simultaneous

$$\begin{aligned} {}^{A}_{Z}X &\longrightarrow {}^{A}_{Z+1}X + \bar{\nu}_e + e^- \\ {}^{A}_{Z+1}X + \nu_e &\longrightarrow {}^{A}_{Z+2}X + e^-\,. \end{aligned} \tag{1.49}$$

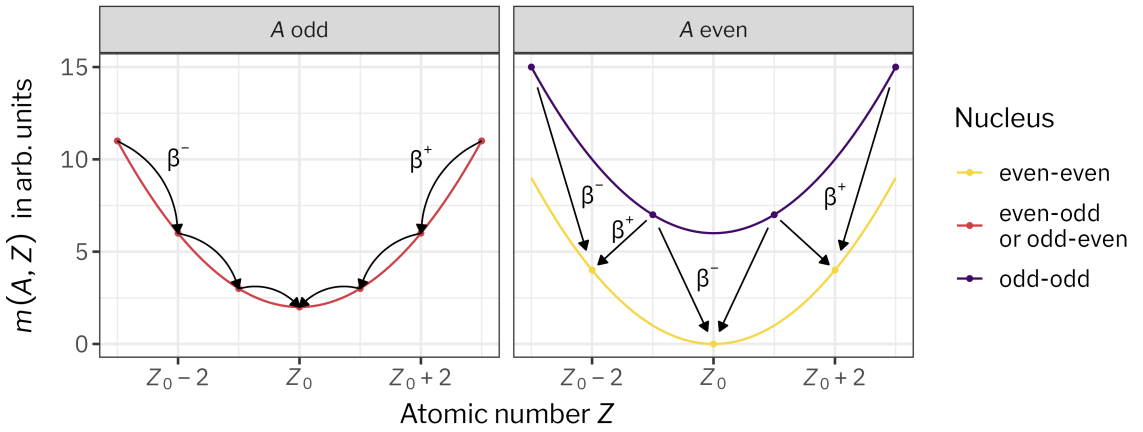

Figure 1.8 **Mass parabola for isobars.** Nuclei with the same number of nucleons, called isobars, can be split into two groups: even or odd number of nucleons A. Their masses m can be described with the Weizsäcker mass formula [Wei35]. For odd A, $m(A, Z)$ is a parabola, with its minimum at the stable isobar with $Z = Z_0$ (left panel). For even A, two parabolas exist (right panel). One for nuclei with an even number of protons and neutrons (even-even), and one for odd-odd nuclei. The arrows mark the possible single beta decays.

The schematic is loosely based on [Zub20].

The emitted right-handed antineutrino $\bar{\nu}_e$ is absorbed again at the same nucleus but as a left-handed neutrino ν_e (see also fig. 1.7). The reaction is possible if the neutrino is its own antiparticle, hence a Majorana particle and total lepton number is violated by two units. [Zub20]

The currently most sensitive experiments in the search for $0\nu\beta\beta$ use xenon-136 and germanium-76, two out of 35 candidates for $2\nu\beta\beta$, and therefore also candidates for $0\nu\beta\beta$ [PDG22]. The GERDA experiment uses germanium diodes, enriched with ^{76}Ge. The diodes are shielded with liquid argon. GERDA sets a limit on the half-life of $0\nu\beta\beta$ of

$$T_{1/2}^{0\nu\beta\beta} > 1.8 \times 10^{26}\,\text{yr} \quad \text{at } 90\,\%\,\text{C.L.}\,, \tag{1.50}$$

coinciding with the sensitivity assuming no signal [Ger20]. The KamLAND-Zen experiment uses a xenon-loaded liquid scintillator and obtains a lower limit of [KLZ16]

$$T_{1/2}^{0\nu\beta\beta} > 1.07 \times 10^{26}\,\text{yr} \quad \text{at } 90\,\%\,\text{C.L.}\,. \tag{1.51}$$

In general, $0\nu\beta\beta$ can also be dominantly induced by other new physic effects violating lepton flavor beyond massive Majorana neutrinos. However, under the assumption that the Majorana neutrino mass is the only source of lepton flavor violation, the decay half-life can be connected to the mass via [PDG22]

$$\frac{1}{T_{1/2}^{0\nu}} = G^{0\nu} \left| M^{0\nu} \right|^2 \left(\frac{m_{\beta\beta}}{m_e} \right)^2 . \tag{1.52}$$

Here, $G^{0\nu}$ is the phase space integral, $M^{0\nu}$ the nuclear matrix element of the transition, $m_{\beta\beta}$ the effective Majorana mass of ν_e and m_e the mass of the electron. The effective Majorana mass is a linear combination of the neutrino mass eigenstates m_i:

$$m_{\beta\beta} = \left| \sum_i m_i U_{ei}^2 \right| . \tag{1.53}$$

using the PMNS matrix U (1.14). [PDG22]

The largest uncertainty contributors in the determination of the Majorana mass from the observed half-life (1.52), are the nuclear matrix elements. Using a variety of different calculations as input, the upper bounds from the decay rates translate into upper bounds for the effective Majorana masses of [Ger20; KLZ16]

$$m_{\beta\beta} < 79 \text{ to } 180\,\text{meV}/c^2 \qquad \text{(GERDA)}\,, \tag{1.54}$$

$$m_{\beta\beta} < 61 \text{ to } 165\,\text{meV}/c^2 \qquad \text{(KamLAND-Zen)}\,. \tag{1.55}$$

The observation of $0\nu\beta\beta$ would not only prove the existence of lepton flavor violations, but also deliver information on massive Majorana neutrinos.

1.4.3 *Direct kinematic approaches*

The two methods presented previously are model dependent. The first depends on the specific cosmological model, the other on nuclear mass matrix elements and the existence of Majorana neutrinos. Now two approaches, purely relying on kinematics, are presented.

1.4.3.1 *Neutrinos from supernovae*

A straight forward kinematic approach to determine the neutrino mass is measuring the neutrino's energy and its flight time between source and detector. Such a measurement is actually possible with supernovae in our, or a neighboring, galaxy and a neutrino detector on Earth.

In 1987, from about 1×10^{28} neutrinos from the supernova SN 1987A about two dozen neutrinos where detected with four different detectors on Earth [LL02]. All observed neutrinos were $\bar{\nu}_e$, with the exception of one event measured at KamiokandeII, which could have been from a ν_e [Zub20]. The spread of arrival times of two neutrinos can be described as [Zub20]:

$$\Delta t = t_2 - t_1 = \Delta t_0 + \frac{L m_\nu^2}{2c} \left(\frac{1}{E_2^2 - E_1^2} \right) . \tag{1.56}$$

The difference of arrival times Δt and their energies E_1, E_2 are measured with the neutrino detector, and L is the distance to source (about 50 kpc for the SN 1987A [Pan+91]). The difference of emission time between the neutrinos Δt_0 and the mass of the neutrino m_ν are not known. Using supernova models to predict Δt_0, sets an upper limit on the neutrino masses of $m_{\bar{\nu}_e} < 5.7\,\text{eV}/c^2$ [LL02].

Nowadays, with further improved neutrino detectors and especially in combination with the detection of gravitational waves, a mass sensitivity of about $1\,\text{eV}/c^2$ can be reached in the event of another supernova [HLS20].

1.4.3.2 *Electrons from beta decay*

Throughout the whole chapter, beta decay was already mentioned a few times, first in connection with the postulation of the neutrino, afterwards in connection with its first direct measurement (inverse beta decay) and then in the search for neutrinoless double beta decay. It also plays a central role in the determination of the absolute mass scale of neutrinos.

Instead of a direct measurement of the neutrino, always connected to large detectors to catch the weakly interacting particle, a measurement of beta-decay electrons to deduce the neutrino mass is possible. In general, many beta emitter exist that are potential candidates to be used for neutrino mass measurements. However, one candidate, namely tritium, is especially suited. Its beta decay scheme is

$$\mathrm{T} \longrightarrow {}^{3}\mathrm{He} + \mathrm{e}^{-} + \bar{\nu}_{\mathrm{e}}\,. \tag{1.57}$$

Tritium decays into its mirror nucleus helium-3. In mirror nuclei the number of protons in one of the nucleus equals the number of neutrons and vice versa, and they have matching spin and parity (1/2+ for T, ^{3}He). Therefore, the transition is super-allowed with a rather short half-life of 12.3 yr, resulting in a high specific activity. Due to its simple structure, precise calculations such as the electronic final states are available for the tritium atom and the molecule T_2. [OW08] Additionally, scattering of beta-decay electrons on tritium has a small cross section.

The inelastic cross section (cf. section 3.3.1.1), scales with the total dipole matrix element squared M^2_{tot} which in turn is dominated by the atomic radius [Ino+81].

The decay energy Q (about 18.6 keV) is shared between the decay products, resulting in their kinetic energy and rest mass. The resulting spectrum for the kinetic energy of the electron E is given by [OW08]

$$\begin{aligned} R_{\beta}(E) = & \frac{d\Gamma}{dE} = \\ & \frac{G_F^2 \cos^2\theta_c}{2\pi^3} |M_{\mathrm{nuc}}|^2 \cdot F(E,Z) \\ & \times \left(E + m_{\mathrm{e}}c^2\right) \cdot \sqrt{(E + m_{\mathrm{e}}c^2)^2 - m_{\mathrm{e}}^2 c^4} \\ & \times \sum_{i,j} |U_{ei}|^2 \cdot P_j \cdot (E_0 - E - V_j) \cdot \sqrt{(E_0 - E - V_j)^2 - m_i^2 c^4} \\ & \times \theta\left(E_0 - E - V_j - m_i c^2\right) \end{aligned} \tag{1.58}$$

where

- Γ is the decay probability, and E the energy of the electron,
- G_F is the Fermi coupling constant with $G_F = 1.166\,378\,8(6) \times 10^{-5}/\mathrm{GeV}^2(\hbar c)^3$ [PDG22],
- θ_c is the Cabbibo angle with $\cos\theta_c = 0.973\,73(31)$ [PDG22],
- m_{e} is the mass of the electron with $m_{\mathrm{e}} \approx 0.511\,\mathrm{MeV}/c^2$ [PDG22],
- $|M_{\mathrm{nuc}}|$ is the nuclear part of the transition matrix. For the super-allowed tritium beta decay it is independent of the electron energy and $|M_{\mathrm{nuc}}|^2 \approx 5.55$ [RK88].

$F(E, Z)$ is the Fermi function, in the non-relativistic approach approximated as

$$F(E, Z) = \frac{z}{1 - \exp z}, \text{ with } z = \frac{2\pi\alpha Z}{\beta}. \tag{1.59}$$

It describes the electromagnetic interaction of the electron with the daughter nucleus ($Z = 2$, α fine structure constant and $\beta = v/c$).

U_{ei} is the electron neutrino part of the PMNS matrix (1.14) and

m_i are the mass eigenstates,

V_j, P_j are the excitation energies V_j and their corresponding probabilities P_j of the daughter nucleus (final states),

$E_0 = Q - E_{\text{rec}}$ is the endpoint, with E_{rec} the recoil of the daughter, and

$\theta\left(E_0 - E - V_j - m_i c^2\right)$ is a Heaviside step function, confining the spectral components to the physical sector. [OW08]

As long as the experimental resolution is significantly broader than the differences between the mass eigenstates (see also fig. 1.2), they can be replaced by a single observable [Zub20]

$$m^2(\nu_e) = \sum_i m_i^2 |U_{ei}|^2 . \tag{1.60}$$

Assuming charge, parity, and time reversal (CPT) symmetry, the masses of neutrino and antineutrino are treated equivalently. Throughout this work, $m(\nu_e)$ is also referred to as effective electron neutrino mass and the observable in beta decay experiments is $m^2(\nu_e)$.

The observable $m^2(\nu_e)$ has the largest effect in the endpoint region of the beta-decay spectrum, as visible in (1.58) and illustrated in fig. 1.9. In the endpoint region where the kinetic energy of the beta-decay electrons is the largest and close to E_0, the decay probability is the smallest. Therefore, any measurement of the neutrino mass requires a high activity source combined with a high energy resolution around E_0.

In the last century, many experiments using tritium to determine the neutrino mass were executed. A selection of them is shown in fig. 1.10. From the first upper limit on $m(\nu_e)$ of $< 1.7\,\text{keV}/c^2$ the possible mass range is now, over seventy years later, restricted to $0.8\,\text{eV}/c^2$ by the latest KATRIN result [Kat22].

Compared to the two predecessor experiments Mainz [Kra+05] and Troitsk [Tro11], KATRIN improved the limit already by a factor of two. KATRIN aims to limit the neutrino mass to $0.2\,\text{eV}/c^2$ (90 % C.L), or to measure it with $5\,\sigma$ significance if it is above $0.35\,\text{eV}/c^2$ [Kat05].

All three experiments use the same type of spectrometer, a MAC-E filter spectrometer which acts as a high-pass filter on the beta-decay electrons, filtering the large amount of low-energy beta-decay electrons and at the same time allowing for high-resolution energy spectroscopy around the endpoint. A more detailed introduction to the measurement principle follows in chapter 2.

One example for a future neutrino mass experiment with tritium is the *Project 8* experiment, which aims to reach sensitivities down to $0.04\,\text{eV}/c^2$ by employing cyclotron radiation emission spectroscopy. [Pro17]

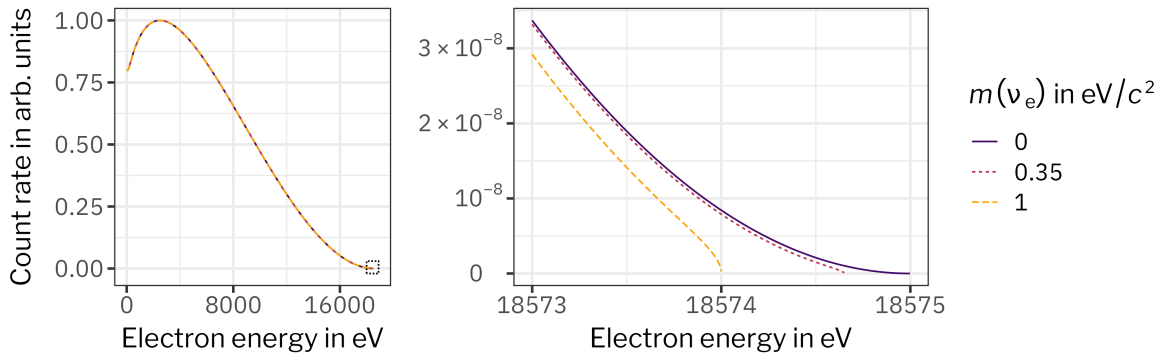

Figure 1.9 **Tritium beta-decay electron spectrum.** The left panel shows the full beta-decay spectrum. The right panel is a magnified view of the endpoint region where the influence of the neutrino mass is largest. The endpoint is fixed arbitrarily to 18 575 eV and the final states are neglected ($V_j = 0$).

The figure is based on [Kat05].

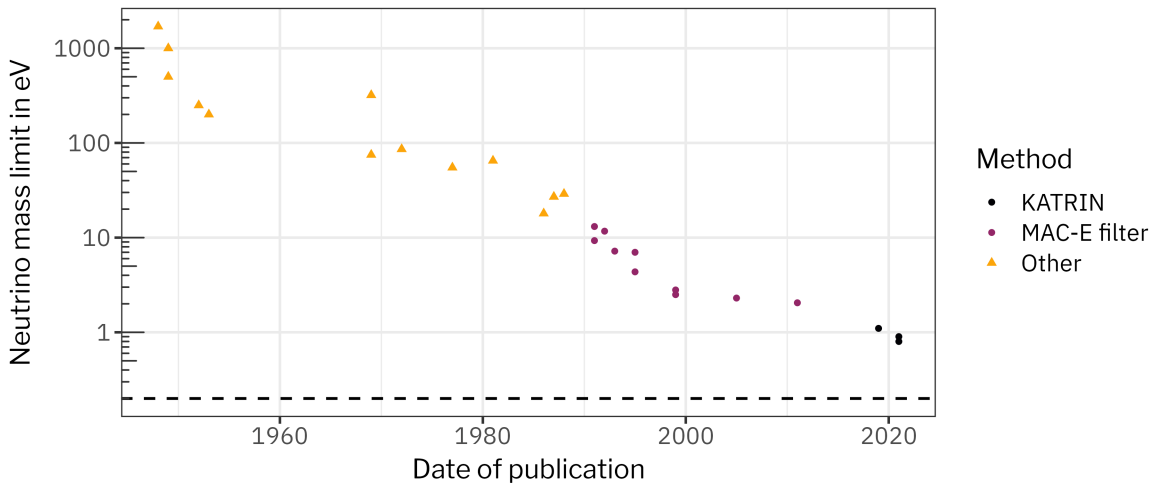

Figure 1.10 **Upper limits on the neutrino mass from tritium beta decay experiments.** This historical timeline spans a period of 72 years. The dashed horizontal line marks KATRIN's sensitivity goal. The selection of experiments is based on [FGR21; PDG20].

The figure is adapted from [Lok+22b], used under CC BY 4.0.

A complementary approach to the neutrino mass measurement with tritium is the employment of holmium-163. It decays via electron capture to dysprosium-163 [Zub20]:

$$^{163}\mathrm{Ho} + \mathrm{e}^{-} \longrightarrow \nu_{\mathrm{e}} + {}^{163}\mathrm{Dy}^{*} \tag{1.61}$$

and emits an electron neutrino in the process. Therefore, in combination with a measurement via β^{-} decay, invariance of CPT symmetry which ensures $m(\nu_{\mathrm{e}}) = m(\bar{\nu}_{\mathrm{e}})$ can be checked.

Except for a tiny fraction of energy ($< 1\,\mathrm{meV}$) taken as recoil energy by the daughter nucleus emitting the neutrino, the energy released during the decay ($Q = 2.8\,\mathrm{eV}$) is shared between the neutrino and the atomic excitations [Gas+17]. By performing a calorimetric measurement of the de-excitation of $^{163}\mathrm{Dy}^{*}$, the endpoint region of the spectrum can be used to determine the neutrino mass, similar to the tritium beta-decay electron spectrum.

One experiment following this path is the ECHo experiment where metallic magnetic calorimeters are employed [Gas+17]. Their most recent publication reports an upper limit of $m(\nu_{\mathrm{e}}) < 150\,\mathrm{eV}/c^2$ [Vel+19]. Another experiment is the HOLMES experiment which uses transition-edge sensors as calorimetric measurement [Alp+15].

Overall, the ongoing efforts with holmium-163 together with the intense research and development for future tritium experiments are nicely complemented with the currently running KATRIN measurement, gathering more statistics and reducing systematics to reach its final sensitivity goal.

2 KATRIN

The Karlsruhe Tritium Neutrino (KATRIN) experiment measures the effective mass of the electron antineutrino (1.60). A sensitivity of $0.2\,\mathrm{eV}/c^2$ (at 90 % confidence level) is targeted after collecting three live years of data. [Kat05]

The KATRIN setup (cf. fig. 2.1) consists of a high-luminosity tritium source and a high-precision integrating spectrometer that combines magnetic collimation and an electrostatic filter [BPT80; LS85; Pic+92a]. Beta-decay electrons from the windowless gaseous tritium source (WGTS) are guided through the transport and pumping section [Mar+21] to the spectrometer and detector section [Ams+15]. The detector is reached only by those electrons whose kinetic energies are large enough to overcome the retarding potential inside the main spectrometer. An integral electron spectrum is accumulated via step-wise adjustments of the retarding potential.

For the neutrino mass determination, the tritium spectrum is measured around its endpoint at 18.6 keV, where the imprint of the neutrino mass is largest.

This chapter begins with an introduction of the KATRIN setup, followed by an introduction to the available tools for energy scale calibrations and concludes with an overview on recent KATRIN results.

2.1 Experimental setup

The setup is explained along the beta-decay electrons' path through the beamline up to the detector (from left to right in fig. 2.1).

2.1.1 *Windowless gaseous tritium source*

The source for the beta-decay electrons is a windowless gaseous tritium source (WGTS). The WGTS is a 10-m long cylindrical tube with a diameter of 90 mm [Kat05]. Gaseous tritium is injected in the center of the WGTS and pumped out at both ends (cf. fig. 2.2), ensuring a constant flow of tritium through the source. Beta-decay electrons are

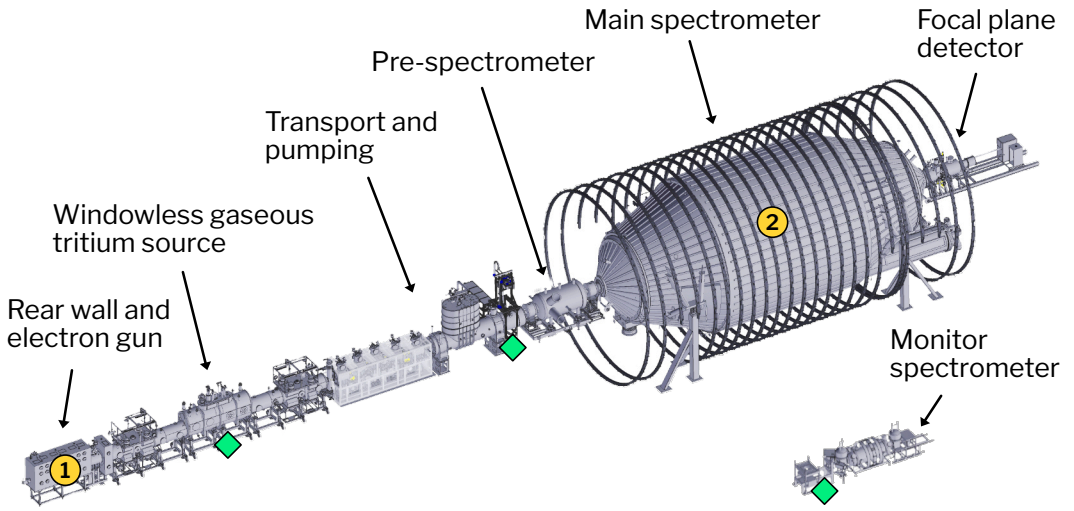

Figure 2.1 **Schematic drawing of the KATRIN beamline.** The main components of the experiment are labeled here and will be explained in section 2.1. The two yellow circles highlight the positions of two specific hardware components: the electron gun (1) and the high-voltage system (2). The green diamonds mark the positions where ^{83m}Kr sources are available for calibration (cf. section 2.2.3).

The schematic is adapted from [Kat18b], licensed under CC BY 3.0. For license terms, see https://creativecommons.org/licenses/by/3.0/.

guided by a homogeneous magnetic field to both ends of the source. Originally, the field strength was chosen as 3.6 T [Kat05], now during standard operation it is fixed to 2.5 T [Kat21c].

The WGTS is operated at low temperatures to reduce the conductance of the tube and with it reduce the necessary tritium throughput. The design temperature for tritium circulation is 30 K [Kat21c] and currently it is operated at 80 K [Mar+22]. A throughput of 40 g tritium per day, equivalent to an activity of 1.5×10^{16} Bq, is needed to obtain the reference column density of $5 \times 10^{17}/\mathrm{cm}^2$ [Kat05].

The continuous supply of tritium is provided by the *inner loop* system [PSB15]. There, the gas pumped from the WGTS is purified by a palladium membrane filter (permeator). The permeator filters non-hydrogen isotopologs and the overall gas amount is balanced by pure (95 %) tritium from storage [PSB15]. The tritium is provided in a batch-wise mode by the *outer loop* system [Wel+17]. Before the gas is injected back into the WGTS, the gas composition is analyzed with laser Raman spectroscopy (LARA) [Stu+10; Kat20c].

In addition to T_2, the gas composition contains other hydrogen isotopologs such as DT, D_2, HT, HD and H_2. The relative concentration of the individual hydrogen isotopologs is measured with a precision on the order of 10^{-3} [Kat20c]. Each of the tritiated hydrogen isotopologs

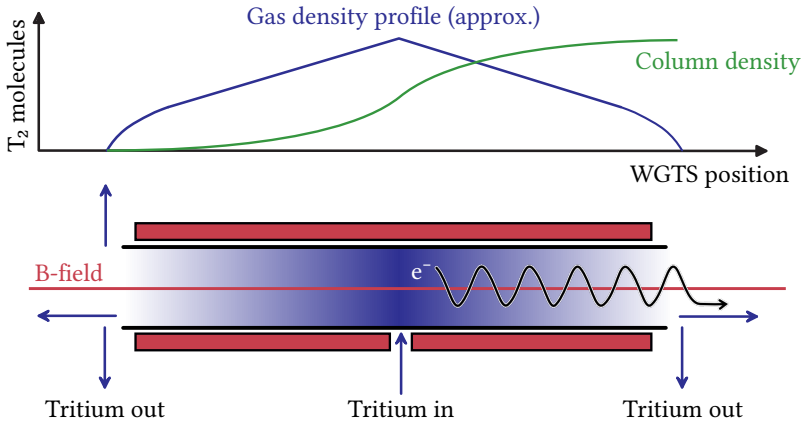

Figure 2.2 **Windowless gaseous tritium source (WGTS).** The upper part illustrates the density profile inside the WGTS. The column density (green curve) is the gas density (blue curve) integrated over the length of the source. In the lower part, the pumping and injection mechanism from which this density profile results is shown. The red rectangles depict superconducting magnets surrounding the beam tube.

The figure was created by A. Marsteller and is adapted from [Mar20], licensed under CC BY 4.0.

contributes beta-decay electrons via

$$\begin{aligned} T_2 &\longrightarrow {}^3HeT^+ + e^- + \bar{\nu}_e\,, \\ DT &\longrightarrow {}^3HeD^+ + e^- + \bar{\nu}_e\,, \\ HT &\longrightarrow {}^3HeH^+ + e^- + \bar{\nu}_e\,. \end{aligned} \tag{2.1}$$

The three possible daughter molecules posses a different final state distribution which in turn produces a different beta-decay spectrum. Therefore, the HT/DT ratio and the tritium purity needs to be known for the neutrino mass analysis. Using LARA, the tritium purity is measured with a precision of $< 10^{-3}$ and a trueness of $< 3 \times 10^{-3}$. For neutrino mass measurements the tritium purity is $> 95\,\%$. [Kat20c]

Not only the gas composition but the overall activity inside the WGTS needs to be monitored. One available method is beta-induced X-ray spectroscopy (BIXS) [Röl+13; Bab+12]. The WGTS is terminated at one side with a gold-coated stainless steel disc, called *rear wall* (cf. fig. 2.1). Beta-decay electrons are guided magnetically to the rear wall and are absorbed. The absorption process generates X-ray radiation that is measured by two silicon drift detectors; the BIXS system.

Another method to monitor the activity is the *Forward Beam Monitor* (FBM) [Beg+22]. The FBM is located in the transport section, roughly at the position of the middle green diamond in fig. 2.1. It consists of two silicon *p-i-n* diodes that can be inserted into the flux tube to measure beta-decay electrons. During neutrino mass measurements, it is located at the outer rim of the flux tube but it can also be moved across the full flux tube for systematic investigations. The FBM measures the rate of beta-decay electrons with a precision of 0.1% within 60 s and an energy resolution of FWHM = 2 keV [Beg+22].

By measuring the gas composition with LARA and the activity with BIXS and the FBM, the overall column density inside the WGTS can be estimated. The column density is an important parameter, since it not only determines the amount of signal electrons, but it also influences their kinetic energy. The beta-decay electrons can lose energy due to scattering on source gas molecules. The scattering probability is directly linked to the column density; with increasing density also the scattering probability increases. The probability distribution for electrons to lose a certain amount of energy is called energy-loss function. Its precision determination using an electron gun (cf. section 2.2.1) is presented in chapter 3. In turn, with the knowledge of the energy-loss function, the column density can be determined. Electrons with well defined energies and angles are shot through the source and after traversing the source, the ratio of unscattered and scattered electrons is measured (more details can be found in [Mar20; Blo22]).

Thermalized electrons and ions from beta decay and subsequent ionization processes form a quasi-neutral plasma inside the source. The plasma is magnetized by the 2.5 T magnetic field [Kuc16]. The plasma potential defines the starting potential of the beta-decay electrons. To reduce systematic effects, the starting potential needs to be as constant as possible over time and space.

2.1.2 *Rear wall*

The rear wall was already introduced as gold-coated disk that terminates the WGTS. The rear wall is a conducting plate perpendicular to the magnetic flux tube and it influences the electric potential within the WGTS. Simulations by Kuckert [Kuc16] show that the potential difference between rear wall and WGTS beam tube determines the homogeneity of the potential distribution. Measurements using tritium and ^{83m}Kr conversion electrons inside the WGTS confirm the influence of the rear wall potential on the plasma potential [Fri20; Mac21].

Since both the rear wall work function and the WGTS beam tube work function can change over time, also the plasma potential can change and needs to be monitored. One ideal tool for investigating the source potential are conversion electrons from ^{83m}Kr (cf. section 2.2.3).

2.1.3 *Transport and pumping section*

The WGTS is open towards the spectrometer section, allowing an unhindered flow of tritium gas and beta-decay electrons towards the spectrometers. The tritium gas needs to be retained, to avoid contamination and unnecessary background sources. A dedicated transport and pumping section has been developed that magnetically guides the electrons and reduces the tritium flow rate.

A two-staged approach reduces the tritium flow rate by more than 14 orders of magnitude [Fri+19]. The first stage is the differential pumping system (DPS). The differential pumping sections at both ends of the WGTS (also called DPS1), together with the DPS (also called DPS2), reduce the gas flow by more than 7 orders of magnitude [Mar+21].

The DPS consists of five beamtube segments. The segments are connected over four pump ports, equipped with turbo-molecular pumps (TMP). Each segment is tilted by 20° relative to the next with iterating tilt direction. Magnets around the segments produce a guiding field for the electrons, whereas uncharged particles collide with the beam tubes and are pumped out by the TMPs. [Kat21c]

Inside the DPS, four dipole electrodes are installed to force ions via $E \times B$ drift to the metallic surface of the electrodes. Here, they are neutralized and pumped out by the TMPs. Additionally, five ring electrodes are installed along the KATRIN beamline for removing positive ions. [Kat21c]

The second stage for tritium flow rate reduction is the cryogenic pumping system (CPS). Instead of removing gas by introducing a molecular flow – the way it is done in the DPS – the gas is removed by a cryo-sorption pump. In a cryogenic pump, the gas is condensed on a cold surface. In order to keep the condensed tritium gas within the CPS, the cryogenic pump is combined with a sorption pump and an argon frost layer is chosen as adsorbent [Kaz+08].

The CPS beam tube is optimized to give as much surface for adsorption as possible. For this purpose, the inner surface is equipped with ninety 2-mm-long fins. Similar to the DPS, the beam tube consists of multiple segments. The inner three segments are tilted relative to each other by 15°. Their formation is similar to a well; the segment in the middle forms the bottom and the two others the walls. This geometry purposely increases the probability of gas hitting the walls. Seven super-conducting solenoids, each one surrounding one of the beam tube segments, produce the guiding field for the beta-decay electrons. [Kat21c]

For radiation safety, the argon frost layer is removed before an activity of 3.7×10^{10} Bq (1 Curie) is accumulated [Fri+19]. The maximum possible operation time before regeneration was estimated from measurements of the DPS flow reduction to be 445(46) days of nominal tritium operation. This is seven times as long as the design goal of a CPS regeneration every 60 days. [Mar+21]

In summary, the transport and pumping section throttles the tritium flow rate to less then 1×10^{-14} mbar L/s while at the same time up to 1×10^{11} tritium beta-decay electrons per second are guided within the magnetic flux to the spectrometer section. The magnetic flux, the magnetic field $\vec{B}$ integrated over the surface element $\vec{A}$,

$$\Phi = \int \vec{B} \cdot \mathrm{d}\vec{A} \tag{2.2}$$

has a design value of 191 T cm^2 and is set to 134 T cm^2 during standard operation. [Kat21c]

2.1.4 *Spectrometer principle*

Electrons guided into the spectrometer section are filtered by two spectrometers acting as high-pass filters, only transmitting electrons above a certain energy threshold. The first spectrometer, the pre-spectrometer, is of lesser importance and can be used as a pre-filter to reduce the flux of the electrons into the second spectrometer, the main

spectrometer. Both spectrometers are based on the same technique, using magnetic adiabatic collimation combined with an electrostatic filter. They are called *MAC-E filter* type spectrometers. [Kat05]

The principle of a MAC-E filter type spectrometer was introduced in [BPT80], later successfully applied by two neutrino mass experiments [LS85; Pic+92a] and now it is employed at KATRIN [Kat05; Kat21c]. A MAC-E filter spectrometer features the unique combination of high resolution and a wide solid-angle acceptance.

The kinetic energy of electrons entering the spectrometer can be divided into two components, one parallel $E_{\parallel}$ and the other perpendicular $E_{\perp}$ to the field lines

$$E_{\text{kin}} = E_{\parallel} + E_{\perp} = \frac{p_{\parallel}^2 + p_{\perp}^2}{(\gamma + 1) \cdot m_{\text{e}} c^2}\,, \tag{2.3}$$

with m_{e} the electron mass, $p_{\parallel}$ the momentum parallel to the field lines and $p_{\perp}$ perpendicular. The Lorentz factor γ for beta-decay electrons with a maximal kinetic energy E_{kin} of 18.6 keV is

$$\gamma = 1 + \frac{E_{\text{kin}}}{m_{\text{e}} \cdot c^2} < 1.04\,. \tag{2.4}$$

Since γ is quite close to 1, the non-relativistic approximation suffices for illustration purposes and is therefore used here.

A retarding potential U_{ret} acts as high-pass filter on electrons. Electrons traversing the spectrometer are decelerated by qU_{ret} which transforms $E_{\parallel}$ into potential energy. Only electrons with enough kinetic energy, more precisely

$$E_{\parallel} \geq qU_{\text{ret}}\,, \tag{2.5}$$

are transmitted. To achieve a sufficient energy resolution, $E_{\perp}$ needs to be small, corresponding to a narrow solid-angle acceptance.

For a wider acceptance, the retarding potential is combined with a collimating magnetic field. Two superconducting solenoids at both ends of the spectrometer create the magnetic field, as illustrated in fig. 2.3. The magnetic field is axially symmetric but highly inhomogeneous along the symmetry axis z. In the center of the spectrometer, farthest away from the solenoids, the magnetic field is the lowest and in between is a magnetic field gradient along z. Such a configuration is also called *magnetic bottle*.

If an electron moves perpendicular to a magnetic field, it performs a circular motion around the magnetic field lines, induced by the Lorentz force. In a constant magnetic field $B = |\vec{B}|$, the electron moves with a unique cyclotron frequency ω given by the equality of centripetal force $m_{\text{e}} v_{\perp}^2 / r$ and Lorentz force $qBv_{\perp}$

$$\omega = \frac{v_{\perp}}{r} = \frac{eB}{m_{\text{e}}}\,. \tag{2.6}$$

However, the magnetic field is not constant but changing along z (cf. fig. 2.3). With decreasing magnetic field, also the cyclotron frequency decreases.

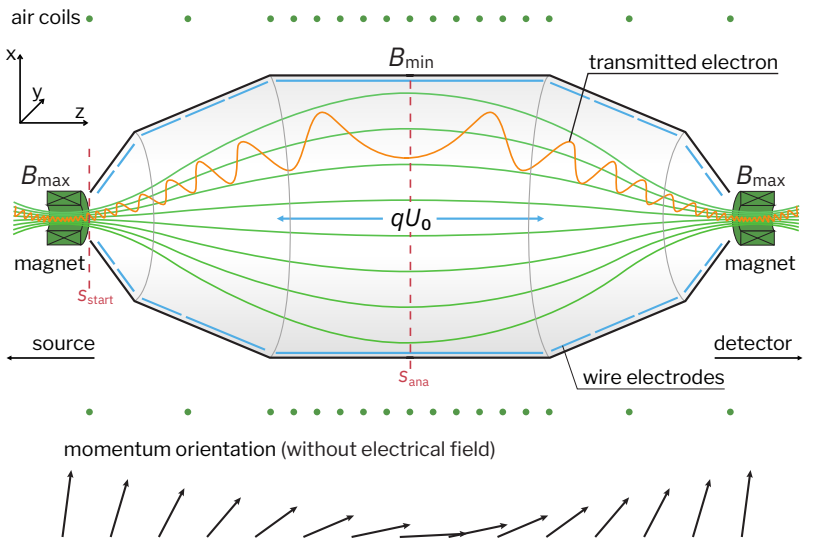

Figure 2.3 **MAC-E filter principle.** The green lines are the magnetic field lines, produced by the two magnets at both ends of the spectrometer. An air coil system, built around the spectrometer, precisely shapes the magnetic field. The retarding potential qU_{ret} (blue arrows) is created by a negative high voltage that is applied directly to the vessel (not shown in the schematic). A wire electrode system, mounted inside the vessel, fine-tunes the electric field.

The schematic is adapted from a figure created by L. Schimpf which is based on [Kat05].

In a magnetic field, the electron exhibits a magnetic moment

$$\mu = |\vec{\mu}| = \frac{e}{2m_e}|\vec{L}|\,. \tag{2.7}$$

Here, $|\vec{L}| = p_\perp r$ is the angular momentum of the electron. Solving (2.6) for r and inserting it into (2.7), it follows

$$\mu = \frac{e}{2m_e} p_\perp r = \frac{e}{2m_e} p_\perp \frac{p_\perp}{eB} = \frac{E_\perp}{B}\,. \tag{2.8}$$

With an axially symmetric field and smoothly diverging or converging flux lines, it can be shown that the magnetic moment is invariant ($d\mu/dt = 0$). [BPT80]

As a consequence of the invariance of μ, it follows that $p_\perp^2 \sim B$. Therefore, for any two planes traverse to z and within the magnetic bottle, the following equation holds:

$$\frac{p_{\perp,1}^2}{B_1} = \frac{p_{\perp,2}^2}{B_2}\,. \tag{2.9}$$

The indices $1, 2$ denote the two planes. By introducing an angle θ between the electron momentum and z, $p_\perp$ can be expressed in terms of $|\vec{p}|$:

$$p_\perp = |\vec{p}| \cdot \sin\theta\,. \tag{2.10}$$

Using momentum conservation gives $\sin\theta \sim p_\perp$ and inserting it into (2.9) yields

$$\frac{\sin^2\theta_2}{\sin^2\theta_1} = \frac{B_2}{B_1}\,. \tag{2.11}$$

In other words, the magnetic field the ratio between the two planes defines the change of θ. Hence, the magnetic bottle inside the spectrometer induces a change of θ (and associated $p_\perp$) for electrons entering the spectrometer with arbitrary $\vec{p}$. [BPT80]

As highlighted in fig. 2.3, $z = s_{\text{start}}$ is defined as the position of the spectrometer entrance and $z = s_{\text{ana}}$ is the spectrometer center also referred to as *analyzing plane*. The magnetic field $B(z = s_0)$ is shortened as B_{min} and $B(z = s_{\text{start}}) = B_{\text{max}}$. Using the change of $p_\perp$ due to the magnetic field ratio between two different planes (2.9) for an electron with $E_\perp(z = s_{\text{start}})$, the remaining $E_\perp$ at the spectrometer center is given by

$$E_\perp(z = s_{\text{ana}}) = E_\perp(z = s_{\text{start}}) \cdot \frac{B_{\text{min}}}{B_{\text{max}}}\,. \tag{2.12}$$

As described above, $E_\perp$ is not affected by the retarding potential. Using the angle θ (2.10) and the full kinetic energy E_{kin} of the electron, (2.12) becomes

$$E_\perp(z = s_{\text{ana}}) = E_{\text{kin}} \cdot \sin^2(\theta) \cdot \frac{B_{\text{min}}}{B_{\text{max}}}\,, \tag{2.13}$$

$E_\perp(z = s_{\text{ana}})$ depends on the ratio of magnetic fields and the total energy of the electron. With the kinetic energy of the electrons at the spectrometer entrance (2.3) and (2.13), $E_\parallel$ at position s_{ana} can be expressed in terms of E_{kin} and θ:

$$\begin{aligned} E_\parallel(z = s_{\text{ana}}) &= E_{\text{kin}} - E_\perp \\ &= E_{\text{kin}} \left(1 - \sin^2(\theta) \cdot \frac{B_{\text{min}}}{B_{\text{max}}}\right)\,. \end{aligned} \tag{2.14}$$

Analogous to (2.5), the transmission condition for the electrons is

$$\mathcal{T}(E_{\text{kin}}, \theta, U_{\text{ret}}) = \begin{cases} 1, & E_\parallel(z = s_{\text{ana}}) > qU_{\text{ret}}\,, \\ 0, & E_\parallel(z = s_{\text{ana}}) \leq qU_{\text{ret}}\,. \end{cases} \tag{2.15}$$

The transmission function for an electron source with an angular distribution $a(\theta)$ is defined as

$$T(E_{\text{kin}}, U_{\text{ret}}) = \int_{\theta_{\text{min}}}^{\theta_{\text{max}}} \mathcal{T}(E_{\text{kin}}, \theta, U_{\text{ret}}) \cdot a(\theta)\,\mathrm{d}\theta\,. \tag{2.16}$$

For a fixed angle ($a(\theta) = \text{const}$), the transmission condition produces a step-shaped transmission function with infinitesimal small width (Heaviside step function). For an isotropic source with angular distribution $a(\theta) = \sin(\theta)$, the integration over θ up to a certain angle θ'

yields

$$\int_0^{\theta'} \sin\theta \,\mathrm{d}\theta = 1 - \cos\theta' \\ = 1 - \cos\left(\arcsin\left(\sqrt{\left(1 - \frac{qU_{\mathrm{ret}}}{E_{\mathrm{kin}}}\right) \cdot \frac{B_{\mathrm{max}}}{B_{\mathrm{min}}}}\right)\right). \tag{2.17}$$

Using the relation $\cos(\arcsin(\sqrt{x})) = \sqrt{1-x}$

In the last step (2.14) was used. After simplifying the expression, introducing the surplus energy $E_{\mathrm{s}} = E_{\mathrm{kin}} - qU_{\mathrm{ret}}$ and the filter width $\Delta E = E_{\mathrm{kin}} \cdot \frac{B_{\mathrm{min}}}{B_{\mathrm{max}}}$, the transmission function can be written as [Kle+19]

$$T(E_{\mathrm{kin}}, U_{\mathrm{ret}}) = \begin{cases} 0, & E_{\mathrm{s}} < 0\,, \\ 1 - \sqrt{1 - \frac{E_{\mathrm{s}}}{E_{\mathrm{kin}}} \cdot \frac{B_{\mathrm{max}}}{B_{\mathrm{min}}}}, & 0 \leq E_{\mathrm{s}} \leq \Delta E, \\ 1, & E_{\mathrm{s}} > \Delta E\,. \end{cases} \tag{2.18}$$

2.1.4.1 *Transmission function of the main spectrometer*

Following the introduction of the transmission function for a generic MAC-E filter, it is now introduced for KATRIN's main spectrometer. For the main spectrometer transmission function the "standard setting" values are used instead of the design values [cf. tbl. 1 Kat21c]. These standard setting values are further referred to as *nominal values*.

At KATRIN, the electron source (WGTS) is inside a magnetic field of $B_{\mathrm{source}} = 2.52\,\mathrm{T}$ which is significantly weaker than $B_{\mathrm{max}} = 4.2\,\mathrm{T}$. As visible in (2.11), θ increases if the electrons travels from a weaker field to a stronger field. If θ increases above 90°, the electron is reflected by the magnetic field. Using (2.11), the maximal acceptance angle θ_{max} inside the source is given by

$$\theta_{\mathrm{max}} < \arcsin\left(\sqrt{\frac{B_{\mathrm{source}}}{B_{\mathrm{max}}}}\right). \tag{2.19}$$

For the nominal field setting, the maximal acceptance angle is $\theta_{\mathrm{max}} = 50.8°$. Electrons with high θ travel a longer path through the source and therefore have a higher scattering probability. Those electrons are suppressed with the reduced acceptance angle; decreasing statistics, but also decreasing systematics [Kat05].

Calculating the remaining $E_{\perp}$ at the spectrometer center (2.13) for $\theta = \theta_{\mathrm{max}}$ gives a filter width of

$$\Delta E = E_{\mathrm{kin}} \cdot \sin^2(\theta_{\mathrm{max}}) \cdot \frac{B_{\mathrm{min}}}{B_{\mathrm{source}}} = E_{\mathrm{kin}} \cdot \frac{B_{\mathrm{min}}}{B_{\mathrm{max}}}\,. \tag{2.20}$$

In the nominal field setting, also called *6 G setting* ($B_{\mathrm{min}} = 0.63\,\mathrm{mT}$), the filter width for an electron with $E_{\mathrm{kin}} = 18.6\,\mathrm{keV}$ is $\Delta E = 2.79\,\mathrm{eV}$.

Other magnetic field settings with lower or higher magnetic fields at the analyzing plane are possible. One example is the *1 G setting*. Due to its excellent energy resolution it is often used for electron gun measurements (cf. section 2.2.1). For standard measurements it is less

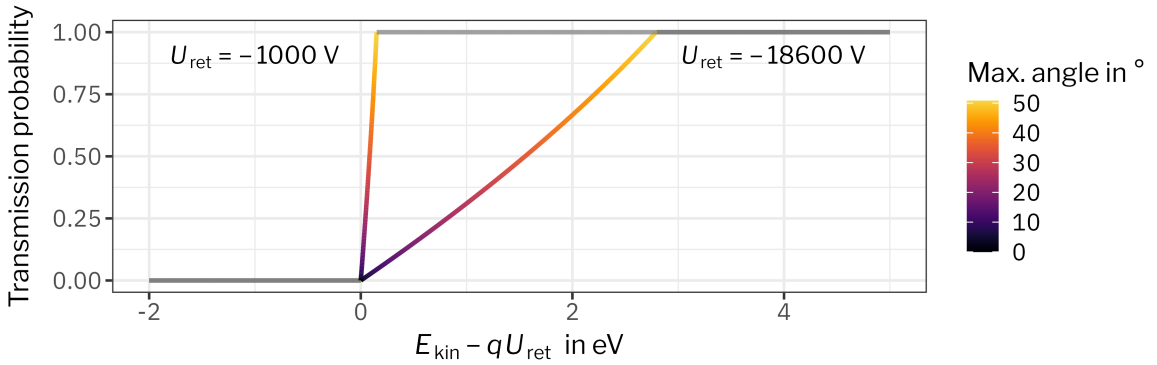

Figure 2.4 **Transmission function for a monoenergetic isotropic source.** The main spectrometer transmission function is shown for the nominal 6 G setting with $B_{min} = 0.63\,\mathrm{mT}$. E_{kin} is fixed, but θ follows an isotropic distribution for angles up to $\theta_{max} = 50.8°$. The x-axis shows the surplus energy of the electrons $E_s = E_{kin} - qU_{ret}$. To illustrate the energy dependency of the filter width, the transmission function for two different retarding potentials and corresponding electron energies is shown. For neutrino mass measurements, only the transmission function for energies around 18.6 keV is relevant.

useful, since the weak magnetic field results in only a fraction of the flux from the WGTS getting mapped to the detector.

The full transmission function of the main spectrometer for an isotropic source is given by (2.18), but adjusted for the changed accepted angles and normalized [Kle+19]:

$$T(E_{kin}, U_{ret}) = \begin{cases} 0, & E_s < 0\,, \\ \dfrac{1-\sqrt{1-\frac{E_s}{E_{kin}}\cdot\frac{B_{source}}{B_{min}}}}{1-\sqrt{1-\frac{B_{source}}{B_{max}}}}, & 0 \le E_s \le \Delta E\,, \\ 1, & E_s > \Delta E\,. \end{cases} \tag{2.21}$$

The transmission function is shown for the 6 G setting in fig. 2.4.

Other field configurations where the analyzing plane is not located at the spectrometer center are possible. One configuration, referred to as *shifted analyzing plane* (SAP), was developed to reduce background effects in the main spectrometer [Lok+22a] and is currently used for neutrino mass measurements.

2.1.5 *Spectrometer hardware*

A dedicated design, including an ultra-high vacuum, a precision magnet system, and a high-voltage system, is needed to achieve a spectrometer with the transmission properties as described above.

The main spectrometer is 23.23 m long with an inner diameter of 9.8 m. Its size is primarily determined by the design values for the flux tube of the source (191 T cm^2), the magnetic field ratio (1:20 000) and the required homogeneity of the fields. [Kat21c]

The design values are $B_{min} = 3 \times 10^{-3}$ T and $B_{max} = 6$ T [Kat05].

The ultra-high vacuum (pressures in the 1×10^{-11} mbar regime) is

needed for the beta-decay electrons to pass the spectrometers undisturbed and to reduce background sources. The vacuum vessel has a stainless steel surface area of 1222 m^2, comprised of 690 m^2 inner surface area and the surface of the wire electrode system [Kat16]. The outgassing rate from this large surface area needs to be pumped by the vacuum system which consists of a combination of cascaded turbo molecular pumps and non-evaporable getter (NEG) pumps. Since radon-219 emanates from the NEG pumps and produces background in the spectrometer, LN2-cooled copper baffles are installed in between the inner spectrometer volume and the NEG pumps. [Frä+11; Kat21c]

As already introduced above, the magnetic field inside the main spectrometer is created by two super-conducting magnets at both ends of the spectrometer. To compensate for stray fields (e.g. the earth magnetic fields) and to fine-tune the shape and strength of the magnetic field, the vacuum vessel is surrounded by a large air coil system [Erh+18]. Additionally, the air coil system is equipped to remove stored electrons by deformation of the magnetic flux tube inside the spectrometer. A short (down to 1 s pulse length) inversion of the current through the individual air coils achieves the deformation. [Kat18c]

A precision high-voltage system creates the retarding potential inside the main spectrometer. It comprises a complex two-layer wire-electrode system, together with two full-metal anti-penning electrodes at the spectrometer entrance and exit [Pra11]. In addition to a flexible fine-tuning of the electric field, the wire electrode system provides an electrostatic shielding for secondary electrons produced inside the vessel hull by muon interactions or radioactive decays. [Val10]

For each of the layers and rings of the wire electrode, individual potentials were planned in the initial design. However, after several bake-out processes of the main spectrometer, parts of the wire electrodes short-circuited [Dyb19]. The inner electrode system offers a dipole mode, where the east and west half of the wire electrodes can be set on different potentials. During nominal settings for neutrino mass measurements, the wire electrodes are operated in single layer mode and without dipole [Kat21c].

The bake-out process during which the spectrometer is heated up to 350 °C is essential to achieve the vacuum conditions inside the main spectrometer [Kat21c].

For orientation: Electrons from the WGTS enter the spectrometer in the south and leave it in the north, where the detector is located.

The main spectrometer high-voltage system, designed to supply the inner electrodes with up to 44 different potentials, is further described in [Res19]. Important for subsequent sections (sections 2.2.1, 3.2 and 4.2), is the modular structure of the retarding potential. The inner electrode has a common potential, referred to as *IE common* which is the common potential for all inner electrode rings. The IE common potential is the sum of the negative vessel potential U_{ms} and an additional negative offset potential U_{ie}.

The individual rings can be set on individual positive potentials U_{offset} relative to IE common. The retarding potential $U_{\mathrm{ret}} = U_{\mathrm{ms}} + U_{\mathrm{ie}} + U_{\mathrm{offset}}$ is defined by the electrode with the most negative potential. Usually, U_{offset} of the electrode defining the retarding potential is short-circuited to U_{ie} and consequential, the retarding potential is given by $U_{\mathrm{ret}} = U_{\mathrm{ms}} + U_{\mathrm{ie}}$.

During normal operation, U_{ie} is fixed at −200 V and U_{ms} is between −34 to −7 kV. The wide range of retarding potentials is needed for

^{83m}Kr measurements (cf. section 2.2.3). For tritium measurements, the retarding potential is usually set to values around –18.6 kV. The rather complex layout is needed to achieve a very high flexibility in the fine-tuning of the electrical field (important for investigations of systematics) and at the same time to fulfill the stabilization requirements during neutrino mass measurements.

The pre-spectrometer setup is much simpler compared to the main spectrometer setup. Magnets at both sides create the magnetic field and the magnet at the pre-spectrometer exit is shared with the main spectrometer [Kat18d]. The inner electrode system consists of two full metal cones at the entrance, with a wire electrode in between. The wire electrode is split into two parts, east and west. Each electrode can be set on an individual potential. [Kat21c]

2.1.6 *Detector system*

Electrons transmitted by the spectrometer section are accelerated by a post acceleration electrode (PAE) and guided using a magnetic field of 2.5 T to the focal plane detector (FPD) where they are counted [Kat21c]. To shift the beta-decay electrons into a region of minimal detector background, the PAE is operated at 10 kV [Ams+15].

The FPD consists of a single silicon wafer with a monolithic 148-pixel p-i-n diode array on top. The pixels are arranged in a pattern similar to a dartboard. Four pixels in the center are surrounded by twelve rings and each of the rings contain twelve pixels. All pixels have the same size of 44 mm^2. Such a pixel pattern is optimized for ring-wise consideration of radial inhomogeneities within the flux tube, given that the center of the flux tube hits the center of the detector. [Ams+15]

The FPD's energy resolution is of secondary importance, since the detector's main task is counting the electrons that are transmitted through the spectrometer and the energy scale of the measured electron spectrum is defined by the MAC-E filter. Still, the FPD system has an average energy resolution of < 2 keV [Kat21c].

To cover the wide range of possible rates, from very low rates around the endpoint, up to higher rates for systematic investigations the detector is equipped to measure total rates up to 5 Mcps [Kat21c].

Such systematic investigations are: measurements deeper into the tritium spectrum, measurements with an electron gun (cf. section 2.2.1), or measurements with ^{83m}Kr sources (cf. section 2.2.3).

2.2 Tools for monitoring and calibrating the energy scale

After the overview of the full KATRIN beamline, now three selected parts are presented further. All three of them are connected to the energy scale of KATRIN and were already briefly mentioned in the previous section.

The electron gun which is used for measuring the energy loss function (see chapter 3) is introduced first. Next, the high-voltage dividers which are an integral part of the precision stabilization of the retarding potential (chapter 4) are described. The third tool presented in this section is ^{83m}Kr, offering an energy calibration against a nuclear

standard (chapter 5).

2.2.1 *Electron gun*

One tool to investigate transmission conditions of electrons through the KATRIN beamline is the electron gun (e-gun) which offers well-defined energies up to 20 keV and angular selectivity. During commissioning measurements of the KATRIN main spectrometer, such an e-gun was mounted at the spectrometer entrance [Beh+17; Zac15; Beh16]. Before implementing the e-gun at the main spectrometer, its design was developed over several years [Val+09; Hug10; Val+11; Zac15]. For investigating the transmission of electrons through the whole KATRIN beamline, an e-gun located inside the rear section (cf. fig. 2.1) was developed by Babutzka [Bab14]. The final setup and the commissioning results are further described in [Sac20; Sch21]. Currently, a new e-gun is commissioned which is designed to deliver higher energies up to 32 keV.

The new e-gun will be described in the PhD thesis of S. Schneidewind (University of Münster).

The e-gun emits electrons via the photoelectric effect. Illumination of the photocathode with photon energies above the photo-cathode's work function frees electrons from the surface. In the case of the rear section e-gun, the photocathode is layered with a thin gold film. The energies of the emitted electrons E_e are spread from energies just above zero, up to a maximum of $hf - \phi$, namely

$$0\,\mathrm{eV} < E_\mathrm{e} < hf - \phi\,. \tag{2.22}$$

Here, $hf = hc/\lambda$ (Planck relation) is the photon energy and ϕ the work function of the photocathode material. Optimizing the photon energy to $hf \approx \phi$, yields a narrow energy distribution but limits the rate of produced electrons. [Beh+17]

Two light sources are available at the rear section e-gun. One is the laser driven light source (LDLS), emitting a continuous spectrum in the range of 190 to 2100 nm. Employing a monochromator, a narrow width (e.g. 10 nm) of wavelengths is selected. [Sch21]

The LDLS is from the manufacturer Energetiq and of type EQ-99XFC LDLS

The other light source is a pulsed UV laser with a wavelength of 266 nm and a pulse length of less than 18 ns (FWHM). The pulsed laser is used for time-of-flight measurements with the e-gun (cf. section 3.2). Independent of the light source, the light path is split to allow monitoring with a photodiode (cf. fig. 2.5).

The laser is from the manufacturer InnoLas and of type Mosquitoo. Its laser medium is Nd:YVO_4 with a frequency-quadrupled wavelength of 1064 nm.

To reach electron energies similar to the energy of beta-decay electrons measured during neutrino mass measurements, for example $E_\mathrm{e} = 18.6\,\mathrm{keV}$, the photocathode is put on a negative potential $U_\mathrm{ph} = -18.6\,\mathrm{kV}$. The *frontplate*, the plate in front of the photocathode, is usually on voltages of about $U_\mathrm{ph} + 4\,\mathrm{kV}$ and acts as first acceleration step for the electrons emitted at the photocathode. Further acceleration is done via three single acceleration electrodes. The first one is on the potential of the frontplate, the second on two third, and the last on one third of the full potential (cf. fig. 2.5).

A long cable from the rear section to the main spectrometer connects the main spectrometer vessel potential U_ms with U_ph and enables a mV-precise adjustment of U_ph relative to the retarding potential $U_\mathrm{ret} = U_\mathrm{ms} + U_\mathrm{ie}$ (cf. section 2.1.5). The full electric setup at the e-gun is explained in more detail in the work [Sch21].

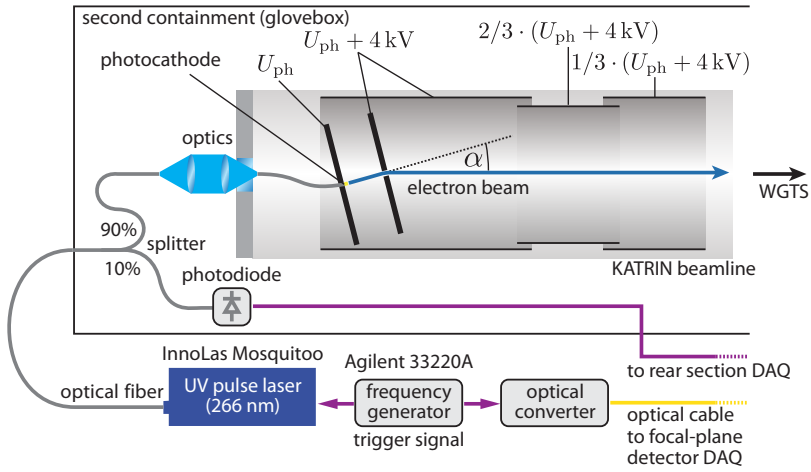

Figure 2.5 **Schematic of the electron gun.** The schematic illustrates the main optical and electrical components as used for the energy loss measurements (cf. chapter 3).

The figure was created by L. Schimpf and is copied from [Kat21b], licensed under CC BY 4.0.

The photocathode and frontplate are electrically isolated but mechanically connected and can be rotated. The rotation (around α in fig. 2.5) changes the angle of the emitted electrons relative to the magnetic field inside the rear section. Hence, rotating the plates produces electrons with different pitch angles θ (cf. section 2.1.4), making it an angular selective photo-electron source.

2.2.2 *Precision high-voltage dividers*

As introduced in section 2.1.4, the retarding potential defines the energy scale of the main spectrometer. Consequently, precision electron spectroscopy is only possible with a precision measurement of the retarding potential.

At the main spectrometer, the retarding potential is measured by two custom-built precision high-voltage dividers K35 [TMW09] and K65 [Bau+13] and 8.5-digit precision digital voltmeters. During standard operation, the high-voltage dividers are connected to the electrode on the lowest high voltage (highest retarding energy qU_{ret}). The high voltage is usually around −18.6 kV. Both dividers provide a scaling of the high voltage by a factor 2000, leading to a reading in the 10-V range. The resistor chain of the K35 is shown in fig. 2.6. The setup of the K65 is similar to the K35, but larger and with more resistors.

The dividers' output voltages of around 10 V at −18.6 kV are chosen deliberately; for this voltage range, high-precision reference multimeters, such as the Fluke 8508A, are available. Using 10-V reference standards, the reference multimeter can be calibrated. During measurement campaigns, the calibration is performed two times per week. A subset of the reference standards is calibrated annually against a Josephson standard [Pöp92].

The naming scheme reflects the total allowed voltage: The K35 can measure voltages up to 35 kV and the K65 up to 65 kV.

The voltmeter is from the manufacturer Fluke and of type 8508A.

The voltage reference standards are from the manufacturer Fluke and of type 732B. They deliver output voltages of 10 V and 1.018 V. According to their specifications, the 10 V output can vary over 2 ppm within one year.

The current voltmeter calibration procedure is described in my master's thesis.

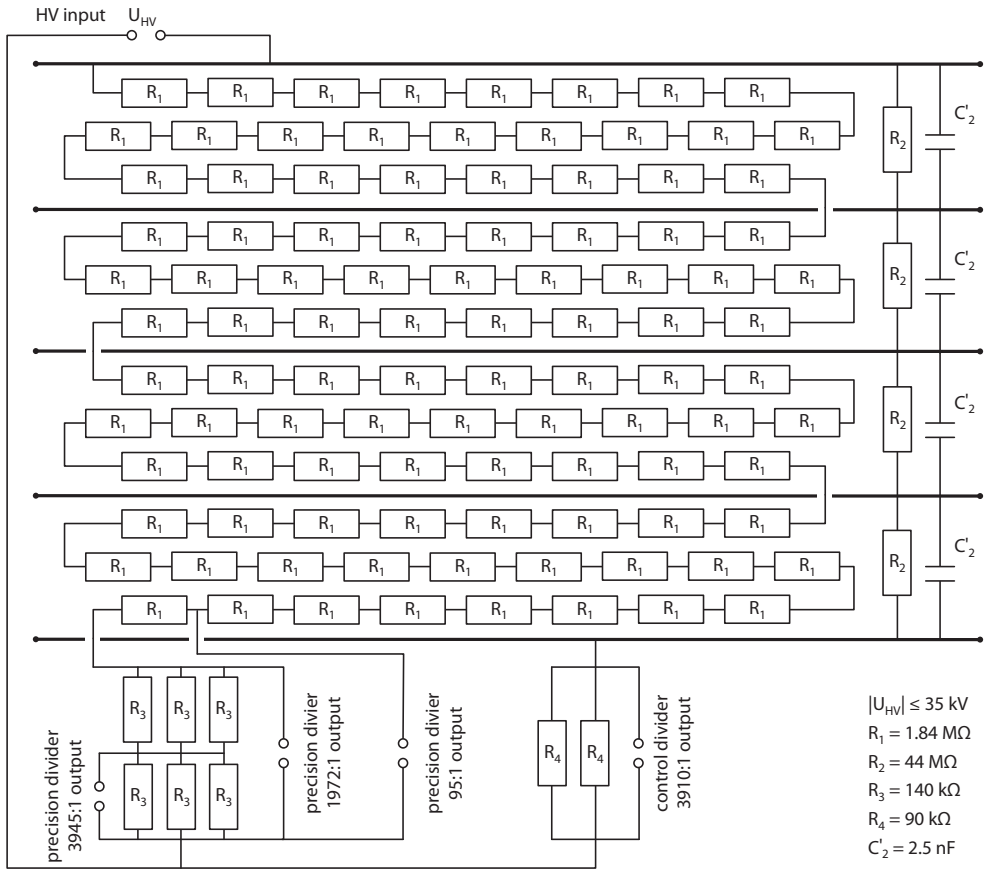

Figure 2.6 **Circuit diagram of the high-voltage divider K35.** The divider consists of a long helix with 100 resistors R_1. The five thick black lines in the schematic are copper electrodes that divide the helix into four compartments and optimize the electrostatic field inside the divider. The copper electrodes are connected with resistors (R_2) and smoothing capacitors (C_2').

The diagram was created by T. Thümmler and is used here with his permission.

For the calibration of the high-voltage dividers, several independent methods exist. One method involves spectroscopic measurements of mono-energetic conversion electrons from ^{83m}Kr electron capture decays [Kat18a], another is the absolute calibration method [Res+19]. The most recent results for the K35 are presented in section 4.5 and include an overview of the calibration history.

It is important to note that since the calibrations are traced back to the Josephson standard, or in case of the ^{83m}Kr measurements traced back to a nuclear standard, not only the precision of the dividers is proven, but also their trueness. By employing regular calibrations, the retarding potential at −18.6 kV can be monitored with an accuracy of 1 ppm (1×10^{-6}).

2.2.3 *Conversion electrons from ^{83m}Kr*

Conversion electrons from ^{83m}Kr were already mentioned as a calibration source for the high-voltage dividers and for the measurement of

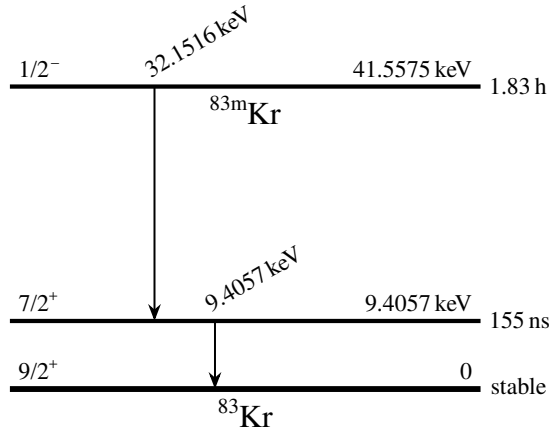

Figure 2.7 **Isomeric transitions of ^{83}Kr.** The values were taken from [Mcu15]. For each nuclear level, the spin-parity value, energy, and half-life are noted.

The figure is adapted from [Rod22], licensed under CC BY 4.0.

the source potential. Similar to the e-gun, ^{83m}Kr is an electron source with well-defined energies and it is also used to investigate the transmission conditions of the KATRIN beamline. But instead of the e-gun's pencil beam which is fixed at the end of the beamline, conversion electrons from ^{83m}Kr are available in different spatial distributions and at different positions. Overall, three different source types are employed: the solid (SKrS), the condensed (CKrS) and the gaseous (GKrS) krypton source.

The isotope rubidium-83 decays to krypton-83 via electron capture

$$^{83}_{37}\mathrm{Rb}_{46} + \mathrm{e}^- \longrightarrow {}^{83}_{36}\mathrm{Kr}_{47} + \nu_\mathrm{e}\,, \tag{2.23}$$

with a half-life of 86.2(1) d [Mcu15]. In 74(5) % ([Mcu15]) of all cases, the metastable (1.83(2) h) daughter nuclide ^{83m}Kr is created. ^{83m}Kr cascades via a 32.2-keV transition followed by a 9.4-keV transition to its ground state (cf. fig. 2.7). The transition is possible via gamma ray emission, or conversion electron emission.

Already KATRIN's predecessor experiments used conversion electrons from ^{83m}Kr as calibration source to characterize their spectrometer [Rob+91; Pic+92b; Bel+08]. The K-shell conversion electrons of the 32.2-keV transition, short K-32 line, are especially suited due to their energies of 17.8 keV, slightly below the tritium endpoint.

Aside from offering an energy scale calibration close to the endpoint, the K-32 lines have a broader line width compared to other conversion electron lines and in combination with tritium they are overlayed by tritium beta-decay electrons. Therefore, other lines more commonly used at KATRIN are the L_3-32 line at 30.5 keV which is the strongest of the 32-keV transitions and the $N_{2,3}$-32 line doublet at 32.1 keV. The $N_{2,3}$-32 doublet is of lower intensity but special due to its vanishing natural line width. A full overview of the different conversion electron lines is given in [Vén+18].

In the case of the solid krypton source, also referred to as implanted source, ^{83}Rb ions are implanted on different substrates. Initially, gold

and platinum foils were used as substrate [Zbo+13], later also highly-oriented pyrolytic graphite (HOPG) [Sle15]. Since the ^{83}Rb generator is located in the source itself, the SKrS is very compact with convenient handling. One drawback is the change of binding energies of ^{83m}Kr over time due to solid state effects [Zbo+13]. Methods exist to characterize the drift and if it is fully characterized, the source can be used for relative investigations of the energy scale [Sle15].

The SKrS is used at the monitor spectrometer which is the refurbished spectrometer of the former Mainz neutrino mass experiment [Pic+92a]. It is reassembled next to the KATRIN main spectrometer and is designed to calibrate and monitor the retarding potential. [Erh+14] During the first two neutrino mass measurement campaigns, the monitor spectrometer was used in parallel to the main spectrometer. The parallel operation was discontinued for now, since the long-term stability of the high-voltage dividers was proven with other more sensitive methods (cf. section 4.5), making the rather complex running of the monitor spectrometer with its own systematic effects less beneficial.

Whereas the implanted source is at an external setup, allowing for parallel measurements, the condensed krypton source is located at the KATRIN beamline between CPS and pre-spectrometer (cf. fig. 2.1). The location makes the CKrS a unique tool to investigate the transmission conditions for electrons of various energies inside the main spectrometer.

At the CKrS, gaseous ^{83m}Kr from ^{83}Rb is frozen as a sub-monolayer film on a substrate. During the earlier versions, a copper substrate was used [Pic+92b], later the substrate was switched to HOPG. To allow for the ^{83m}Kr to freeze on the surface, the substrate is cooled below 30 K with a cryo-cooler system [Dyb19]. Similar to the SKrS, the absolute line positions of the conversion electron lines are shifted due to solid state effects [Ost09]. The setup and first commissioning results of the CKrS at KATRIN are described in [Dyb19] and further measurement results can be found in [Fed19; Ful20].

The third source is the gaseous krypton source. Similar to the CKrS, gaseous ^{83m}Kr is emanated from a ^{83m}Kr generator, but instead of freezing it on a surface, the gas is circulated in the WGTS. The ^{83}Rb for the ^{83m}Kr generator is stored in small zeolite beads with about 2-mm diameter. [Sen+18]

Different circulation modes are possible. For example, only ^{83m}Kr can be injected, or it is injected together with tritium. The very first KATRIN measurements with electrons from a gaseous source were performed with only ^{83m}Kr inside the WGTS [Kat18b]. To avoid freezing of ^{83m}Kr inside the WGTS, those measurements where performed at a WGTS temperature of 100 K [Kat18b].

As a compromise between the ideal temperature to avoid tritium condensation (30 K) and a temperature high enough to avoid freezing of ^{83m}Kr, the new standard WGTS operation temperature was defined to be 80 K. Within 30 minutes, the circulation can be switched from co-circulation of ^{83m}Kr and tritium to only tritium. [Mar+22]

As outlined by Machatschek [Mac21], temporal or spatial variations of the potential can lead to distortions of the beta spectrum caused by averaging over multiple beta spectra accumulated at different starting

potentials. A gaseous ^{83m}Kr source with its mono-energetic conversion electrons and which can be co-circulated in gaseous form with tritium is ideal for an in-situ energy calibration of the temporal as well as spatial potential variations. With the simple switching between both modes, the energy calibration achieved during the co-circulation is transferable to the mode with only tritium as it is used for neutrino mass measurements.

Going a step further, the absolute energy scale is accessible by comparing the line positions of the ^{83m}Kr conversion electrons to literature. Currently, this comparison is limited by the uncertainty on ^{83m}Kr transition energies. In chapter 5, a method for determining the transition energies at KATRIN is presented.

2.3 Neutrino mass results

In 2018, the KATRIN beamline was operated for the first time with tritium. As a first commissioning run, the WGTS was run with deuterium mixed with traces of tritium (1% DT) at nominal column density, leading to 0.5% of nominal activity [Kat20a]. Afterwards, during the first neutrino mass measurement campaign (KNM1), high-purity tritium (95% T_2) was used at roughly one fifth of the nominal column density [Kat19]. The most recently published result is from the second campaign (KNM2), where the WGTS was run with almost nominal column density (84% of the nominal value) and high-purity tritium [Kat22].

In all campaigns, a stable source and stable potentials are needed for successful neutrino mass measurements. The source is kept at constant conditions and the retarding potential at the main spectrometer is changed in steps and measured with the precision measurement chain (cf. section 2.2.2). The time spent at each retarding potential is defined by the measurement time distribution (MTD).

As described in section 2.1.4, the rate measured at the detector is an integral spectrum; all electrons with energies above the retarding threshold are counted. The expected rate measured at the detector for a given retarding energy qU_{ret} is

$$R(qU_{\mathrm{ret}}) = A_s N_T \int_{qU_{\mathrm{ret}}}^{E_0} R_\beta(E) f(E, qU_{\mathrm{ret}}) \mathrm{d}E + R_{\mathrm{bg}}(qU_{\mathrm{ret}}) \,. \tag{2.24}$$

The quantities A_s, N_T are normalization factors, $R_\beta(E)$ is the beta-decay spectrum (1.58) and $f(E, qU_{\mathrm{ret}})$ is the experimental response function. [Kat22] The response function is given by the transmission function of the main spectrometer (2.21) and the energy loss inside the source (cf. chapter 3).

The quantity $R_{\mathrm{bg}}(qU_{\mathrm{ret}})$ is the rate of background events. The background is characterized during measurements without tritium and is dominated by background proccesses induced due to polonium-210 α decay [Frä+22]. To monitor the background during neutrino mass measurements, additional points above the tritium endpoint E_0 are added to the MTD (cf. fig. 2.8).

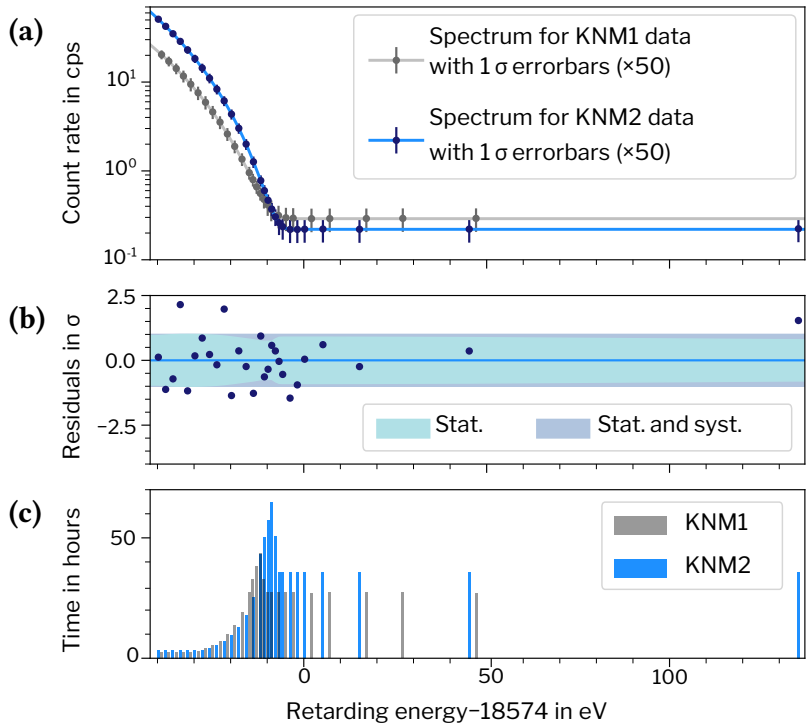

Figure 2.8 **Results from the first and second neutrino mass measurement campaign.** Panel (a) shows the accumulated count rates during KNM1 and KNM2. The colored lines are the best-fit model for each dataset. For the fit on the KNM2 data, the normalized residuals are plotted in (b). The statistical and systematic uncertainties are depicted by the shaded areas. In (c), the accumulated measurement time at each retarding energy is displayed, illustrating the measurement time distribution.

The figure is adapted from [Kat22] under license CC BY 4.0; the second and third panels of the original were removed.

The measured integral spectrum, including a fit using the expected spectrum (2.24), is presented for the measurement phases KNM1 and KNM2 in fig. 2.8. Comparing the two phases, one can see the increase in statistics, caused by a higher source activity combined with a background decrease of about 25 %. Prior to KNM2, the spectrometer was heated up to 200 °C for about two weeks, causing the decrease of the background. [Kat22]

2.3.1 *Systematic effects*

For efficient data taking, systematic and statistic uncertainties should match. Therefore, the overall systematic budget for all possible systematics has been defined as $0.017\,\mathrm{eV}^2/c^4$, roughly matching the aimed total statistical uncertainty of $0.018\,\mathrm{eV}^2/c^4$ on m_ν^2 [Kat05]. In KATRIN's design report [Kat05], multiple possible systematic effects were investigated and five major effects were identified out of those. Therefore, the overall budget was split in five and it was required that no systematic effect should introduce a neutrino mass shift larger than

$7.5 \times 10^{-3}\,\mathrm{eV}^2/c^4$. High-voltage fluctuations of the retarding potential (cf. chapter 4) and the determination the energy-loss function (cf. chapter 3) are two of these five major effects.

During KNM2, the dominant systematic effect is the background, followed by uncertainties on the WGTS potential [Kat22]. In contrast, the uncertainties due to the energy-loss function and due to retarding potential fluctuations are negligible in comparison. The retarding potential was already a negligible uncertainty during KNM1 ($\Delta m_\nu^2 \approx 3 \times 10^{-3}\,\mathrm{eV}^2/\mathrm{c}^4$). After KNM1, it was improved with a new stabilization loop (cf. section 4.2), leading to a further uncertainty reduction of about a factor ten.

For the campaigns following KNM2, improvements were implemented to reduce the effects of the new major systematics. For example, the WGTS is operated at 80 K, improving the WGTS potential investigations with $^{83\mathrm{m}}$Kr (cf. section 2.2.3). The background is reduced by a factor of two, with a new magnetic and electric field configuration that shifts the analyzing plane closer to the detector [Lok+22a].

3 Inelastic scattering of electrons inside the tritium source

The main results presented in this chapter are published in the paper [Kat21b] by the KATRIN collaboration. My contributions include: the first demonstration of the use of a time-of-flight method to measure the energy-loss function on deuterium as well as on tritium in a differential mode; establishing an analysis routine for the differential measurements, developing methods to reduce the effect of background in the differential measurements, and enhancing the final fit of the energy-loss parametrization.

To date, two other PhD theses exist which study the results that went into [Kat21b]. The first by Sack [Sac20] discusses the initial parametrization of the energy loss function for deuterium and the second by Schimpf [Sch21] discusses the analysis routine for the integral dataset, a combined fit of the integral and differential datasets both with deuterium and tritium as well as a detailed characterization of systematic effects.

Whereas the work [Kat21b] contains a comprehensive overview of the main results, this chapter explores in more detail a number of topics which were selected based on the areas of my contributions. Results mentioned in this chapter and also published in [Kat21b] or [Sac20; Sch21] are referenced appropriately.

Beta decay electrons inside KATRIN's windowless gaseous tritium source (WGTS) can lose energy due to scattering on gas molecules. The overall scattering probability is related to the source density. The probability to lose a certain amount of energy due to the scattering is called the *energy-loss function*. The measured beta-decay spectrum at KATRIN is distorted by the energy loss inside the source. Only if the energy-loss function is well-known, the spectrum can be fitted to determine the neutrino mass.

This chapter starts with a general overview on external measurements of electron scattering on hydrogen isotopologs. Afterwards, the analysis of differential energy-loss data is presented. The energy-loss

model, obtained by a combined fit to the differential data, is presented and compared to a combined fit of differential and integral data.

3.1 Electron scattering on hydrogen isotopologs outside of KATRIN

The scattering of electrons on hydrogen molecules has been studied both experimentally and theoretically. Due to its simplicity, the H_2 molecule is an ideal candidate for the comparison between theoretical models and experiment. In the standard energy-loss measurement setup an electron source with well defined electron energies is used. The electrons are guided through the individual test chamber where the scattering is to be investigated. Afterwards the energy of the electrons is measured and the amount of energy loss determined. In all setups one always needs to account for angular change, and some of the setups are sensitive to the angular change and also for the probability of multiple scatterings, depending on the source density.

One example are the measurements from Geiger [Gei64] where the scattering of 25 keV electrons on H_2 is investigated and compared to theoretical predictions. The results are displayed in fig. 3.1. The scattering can be of elastic or inelastic nature. For elastic scattering the main distribution of angular change is within 2°. For inelastic scattering the angular change is significantly lower; The overall scattering cross section is the largest for small angles ($\approx$ 0.006°) and decreases with higher angular changes ($\approx$ 0.6°) by about three orders of magnitude. For small angular changes, the inelastic scattering is the dominant process and roughly three orders of magnitude larger. Beginning with angular changes of about 0.6°, the elastic scattering is the dominant process.

Geiger [Gei64] shows that not only the overall scattering probability depends on the scattering angle but also the probability of a certain energy loss. For very small angular changes ($< 0.014°$) the energy loss is dominated by a peak around 12.6 eV. The loss of about 12.6 eV is due to electronic excitations of the H_2 molecule, mainly excitations of the $B(2p\sigma\,^1\Sigma_u^+)$ and the $C(2p\pi\,^1\Pi_u)$ state. With larger angular changes (e.g. 1°) the energy loss due to electronic excitations persists, but the contribution of energy losses due to ionization is increased. (For energy exchanges above $\approx$ 15.4 eV the H_2 molecule can be ionized.) By focusing on only very small angular changes ($< 0.017° = 3 \times 10^{-4}$ rad), the energy resolution of the measurement method applied by Geiger [Gei64] was improved further from 1 eV to about 40 meV. With this high resolution the scattering-induced electronic transitions to the different vibrational or rotational states (in short: rovibrational states) can be resolved.

Later the setup was improved to a resolution of about 10 meV and precision energy-loss spectra with 34 keV primary electrons were acquired for H_2, D_2 and HD [GS69]. These measurements can be used to compare the band intensities for the different isotopes. Again, for these measurements only scattering with angular changes up to 0.017° is taken into account.

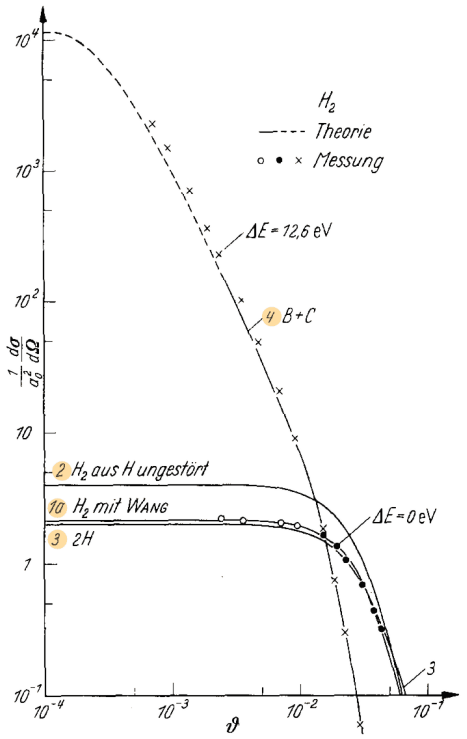

Figure 3.1 Angular distribution of electrons scattered elastically and inelastically on hydrogen. The differential cross section $d\sigma$ per molecule, divided by the solid-angle element $d\Omega$ and the Bohr radius a_0 squared, is plotted against the scattering angle ϑ (in radian). (1a), (2) and (3) show the elastic scattering and (4) is the sum of the differential cross sections for the excitation of the B and C state. Measurement results are plotted as dots, circles, and crosses and theoretical predictions are plotted as a line.

The figure is copied from [Gei64]. Reproduced with permission from Springer Nature.

For neutrino mass measurements with a tritium source, not only the small scattering angles are of importance although they are the dominant part of the inelastic scattering, but the overall energy and angular change due to the scattering. For setups with the MAC-E filter principle, any angular change directly corresponds to an effective energy change. At KATRIN with the nominal 6.3 G setting (cf. section 2.1), a 2° angular change corresponds approximately to a 6 meV change which is negligibly small. However, as shown in the work by Geiger [Gei64], the individual intensity of the rovibrational states and especially the amplitude of the ionization depends on the scattering angle. Therefore it is important to characterize the energy-loss function for the individual setup to account for the unique geometry and gas composition.

For the Troitsk and Mainz neutrino mass experiments the energy-loss function in gaseous tritium and quench condensed deuterium films was determined [Ase+00]. The K-32 conversion electron line from ^{83m}Kr was used as 17.8 keV electron source to determine the energy-loss function in the deuterium films. For the Troitsk setup,

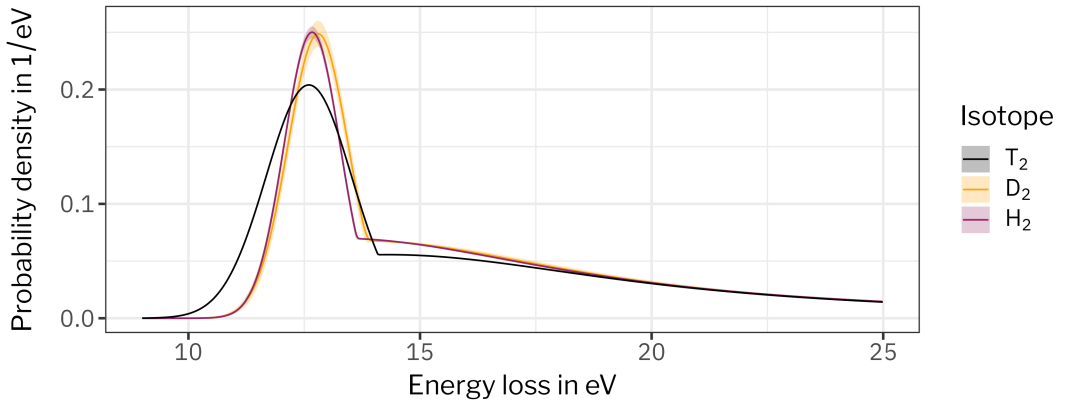

Figure 3.2 **Energy-loss functions for the scattering of electrons on hydrogen isotopologs.** 18-keV electrons are used for the energy-loss function on gaseous T_2 [Ase+00]. For the energy-loss measurements on D_2 and H_2, different electron energies (14 keV, 17 keV, 19 keV, and 25 keV) were chosen. The results for different energies were compatible within the measurement uncertainty and one combined result is given [Abd+17]. The shaded areas behind the functions are 1-σ uncertainty bands for the function. (In the T_2 case, the error is too small to be seen.)

an electron gun at 18 keV was used. Later, using a new spectrometer at Troitsk with about two times improved energy resolution, the measurements were repeated for the isotopes deuterium and hydrogen [Abd+17].

As a parametrization for the measured energy-loss function, the electronic excitations around 12.6 eV are described by a Gaussian and the continuum is described by a Lorentzian. The resulting parametrization is step-wise defined as

$$f(\Delta E) = \begin{cases} A_1 \cdot \exp\left(-2\left(\frac{\Delta E - E_1}{w_1}\right)^2\right), & \Delta E < E_c\,, \\ A_2 \cdot \frac{w_2^2}{w_2^2 + 4(\Delta E - E_2)^2}\,, & \Delta E \geq E_c\,. \end{cases} \tag{3.1}$$

For the analysis of the T_2 measurements, E_1 was fixed in the fit to 12.6 eV [Ase+00], whereas it is a free parameter in the analysis of the D_2 and H_2 measurements [Abd+17].

The free fit parameters of the parametrization, E_1, E_2 are the positions, w_1, w_2 the widths and A_1, A_2 the amplitudes of the Gaussian and Lorentzian, respectively. The junction point of the Gaussian and Lorentzian E_c is an additional fit parameter. The position E_c is determined by the fit in a way that the Gaussian and Lorentzian have a smooth connection at E_c. [Ase+00]

The resulting energy-loss functions are shown in fig. 3.2. The previously obtained energy-loss functions were used for KATRIN studies (e.g. [Kle+19]), but to reach KATRIN's sensitivity goal, in-situ energy-loss measurements at the KATRIN setup are indispensable.

3.2 Time-of-flight measurement principle

For the in-situ energy-loss measurements at KATRIN, the angular-selective rear-section electron gun (e-gun) is used (cf. section 2.2.1). It can produce mono-energetic electrons with well-defined energies E_{source}. For the energy-loss measurements the electron's pitch angle between the magnetic field lines and the electron's momentum vector is fixed to approximately $\theta = 0°$.

The electrons from the e-gun are guided from the rear-section into the WGTS and from there through the full KATRIN beamline to the spectrometer and detector. Their way from the WGTS to the spectrometer is the same as for any beta-decay electron, including the probability to lose energy on their way. With well-known E_{source}, the electron's energy loss ΔE on the way to the detector can be evaluated by measuring the electron's energy with the spectrometer.

As described in section 2.1.4.1, KATRIN's uses a MAC-E filter type spectrometer that measures an integral spectrum. Only electrons with a surplus energy $E_s \geq 0$ above the spectrometer's retarding threshold are transmitted and counted at the detector. The value of E_s is not measured. By changing E_s, an integral spectrum $R(E_s)$ is recorded. The measured spectrum consists of the transmission function $T(E_s)$ for the e-gun electrons inside the main spectrometer combined with the overall scattering probability $F(\Delta E, \mu)$ for electrons inside the gaseous source.

The scattering probability is the energy-loss spectrum, weighted by the probability $P_n(\mu)$ for n-fold scattering. The mean scattering rate $\mu(\theta)$ of an electron after traversing the full WGTS is constant and only depends on the source density (assuming a stable source density over time) and the electron's angle θ:

$$\mu(\theta) = \frac{\rho d \sigma_{\text{tot}}}{\cos\theta} \,. \tag{3.2}$$

The source density is given by the column density ρd inside the WGTS. The nominal column density is defined as $\rho_0 d = 5{\times}10^{21}\,\text{molecules}/\text{m}^2$ [Kat05]. The total inelastic cross section is $\sigma_{\text{tot}} = 3.64 \times 10^{-22}\,\text{m}^2$ [Kat21a]. The scattering events itself are independent of each other; each scattering does not change the probability for another scattering event. Therefore, $P_n(\mu)$ can be described by a Poisson distribution [Han+17]:

The angular change due to scattering is small (cf. section 3.1) and hence does not change the probability of subsequent scattering events significantly.

$$P_n(\mu) = \frac{\mu^n(\theta)}{n!} \exp\left(-\mu(\theta)\right), \quad \text{with } n = 0,\ 1,\ 2, \ldots . \tag{3.3}$$

Together with the energy-loss function $f(\Delta E)$ it follows

$$\begin{aligned} F(\Delta E, \mu) =& P_0(\mu) \cdot \delta(\Delta E) \\ &+ P_1(\mu) \cdot f(\Delta E) \\ &+ P_2(\mu) \cdot f(\Delta E) * f(\Delta E) + , \ldots . \end{aligned} \tag{3.4}$$

For the unscattered electrons the energy stays unchanged, corresponding to a Dirac delta function $\delta(\Delta E)$. For n-fold scattering, $P_n(\mu)$ is multiplied with the n-fold convoluted energy-loss function with itself. [Kle+19]

$T(E_s)$ is determined in-situ during the energy-loss measurements. As known from the Geiger [Gei64] and Aseev et al. [Ase+00] measurements, the energy loss starts around $\Delta E_{min} = 10\,\text{eV}$. The measurement of unscattered electrons, $R(E_s)$ measured at the detector for $E_s < \Delta E_{min}$, corresponds directly to $T(E_s)$. In that way, the e-gun characteristics such as angular and energy distribution are directly considered together with the transmission function of the main spectrometer. The complete spectrum measured at the detector is

$$R(E_s) = F(\Delta E, \mu) * T(E_s)\,. \tag{3.5}$$

To access $f(\Delta E)$ from such a measurement, the multiple scattering and the transmission function needs to be deconvolved [Han+17]. This shows a clear limitation of a MAC-E filter type spectrometer. As long as a functional description exists for the observed electron distribution and for the spectrometer response, as it is the case for the beta decay spectrum, or conversion electrons from ^{83m}Kr, the observed integral spectrum can be analyzed by integrating the expected electron distribution and fitting it together with the spectrometer response. If no functional description exists deconvolution is necessary. For the energy-loss measurements by Aseev et al. [Ase+00] this was solved by introducing a simplified parametrization for $f(\Delta E)$ (3.1) and fitting it to the measurement data.

As written above, only electrons with $E_s > 0$ arrive at the detector. The detector has no information about the value of E_s. However, the MAC-E filter filters by decelerating the electrons inside the spectrometer and their flight time after deceleration depends on their energy E_s; Electrons with larger E_s traverse the filter faster than electrons with smaller E_s. If the electron's flight time is known, the information can be used in the analysis to determine a differential spectrum from the integral one.

To determine the flight time of an electron, the time it enters and exits the filter needs to be measured. The exit time can be connected to the time it is detected at the detector. The timing resolution of the detector depends on the shaping time. For a shaping time of about 1.6 µs, as during the energy-loss measurements [Kat21b], the timing resolution is $\mathcal{O}(100\,\text{ns})$ [Ams+15]. The time the electron enters the spectrometer is more difficult to measure.

At the Mainz neutrino mass measurement setup, the ^{83m}Kr source could be pulsed by applying a high voltage to reduce the starting potential of the conversion electrons so that they are blocked by the retarding potential [Bon+99]. The electrons were blocked for a time period of 2.5 µs, followed by a 2.5 µs open period. Electrons arriving during the "blocked period" after a certain waiting time (1.1 µs) at the detector have "long" flight times. The length of the blocked period and the waiting period are uniquely chosen for the Mainz setup. By selecting only electrons with long flight times (corresponding to lower E_s) a low-pass filter is added to the high-pass (MAC-E) filter, resulting in a band-pass filter. With the band-pass filter a differential spectrum is obtained. Its energy resolution is defined by the width of the band-pass filter.

After these first successful measurements at the Mainz experiment, the idea to combine the MAC-E filter technique with a time-of-flight

(ToF) method was pursued further. For example, its feasability for improving the neutrino mass sensitivity was investigated by Steinbrink et al. [Ste+13] and Fulst et al. [Ful+20]. At the Mainz setup, a pulsed e-gun was developed and time-of-flight test measurements were performed [Val+09]. Later, a test at KATRIN with a further devoleped e-gun [Beh+17] was performed [Ste17]. Additionally, the e-gun ToF measurements were used to validate the three-dimensional electrostatic field calculation for the main spectrometer [Bar16]. Building on that, C. Weinheimer proposed to use the rear section e-gun in a pulsed mode and apply the ToF method to measure the energy-loss function in a differential mode.

The full measurement proposal by C. Weinheimer (Aug. 2018) is available here. (Note: purple links are not publicly accessible.)

In such a differential energy-loss measurement, $R(E_s)$ directly corresponds to $F(\Delta E, \mu)$. It is only broadened by the finite resolution of the band-pass filter. By choosing a very small column density, $F(\Delta E, \mu)$ is dominated by the unscattered and one-fold scattered electrons. Therefore, $f(\Delta E)$ is directly visible in $R(E_s)$ and no deconvolution is needed to access $f(\Delta E)$.

The first proof of concept differential energy-loss measurement was a 12 h long measurement with about 5 % deuterium inside the WGTS. On this dataset the analysis routine for the ToF method was established. This first dataset had already sufficiently small statistic uncertainty to develop a new semi-empirical parametrization for $f(\Delta E)$ [Sac20]. In parallel, the deconvolution method was applied to energy-loss measurements in the standard integral mode. The analysis of the integral data and deconvolution result is described by Schimpf [Sch21].

For more details see my talk at the KATRIN collaboration meeting (Nov. 2018).

It was found that the most precise description for the energy loss on deuterium is achieved by a combined fit of the integral and differential measurements using the new semi-empirical parametrization [Sac20; Sch21]. After this success with the deuterium data, more data was acquired with tritium instead of deuterium and with both the differential and integral measurement mode. A further developed fit is described by Schimpf [Sch21] and also published in Aker et al. [Kat21b].

In the following section, the measurement results and the analysis details for the differential energy-loss measurements are presented.

3.2.1 *Measurements*

For the measurements, the e-gun is used with a 266 nm pulsed UV laser (cf. section 2.2.1). The laser pulse is controlled via a Q-switch that can be externally triggered. During the differential measurements the laser is triggered with 20 kHz. The trigger pulse is scaled down by 1024 and fed via an optical cable into the data acquisition unit of the detector (cf. fig. 2.5). With this, a time relative to each laser pulse τ can be determined for each event recorded at the detector.

The KATRIN beamline is 70 m long and the e-gun is on the opposite side from the detector (cf. fig. 2.1).

The timing signal reaches the detector with a delay consisting of two main components. The first is the approximately 100 m length of the optical cable. Assuming a typical delay for optical cables of 5 ns/m gives a total delay of 0.5 µs. The second is the delay between pulse generator and the pre-scaler which is measured to be about 0.43 µs.

The estimation based on the measurements was done by J. Behrens and details can be found here.

During the measurements, the energy of the electrons emitted by

the e-gun is defined by

$$E_{\text{source}} = qU_{\text{ph}} + hf - \Phi_{\text{eg}}\,. \tag{3.6}$$

The photon energy, given by the Planck relation, is $hf = 4.66\,\text{eV}$. The work function of the gold photocathode Φ_{eg} was determined to be 4.43 eV [Sac20]. U_{ph} is the potential applied to the photocathode and q the charge of the electron. U_{ph} is the sum of the main spectrometer vessel potential U_{ms} (a long cable along the KATRIN beamline to the e-gun) and an offset voltage U_{s} on top of U_{ms}. The retarding potential U_{ret} is the sum of U_{ms} and the inner electrode common potential U_{ie} (cf. section 2.1.5). The actual potential seen by the electrons is U_{ret} reduced by the work function of the main spectrometer Φ_{MS} and the potential depression U_{dep}. U_{dep} depends on the electromagnetic field setting in the main spectrometer and can be determined from simulations. Combining all this with (3.6), the surplus energy of the electrons is defined as

$$\begin{aligned} E_{\text{s}} &= E_{\text{source}} - \left(q \cdot \left(U_{\text{ret}} - U_{\text{dep}}\right) - \Phi_{\text{MS}}\right) \\ &= q \cdot \left(U_{\text{ph}} - U_{\text{ret}} + U_{\text{dep}}\right) + hf - \Phi_{\text{eg}} + \Phi_{\text{MS}} \\ &= q \cdot \left((U_{\text{s}} + U_{\text{ms}}) - (U_{\text{ms}} + U_{\text{ie}}) + U_{\text{dep}}\right) + hf - \Phi_{\text{eg}} + \Phi_{\text{MS}} \\ &= q \cdot \left(U_{\text{s}} - U_{\text{ie}} + U_{\text{dep}}\right) + hf - \Phi_{\text{eg}} + \Phi_{\text{MS}}\,. \end{aligned} \tag{3.7}$$

The surplus energy is varied by changing U_{s}; all other parameters stay unchanged. U_{s} is continuously ramped in a triangle wave pattern with a period of 1 hour and a peak-to-peak voltage of 65 V (cf. top panels in fig. 3.3). By changing U_{s}, E_{source} is also changed. During the tritium measurements, the minimum E_{source} is about 18 568 eV and the maximum at about 18 633 eV.

During the deuterium measurement, the peak-to-peak voltage was only 60 V, which corresponds to a ramping speed of 33 mV/s. The ramping speed during the tritium measurements was slightly faster at about 36 mV/s.

During each half period of the triangle wave of U_{s}, one single measurement at the detector is acquired. Throughout the rest of this chapter, such a measurement is referred to as one *run* and a sequence of multiple runs is called one measurement. The measured events at the detector during one 30 minute run are shown in fig. 3.4 as an example. To minimize any angular-dependent broadening, a minimal magnetic field setting with about $1 \times 10^{-4}\,\text{T}$ at the analyzing plane is chosen and kept the same for all measurements (cf. section 2.1.4.1). A summary of all differential measurements is given in table 3.5.

During the deuterium measurements, the earth magnetic field compensation coils were changed compared to the tritium measurements. The change only had a negligible effect on the magnetic field at the analyzing plane but it slightly modified the path of the e-gun electrons through the main spectrometer which is visible in a different position of the electron beam at the detector.

3.2.2 *Time-of-flight selection*

As explained above, the flight time of the electron from the e-gun to the detector can be estimated with the time-difference τ between the time of the event at the detector and the trigger pulse of the laser. In fig. 3.4, τ is plotted for each event against the time of the event.

In fig. 3.6a, the expected flight times for electrons flying through the main spectrometer is plotted. Only flight times up to 50 µs can be distinguished. Electrons with longer flight times coincide with the subsequent laser pulse. (The laser is pulsed with 20 kHz resulting in a laser pulse every 50 µs.) By selecting electrons with flight times between 35 µs and 50 µs, electrons with $E_{\text{s}} \in [0.03\,\text{eV}, 0.16\,\text{eV}]$ are selected (cf. fig. 3.6b), resulting in a resolution of 0.13 eV for the

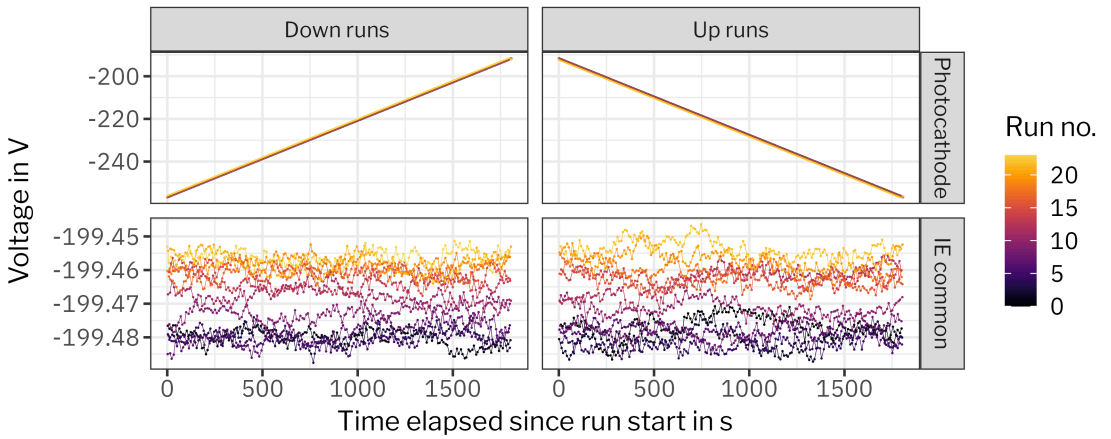

Figure 3.3 **Voltages during an energy-loss measurement.** The top row shows the voltage U_s at the e-gun's photocathode which is ramped continuously in a triangle wave during the measurement. The lower row shows the inner electrode common voltage U_{ie}. Any change in the difference between U_{ie} and U_s causes a change in the surplus energy E_s (3.7) of the e-gun electrons. The left column shows the voltages during runs with decreasing E_s (down runs) and the right column during runs with increasing E_s (up runs). The voltages shown here for illustration are the voltages observed during the energy-loss measurement on tritium with $22\,\%\ \rho_0 d$. The other measurements show a similar pattern.

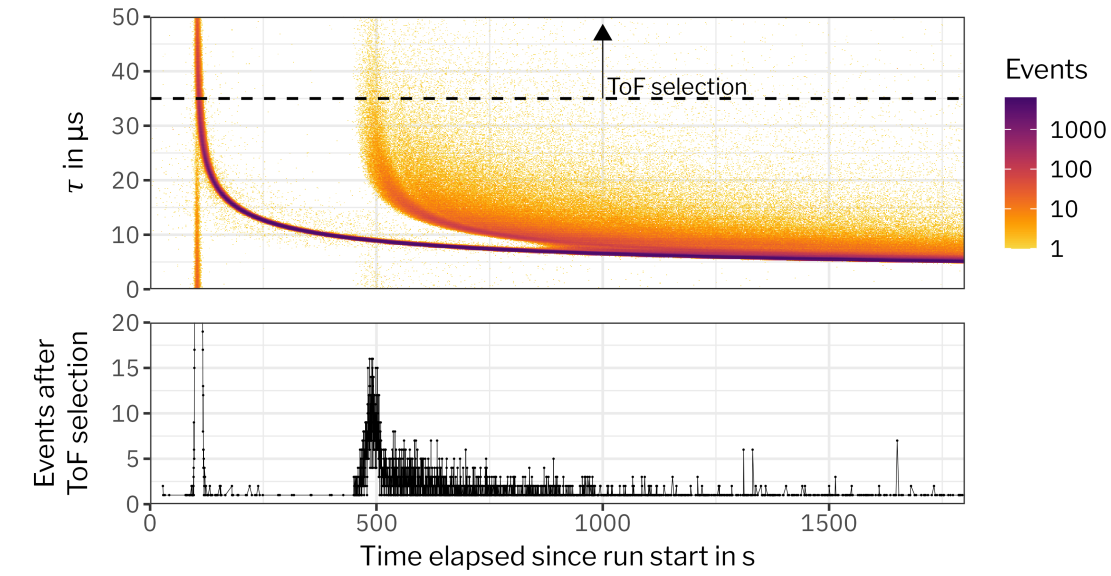

Figure 3.4 **An energy-loss measurement on deuterium.** The top panel shows for one 30-minute run the electron flight times τ. Each bin has a height of 0.1 µs (bin size for τ) and a width of 2 s. The color indicates the number of events per bin, and bins with 0 events are not drawn. The bottom panel shows for each x-axis bin the number of events with $\tau > 35$ µs.

Table 3.5 Overview of differential energy-loss measurements. The table shows selected properties of differential energy-loss measurements with deuterium or tritium in the source. The rate is the peak rate measured at the detector for the highest surplus energy. It can be used to approximate the laser intensity during the measurements. The range for E_s is obtained from the minimum and maximum energy of the spectra after the energy scale calibration has been applied (cf. section 3.2.3). The column density values are given in percent of nominal column density $\rho_0 d = 5 \times 10^{21}\,\mathrm{molecules/m^2}$ [Kat05]. They are estimated from the mean scattering probability μ (3.2), which is a free parameter in the energy-loss fit (see section 3.3), and under the assumption that $\theta = 0°$.

Source	CD $\%\,\rho_0 d$	Rate kcps	E_s range eV	U_s slope mV/s	No. runs	Run identifiers
D_2	5	14	$[-3.2, 55.6]$	33.168(2)	24	44109-44132
T_2	15	6	$[-4.8, 58.9]$	36.936(2)	33	49410-49442
T_2	39	6	$[-4.3, 58.8]$	35.955(2)	23	50119-50141
T_2	5	6.5	$[-5.2, 59.4]$	35.936(2)	7	50892-50898
T_2	5	6.5	$[-5.3, 89.5]$	35.961(6)	16	50924-50939
T_2	22	7	$[-5.0, 59.0]$	35.952(2)	23	52084-52107
T_2	84	6	$[-5.0, 58.9]$	35.952(2)	28	52160-52187

band-pass filter. Choosing a wider selection interval by decreasing the minimal flight time increases the statistic but widens the energy resolution. The selection interval was chosen as the best trade-off between energy resolution and reasonable statistics.

The simulations only describe the flight time through the spectrometer. The flight time from the e-gun electrons to the spectrometer is simplified as the time t_e an electron with $E_{source} = 18\,573\,\mathrm{eV}$ travels over a distance s:

$$t_e = \frac{E_{rel}}{p} \cdot s, \text{with } \; p = \sqrt{E_{rel}^2 + m_e^2 c^4}, \; E_{rel} = E_{source} + m_e c^2 \,. \tag{3.8}$$

With the mass of the electron $m_e \approx 511\,\mathrm{keV}/c^2$, and the distance between the e-gun and the main spectrometer entrance $s \approx 50\,\mathrm{m}$, follows $t_e \approx 0.64\,\mu\mathrm{s}$. The simulation result is shifted by t_e and plotted in fig. 3.7 together with the measurement results.

The results from simulation and measurement agree very well in their shape. The absolute flight time of the electrons τ, is not known and can only be approximated. One source for a shift of the measured τ is already approximated by the shift of the start signal of the laser trigger, causing overall longer flight times. Other additional unknown offsets from the measurement chain or the simulation are possible, but are not investigated here in detail.

In the bottom panel of fig. 3.4, a ToF selection is applied to the data;

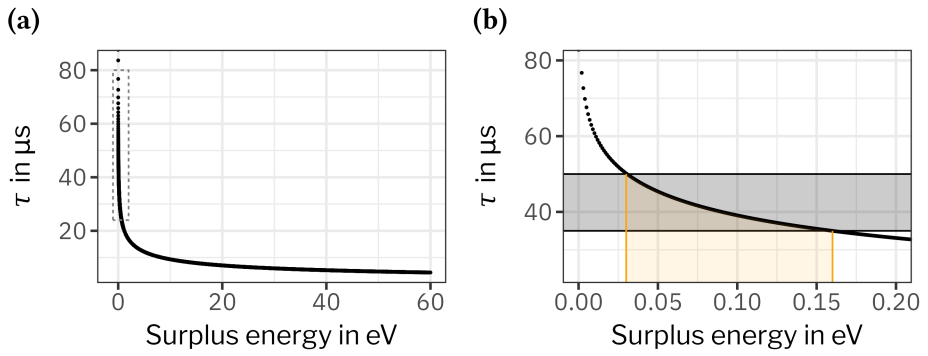

Figure 3.6 **Flight time of an electron through the main spectrometer.** The simulated flight time for electrons with $\theta = 0$ and with energies ranging from $E_{\text{source}} = 18\,573\,\text{eV}$ to $18\,633\,\text{eV}$ is plotted against E_s. The main spectrometer retarding potential was fixed to $U_{\text{ret}} = -18\,573\,\text{V}$. The simulation used to obtain these results is introduced in section 4.1. In plot (b) a subset of plot (a) is shown and the standard ToF selection region from 35 µs to 50 µs is marked in gray. The orange lines indicate the range in E_s obtained with the ToF selection.

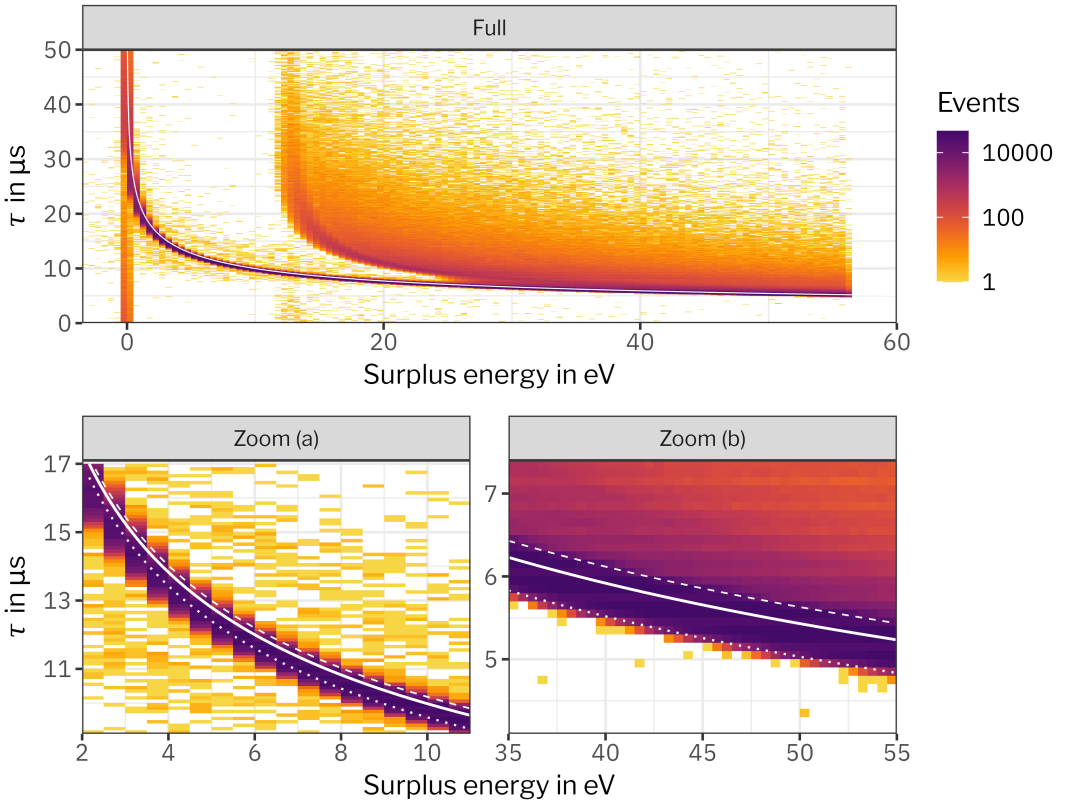

Figure 3.7 **Comparison of simulated and measured flight times.** The solid white curve is the sum of the simulation result plotted in fig. 3.6 and the approximated flight time of the electron from the e-gun to the spectrometer (3.8). Two lines shifted relative to the white curve are added for illustration purposes. The dashed line is shifted by 0.2 µs and the dotted line by −0.4 µs. The colored heatmap which the lines are overlayed upon shows the single-run ToF data also displayed in fig. 3.4. The measurement is not corrected for any delays (e.g. the delay of the start signal).

All events with $\tau \in [35\,\mu s, 50\,\mu s]$ are summed up and plotted against their event time. Since E_{source} is continuously changing within 60 eV, the band-pass filter is applied to different E_{source} resulting in a continuous differential energy loss spectrum for energy losses up to about 60 eV. Due to the limited knowledge of τ, the exact surplus energies that are filtered by the band-pass filter are not known. Therefore, at this point the energy scale of the resulting differential spectrum is not yet defined. In the following section, a method is presented how the energy scale can still be extracted from the measurements despite these limitations.

3.2.3 *Energy scale*

The exact value for the energy of the e-gun electrons (3.6) depends on three parameters: the work function of the e-gun, the wavelength of the laser and the potential at the e-gun backplate. All three parameters can be determined with external measurements. For example, the potential U_{ph} which is of $\mathcal{O}(-18.6\,kV)$ is in part measured by the precision measurement chain of the main spectrometer high-voltage setup (cf. section 2.2.2). The other part, the offset voltage U_s, is monitored with a 6.5-digit voltmeter. Overall, U_{ph} is measured with a precision of about 1 ppm. The work function Φ_{eg} can be determined via the Fowler method with an uncertainty of approximately 30 meV [Sac20].

The voltmeter is from the manufacturer Fluke and of type 8846A.

Not only the absolute energy of the electrons needs to be known but also their surplus energy (3.7). For this, two more parameters need to be determined: the potential depression U_{dep} and the main spectrometer work function. The main spectrometer work function is the dominant uncertainty and can be determined with e-gun measurements with an uncertainty of about 100 meV [Sac20].

Instead of determining and using all these input parameters, the energy scale for the energy-loss measurements is determined in-situ. Each energy-loss measurement includes a measurement of the unscattered electrons. As described above, for $E_s < 10\,eV$ the rate measured at the detector $R(E_s)$ consists of the unscattered electrons with

$$R(E_s < 10\,eV) = T(E_s)\,. \tag{3.9}$$

$T(E_s)$ directly corresponds to the angular and energy distribution of the electrons and the transmission shape of the spectrometer. In case of the integral measurements, $T(E_s)$ can be described by an error function (more details on this can be found in [Sch21; Beh16]) and for the differential measurements it resembles a normal distribution. The mean of the normal distribution corresponds to $E_s = 0\,eV$. The mean, and thus also, $E_s = 0\,eV$ corresponds to a distinct time within a run (cf. fig. 3.4). Since the U_s is continuously ramped and the ramping speed is known from measurement (cf. fig. 3.3) while everything else is kept constant, each time within a run can be transformed into E_s.

Detailed investigations of U_s show that the ramping speed is not perfectly constant over time but varies slightly within about $10\,\mu V/s$. The distribution of slopes for one measurement is shown in fig. A.12 in the appendix as an example. For each measurement the average slope value and the standard deviation ($\mathcal{O}(2\,\mu V/s)$) from all slopes is listed in table 3.5.

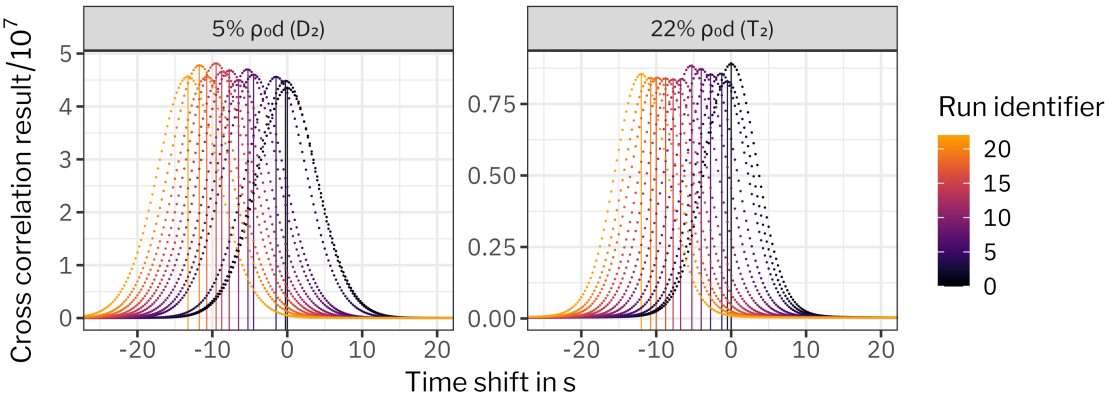

Figure 3.8 **Cross-correlation results.** The cross-correlation result (3.11) to determine the shift in time from one run to the next is shown for the up runs of two selected energy-loss measurements. The vertical lines mark the shift of each run relative to the first run.

Since the start of each run and the start of the triangle wave can not be perfectly matched, each run will have a slightly different timing. In addition, as shown in fig. 3.3, the inner electrode common voltage is changing slightly over time which influences E_s and therefore produces a shift of the rates in time. To minimize these effects and to still combine all runs, their cross correlation is calculated to determine the time shift from one run to the next.

For two similar functions f and g

$$(f * g)(\Delta t) = \int_{-\infty}^{\infty} f(t) \cdot g(t + \Delta t) \mathrm{d}t \tag{3.10}$$

can be determined. The maximum of $(f * g)(\Delta t)$ corresponds to the relative displacement of f and g. Here it is applied to discrete measurement data and calculated as

$$(f * g)[\Delta t] = \sum_{i=t_{\text{start}}}^{i=t_{\text{end}}} f[i] \cdot g[i + \Delta t] \,. \tag{3.11}$$

The times $t_{\text{start}}, t_{\text{end}}$ correspond to the start/end of each run. $(f * g)[\Delta t]$ is determined individually for up and down runs. The result is plotted in fig. 3.8 with up runs of two measurements picked as example. Each run is then shifted in time by the determined shift and afterwards all runs are stacked.

With this method, only shifts of the energy scale that occur during one run (30 minutes) are neglected in the analysis. All other parameters influencing the energy scale, such as work functions, potential depression, or the energy shift due to the ToF selection, do not need to be determined but are accounted for.

3.2.4 *Energy-loss spectra*

By combining all runs and determining the energy scale as described above, the differential energy-loss spectra are obtained. In addition

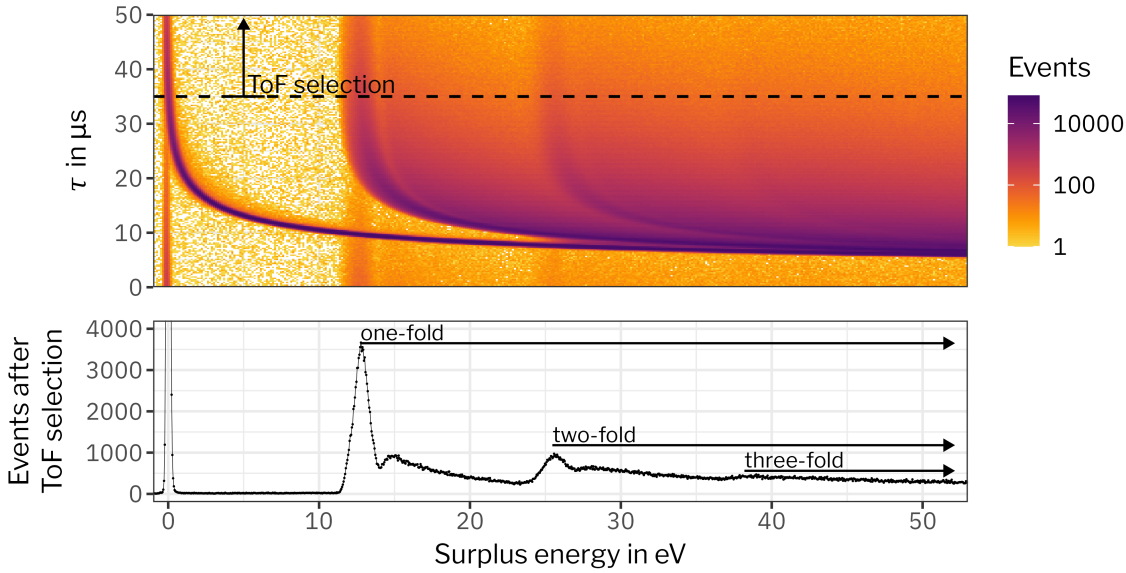

Figure 3.9 **Differential energy-loss measurement at 86 % of nominal column density.** The top panel shows for all detector events the electron flight time versus the surplus energy. Each bin has a width in energy of about 0.13 eV and a height in τ of 0.25 µs. The bottom panel shows the differential data, gained by the ToF selection with $\tau \in [35\,\mu s, 50\,\mu s]$. The arrows indicate the n-fold scattering.

The figure is adapted from [Kat21b], licensed under CC BY 4.0.

to the steps described above, the detector data is corrected for pile-up with a pile-up reconstruction scheme that was optimized for the pulsed electron beam of the e-gun [Sch21].

More information about the pile-up reconstruction can be found in this presentation by S. Enomoto during a KATRIN collaboration meeting in Nov. 2018.

The result for the differential measurement at 86 % nominal column density $\rho_0 d$ is shown in fig. 3.9. The prominent hyperbolic structures visible in the top panel correspond to the flight time of the unscattered, one-fold and two-fold scattered electrons. Already in the spectrum of a single run (fig. 3.4), the hyperbolic structure of the unscattered and one-fold scattered electrons is visible but less pronounced. The single run contains about 1/28th of the statistics compared to the combined runs shown in fig. 3.9. Not only the difference in statistics is easily visible, but also the difference in column density. The measurement shown in fig. 3.9 is at a high column density of 86 % $\rho_0 d$, the single run shown in fig. 3.4 is at a very low column density of about 5 % $\rho_0 d$. Therefore, no two-fold scattering is visible in the single run.

The bottom panel in fig. 3.9 is the differential energy-loss spectrum derived with the ToF selection. The one- and two-fold scattering peaks are clearly resolved and also a small amount of three-fold scattering is visible.

In fig. 3.10, all differential energy-loss spectra are shown in one plot. Supplemental information to each measurement is given in table 3.5. At 5 % $\rho_0 d$ an additional measurement was performed with increased energy range (covering 95 eV instead of the usual 65 eV). At this low column density, the probability for more than one-fold scattering is

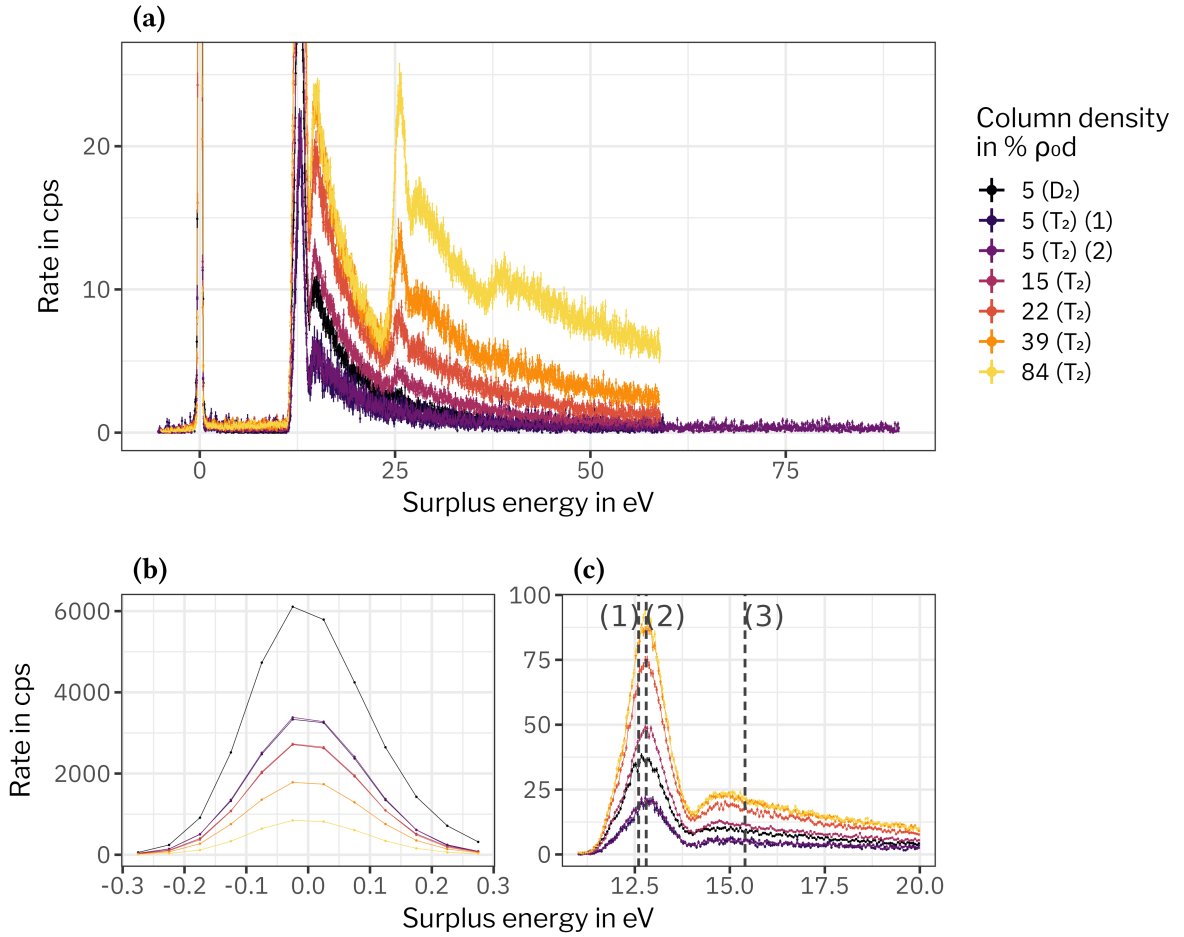

Figure 3.10 **Overview of energy-loss measurement at different column densities.** All energy-loss spectra obtained in the differential mode with tritium or deuterium inside the source are displayed. Panel (a) shows the full energy range with a focus on the lower range of rates. Panel (b) shows the energy range of the unscattered electrons and panel (c) shows the energy range of the one-fold scattering. In panel (c), the first dashed line at 12.6 eV corresponds to the position of the Gaussian that describes the electronic excitations in the Aseev et al. [Ase+00] model and the second dashed line at 12.8 eV corresponds to the position determined by Abdurashitov et al. [Abd+17]. The third dashed line marks the ionization threshold at 15.4 eV.

very low. Therefore, the spectrum above 15.4 eV is dominated by the energy loss due to ionization.

In order to reduce systematic effects due to pile-up, the laser intensity was reduced for the tritium measurements. The higher intensity during the deuterium measurements is visible in fig. 3.10b.

As a crude estimation of the scattering probability, the integrated counts of unscattered electrons (integral of fig. 3.10b) can be compared to the integrated counts of one-fold scattered electrons (integral of fig. 3.10c). This leads to a scattering probability of 6 % for the deuterium and tritium measurements at 5 % $\rho_0 d$. For the tritium measurement at 84 % $\rho_0 d$, the scattering probability for one-fold scattering can be

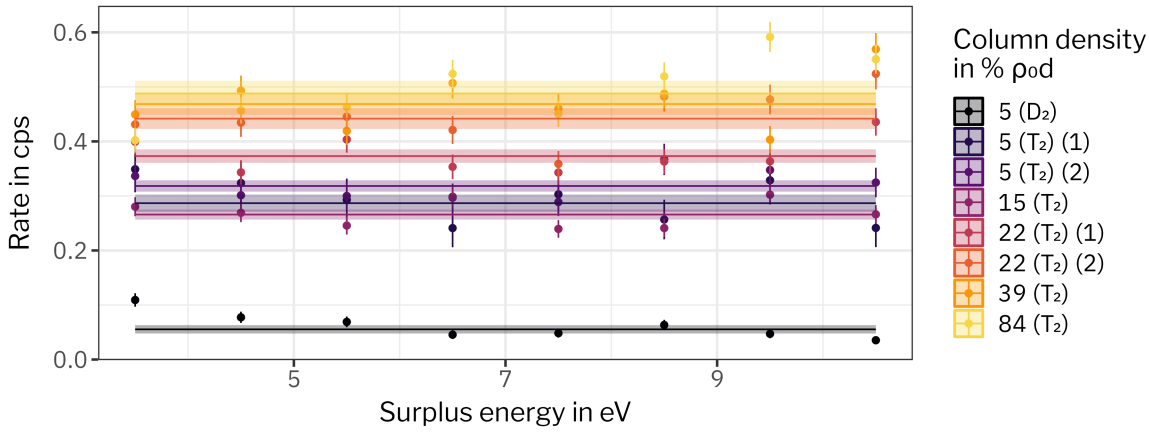

Figure 3.11 **Background rates in energy-loss measurements.** The plot shows the rates after the ToF selection in the energy region between unscattered and scattered electrons. The colors indicate the column density (CD) during each measurement. The average rate for each dataset is plotted as a line with the corresponding 1-σ uncertainty band.

estimated with this simplification as 52 %, and for two-fold scattering as 25 %.

In order to make a very first comparison to previous energy-loss measurements [Ase+00; Abd+17], the position of the Gaussian describing the electronic excitation is marked. One can see that the position of the main peak agrees with the peak position as measured by Abdurashitov et al. [Abd+17]. However, in addition to the single Gaussian (cf. section 3.1), another Gaussian structure is visible at 15 eV before the ionization continuum starts. It is important to note that this comparison is possible since the differential spectrum gives almost direct access to the energy-loss spectrum. As described above, the measured rate at the detector (3.5) is the multi-fold scattering $F(\Delta E, \mu)$ (3.4) folded with $T(E_s)$, which corresponds in the differential case effectively to a broadened $F(\Delta E, \mu)$.

3.2.5 *Background*

For surplus energies below the threshold for electronic excitations (at about 11 eV), only unscattered electrons are expected in the differential spectrum. As visible in fig. 3.10, the main peak of the unscattered electrons expands to about $E_s = 0.3\,\text{eV}$. In between the region of unscattered and scattered electrons, a non-zero rate is visible in the differential spectrum. This unexpected rate is now called background.

In fig. 3.11 the rates for $E_s \in (3\,\text{eV}, 11\,\text{eV})$ are plotted. Overall, the rate is constant over the energy region. With deuterium in the source, the rate in this region is very small (0.055(7) cps). With tritium in the source, the rate depends on the source density: higher source density corresponds to an increased rate.

For a more detailed investigation, the average rates are plotted against the source density and colored by the time of the measurement

During the first measurement at about 22 % $\rho_0 d$, the e-gun beam was not perfectly steered through the rear section. Therefore, for higher surplus energies a decrease in rate was observed, making the measurements unusable for the final energy-loss analysis. For the background investigations the rate decrease is not relevant since it does not start for $E_s < 11\,\text{eV}$. To avoid confusion, this measurement is omitted from table 3.5.

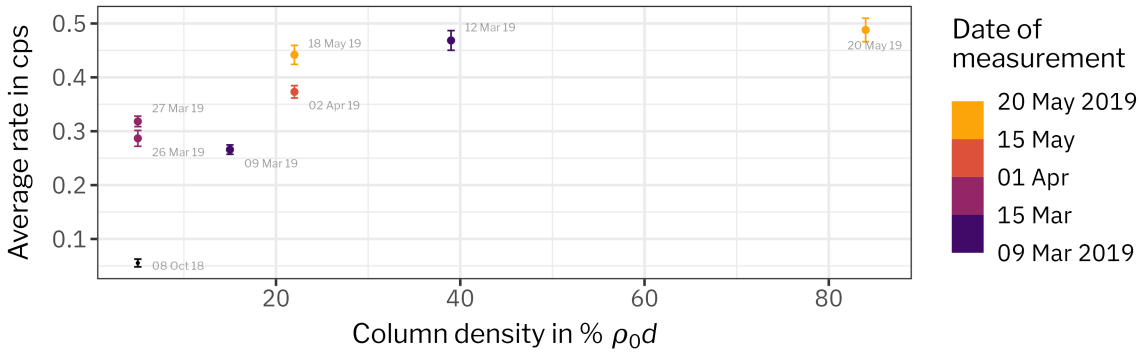

Figure 3.12 **Average background rates in energy-loss measurements.** The average rates (also shown in fig. 3.11) are plotted against the column density (CD). The black point in the lower left is from the deuterium measurement; all other measurements are with tritium.

in fig. 3.12. Not only a dependency on the source density is visible but also on the time of measurement. The later measurements at 5 % $\rho_0 d$ have an overall higher average rate than the measurements at 15 % $\rho_0 d$. Also the two successive measurements at 5 % $\rho_0 d$ show an increase of the background within two days. The later two measurements at 22 % $\rho_0 d$ show the same: the earlier measurement has a smaller rate than the later one.

To further investigate the origin of the observed background, measurements were performed with the e-gun on high voltage, but without the laser. During these tests, the events measured by the detector are correlated to E_s and display something similar to a standard transmission function shape. Without the laser, no electrons should be created via the photo effect. For the initial tests the column density was at about 22 % $\rho_0 d$, and an overall background rate of $\mathcal{O}(1\,\text{cps})$ was visible. The result is displayed in fig. A.13 in the appendix.

Almost half a year later, more background measurements with longer measurement times (thirty half-hour runs instead of only six as before) were performed. At that time the background rate was increased to $\mathcal{O}(10\,\text{cps})$ at about 22 % ρ_0. The measurement result is displayed in fig. 3.13. Not only a transmission function shape from the unscattered background electrons is visible but also a second small step corresponding to one-time scattered background electrons.

For the analysis of the background measurement, the energy scale is reconstructed differently as for the general energy-loss measurements (cf. section 3.2.3). The determination of the $E_s = 0$ position is more difficult, due to the wider distribution and the lower statistics compared to an energy-loss scan. To understand the background process it is of interest to determine the energies of the background electrons. Their surplus energy E_s' is defined the same as the surplus energy (3.7) for the electrons created by the photo-effect but without the term for the photon energy:

$$E_s' = q \cdot (U_s - U_{ie} + U_{dep}) - \Phi_{eg} + \Phi_{MS}\,. \tag{3.12}$$

E'_s is used as energy scale in figs. 3.13 and A.13. $\Phi_{MS} = 4.31\,\text{eV}$ is used for the main spectrometer work function [table 5.2 Sac20]. The value was estimated from an energy-loss measurement three days before the background measurement. As value for the e-gun work function $\Phi_{eg} = 4.47\,\text{eV}$ [Sac20] is used.

Some words of caution to the determination of E'_s. Both work functions are determined with e-gun measurements and the work function of the main spectrometer is extracted from energy-loss measurements. In addition, but with lesser overall impact, for the later dataset no voltmeter measurement during the measurements is available for U_s. The value for U_{ie} is estimated from a voltmeter measurement close to the measurement itself. Since a better power supply was used with smaller variations over time during the later dataset, the voltmeter measurement during the measurement itself is less important. The new supply variates within 1 mV over one hour, which is about a factor ten better than the stability of the old power supply during normal energy-loss measurements (cf. fig. 3.3). Therefore, absolute energies of the background electrons can have a systematic shift of unknown size, possibly within about ±0.2 eV.

With the energy scale defined in this way, the first part of the transmission function (the part of the unscattered electrons) can be described by an error function with amplitude A and shifted by a constant b:

A more elaborate fit was performed by Schimpf [Sch21], where not only the unscattered electrons are fitted but the whole dataset with the full energy-loss parametrization (cf. section 3.3).

$$f(E'_s) = \frac{A}{2} \cdot \left(1 + \operatorname{erf}\left(\frac{E'_s - \mu}{\sigma}\right)\right) + b,$$
$$\operatorname{erf}(x) = \frac{1}{\sqrt{2\pi}\sigma} \int_0^x e^{-\tau^2}\, d\tau. \tag{3.13}$$

Fitting $f(E'_s)$ to the data leads to a width $\sigma = 1.1(1)\,\text{eV}$ and position $\mu = -2.08(9)\,\text{eV}$. The result is plotted in fig. 3.13. Judging from the reduced χ^2 value of 2.9(2), the fit is not a perfect description of the data. Still, if the fit is used as an approximation of the background electron distribution, the electrons created at the e-gun photocathode have a starting energy of about 2 eV. For the earlier dataset with reduced statistics and overall lower background rate, the starting energy is compatible but the width is only half as large (cf. fig. A.13 in the appendix). Part of the transmission function width can be explained by the angular distribution of the electrons at the e-gun. The measurements were performed in a 1.0 G setting. The measurement of an electron source with isotropic angles in this setting would have a transmission width due to the angles of 0.45 eV peak-to-peak. Therefore, a part of the width can be explained by an angular distribution and the remaining part is caused by the energy distribution of the electrons.

In conclusion, during measurements with the e-gun on high voltage but without light source, background electrons are produced. Their dependency on U_s and the transmission function shape that is measured at the detector indicate that their energies are about 2.08(9) eV higher than the energies of the electrons produced via the photo-effect. Their energy and angular distribution produces a transmission function that is an order of magnitude larger in width than the photo-effect

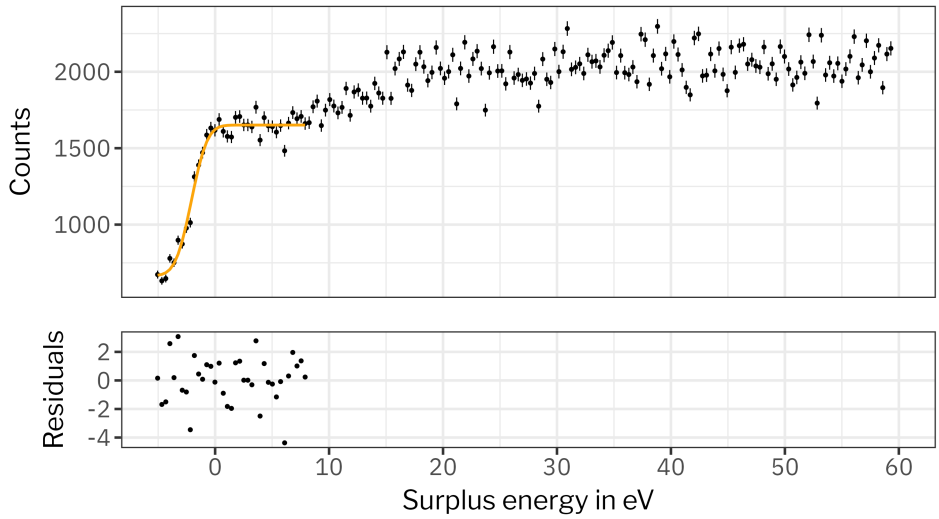

Figure 3.13 **Measurement of the e-gun background.** The accumulated event counts of 30 runs during e-gun background measurements. The setup was similar to the standard energy-loss measurements but with the laser turned off. During the measurements, the source was filled with tritium at about 22 % $\rho_0 d$. The surplus energy E_s' (3.12) is determined with a procedure different from normal energy-loss measurements. Due to imperfect synchronization, not all runs contain the same surplus energies, therefore events with surplus energies below −5.2 eV and above 60 eV have been removed. The orange line is an error function fit (3.13) with its residuals shown in the bottom panel. The fit is only for $E_s' < 8$ eV so that only unscattered electrons are considered.

electrons (about 0.1 eV). To explain these background electrons, a secondary process needs to exist that creates low-energy electrons at the photocathode. The dependency of the background rate on the column density, the accumulation over time and the very low background rates during the deuterium measurement give a strong indication that this secondary process is caused by tritium. More precisely, electrons from the tritium beta decay that impinge on the photocathode and produce secondary electrons.

For the integral measurements, this background is not as important as for the differential measurements. The rate of background electrons $\mathcal{O}(1\,\text{cps})$ is small compared to the signal electrons $\mathcal{O}(6\,\text{kcps})$ [Sch21] in the integral mode. The additional electrons only produce a smearing of the transmission function due to their different angular and energy distribution.

For the differential measurements the background is more critical. Any electron not produced in synchronization with the laser pulse has no defined flight time τ (cf. section 3.2.2). Without the knowledge of the flight time, the ToF selection just arbitrarily picks electrons with different surplus energies, and the differential spectrum is lost. As visible in fig. 3.9 (top panel), the events are homogeneously distributed in τ between the hyperbolic structure of the unscattered and the one-fold scattered electrons. With the ToF selection, only 30 % of the back-

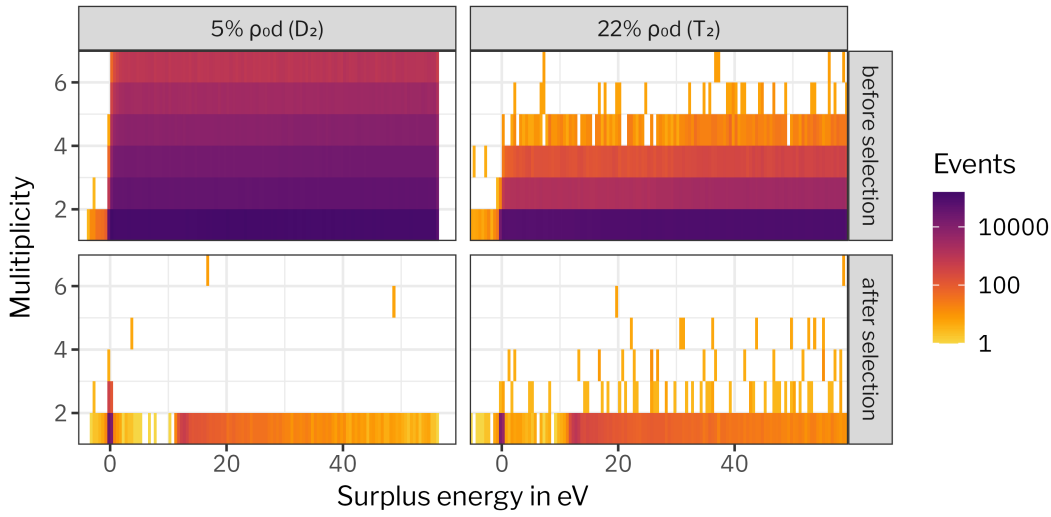

Figure 3.14 **Event multiplicity during energy-loss measurements.** The left column shows one run from the deuterium measurements. The right column shows one run from the tritium measurements. In the first row, the event multiplicity for all events is plotted against the surplus energy. In the second row, only events remaining after the ToF selection ($\tau \in [35\,\mu s, 50\,\mu s]$) are shown.

ground is selected and the result is visible in fig. 3.11. The very low background rate visible in fig. 3.11 for the deuterium measurements is also reflected in the top panel of fig. 3.4, where almost no events are visible in the region between the unscattered and one-fold scattered electrons.

The background spectrum is an integral spectrum on top of the differential spectrum. For regions with high rates (e.g. unscattered electron peak) it is less critical. But for regions with low rates, such as the tail of the energy-loss spectrum (above the ionization threshold) it becomes critical and needs to be considered in the energy-loss analysis.

3.2.6 *Event multiplicity*

The multiplicity of each event registered at the detector can be estimated from the event pile-up reconstruction in the detector analysis. The event multiplicity corresponds to the number of electrons that are registered as one single event at the detector.

For two single runs, one from the deuterium measurements and one from the tritium measurements, the multiplicity is plotted against the surplus energy in fig. 3.14. During the deuterium measurement, a higher laser intensity was used (cf. table 3.5), leading to higher multiplicities compared to the tritium measurements (first row in fig. 3.14). After the ToF selection (second row in fig. 3.14), mostly events with single multiplicity remain.

Electrons created by one laser pulse at the photocathode have the same starting time but not necessarily the same energy. The energies of electrons from one pulse are distributed along the energy distribu-

tion from the e-gun of about 0.1 eV width. When the electrons arrive at the spectrometer, their energies can have changed even more due to different energy loss inside the source. Due to their different energies and angles, and therefore also different surplus energies, the electrons need different times to traverse the spectrometer. The ToF selection only selects electrons with small surplus energies. For small surplus energies, the electrons' flight times through the spectrometer diverge (cf. fig. 3.6). Pile-up is caused by electrons arriving in a time interval shorter than the detector's shaping length (1.6 µs). Therefore, it is very unlikely for electrons within the ToF selection to be connected to pile-up events at the detector.

The minimum time interval during which the detector can distinguish between two events is only in a simplified model determined by the shaping length, in reality it is more complex. However, here it is enough to know that it is $\mathcal{O}(2\,\mu s)$. More details can be found in this presentation by S. Enomoto at a KATRIN analysis workshop (Mar. 2021).

As visible in fig. 3.14, the multiplicity in the deuterium data set after the ToF selection consists mainly of a multiplicity of 1. Except for the region of the unscattered electrons, where some events with higher multiplicities are visible. Due to the low column density in the deuterium measurements and the high laser intensity, many unscattered electrons arrive at the detector. For the tritium measurements, higher multiplicity events remain after the ToF selection not only at the position of unscattered electrons but also for higher surplus energies. This seemingly homogeneous distribution of events with multiplicity > 1 is also visible in the other tritium energy loss measurements but not in the deuterium measurement.

Background events are uncorrelated to the laser pulse and produce an integral spectrum above the differential one (cf. section 3.2.5). Since the background rate during the tritium measurements is almost about a factor eight higher than during the deuterium measurements (cf. fig. 3.12), the obvious explanation for the high multiplicity events persistent after the ToF selection is the background. The multiplicity of events during a pure background measurement is plotted in fig. A.14 in the appendix. In addition to events with one-fold multiplicity, also events with higher multiplicities are visible.

To reduce the background rate as far as possible in the differential energy-loss analysis, a multiplicity cut is introduced. After the ToF selection is applied to the data, only events with one-fold multiplicity are selected. In this way, the background is reduced but not fully eliminated. The remaining background is not a pure integral spectrum on top of the differential one anymore but slightly distorted.

A detailed background simulation can be found in the work by Schimpf [Sch21] and the master's thesis of C. Schwachtgen (Dec. 2020), and a shorter overview of the results in the work [Kat21b].

3.3 Scattering of electrons on tritium

The energy-loss function for the scattering of electrons on tritium can be extracted from the measurements that were introduced in the previous section. By comparing the differential spectrum obtained from the measurements at the KATRIN beamline (cf. bottom panel of fig. 3.9) with the measurements obtained at the Troitsk and Mainz setup (fig. 3.2), it is obvious that the previous parametrization (3.1) is not sufficient anymore. For example, due to the higher energy resolution with the KATRIN setup the electronic excitations (around 12.8 eV) are not only visible as one peak but as two separate peaks.

As presented in section 3.1, the individual molecular states can be

resolved with the very-high resolution (40 meV and later 10 meV) measurements of Geiger [Gei64]. The observed excitations can be divided into three groups, the vibrational excitations of the $B(2p\sigma\,^1\Sigma_u^+)$, the $C(2p\pi\,^1\Pi_u)$, and the $D(3p\pi\,^1\Pi_u)$ state. Based on this, the new parametrization includes three Gaussians to describe the electronic excitations as measured at KATRIN. To describe the ionization continuum, the relativistic binary encounter dipole (BED) model by Kim et al. [KSP00] is used and denoted as f_{BED} here. The full parametrization to describe the energy-loss function is [Kat21b]

Different models were tested and the model by Kim et al. [KR94] was identified to describe the deuterium data the best [Sac20]. For the final tritium fit the further developed relativistic model by Kim et al. [KSP00] was used.

$$f(\Delta E) = \begin{cases} \sum_{i=1}^{3} a_i \exp\left(-\frac{(\Delta E - m_i)^2}{2\sigma_i^2}\right), & \Delta E \leq E_{\mathrm{ion}} \\ \frac{f(E_{\mathrm{ion}})}{f_{\mathrm{BED}}(E_{\mathrm{ion}})} \cdot f_{\mathrm{BED}}(\Delta E), & \Delta E > E_{\mathrm{ion}}\,. \end{cases} \tag{3.14}$$

The ionization threshold E_{ion} is fixed to $E_{\mathrm{ion}}(\mathrm{T}_2) = 15.486\,\mathrm{eV}$ [KR94; WJH99]. a_i, m_i and σ_i with $i \in [1, 2, 3]$ are the amplitude, position and width of the three Gaussians, respectively. The amplitude of f_{BED} is fixed to $f(E_{\mathrm{ion}})$ to ensure a smooth connection of both parts of the stepwise defined function. As described in section 3.2, the n-fold scattering (3.4) and the response of the system (3.5) needs to be considered.

In the following section, the results for $f(\Delta E)$ from a fit to the differential measurements are presented. Afterwards, the results are compared to the result from a combined fit on both the integral and differential measurements, as published in the work [Kat21b].

3.3.1 *Fit to the differential data*

The data from differential measurements are prepared along the analyzing procedure described in section 3.2 with slight adjustments. Instead of the cross-correlation method, the peak of the unscattered electrons is fitted with a Gaussian and its position is used to define the $E_{\mathrm{s}} = 0\,\mathrm{eV}$ position for each run. Additionally, the rate measured at the detector is corrected by the light intensity of the laser as measured by a photo-diode [Sch21]. The measurement data is binned in 50 meV bins.

The full analysis chain for the differential data is available on the KATRIN-internal git repository.

3.3.1.1 *Inelastic scattering cross section*

During the measurements, the kinetic energy of the electrons E_{source} is changed (cf. section 3.2.1). Since the inelastic scattering cross section has an energy dependency, a change in energy also changes the scattering probability for the electron. A description for the electron's inelastic total cross section in the Born approximation was derived by F. Glück and is based on the works [Liu73; Liu87; Ino71]. It is described as

Presented by F. Glück during a KATRIN analysis call in July 2019 available here.

$$\sigma_{\mathrm{inel}}(E) = \frac{4\pi a_0^2}{T/R}\left[M_{\mathrm{tot}}^2 \cdot \ln\left(4c_{\mathrm{tot}} \cdot \frac{T}{R}\right) + \delta_E\right] \tag{3.15}$$

with the non-relativistic kinetic energy T

$$T = \frac{1}{2} \cdot m_e \cdot \beta^2 = \frac{1}{2} \cdot m_e \cdot \left(1 - \frac{m_e^2}{(m_e + E_{\mathrm{source}})^2}\right). \tag{3.16}$$

The sum of dipole transition probabilities from the initial ground state to all excited and ionized states is determined as $M^2_{tot}(T_2) = 1.5356$. $R = 13.606\,\text{eV}$ is the Rydberg energy and a_0 the Bohr radius with $a_0^2 = 28.003 \times 10^{-18}\,\text{cm}^2$. δ_E is a relativistic correction term, and for tritium and electrons with energies around the endpoint $\delta_E = -0.01$.

For small changes in T, the total cross section changes linearly. The scattering probability increases with decreasing T. $\sigma_{\text{inel}}(E)$ changes by about 0.3 % over the full energy range ($E_{\text{source}} \in [18\,568\,\text{eV}, 18\,633\,\text{eV}]$) of the energy-loss measurements.

To account for the changing scattering probability due to the changing E_{source} in the measurements, the mean scattering rate μ (3.2) is scaled by a correction factor $\sigma_{\text{inel}}(E_{\text{source}})/\sigma_{\text{inel}}(E_{\text{fix}})$. E_{fix} is defined as the energy of the electrons at $E_s = 0\,\text{eV}$ during the measurement and is fixed for the fits to 18 572.68 eV.

μ is a free parameter in the energy-loss fit function (3.17). Therefore, the value of μ is scaled instead of dircetly using $\sigma_{\text{inel}}(E_{\text{source}})$.

If the electron loses energy due to scattering in the source, the scattering probability for the second scattering is slightly increased. For example, an energy loss of about 12.8 eV corresponds to a change of $\sigma_{\text{inel}}(E)$ by about 0.06 %. This violates the assumption that the scattering can be described by a Poisson distribution (3.3). Since it is only a small effect, especially for the dominant one-fold scattering, it is neglected in the analysis. If such an effect is to be considered in the future, first $\sigma_{\text{inel}}(E)$ should be verified experimentally at KATRIN. By performing energy-loss measurements at different e-gun electron energies E_{fix} but stable column density, the change in μ can be compared to the expectation from σ_{inel}. Or, even simpler, it can be verified by performing column density measurements [see Blo22] at different e-gun electron energies.

3.3.1.2 *Transmission function*

During each energy-loss measurement, the transmission function $T(E_s)$ is determined in-situ with the measurement of the unscattered electrons (cf. section 3.2.3). The part of the measured energy-loss spectrum with $E_s \in [-1\,\text{eV}, 1\,\text{eV}]$ (cf. fig. 3.10) is convolved with $F(\Delta E, \mu)$ and gives the model $R(E_s, \mu)$ for the rate measured at the detector (3.5).

3.3.1.3 *Background*

As introduced in section 3.2.5, for the differential measurements the background electrons need to be considered in the analysis. Initially, an integral spectrum was added to the differential one with a free amplitude in the fit. The integral spectrum was the integrated version of the differential measurement result. Since the background electrons have a different energy distribution compared to the electrons created by the photo-effect, this method was a small improvement but not a solution.

Further information about the background model is also presented in the master's thesis of C. Schwachtgen (Dec. 2020).

To reduce the background as far as possible, a multiplicity selection is applied on the data (cf. section 3.2.6). In addition, a dedicated background model of the remaining background electrons after the multiplicity cut was developed [Sch21]. The background shape $B(E_s, \mu)$ is added to the fit with its amplitude as a free fit parameter.

3.3.1.4 *Least squares minimization*

The measured rate R is described with a fit model consisting of the nine parameters of the energy-loss function (3.14). Additionally, the following nuisance parameters are added to the model: background amplitudes b_i, normalization factors c_i and the mean scattering probabilities μ_i for each dataset $i = 1, 2, ..., N$.

A least squares minimization was performed with the following χ^2 function to fit the model to the data.

$$\chi^2(\mathscr{P}) = \sum_i^N \sum_j \left(\frac{c_i R_i(E_\mathrm{s}, \mu) + b_i \cdot B_i(E_\mathrm{s}, \mu) - y_{i,j}}{\sigma(y_{i,j})} \right)^2 + \left(\frac{\int_0^{E_\mathrm{max}} f(\Delta E)\mathrm{d}\Delta E - 1}{\delta} \right)^2 . \tag{3.17}$$

$\mathscr{P}$ is the vector of free fit parameters. The measured rates are $y_{i,j}$ and their uncertainties $\sigma(y_{i,j})$, with j denoting the data points of each dataset [Kat21b]. The second summand is a penalty term that forces the integral of $f(\Delta E)$ from $E_\mathrm{s} = 0\,\mathrm{eV}$ to

$$E_\mathrm{max} = \frac{(E_\mathrm{fix} - E_\mathrm{ion})}{2} \approx 9.28\,\mathrm{keV} \tag{3.18}$$

to one.

The fit is performed on four of the tritium datasets (cf. table 3.5): at 15 %, 22 %, 39 %, and 84 % $\rho_0 d$. The two datasets at 5 % $\rho_0 d$ are omitted from the fit. The dataset with the normal scan range has lower statistics compared to the other data sets (of about a fourth of the measurement time) in addition to the lower scattering probability due to the small column density. Also combined with the dataset with the extended scan range, the statistics for scattered electrons are only one third of the statistics available from the 15 % $\rho_0 d$ dataset. With lower statistics, also the signal to noise ratio is decreased and no dedicated background measurement exists at 5 % $\rho_0 d$.

During the measurement planning an increased measurement time was allocated to account for the lower scattering probability, but due to hardware problems parts of the measurement time were not usable.

3.3.1.5 *Result*

The result of the least squares minimization in shown in fig. 3.15. The reduced χ^2 value for the fit is 1.08(2). It is not compatible 1 within the uncertainties, but very close. At first glance, the residuals over the full fit range show no significant structures, except for small sinusoidal structures around $E_\mathrm{s} = 14\,\mathrm{eV}$ (fig. 3.15a). A linear fit to the residuals for $E_\mathrm{s} > 17\,\mathrm{eV}$ showed no significant drift for any of the datasets.

The minimization is conducted via `iminuit` in `Python` and the full fit routine is available on the KATRIN-internal git repository.

In the residuals plotted in fig. 3.15b, two periods of a sinusoidal beginning around 13 eV and ending around 15 eV with an amplitude of roughly 2.5 can be identified. Since the residuals are normalized by the uncertainties, the amplitude corresponds to a 2.5 σ deviation. Less pronounced is a small dent in the residuals at 11.3 eV (within 2.5 σ), followed by an even smaller increase. These structures occur in all datasets.

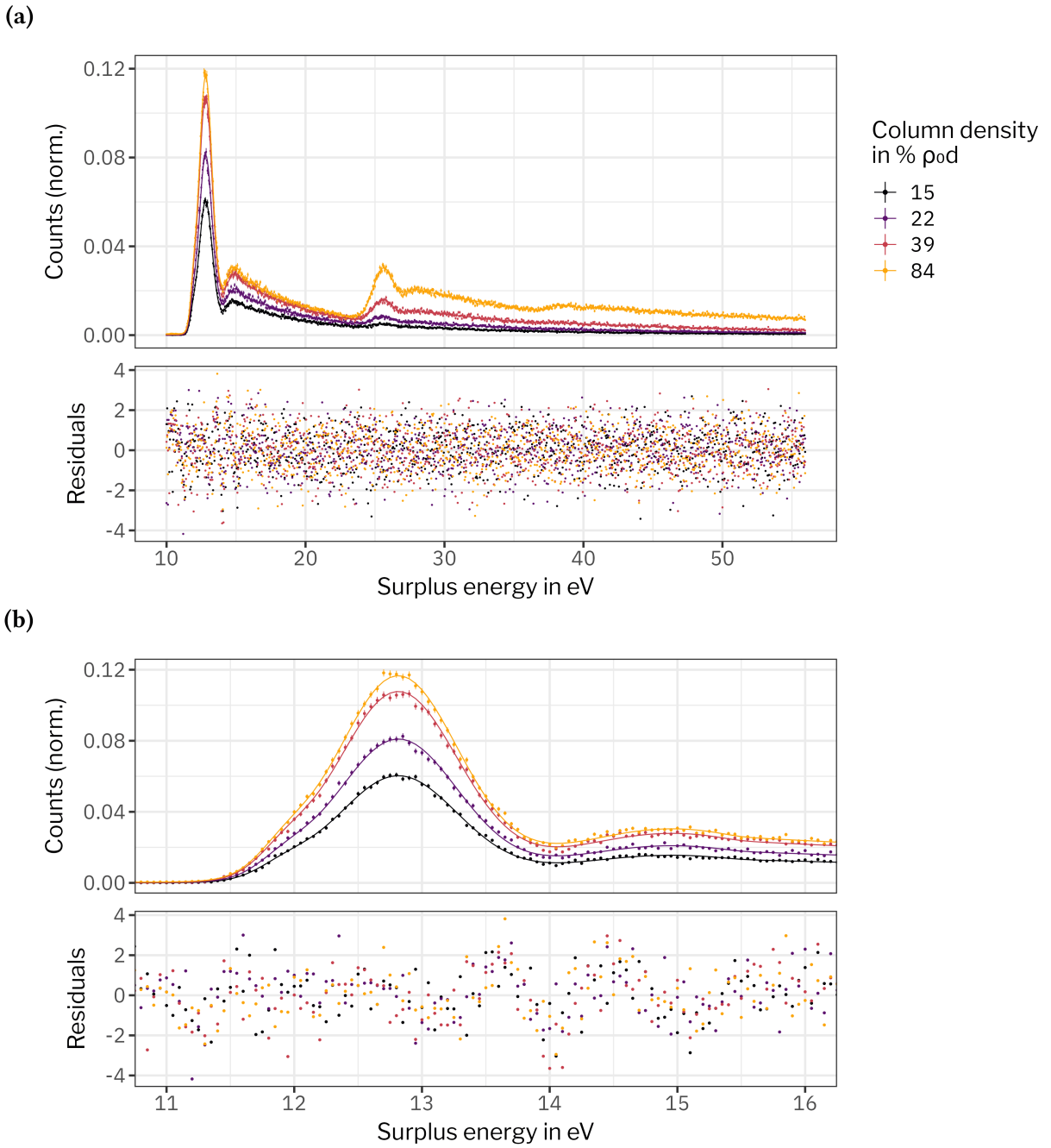

Figure 3.15 **Combined fit result for the differential data.** For all four datasets that are used in the combined fit, the measurement points and the resulting fit model (colored lines) are shown. The measured counts are normalized by the area below all counts within −1 eV to 56 eV. The residuals are normalized by the uncertainties of the observation. Plot (a) shows the full fit range and plot (b) is a magnified view of the region of the one-fold scattering. The best-fit parameters are listed in table A.15.

It is important to note that the parametrization is a semi-empirical parametrization of the energy-loss function. The three Gaussians of the fit describe a whole set of discrete excitation states which are smeared to Gaussian-like structures due to the limited energy resolution in the measurement. The small structures within 2.5σ show the limitation of the approximation with a Gaussian.

In the top panel of fig. A.16 in the appendix, the correlation matrix of the fit result is displayed. The absolute correlation values of the nine energy-loss parameters to the nuisance parameters for the datasets are small and ≤ 0.3. Within the nuisance parameters, one can see a correlation between the background amplitudes, the normalization factors and the mean scattering probabilities within each dataset. All three effect the scaling of the energy-loss function and are therefore naturally correlated. The highest correlation values are for the parameters of the three overlapping Gaussians m, a, σ. Here nothing unexpected is visible. For example, the width of the second Gaussian has a large correlation to all other parameters which is directly connected to the second Gaussian being positioned in between the other two.

The resulting $f(\Delta E)$ from the fit is displayed in fig. 3.16. It can be used to calculate the mean energy loss $\Delta E(T_2)$. The mean energy loss for losses up to $E_{\text{max}} = 9.28\,\text{keV}$ is

$$\Delta E(T_2) = 30.70(2)\,\text{eV}\,. \tag{3.19}$$

The result is compatible with the the result reported in the work [Ase+00]:

$$\Delta E(T_2) = 29.9(10)\,\text{eV}\,. \tag{3.20}$$

3.3.2 *Combined fit of integral and differential data*

Instead of using only the differential datasets, now also the integral datasets are included. Three integral datasets at about 14 %, 41 %, and 86 % $\rho_0 d$ are added to the four differential datasets. The integral datasets are described in [Sch21]. The fit presented in this section is published in [Kat21b]. For better readability the following shorthands are defined. The fit on only the differential datasets is called *tof-only fit*, the one on both the integral and differential datasets is called *combined fit*.

The least squares minimization is the same as described above, only with an additional summand for the integral dataset. With the integral dataset, the χ^2 function (3.17) is changed to

$$\begin{aligned}\chi^2(\mathscr{P}) = &\sum_i^{N_{\text{tof}}} \sum_j \left(\frac{c_{\text{tof},i} R_{\text{tof},i}(E_\text{s}, \mu) + b_{\text{tof},i} \cdot B_{\text{tof},i}(E_\text{s}, \mu) - y_{\text{tof},i,j}}{\sigma(y_{\text{tof},i,j})} \right)^2 \\ &+ \sum_i^{N_{\text{int}}} \sum_j \left(\frac{c_{\text{int},i} R_{\text{int},i}(E_\text{s}, \mu) + b_{\text{int},i} \cdot B_{\text{int},i}(E_\text{s}, \mu) - y_{\text{int},i,j}}{\sigma(y_{\text{int},i,j})} \right)^2 \\ &+ \frac{\left(\int_0^{E_{\text{max}}} f(\Delta E) \mathrm{d}\Delta E - 1 \right)^2}{\delta^2}\,.\end{aligned} \tag{3.21}$$

To distinguish between the differential and integral datasets, the indices are expanded by "tof" to mark the differential datasets and "int" for the integral datasets. The integral datasets are fitted between −3 eV up to 56 eV, and the differential datasets between 10 eV up to 56 eV.

The fit result is shown in fig. A.17 in the appendix. The reduced χ^2 value is 1.13(2) and slightly increased (about 0.05) compared to the χ^2 value of the tof-only fit.

The residuals for the differential datasets are very similar to the tof-only fit which is discussed in detail in section 3.3.1.5. No obvious structures are visible in the residuals of the integral datasets. The slight oscillations visible in the residuals of the differential data do not appear in the integral data. Instead, a small dent is visible around 20 eV for all three datasets. Also a small overall increase of the residuals towards higher surplus energies is visible. Here it is important to note that for higher surplus energies also the overall count rate at the detector increases which makes the pile-up correction more important.

The correlations between the fit parameters are shown in fig. A.16 (bottom panel) in the appendix. The absolute correlation values between the nuisance parameters and the nine energy-loss function parameters are < 0.2 and overall about 0.1 smaller than in the tof-only fit. In the tof-only fit, the absolute correlation values for the background amplitudes $b_{\mathrm{tof},i}$ and the normalization factors $c_{\mathrm{tof},i}$ to the energy-loss function parameters are similar but have opposite signs. The integral background amplitudes have no correlation to the energy-loss parameters.

It is interesting that the correlation between the mean scattering probabilities μ, the background amplitudes b and the normalization factors c is different for the integral datasets compared to the differential datasets. $b_{\mathrm{int},i}$ and $\mu_{\mathrm{int},i}$ have correlation values around zero whereas $b_{\mathrm{tof},i}$ and $\mu_{\mathrm{tof},i}$ have a correlation of −0.6. This difference can be caused by two effects, the background and different fit ranges.

For the integral data the signal to noise ratio is much higher and almost constant for surplus energies above 10 eV. For the differential data the signal to noise ratio is much smaller and it changes with the surplus energy (cf. section 3.2.5). Since the fit range for the differential data starts at $E_{\mathrm{s}} > 10\,\mathrm{eV}$, the mean scattering probability is only estimated by the ratio of the one-fold and two-fold scattering. Both regions are differently affected by the background causing the correlation between $\mu_{\mathrm{tof},i}$ and $b_{\mathrm{tof},i}$.

In an ideal fit result, the nuisance parameters of one dataset should not be correlated to another dataset. However, this is the case for c and μ in the integral dataset and especially for the datasets two and three.

For a more direct comparison, the resulting $f(\Delta E)$ from both fits is plotted in fig. 3.16. Not discussed before, but added to the plot is an additional fit that is performed on the integral datasets only, called *integral-only fit*. The integral-only fit has the largest uncertainty in the region of the electronic excitations. The uncertainties of the tof-only fit and the combined fit are very similar. They are slightly increased for the tof-only fit which can be caused by less nuisance parameters compared to the combined fit.

Comparing the relative difference between $f(\Delta E)$ from the tof-only

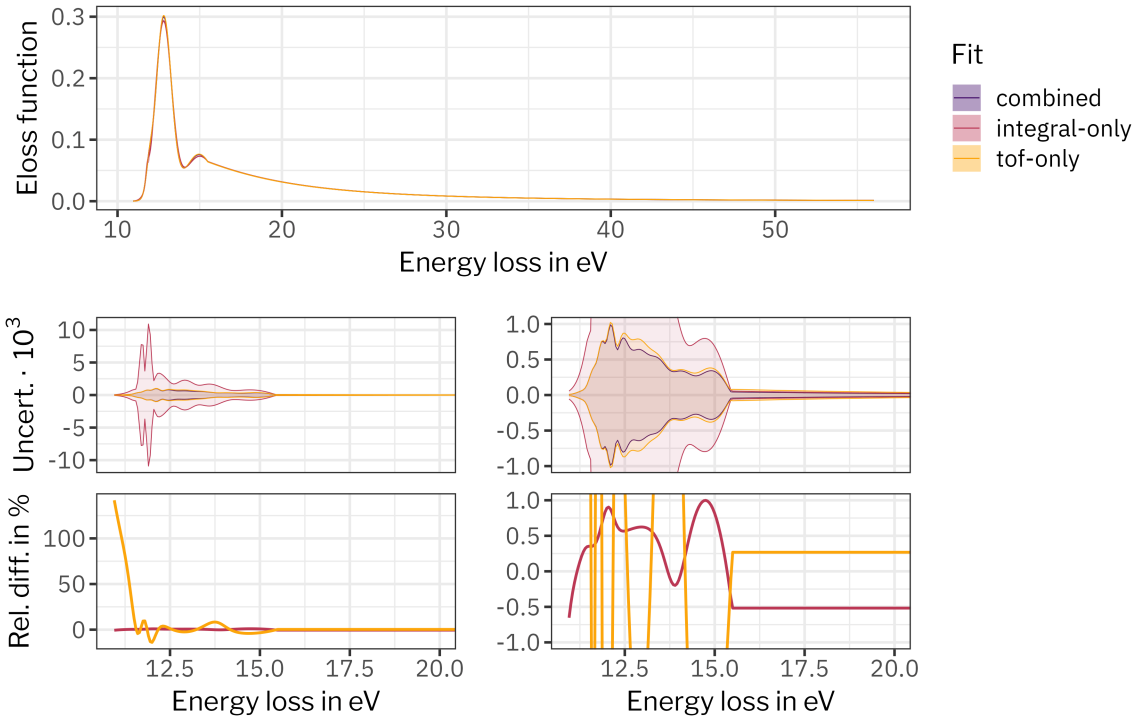

Figure 3.16 **Energy-loss function fit results.** The figure shows three different energy-loss functions. The orange and red functions result from a fit on only the differential and only the integral dataset, respectively. The purple function results from a fit on the combined datasets. The 1-σ uncertainty band is very small and therefore additionally shown in the second row and multiplied by 1×10^3. To further highlight the differences between the integral-only and the combined fit as well as between the tof-only and the combined fit, their relative differences are shown in the third row.

fit and the combined fit, differences within 1.5 % are visible. The ionization tail is shifted to 0.5 % lower values in the tof-only fit. In the region of electronic excitations the differences oscillate within 1 %. These differences reflect the slightly different Gaussians in both fit results.

It is possible to evaluate the individual importance of the differential and the integral datasets on the combined fit by comparing the relative differences between the tof-only or integral-only fit to the combined fit (third row in fig. 3.16). The ionization tail is mainly determined by the integral datasets (the difference to the combined dataset is almost zero in this region). In the tail region the integral data has high count rates and low uncertainties whereas the differential data has lower count rates and higher uncertainties. In contrast, the differential dataset is dominating the combined fit in the region of the electronic excitations.

The resulting $f(\Delta E)$ from the combined fit can be used for the determination of the mean energy loss for losses up to $E_{\mathrm{max}} = 9.28\,\mathrm{keV}$:

$$\Delta E(T_2) = 30.79(1)\,\mathrm{eV}\,. \tag{3.22}$$

Table 3.17 **Mean energy loss for different fit results.** The mean energy loss is calculated for a comparison of the fit result based on different data sets. The mean energy loss of the region below and the region above the position of the ionization energy is shown in the first and second row, respectively. The full mean energy loss $\Delta E(T_2)$ for losses up to $E_{\mathrm{max}} = 9.28\,\mathrm{keV}$ is shown in the last row.

Mean energy loss	combined	tof-only	integral-only
$\int_0^{E_{\mathrm{ion}}} f(\Delta E) \cdot \Delta E \,\mathrm{d}\Delta E$	6.412(5)	6.446(9)	6.394(7)
$\int_{E_{\mathrm{ion}}}^{E_{\mathrm{max}}} f(\Delta E) \cdot \Delta E \,\mathrm{d}\Delta E$	24.38(2)	24.25(3)	24.44(3)
$\int_0^{E_{\mathrm{max}}} f(\Delta E) \cdot \Delta E \,\mathrm{d}\Delta E$	30.79(1)	30.70(2)	30.83(2)

The result is not compatible within the uncertainties to the mean energy loss determined with the the tof-only fit result (3.19). In both cases, the uncertainties are determined from the fit uncertainties. For the integral-only fit, the value is higher and $\Delta E(T_2) = 30.84(2)\,\mathrm{eV}$.

Comparing the results of the mean energy loss for energies within $[0, E_{\mathrm{ion}}]$ and $[E_{\mathrm{ion}}, E_{\mathrm{max}}]$ (cf. table 3.17), the dominance of the integral dataset in the ionization tail region is again visible. Since the largest part of the mean energy loss (24 eV of the full 30 eV) is located in the tail region, it is reasonable that the mean energy loss of the integral-only fit result is closer to the combined-fit result than the tof-only fit.

3.3.3 *Impact on the neutrino mass*

Instead of comparing the shape and parameters of the different energy-loss fit results, the different results can also be used as input for neutrino mass fits. For this, measurement data is generated with Monte Carlo (MC) simulations embedded in the `KaFit` framework [Kle14].

The dataset is based on the second KATRIN neutrino mass campaign (KNM2) with the neutrino mass fixed to zero. The energy-loss model that was used for the KNM2 analysis is used to generate MC data. Internally this model is called *KNM2 T2* model. It was the first fit result of the combined integral and differential dataset and was used for the neutrino mass results presented in [Kat22]. The combined fit result that was presented in the previous section and published in [Kat21b] is internally called *KNM3 T2* model.

Between the KNM2 and the KNM3 model, the following changes were implemented: The BED tail implementation was corrected, the fit accounts for the changing kinetic energy, the background model was improved and some minor adjustments were implemented. Since the KNM2 model was used for the published KNM2 neutrino mass analysis it is used in the following comparison as a reference.

In the fit routine, as used for the KNM2 T2 model, the wrong kinetic energy was implemented in the BED model. Instead of the non-relativistic energy (3.16)*, as needed for the BED model by Kim et al. [KR94], the relativistic energy was used.*

A full documentation of all changes is given in an internal report.

Table 3.18 Influence of different energy-loss models on the neutrino mass. Neutrino mass shifts observed in fits on Monte Carlo data using different $f(\Delta E)$.

Model	Δm_ν^2 in $10^{-3}\,\mathrm{eV}^2/\mathrm{c}^4$
KNM2 T2	−0.52 ± 63.00
combined	−12.7 ± 65.0
integral-only	−23.2 ± 66.0
tof-only	11.85 ± 64.00

The MC data was fitted using different $f(\Delta E)$ in the model. The parameter errors of the $f(\Delta E)$ fit results are considered with penalty terms in the neutrino mass fit model. To estimate the robustness of the method, the same $f(\Delta E)$ was used in the model as was used to generate the MC data (KNM2 T2). The result is listed in table 3.18. Due to implementation details, the MC data was generated pixel-wise but the fit is uniform over all pixels; this introduces a small shift of $0.5 \times 10^{-3}\,\mathrm{eV}^2/c^4$. The shifts due to the different $f(\Delta E)$ models are significantly larger. The uncertainties on the neutrino mass shift are on the order of $65 \times 10^{-3}\,\mathrm{eV}^2/c^4$ and are caused by the limited statistics of the KNM2 dataset.

The Δm_ν^2 for the tof-only fit is in a different direction than the one for the integral-only fit and the Δm_ν^2 for the combined fit is in between both. The distance to the Δm_ν^2 of the combined fit is larger for the tof-only fit than for the integral fit. This is the same effect that is also visible in the mean energy loss values of the three different fits (cf. section 3.3.2).

3.3.4 *Summary*

Judging from the impact on the neutrino mass analysis, the mean energy loss values, and the differences shown in fig. 3.16, both datasets (integral and differential) pull the result in different directions. A full overview on the individual measurement systematics and how they can be treated is described in [Kat21b; Sch21]. The investigations show that each of the discussed systematic effects has a negligible influence compared to the statistical uncertainties of the fit result.

However, the results presented above show that both datasets give different results that are not agreeing within their statistical uncertainties (e.g. the result for the mean energy loss). Only judging from the χ^2 result, the tof-only fit seems slightly superior. Since both measurement modes have their individual characteristics and influence the fit result in different directions, we chose to combine both.

For the D_2 measurements $\chi^2 = 1.57(2)$ and for T_2 (combined fit) $\chi^2 = 1.13(2)$. For a possible explanation for the deviation from $\chi^2 = 1$ see the discussion on the residuals in section 3.3.1.5.

The combined fit result is shown in fig. 3.19. To be consistent with the publication [Kat21b], the uncertainties of the data points were inflated by a factor of $\sqrt{\chi^2/N_{\mathrm{dof}}}$ (with the number of degrees of freedom N_{dof}), obtaining a reduced $\chi^2 = 1$. In comparison to the other energy-loss functions, the combined fit result on T_2 has the smallest uncer-

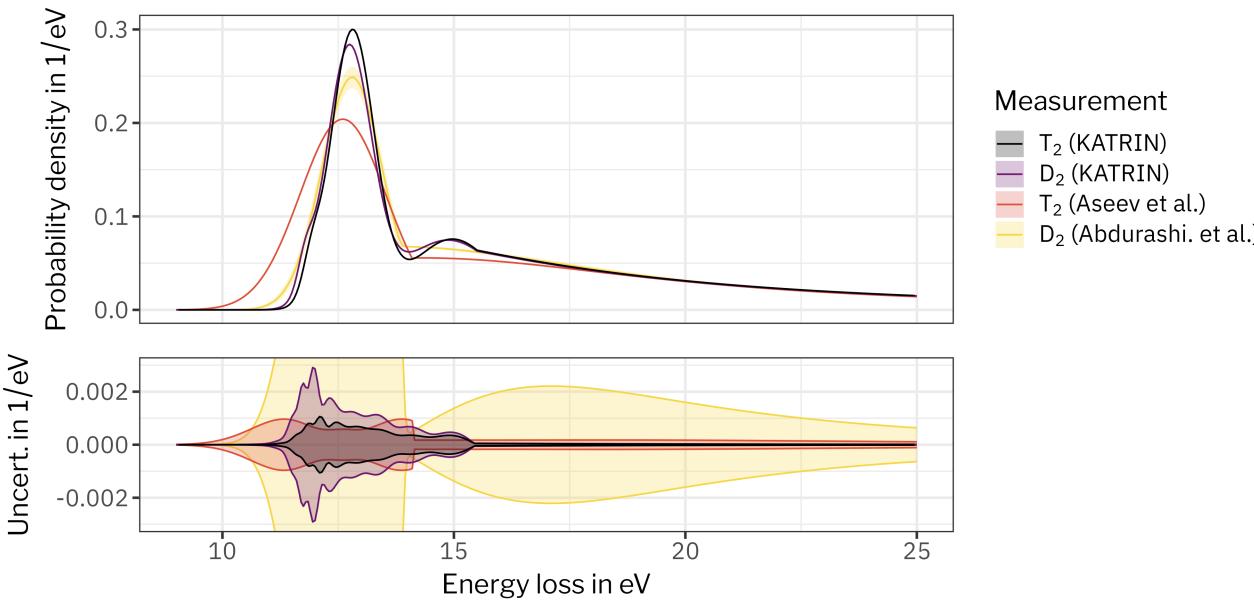

Figure 3.19 **Energy-loss functions for scattering of electrons on tritium and deuterium.** The energy-loss function from the combined fit for T_2 (presented in this chapter and published in [Kat21b]) is plotted together with the T_2 result from [Ase+00], the D_2 result from [Abd+17] (cf. section 3.1), and the D_2 result determined at KATRIN [Kat21b]. The uncertainties for the two external measurements are calculated without considering the correlations between the parameters.

tainties. The improvement in energy resolution to the measurements described in [Ase+00; Abd+17] is clearly visible.

Comparing the two measurements at KATRIN (cf. [Kat21b]), the first Gaussian is less pronounced for the scattering on T_2 than on D_2. Additionally, the positions of the second and third Gaussians are shifted between the result with T_2 and D_2.

3.4 Conclusion

The energy-loss function for electrons inside the WGTS composes together with the spectrometer transmission function the response function of the full KATRIN experiment and is therefore essential for the neutrino mass analysis. Instead of compiling the energy-loss function based on previous measurements or theoretical models, it has been determined in situ.

Electrons from a mono-energetic electron source, namely the e-gun, were used and their energy loss inside the WGTS was measured with the spectrometer. Instead of the normal integral mode of the spectrometer, a differential mode is possible with the pulsed electron beam of the e-gun. The differential mode is achieved using a time-of-flight selection wherein only electrons with long flight times (which correspond to small surplus energies inside the spectrometer) are selected

for analysis.

Such a time-of-flight selection always includes dead-times of the system and the removal of many events (electrons with larger surplus energies) but it delivers a differential spectrum. Since the e-gun provides electron rates of about 5 kcps, statistics are not an issue. However, the exact shape of the energy-loss function which consists of a variety of rovibrational states was not known before the measurement. An integral spectrum would therefore require a numeric deconvolution of the measurement. With a differential measurement, the energy-loss function is directly accessible, which more than makes up for the disadvantage of reduced statistics resulting from the time-of-flight selection.

The differential data was used to parametrize the energy-loss function and to perform a combined fit with the differential and integral measurements. One important aspect of the analysis of the differential measurement data is the reconstruction of the energy scale for the energy loss inside the source. Instead of a complex determination of the e-gun and spectrometer work functions, the energy was determined relative to the mean position of the subset of electrons that reaches the detector without inelastic scattering. In a similar way it was done for the e-gun's energy distribution, by including the unscattered electrons in the energy-loss fit.

The resulting functional description of the energy-loss on tritium and deuterium inside KATRIN's WGTS consists of three Gaussians for the electronic excitations and the relativistic binary encounter dipole model for the ionization continuum. The result is currently used as an input for the neutrino mass analysis and for the determination of the column density which is itself a parameter in the neutrino mass analysis.

The energy-loss measurements are not only important because they are determined for the unique KATRIN beamline, they also are a significant improvement in energy resolution compared to previous energy-loss measurements at predecessor neutrino mass experiments such as the setup in Troitsk or Mainz.

For the future, two important tasks remain and efforts to complete them are already ongoing. First, the measurements presented in this chapter are taken at a WGTS temperature of 30 K. As described in section 2.1, neutrino mass measurements are currently performed at 80 K, therefore additional energy-loss measurements should be performed at the same temperature. Second, in addition to the energy-loss function determined at electron energies of 18.6 keV, a measurement at around 30 keV is needed for plasma investigations with ^{83m}Kr.

The results will be described in the PhD thesis of S. Schneidewind (University of Münster).

4 Wideband precision stabilization of the retarding potential

The main results presented in the first three sections of this chapter have been published in [Rod+22]. In addition to authoring significant portions of the published work and organizing the publication as first and corresponding author, I developed the simulations to establish the requirements, I optimized the post-regulation system and integrated it into the general KATRIN control structure, and I worked on the experimental performance evaluation. The simulations and performance evaluations are discussed here in more detail than in the published paper. The parts of that paper pertaining to the conceptual design and its technical realization are contributions by S. Wüstling and are replaced in this chapter with my own more general overview. Except where cited explicitly, all passages in this section which closely resemble passages from the publication were originally authored by me.

The retarding potential of the main spectrometer, which defines the energy threshold for the electrons, needs to be stabilized and set with sufficient precision for successful neutrino mass measurements. Any unknown broadening of the energy scale, for example caused by an unstable retarding potential, leads to a shift of the measured neutrino mass by [RK88]

$$\delta m_\nu^2 = -2\sigma^2 \ . \tag{4.1}$$

A maximum allowed neutrino mass shift of $7.5 \times 10^{-3}\,\mathrm{eV}^2/c^4$ was specified for the high-voltage system (cf. section 2.3.1) in the KATRIN design report [Kat05], leading to a maximum allowed broadening of the energy scale of

$$\sigma = 60\,\mathrm{meV}\,. \tag{4.2}$$

This is equivalent to an unknown Gaussian broadening of the retarding potential with a maximal standard deviation of 60 mV (corresponding to 3 ppm at −18.6 keV).

The broadening of the energy scale by the retarding potential can happen on different time scales where the high voltage is unstable. For example, noise on the retarding potential from a variety of noise sources (e.g. 50 Hz power grid interference). Time scales ranging from minutes to hours are dominated by drifts from the high-voltage source. On time scales from days to weeks, the calibration of the measurement chain including the high-voltage dividers becomes important. For the neutrino mass analysis the energy scale needs to be stable over one measurement campaign, limiting the required stability period to about 10 weeks [Kat21c].

This chapter starts off with evaluating the effect of noise at the retarding potential on the transmission function. Afterwards, the well-established post-regulation system is presented with its recent upgrades and performance checks. The chapter concludes with a presentation of the current calibration methods for the high-voltage dividers, and updated calibration histories are presented.

4.1 Influence of a time-dependent noise on the retarding potential

A simulation using time-of-flight calculations of the electrons inside the main spectrometer was performed to quantify the effect of noise on the retarding potential. The simulation results further define the requirements for the high voltage stability.

Electrons traveling through the main spectrometer experience the Lorentz force

$$F = q \cdot \vec{E}' + q\vec{v} \times \vec{B} \tag{4.3}$$

with the electric field $\vec{E}'$, the magnetic field $\vec{B}$ and the charge $q = -e$ of an electron with the velocity $\vec{v}$. For the investigations of a time-dependent ripple on the retarding potential, the following simplifications are applied. Only electrons "on-axis", the electrons are following a field line along the beam axis z ($x = y = 0$) inside the spectrometer, are evaluated. Their cyclotron movement around z is neglected and only their guiding center motion is tracked.

The beam axis z is chosen as the axis along the 70 m length of the KATRIN beamline. x and y represent the width and height.

The electric field $\vec{E}' = -\nabla\phi - \frac{\partial A}{\partial t}$ with A defined by $B = \nabla \times A$, is reduced to the static case and the z-component

$$\vec{E} = -\nabla\phi = -\frac{\partial U(z)}{dz}\,. \tag{4.4}$$

For the simulations shown in the following, the simplified axial model of the main spectrometer in Kassiopeia is used. One of the simplifications is the replacement of the wire electrode with solid electrodes.

The potential inside the spectrometer along z can be described as $U(z) = a(z) \cdot U_{\mathrm{ret}}$. The z-dependence of the potential $a(z)$ is defined by the geometry of the spectrometer and is determined with the Kassiopeia simulation framework [Fur+17]. Introducing a time-dependent

fluctuating potential $\Delta U(t)$, the potential becomes:

$$\begin{aligned} U(z,t) &= a(z) \cdot (U_{\text{ret}} + \Delta U(t)) \\ &= U(z) + a(z) \cdot \Delta U(t) \cdot \frac{U_{\text{ret}}}{U_{\text{ret}}} \\ &= U(z) \cdot \left(1 + \frac{\Delta U(t)}{U_{\text{ret}}}\right). \end{aligned} \tag{4.5}$$

The electric field is:

$$E(z) = -\frac{\partial U(t,z)}{\partial z} = -\frac{dU}{dz}\left(1 + \frac{\Delta U(t)}{U_{\text{ret}}}\right). \tag{4.6}$$

The simulation tracks the electrons inside the main spectrometer in small ($\approx$ cm) steps along the z-axis. At each step Δz, the electron's flight time and kinetic energy is calculated. The electron's flight time from position s to s' along the z-axis is determined by

$$\tau = \int_s^{s'} \frac{1}{v_\parallel}\,\mathrm{d}z = \int_s^{s'} \frac{E_{\text{rel}}(z)}{p_\parallel(z,\theta)\cdot c^2}\,\mathrm{d}z, \tag{4.7}$$

where $v_\parallel$ and $p_\parallel$ are the velocity and the momentum parallel to the magnetic field lines and $E_{\text{rel}}(z) = E_{\text{kin}}(z) + m_e c^2$, with the kinetic energy $E_{\text{kin}}(z) = E_{\text{source}} - \Delta E(z)$ and E_{source} is the kinetic energy of the electron before entering the spectrometer. [more details also in Ste+13; Ful+20]

The electric field inside the spectrometer changes E_{source} by

$$\Delta E(z) = \int_s^{s'} F(z)\,\mathrm{d}z = q\int_s^{s'} \frac{\partial U}{\partial z}\left(1 + \frac{\Delta U(t)}{U_{\text{ret}}}\right)\mathrm{d}z. \tag{4.8}$$

The momentum parallel to the magnetic field lines $p_\parallel$ is defined in terms of $E_{\text{rel}}(z)$ and the perpendicular momentum $p_\perp$:

$$p_\perp^2(z,\theta)c^2 = \left(\left(E_{\text{source}} + m_e c^2\right)^2 - \left(m_e c^2\right)^2\right)\cdot \sin^2\theta \cdot \frac{B(z)}{B_{\text{source}}}, \tag{4.9}$$

$$p_\parallel^2(z,\theta)c^2 = E_{\text{rel}}^2(z) - \left(m_e c^2\right)^2 - p_\perp^2(z,\theta)\cdot c^2, \tag{4.10}$$

with the magnetic field along the z-axis $B(z)$, the magnetic field at the electron source B_{source} (e.g. WGTS with 2.52 T) and the pitch angle θ which is the angle between the magnetic field lines and the electron's momentum vector. For further details on the implementation refer to appendix A.1.

Unless otherwise noted, all simulation results shown in the following sections are performed with

$$U_{\text{ret}} = -18\,500\,\text{V}, \tag{4.11}$$

and the nominal magnetic and electrical fields.

For the static case, the electric field inside the main spectrometer is plotted in fig. 4.1. Only at the entrance and the exit, the electric field is significant different from zero. At the entrance (exit) the electrons are decelerated (accelerated) by $\vec{F} = q\vec{E}$. For the nominal configuration

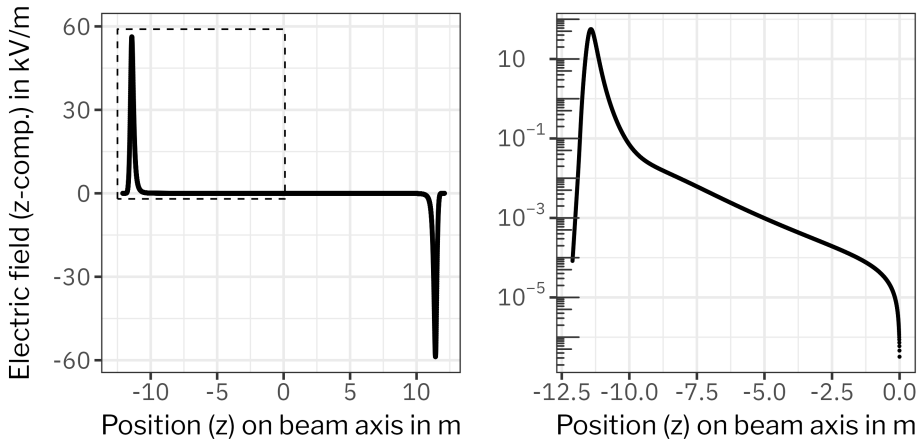

Figure 4.1 **Electric field.** The left panel shows the z-component of the electric field in the nominal configuration along the beam axis inside the main spectrometer (the position $z = 0$ is the center of the spectrometer). The retarding potential of $U_{\text{ret}} = -18\,500\,\text{V}$ matches the standard measurement window below the tritium endpoint. The right panel is a magnified view of the region marked with the dashed rectangle.

that is shown here, the absolute electric and magnetic field is minimal at $z = 0$. The $x - y$ plane at $z = 0$ is called *analyzing plane* (cf. section 2.1.4). In the center of the spectrometer (around $z = 0$), the electric field is close to zero (Faraday cage). Therefore, the force acting on the electrons is very small and with it also the change in E_{source} (4.8) due to any time-dependent ripple with $\Delta U(t) \ll U_{\text{ret}}$ is very small.

The flight time for an electron through the spectrometer entrance (4.7), is plotted for the case without noise on the retarding potential ($\Delta U(t) = 0$) in fig. 4.2. The electron's travel time from the z-position where the electric field starts to increase ($> 1\,\text{V/m}$) to the z-position where the electric field starts decreasing again to values below $10\,\text{V/m}$ is within 1×10^{-3} to $0.1\,\mu\text{s}$ and is hereafter called t_{trav}.

To test the simulations, the calculations described above are checked by using a Heaviside step function as test noise on the retarding potential. After the verification, a sinusoid-shaped noise is used to investigate its effect on the transmission function.

4.1.1 *Testing with a Heaviside step function*

A very simple time-dependent change of the retarding potential is a sudden step in the potential with a well-defined amplitude. More generally, a Heaviside step function

$$H(t) = \begin{cases} 0, & t < t_{\text{step}} \\ A, & t \geq t_{\text{step}} \end{cases} \tag{4.12}$$

with step position t_{step} and amplitude A. Even if this case is quite unphysical (in reality each voltage step would have some expansion in t), it proved beneficial as a validity check of the simulation.

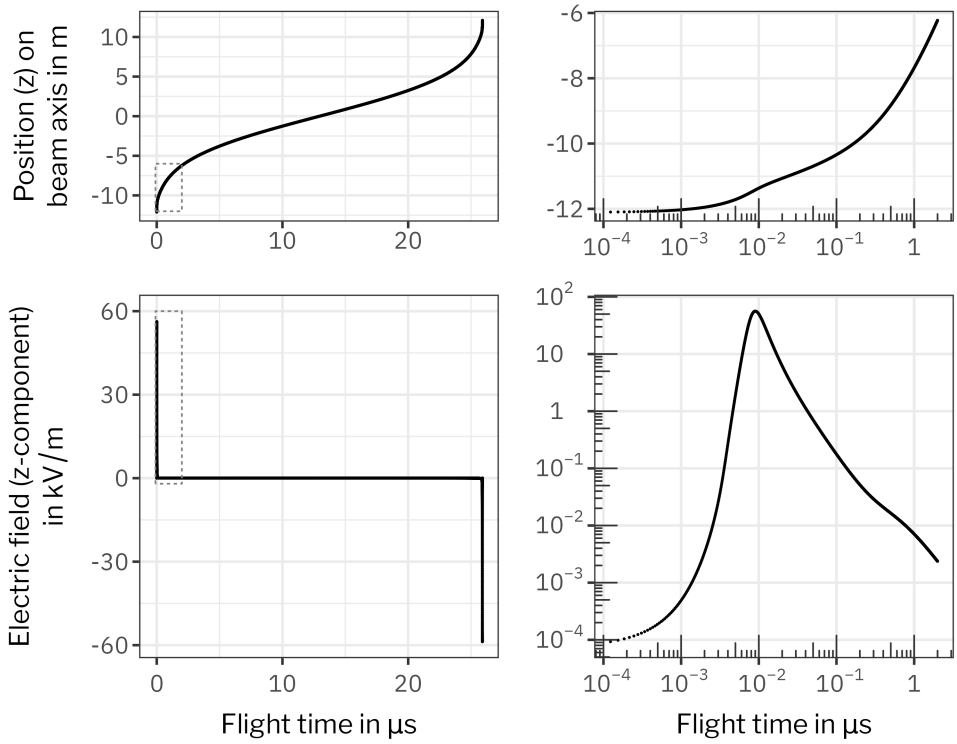

Figure 4.2 **Flight of an electron through the electric field.** The flight time is calculated for an electron with a surplus energy of 0.5 eV and pitch angle $\theta = 0$ at a retarding potential of $U_{\text{ret}} = -18\,500\,\text{V}$. The upper left panel shows the z-position reached by the electron after a certain amount of time. In the lower left panel, the z-position is replaced by its corresponding z-component of the electric field in nominal configuration. The right column shows magnified views of the regions marked in the left column with dashed rectangles.

For very early onsets of the step ($t_{\text{step}} \approx t_0$ with t_0 the time the electron is entering the spectrometer) and $A > 0\,\text{V}$, the retarding potential is increased and the energy threshold for the electron to pass through the spectrometer is lowered by A. As shown in fig. 4.3a, this expectation is met: For a small $t_{\text{step}} = 0.0001\,\mu\text{s}$ and $A = 0.5\,\text{V}$ electrons need 0.5 eV less to be transmitted. Not shown here, but checked for consistency, for a negative amplitude A the energy threshold is increased.

Electrons with small surplus energies E_{s} (amount of energy above the fixed retarding threshold qU_{ret}) have longer flight times through the spectrometer than electrons with higher surplus energies, resulting in the characteristic $1/\sqrt{E_{\text{s}}}$-dependence of the flight time τ (cf. fig. 3.6). The characteristic is visible in fig. 4.3a for different energy thresholds.

To check the correct implementation of the time dependency, the onset t_{step} of the Heaviside function is changed. The different t_{step} are marked as dashed lines over the electric field in fig. 4.3b. If the onset starts before the electron has traveled through the part with the highest electric field, the change by $H(t)$ has a full effect. In this case, the voltage creating the retarding potential is lowered by $H(t)$ before the electron is decelerated by it. If the onset starts afterwards, while

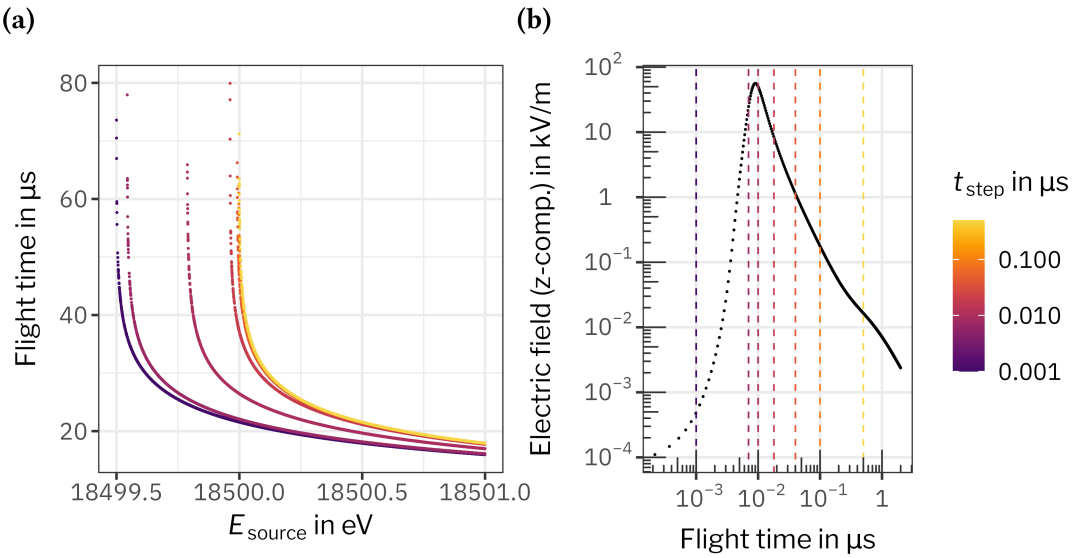

Figure 4.3 **Flight time of electrons for a step-shaped ripple on the retarding potential.** A Heaviside step function $H(t)$ with fixed amplitude $A = 0.5\,\mathrm{V}$ and several different step time-points $t_{\mathrm{step}} \in [0.001\,\mu\mathrm{s}, 0.5\,\mu\mathrm{s}]$ is added to the retarding potential $U_{\mathrm{ret}} = -18\,500\,\mathrm{V}$. For each of the selected t_{step} values, 10 000 electrons with random start energies $E_{\mathrm{source}} \in [18\,499\,\mathrm{eV}, 18\,501\,\mathrm{eV}]$ are simulated with fixed start time $t_0 = 0$, all of them with an angle $\theta = 0°$ to the magnetic field lines. In panel (a), the electrons' flight time through the spectrometer is plotted against their start energy E_{source}. In panel (b), the z-component of the electric field is plotted against the flight time of an electron with 0.5 eV surplus energy (c.f. fig. 4.2). The different t_{step} are marked with dashed lines to visualize at which point in the electron's flight the ripple would affect it.

the electron travels through low electric fields, $H(t)$ has a negligible effect (for $A \ll U_{\mathrm{ret}}$). The dependency of the lowered energy threshold on t_{step} is shown in fig. 4.3a.

In more general terms, the shift of the energy threshold due to $H(t)$ is defined as:

$$\delta E_{\mathrm{ana}} = \int_{s_{\mathrm{start}}}^{0} q \cdot \frac{\partial U(z)}{\partial z} H(t) dz\,, \tag{4.13}$$

where $z = s_{\mathrm{start}}$ is the spectrometer entrance and $z = 0$ the analyzing plane. δE_{ana} is plotted for different t_{step} in fig. 4.4.

δE_{ana} is independent of the electron's initial energy E_{source}, except that it can only be determined for electrons with enough surplus energy to reach the analyzing plane. For $t_{\mathrm{step}} < 0.5 \times 10^{-3}\,\mu\mathrm{s}$, δE_{ana} is reduced by $-0.5\,\mathrm{eV}$. For $t_{\mathrm{step}} > 0.1\,\mu\mathrm{s}$ the influence of the changed absolute retarding potential vanishes; the voltage creating the retarding potential is lowered by $H(t)$ after the electron is decelerated. For t_{step} within $[0.5 \times 10^{-3}\,\mu\mathrm{s}, 0.1\,\mu\mathrm{s}]$, $H(t)$ only partially affects the retarding threshold. Here, the dependency of δE_{ana} on t_{step} ($\delta E_{\mathrm{ana}}(t_{\mathrm{step}})$) resembles a slightly skewed error function.

The shape of $\delta E_{\mathrm{ana}}(t_{\mathrm{step}})$ can also be predicted purely from the electric field as a function of the electron's flight time, as depicted in fig. 4.2.

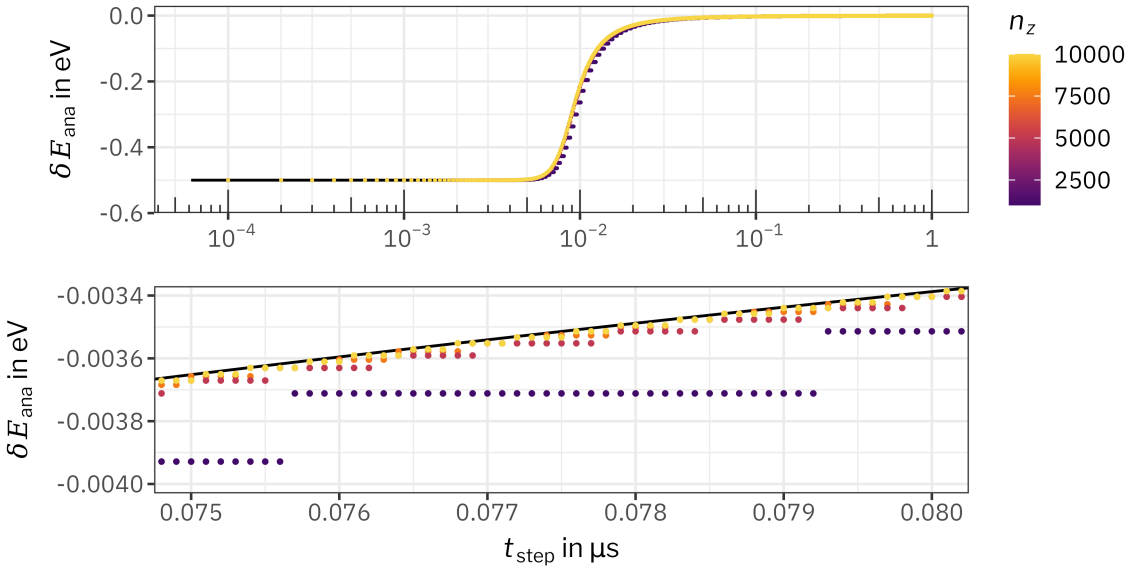

Figure 4.4 **Lowering of the retarding potential threshold by a step-shaped ripple.** The lowering of the retarding potential threshold δE_{ana} is plotted against the onset t_{step} of the Heaviside step function $H(t)$. The calculations for δE_{ana} were done with different numbers of steps n_z for the integration from s_{start} to $z = 0$. The black line is the normalized and shifted cumulative sum over the electric field as shown in fig. 4.2. The lower panel is a magnification of a small region in the top panel.

For an arbitrary function $f(t)$ the following identity holds:

$$f(t) * H(t) = \int_{-\infty}^{\infty} f(u)H(t-u)\mathrm{d}u = \int_{-\infty}^{t} f(u)\mathrm{d}u\,, \tag{4.14}$$

In other words, the convolution of $f(t)$ with $H(t)$ corresponds to the cumulative distribution function of $f(t)$. Here, $f(t)$ is the electric field at different flight times for an electron. The simulation result plotted in fig. 4.4 is the outcome of applying H(t) with different t_{step} on the potential creating the electric field. The cumulative sum over the electric field is calculated, normalized (divided by 2 times of its maximum value), shifted about −0.5 eV (effect of the ripple $H(t)$ with amplitude of 0.5 V) and plotted in darkgreen in fig. 4.4. It shows a very good agreement with the simulation result, especially for simulations with higher n_z.

Additionally, $\delta E_{\text{ana}}(t_{\text{step}})$, is used to evaluate a good number of steps n_z for the simulation. Too small n_z results in a discrete and also slightly shifted change of δE_{ana} (c.f. fig. 4.4). Increasing the number of steps and with it decreasing the distance between each step, reduces the effect but it does not remove it. This shows the limitations of this numeric calculation.

In summary, the first test with a Heaviside step function as time-dependent potential shows quite expected results and therefore proofing the functionality of the simulation. It is also possible to see the first numeric limitations: for small changes in t_{step} of 1×10^{-4} µs it is

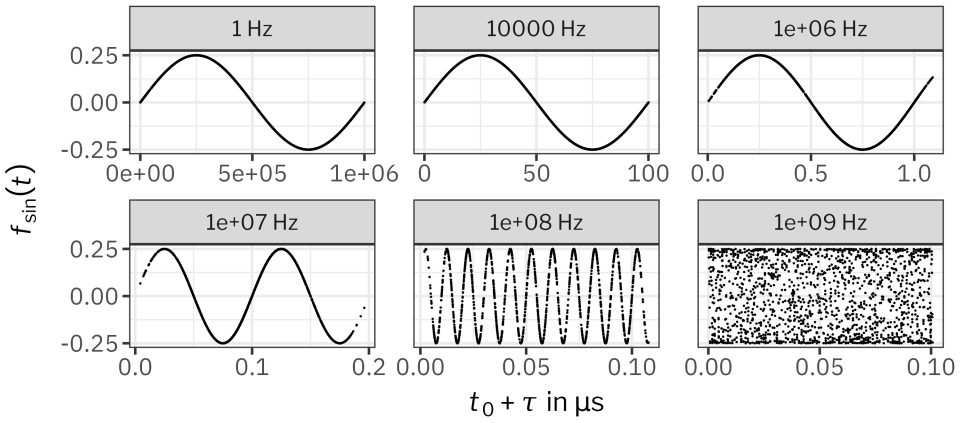

Figure 4.5 Sampling from a sinusoidal function for different frequencies. For each frequency f, 10 000 values are picked from $f_{\sin}(t)$ with random $t_0 \in [0\,\mu s, 1/f]$, random $\tau \in [0\,\mu s, 0.1\,\mu s]$, and fixed $A = 0.25\,V$.

necessary to choose a fine enough step size in z. Judging from fig. 4.4 a minimum n_z should be 2500 and for studies sensitive to $1 \times 10^{-4}\,\mu s$ the minimum should be 10 000.

4.1.2 *Sinusoidal ripple*

Instead of a Heaviside step function, a sinusoidal function

$$f_{\sin}(t) = A \cdot \sin(2\pi \cdot f \cdot t) \tag{4.15}$$

with amplitude A and frequency f is used as time-dependent varied potential. The start time t_0 of the electrons is randomly picked from $[0\,\mu s, 1/f]$.

For a first insight on the effect, $f_{\sin}(t)$ is plotted in fig. 4.5 for different frequencies. $f_{\sin}(t)$ is evaluated for $t_0 + \tau$, with the flight time $\tau \in [0\,\mu s, 0.1\mu s]$. The upper limit of τ is chosen to fit the flight time of the electron through the spectrometer entrance t_{trav}.

For frequencies up to 10 MHz, the amplitude change is slow compared to t_{trav}. Beginning with 10 MHz the amplitude changes within t_{trav}.

For lower frequencies ($f < 10\,\text{MHz}$), the ripple amplitude at t_0 determines the retarding potential for the electron, since changes of the ripple amplitude within t_{trav} are negligibly small. Therefore, the transmission threshold should change within ±0.5 eV following the density distribution of $f_{\sin}(t)$ (cf. fig. 4.6a).

A reference transmission function is created by sampling for different electron energies, changed along the density distribution. The reference is plotted together with a simulation result at $f = 100\,\text{Hz}$ in fig. 4.6b, showing a very good agreement of both.

For a full picture of a wide range of frequencies ($f \in [1\,\text{Hz}, 1\,\text{GHz}]$), the effect of $f_{\sin}(t)$ is plotted in fig. 4.7. The broadening of the transmission function is independent of the frequency of $f_{\sin}(t)$ up to frequencies of about 10 MHz and has the structure as predicted by the frequency distribution of $f_{\sin}(t)$. For $f \in [10\,\text{MHz}, 400\,\text{MHz}]$, the width

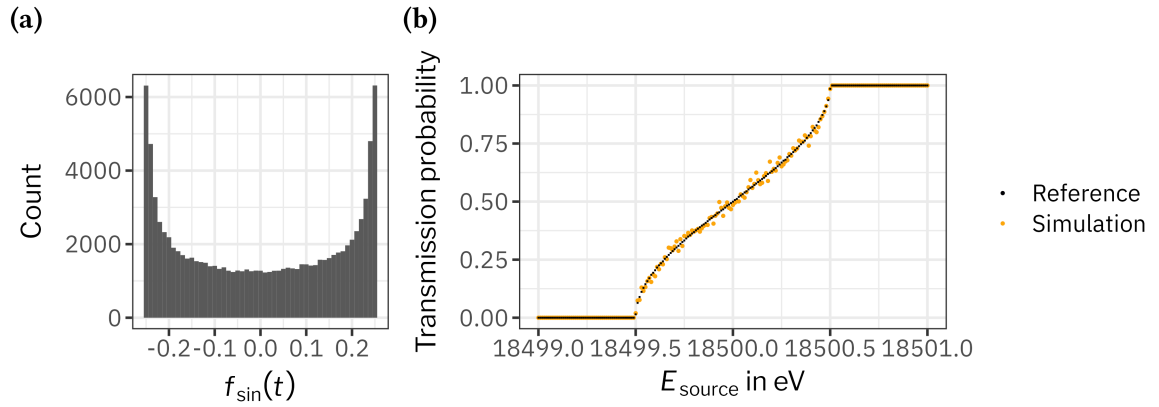

Figure 4.6 **Transmission function for a sinusoidal ripple.** Panel (a) shows the density distribution for $f_{\sin}(t)$ at fixed f (independent of the frequency). Panel (b) shows in orange the result of the simulations for $f = 100\,\text{Hz}$. The black points are the transmission function predicted by sampling 5×10^7 electron energies $E_{\text{source}} + f_{\sin}(t)$ and applying the transmission condition ($E_{\text{source}} \geq 18\,500\,\text{eV}$).

of the transmission function gets smaller with increasing frequency. For frequencies above 400 MHz, the influence of the ripple vanishes.

To investigate the dependency on different amplitudes A in $f_{\sin}(t)$, the simulation is repeated for $A \in [0.01\,\text{eV}, 1000\,\text{eV}]$ (c.f. fig. A.18 in the appendix). For 50 Hz, the amplitude directly translates into the broadening of the transmission function. For 5×10^8 Hz, the effect of the ripple amplitude is reduced by a factor of about 1000.

In summary, up to frequencies of about 10 MHz, the frequency is not important to evaluate the influence of a sinusoidal noise on the retarding potential. For frequencies above that, the influence of a sinusoidal noise is reduced and even vanishes for small enough amplitudes ($< 10\,\text{V}$).

4.1.3 *Isotropic angular distribution*

Although electrons from the source have an isotropic angular distribution, up to now, only electrons with $\theta = 0$ have been considered. As explained in section 2.1.4, the magnetic field gradient inside the spectrometer adiabatically collimates the momentum and transfers $p_\perp$ into $p_\parallel$. Since not the full $p_\perp$ is translated into $p_\parallel$, the transmission condition is angular-dependent.

At fixed E_{source}, a larger $p_\perp$ (or equivalently a larger θ) corresponds to a longer flight time of the electron through the main spectrometer, since it has less surplus energy after being decelerated by the electric field.

The location of the analyzing plane at $z \approx 5\,\text{m}$ is only true for on-axis electrons that are considered in the simulation. In reality, the analyzing plane is a curved surface [Lok+22a].

For further exploration, two different magnetic field settings are investigated: The nominal setting ($B_{\text{ana}} = 6.3 \times 10^{-4}\,\text{T}$, cf. section 2.1.4.1) and the shifted analyzing plane configuration "SAP" ([Lok+22a]). In the shifted analyzing plane configuration, the analyzing plane is not at $z = 0$ but shifted towards the detector to $z \approx 5\,\text{m}$. In general, the simulation can be used with any magnetic and electric field configuration used as input.

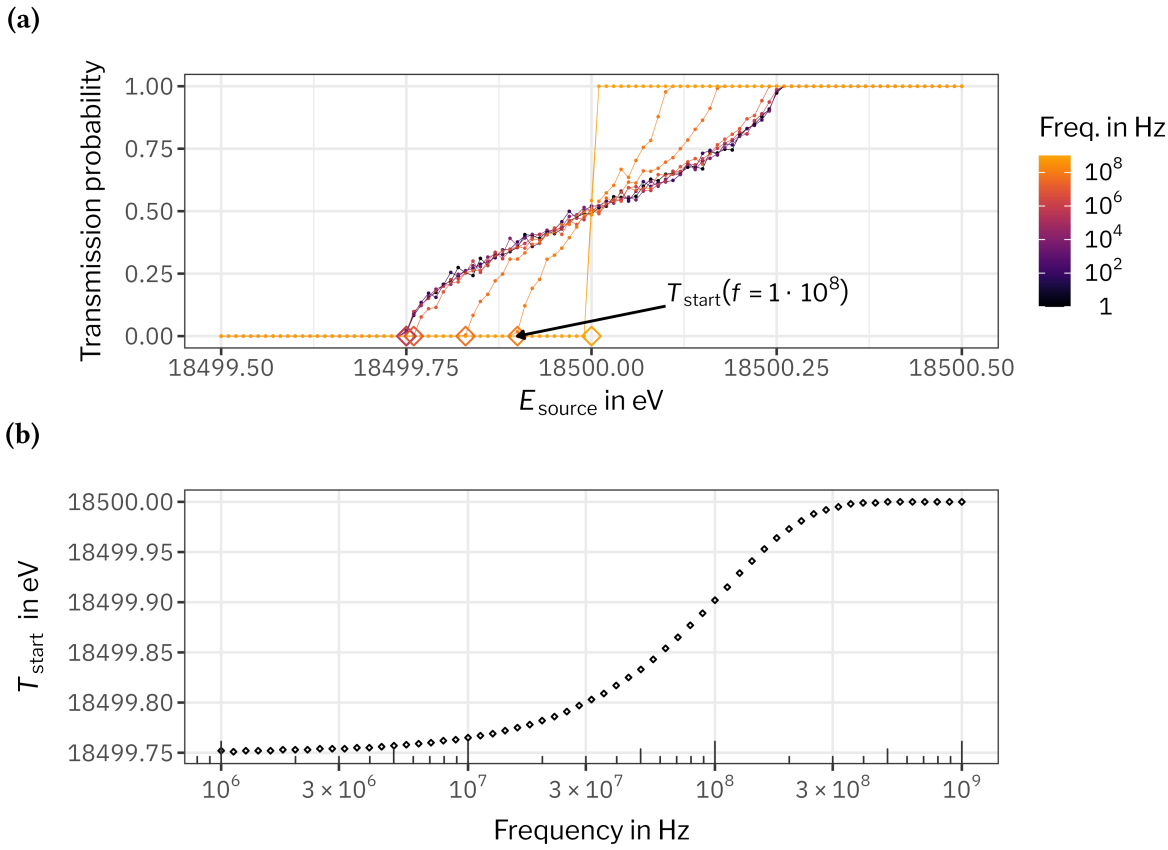

Figure 4.7 **Transmission function for a sinusoidal ripple at various frequencies.** $f_{\sin}(t)$ is used as time-dependent ripple in the simulation, with a fixed amplitude of 0.25 V and at various frequencies f. For each frequency, 100 000 electrons with pitch angle $\theta = 0°$, starting potential $E_{\text{source}} \in [18\,499.5\,\text{eV}, 18\,500.5\,\text{eV}]$, and randomized start times $t_{\text{start}} \in [0, 1/f]$ are generated. Their transmission probability is shown in panel (a). T_{start} is defined as the minimal E_{source} that is sufficient for the transmission of the electron. Panel (b) shows T_{start} as a function of frequency.

The figure is adapted from [Rod+22], used under CC BY 4.0.

The flight times of electrons to the analyzing plane for the nominal and SAP configuration is plotted in fig. 4.8. The deceleration at the spectrometer entrance is quite similar for the different field settings, and the different electron angles. Therefore, the general frequency dependency for any noise is expected to be very similar to the behavior for $\theta = 0$ as it was discussed above.

The full transmission function with $f_{\sin}(t)$ (using $A = 0.25\,\text{V}$, $f =$ 50 Hz, 1 GHz) as ripple on the retarding potential for the nominal and SAP settings is shown in fig. A.19 in the appendix. For $f = 1\,\text{GHz}$, the transmission function matches the transmission function without noise on the retarding potential. For $f = 50\,\text{Hz}$, the transmission function is broadened by about A. The broadening for the nominal and SAP settings is indeed very similar.

In summary, the results agree with the ones presented for $\theta = 0$, showing that the two different field settings and the different angles have a negligible impact on the effect of a time-dependent noise on the transmission condition.

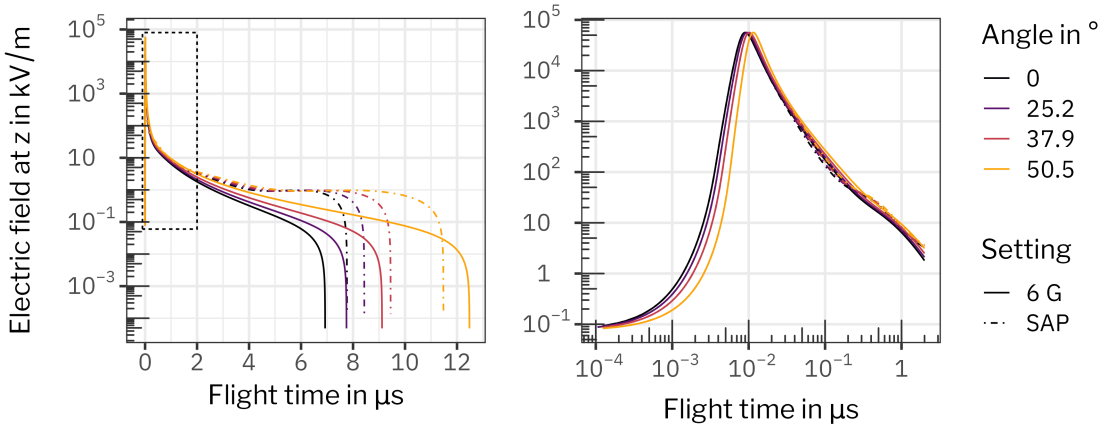

Figure 4.8 **Electron flight times for different angles and field settings.** The time it takes for an 18 503.5-eV electron to travel from the spectrometer entrance to the analyzing plane with different θ is calculated for the nominal setting (6 G) and the SAP setting. The retarding potential is at −18 500 eV, without any noise superimposed. The right panel is a magnification of the region at the spectrometer entrance, marked with a dashed rectangle in the left panel.

4.2 Post-regulation

The simulations in the previous section show the necessity to stabilize the retarding potential of the main spectrometer on a wide range of timescales to minimize broadening of the transmission function by an unstable retarding potential.

Any fluctuations on longer time scales ($> \mathcal{O}(1\,\mathrm{s})$) are measured by the precision measurement chain as described in section 2.2.2. Any noise, such as 50 Hz power grid interference, or switching frequency of the power supply ($\mathcal{O}(10\,\mathrm{kHz})$) is not visible with the measurement chain and therefore leads to an unknown broadening.

In an ideal setup the main spectrometer would be placed into a Faraday cage to minimize noise sources down to the noise by the power supply itself. At the former neutrino mass experiments in Mainz and Troitsk setup, the retarding potential was applied to the inner electrodes where it was shielded by the vacuum vessel itself [Pic+92a; Lob03]. At KATRIN, the high voltage is put directly on the large steel vacuum vessel, with a lightweight inner electrode system inside [Kat05]. Any equipment (e.g. turbo-molecular pumps for the vacuum and their power supplies) directly attached to the main spectrometer is on the retarding potential, adding potential noise sources. At the very least, noise from these sources needs to be measured, or better yet reduced by a regulator. As a solution, a nested regulator structure later called *post-regulation system* was developed by S. Wüstling.

Presented in two talks during KATRIN collaboration meetings (Nov. 2004 and Sep. 2005).

The retarding potential is the sum of the potential applied to the vessel and the IE (inner electrode) common potential ($\mathcal{O}(100\,\mathrm{V})$), as introduced in section 2.1.5. In the nominal configuration, the retarding potential is measured by one of the precision high-voltage dividers K35 or K65 (cf. section 2.2.2). The post-regulation regulates the potential

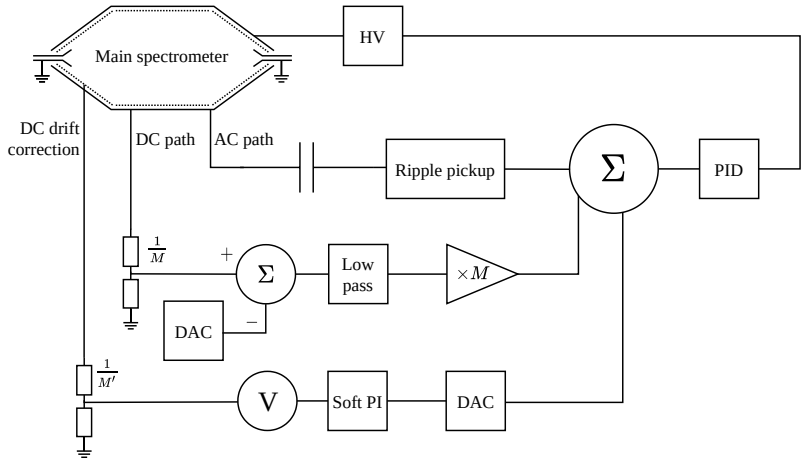

Figure 4.9 **Schematic diagram of the regulator structure.** The schematic shows the nested approach with the three paths: AC path, DC path, and outer loop with DC drift correction. The dashed line in the main spectrometer visualizes the inner electrode system (cf. section 2.1.4.1). A more detailed block diagram is shown in fig. A.20 in the appendix.

The figure is copied from [Rod+22], licensed under CC BY 4.0.

applied to the vessel. The IE common potential is usually kept constant during neutrino mass measurements and only the vessel potential is varied.

4.2.1 *Setup*

The high voltage for the vessel potential is supplied by a commercial power supply. For neutrino mass measurements the retarding potential is at −18.6 kV and any unknown noise on top of it needs to be below 60 mV, therefore a change on the ppm-level needs to be measured and regulated. To solve this, the regulator is split into an AC and DC path (cf. fig. 4.9).

The AC component is separated from the DC component with a high-voltage decoupling capacitor. The capacitor consists of a series of fifteen 150-nF foil capacitors which are combined with a protection circuit and an amplifier. The full composition is called *ripple probe* from this point on.

In the DC path, the vessel potential is measured with an auxiliary divider and compared to the setpoint. The deviation from the setpoint, and the noise measured over the AC path, are the error signal that needs to be regulated. The regulation is done via a high-voltage vacuum shunt triode, as has been used for the stabilization of the cathode ray tube (CRT) acceleration voltage for color TVs. The voltage is regulated by adjusting the current flow to the anode of the triode via the control grid. The overall power flowing through the triode should be below 30 W to avoid damage.

In addition to the DC path with the auxiliary divider, a third path, called *DC drift correction* exists. This is an optional operation mode

that enables an improved long-term stability by using the precision measurement chain with the K35 or K65. The divider measures the retarding potential and by subtracting the IE common voltage, it can be used as a measurement of the vessel voltage. The deviation of the vessel voltage to the setpoint is used as error signal for a software proportional integral (PI) regulation loop. The control value of the PI regulation loop is merged via an analog input with the error signal that is obtained by the DC and AC path. The analog input is called *fast-stepping* or *correction* input (cf. fig. A.20 in the appendix). A correction voltage of ±1 V can be added to the error signal over the fast-stepping input.

The bandwidth of the ripple probe is limited to about 1.6 MHz. One possible noise source with frequencies above the post-regulation's cut-off frequency are standing waves along the z-axis of the main spectrometer. A standing wave with the wavelength λ needs to fulfill the condition:

$$d = \frac{p\lambda}{2} \tag{4.16}$$

with p the number of half-waves along the distance d. The resonance frequency is

$$f = \frac{c\sqrt{\epsilon_\mathrm{r}\mu_\mathrm{r}}}{\lambda} = c\sqrt{\epsilon_\mathrm{r}\mu_\mathrm{r}} \cdot \frac{p}{2d} \tag{4.17}$$

with the relative permittivity ϵ_r, the relative permeability μ_r and the speed of light c. [Nic19]

For the spectrometer of length $d = 23\,\mathrm{m}$ with vacuum conditions ($\epsilon_\mathrm{r} = \mu_\mathrm{r} = 1$) and $p = 1$ follows a resonance frequency of 6.5 MHz.

To cover the frequencies above the cutoff frequency of the post-regulation system, three 7-nF high-voltage filtering capacitors are installed in a rotationally symmetric pattern around the beam-tube insulator at the spectrometer entrance. They provide a low AC impedance ($1/\omega C$) of about 7.6 Ω, for 1 MHz.

4.2.2 *Dynamic setpoint control*

For measurements done with the main spectrometer, the retarding potential needs to be changed synchronously with data taking at the detector. Therefore, the control of the post-regulation is done in close connection with the data acquisition system for detector data. For most of the measurements (tritium spectrum measurements or $^{83\mathrm{m}}$Kr conversion electron spectroscopy), the setpoint of the retarding potential must not only be reached as fast as possible but also be stable and reproducible on the ppm-level [Kat21a].

The logic of setting a voltage value is shown in detail in fig. 4.10. First, the voltage value is set coarsely $\mathcal{O}(100\,\mathrm{mV})$. For this operation two inputs, an offset value c and a scale factor M are needed. The setpoint for the primary high voltage supply needs to be by an offset c more negative than the required spectrometer voltage. The offset depends on the individual setup; i.e. how many and which dividers are connected to the main spectrometer, which power supply is used (as they can have varying absolute setpoint precision) and the resistance

of the shunt regulator series resistor. The offset c needs to be chosen in a way that the shunt triode is not overloaded (limited to 30 W) but is still in its optimal operating range of 0.5 to 0.9 mA. During commissioning measurements, c is determined for each setup and stored in a look-up table. The second input is the scale factor M of the auxiliary divider. For new voltage setpoints U_0, $M(U_0)$ is determined by values estimated during commissioning measurements and updated after each successful setting of the voltage.

After setting the voltage coarsely, the actual voltage is measured with one of the precision dividers. If necessary, M is adjusted until the voltage value has reached its setpoint within ±50 mV. The DC drift correction is subsequently activated, regulating any remaining deviation and forcing the voltage to the desired U_0. Usually during data, taking a loop that determines and stores the actual M continuously (not drawn in fig. 4.10) is activated. For small voltages steps $< |50\,\mathrm{V}|$, the most recent value of M is used, instead of the $M(U_0)$ from the look-up table. For this step-size, changes over time (mainly temperature related) have higher relevance than the voltage dependency of the auxiliary divider.

Due to the dynamic logic of the setpoint algorithm, the overall settling time for each voltage setpoint depends on the overall step size, the repetition of voltage steps, and especially the required precision. For $^{83\mathrm{m}}$Kr measurements it takes on average 22 to 25 s, depending on the step size; the smaller the overall step size, the shorter the average settling time. For standard tritium beta scans, one step takes 29 s on average and is larger than for $^{83\mathrm{m}}$Kr measurements. One dominant factor of the settling time is the averaging time over multiple measurements to ensure the setpoint precision before starting a physics measurement. During these measurements, data is taken continuously at the detector, but separated into "usable" periods with start/stop time stamps. In the analysis, the waiting time can be recovered again by using the measured voltage values to redefine the start/stop time of a physics measurement. With this, the average settling time is reduced for beta scans to 23 s without losing any precision.

More details can be found in a presentation by S. Enomoto at a KATRIN collaboration meeting in Nov. 2019.

4.3 Performance measurements

Already during the development of the post-regulation system, several quality and performance checks were carried out [Kra16; Res19]. At present, four different methods allow for a measurement of the remaining ripple on the main spectrometer retarding voltage on different time scales. In this section, the performance of the final implementation, as it is used for neutrino mass scans, is evaluated with these methods.

The oscilloscope is from the manufacturer Digilent and of type 410-321. Details of the installation in May 2019 are reported in the electronic logbook. The analysis software and control for the oscilloscope was developed by S. Enomoto.

4.3.1 *Ripple probe*

The ripple probe allows for a measurement of the AC noise on the retarding potential. To have a remote controlled readout of the ripple probe measurement, a USB oscilloscope was installed. All traces ac-

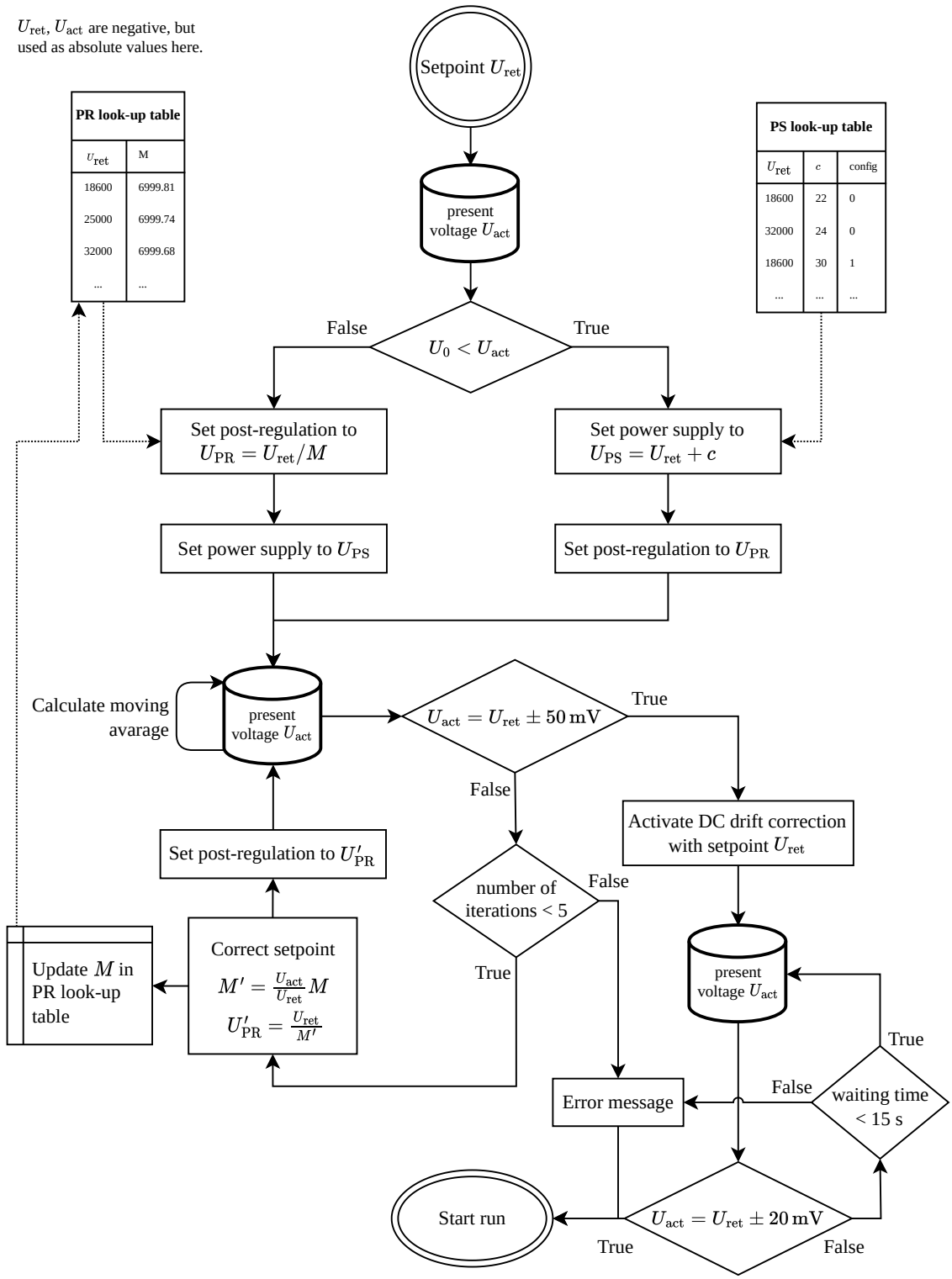

Figure 4.10 **Dynamic setpoint control.** Schematic of the logic for a new voltage setpoint. "Start run" means the start of data taking at the KATRIN beamline with a new voltage setpoint.

The figure is adapted from [Rod+22], licensed under CC BY 4.0.

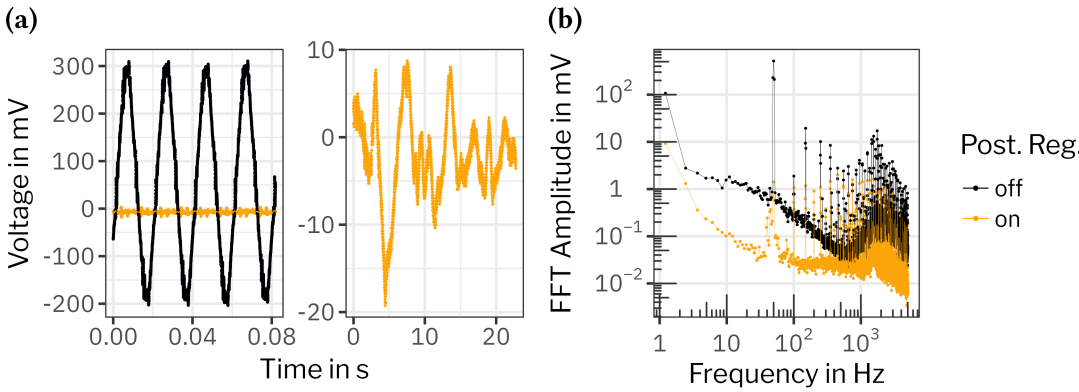

Figure 4.11 **Oscilloscope readout of ripple pick-up probe.** Two traces taken with the ripple pick-up probe at a −18.3-kV main spectrometer potential are shown. Plot (a) shows a measurement without the post-regulation at a sample rate of 10 kHz, and with active post-regulation at a sample rate of 250 Hz. Plot (b) shows the Fourier spectrum for both cases.

The figure is adapted from [Rod+22], licensed under CC BY 4.0.

quired at the oscilloscope are accessible over IDLE (Intermediate Data Layer for Everyone). During neutrino mass measurements, traces are automatically acquired at selected voltage steps.

More information here.

Traces of the ripple pick-up probe at −18.3 kV are shown in fig. 4.11. Without the post-regulation, the AC noise is dominated by a sinusoidal 50-Hz signal, with amplitudes of about 0.25 V. With the post-regulation active, the sinusoidal noise is suppressed and only fluctuations within less than 0.03 V remain.

To analyze the AC components further, 100 traces at a sampling rate of 10 kHz are taken. Each trace was limited to 8192 samples. To remove any remaining DC part, the mean voltage value is first calculated for each trace, which is then subtracted from each voltage value within one trace. A fast Fourier transformation with a Hamming window (window function) is applied on the net trace and plotted in the right plot of fig. 4.11. Comparing the Fourier spectrum with and without active post-regulation, one can see a noise reduction on a wide range of frequencies. The largest noise component (50 Hz) is suppressed by two orders of magnitude.

4.3.1.1 *Effect on the transmission function*

To investigate the effect of the post-regulation, the ripple probe measurements are used as input for the simulations described in section 4.1. Since the ripple without active post-regulation is dominated by the 50-Hz sinusoidal ripple, the broadening of the transmission function is very similar to the one shown in section 4.1.2. The result is shown in fig. A.21 in the appendix. In this particular case, the measured ripple is slightly asymmetric (0.3 V, −0.2 V), this asymmetry is directly reflected in the asymmetric broadening of the transmission function around U_0.

For the case with active post-regulation, the result is shown in fig. 4.12. Here 100 samples of ripple probe measurements during tri-

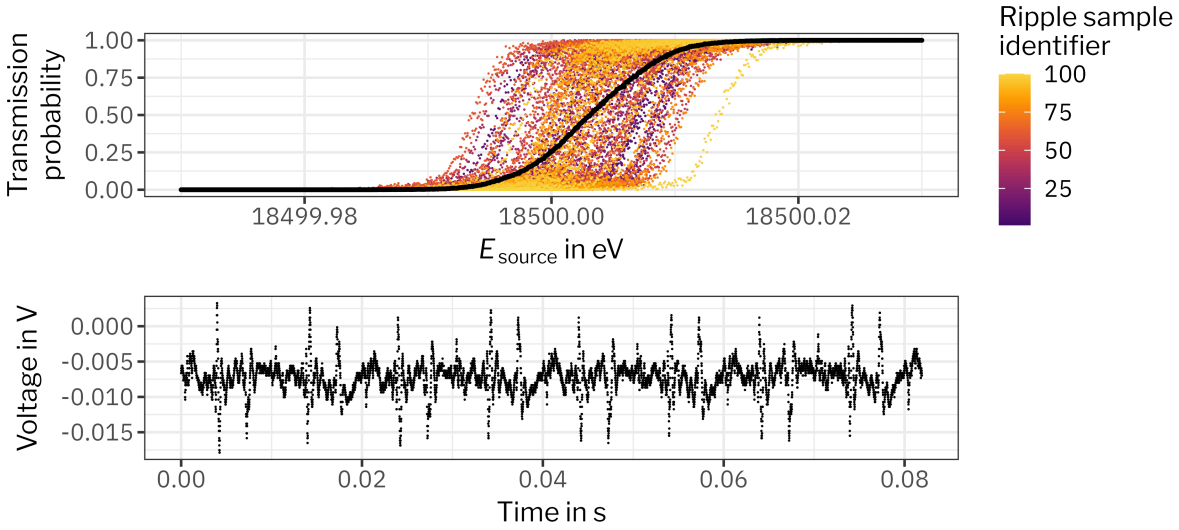

Figure 4.12 **Broadening of the transmission function with active post-regulation.** For the simulation, 100 different ripple probe measurements were used as time-dependent ripple (one example shown in the bottom panel). For each ripple probe measurement, 100 000 electrons with $\theta = 0°$, starting potential $E_{\text{source}} \in [18\,499.9\,\text{eV}, 18\,500.1\,\text{eV}]$, and randomized start times $t_{\text{start}} \in [0\,\text{s}, 0.08\,\text{s}]$ are generated. Their transmission probability is shown in the top panel, colored by the identifying number of the ripple probe measurement. The average transmission probabilities of each of the 100 different simulations are plotted in black.

tium scans in March 2021 were picked. One example is shown in the bottom panel of fig. 4.12. Each measurement is a short (0.08 s long) sample, each of them with different residual ripples. In the top panel of fig. 4.12 one can see that all result in a different broadening. To get an overall picture of an effective broadening during longer measurements, the average transmission probability for all of them is calculated.

In principle, it is possible to repeat these simulations for even more ripple-probe measurements already on disc and include them in the analysis. For the subset shown here, the effective broadening of the transmission function by the residual ripple is within [−21 mV, 18 mV]. Since the broadening is well-within the required 60 mV, it is negligible for standard neutrino mass scans. For high-precision measurements where this broadening would pose a limiting factor (e.g. ^{83m}Kr spectroscopy of the $N_{2,3}$-32 line doublet), this method can be used as an input for the analysis.

4.3.2 *Conversion electrons from ^{83m}Kr*

Measurements with conversion electrons from ^{83m}Kr provide an independent method to the ripple pick-up probe measurements. The conversion electrons from ^{83m}Kr are equally sensitive to the ripple as the beta decay electrons whereas the ripple pick-up probe is only attached to the outside of the main spectrometer vessel. Therefore,

the electrons are an ideal tool for an independent cross-check of the post-regulation performance.

Measurements of ^{83m}Kr conversion electron lines are a standard method at KATRIN [Kat18a; Vén+18; Kat20b] (cf. section 2.2.3). The measurements discussed here were performed with the *condensed krypton source* (CKrS) during a measurement campaign described in [Ful20]. They consist of measurements from three conversion electron lines, following the 32-keV gamma transition, but from different shells: K-32 at 17.8 keV, L_3-32 at 30.5 keV and the line doublet N_2N_3-32 at 32.1 keV.

For a typical transmission function scan of a conversion electron line with the main spectrometer, the retarding potential is changed in small steps (0.1 to 0.5 V) around the expected line position. The width of the measured transmission function depends on the spectrometer resolution and the natural line width. Each transmission function has a retarding potential at which the rate is half of the rate compared to full transmission, called the middle of transmission. The rate in the transmission region is correlated with the retarding potential. For small variations of the retarding potential δU_{ret} around the middle of transmission, the measured electron rate at the detector is linearly dependent on the retarding potential. The investigated δU_{ret} is limited to be within about 1 V by the width of the transmission function and the conversion electron line.

By measuring the shape of the transmission function in a dedicated measurement, the linear dependency of the rate on the retarding potential can be estimated. In a second step, the rate at the middle of transmission is measured. Assuming a perfectly stable source, any fluctuations of the rate can then be accounted as fluctuations of the retarding potential.

The measurements focus on the largest noise part, coming from the 50-Hz power grid interference. The dedicated grid synchronization signal at KATRIN's focal plane detector (FPD) measures the $\approx$ 50 Hz of the mains power and outputs a synchronization pulse (called the *grid sync pulse*) for each new mains power period [Kat21c, cf. p. 79]. With this, each event measured at the FPD has a relative time to the start of a new mains power period t_{rel}.

Measuring the rate at the middle of transmission, and stacking the measured events at the detector along t_{rel} modulo 20 ms, reveals directly any 50-Hz noise seen by the electrons on their way through the spectrometer. Hereafter, this type of measurement is called the *line-center* method. The result of such a measurement is plotted in fig. 4.13. Panel (a) is without post-regulation. Here, the rate at the middle of transmission is following a 50-Hz sinusoidal ripple. In a dedicated transmission function scan, the slope around the middle of transmission is determined. With the slope, the rate change can be transformed to a voltage ripple with an amplitude of about 0.25 V. With active post-regulation (fig. 4.13b), the sinusoidal structure is not as distinct despite a 43-fold increased measurement time. This clearly shows the ability of the post-regulation to decrease the 50-Hz sinusoidal ripple by at least two orders of magnitude.

By repeating the line-center method at different line positions, a possible dependency on the retarding potential can be investigated. It

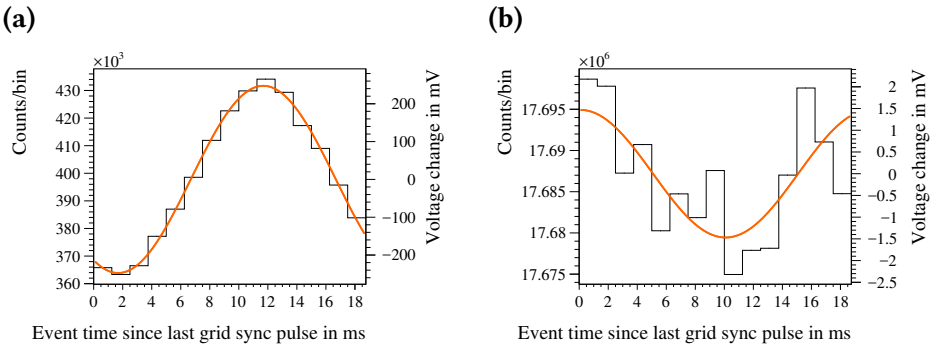

Figure 4.13 **Line-center measurements.** Results of the line-center measurement with the L_3-32 line. Panel (a) shows a 10.5-minute measurement without post-regulation. A clear sinusoidal ripple with an amplitude of 33 922(231) counts, transforming to a voltage ripple amplitude of 247(2) mV is visible. The 7.5-hour measurement with active post-regulation is shown in panel (b). The fit (orange line) results in an amplitude of 7741(1592) counts, transforming to a voltage ripple amplitude of 1.5(3) mV. The analysis shown here was done by S. Enomoto.

The figure is copied from [Rod+22], licensed under CC BY 4.0.

also allows the comparison of the amplitude measured at the ripple probe with the amplitude determined by the line-center method. To investigate the sensitivity of the method, measurements with different power supplies and without post-regulation were performed.

Without post-regulation, the ripple amplitudes as measured with the ripple probe and the line-center method are in good agreement, see results in table 4.14. The only exception is the measurement with power supply B. Here the deviation between both methods is larger than for devices A and C but most likely due to a drift of the device between the ripple probe and the line-center measurement. This device was added to the measurements to have a larger variety of devices but is not used in normal measurement campaigns, due to its increased instabilities and fluctuations compared to devices of the same type. Note that any drift of the power supply would be compensated by the post-regulation within its regulation limit.

The variety of tests show that the ripple probe measurement and the line-center method yield very similar results for the amplitude of the 50-Hz noise. This proves, at least for the 50-Hz noise, that the ripple probe readout matches the ripple seen by the electrons inside the main spectrometer.

With active post-regulation, the comparison of both methods is more difficult. Here the sinusoidal 50-Hz noise is not the dominant part (c.f. fig. 4.11) and the line-center method is only sensitive to the 50 Hz. Still, both methods show the clear mitigation of the 50-Hz ripple by the post-regulation.

Table 4.14 **Ripple amplitudes without post-regulation.** The amplitudes are estimated using two different measurement methods (line-center and ripple probe), for different power supplies. For both methods, the ripple amplitude is determined by fitting a sinusoidal with free amplitude.

Line	Ret. pot. in kV	Power supply	Ripple probe in mV	Line-center in mV
K-32	−17.8	A	225(1)	219(4)
		B	234(1)	222(4)
		C	210(1)	204(4)
L_3-32	−30.5	A	248(1)	246(2)
		B	258(1)	248(2)
		C	229(1)	231(2)
N_2N_3	−32.1	C	233(1)	237(6)

4.3.3 *Precision high-voltage divider*

As described in section 2.2.2, a continuous measurement of the retarding potential with a readout rate of 1/2 Hz with a precision high-voltage divider is in place. The stability of an exemplary one hour measurement at fixed retarding potential of −18.6 kV is shown in fig. 4.15. Without the DC drift correction, a random-walk-like structure within ±3 ppm is visible. With active DC drift correction, the measured voltage has a standard deviation of 11 mV. This Gaussian-like distribution is valid at all times from a few minutes to two weeks. It is only limited by the long-term stability of divider and voltmeter.

To cover the gap in frequency between the sensitivity range of divider and ripple probe measurement, an additional measurement system, the *fast-measurement system*, was temporarily installed. The development, setup and first measurements of the setup were performed by Rest [Res19].

The fast-measurement system measures the vessel potential as a difference voltage to a reference potential. The reference potential is supplied by a sufficiently stable power supply. For instance, when aiming for a measurement in the range of −18 600 V, the reference potential is set to a value close to this voltage (e.g. −18 590 V) such that the difference voltage is on the order of 10 V. Voltages of $\mathcal{O}(10\,\mathrm{V})$ can be measured directly with a voltmeter without a high-voltage divider inbetween. Therefore, a 6.5-digit measurement offers a more than sufficent precision (mV resolution is sufficient) and allowing a fast and precise measurement with a sample rate of 3 Hz. The reference potential is monitored with the K35, scaling the reference potential down by a factor of about 2000 and measuring it with 8.5-digit precision at a readout rate of 1/4 Hz. In the analysis, the vessel potential is then estimated by adding the difference voltage to an interpolated value of the reference potential.

The power supply used for this setup is from the manufacturer FuG and of type HCP 70M-35000. Its stability is verified to be 2 ppm over 8 h [Res19].

The voltmeter used for this measurement is from the manufacturer Fluke and of type 8846A.

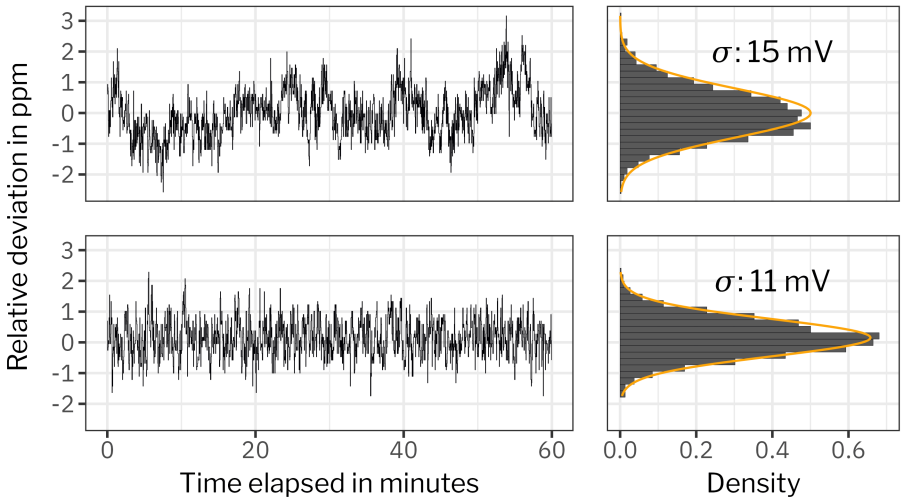

Figure 4.15 **Stability measurements.** Measurements of the voltage at the 2000:1 output of the high-voltage divider K35 over 1 h at a retarding potential of −18.6 kV. The top row shows the performance without the DC drift correction, the bottom row shows the performance with the DC precision loop active.

The figure is adapted from [Rod+22], licensed under CC BY 4.0.

The measurement was chosen from the measurements perfomed in Apr. 2017, by O. Rest et al., more details here.

One exemplary measurement over 20 minutes is shown in fig. 4.16. During the measurement, the DC drift correction was not used. The relative deviation over time is similar to the one measured with the standard measurement setup (top row in fig. 4.15); the voltage is changing randomly within ±3 ppm.

4.3.4 *Evaluation over the full frequency range*

As presented above, with all three methods: high-voltage divider, fast-measurement system and ripple probe, the stability of the retarding potential was investigated at a fixed value of −18.6 kV. To evaluate the stability on different time scales even further, the Allan variance method [All66] is used.

The Allan variance provides a tool to estimate the stability of a sensor due to noise sources on all time scales, limited by the measurement frequency and the sample size. It is calculated as:

$$\sigma_y^2(\tau) = \frac{1}{2} E(\bar{y}_{n+1} - \bar{y}_n)^2 \,. \tag{4.18}$$

The data $y(t)$ is divided into n parts with n being a multiple of the measurement frequency and τ is the duration of each part. The mean value and its deviation to the subsequent mean value is calculated for all parts. For each τ, the expectation value E of the deviations is determined. Calculating the square root of the Allan variance gives the Allan deviation. For all three measurement methods, the Allan deviation is determined and plotted in fig. 4.17.

The Allan deviation, evaluated for the ripple probe measurement, has a slight drop in amplitude for $\tau > 2$ s, showing the high-pass character of the ripple probe. For smaller τ, the Allan deviation a similar

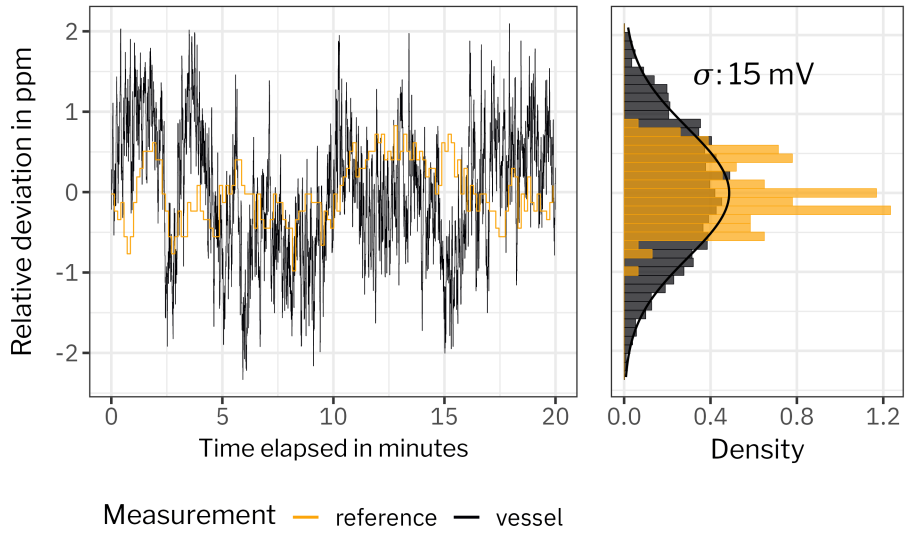

Figure 4.16 **Stability measurement with the fast-measurement system.** The relative deviation of the reference potential as measured by the high-voltage divider K35 is plotted in orange. The relative deviation of the vessel potential (at −18.6 kV) is plotted in black. The vessel potential is the sum of reference potential and difference voltage.

The figure is adapted from [Rod+22], licensed under CC BY 4.0.

shape compared to the values obtained via the fast-measurement system, but overall smaller amplitudes.

The distinct offset in amplitudes between both measurements can be explained by the slightly different setup. The fast-measurement system data was taken in 2017, this means before the last improvements at the post-regulation. The improvements included an exchange of the filament heating transformer of the shunt triode to make the system work at −35 kV, before it was only possible to use it down to −20 kV [Kat18b]. Since no ripple probe traces are available from the measurements with the fast-measurement setup, no further comparison is possible at this point.

Comparing the measurement with the fast-measurement system and the ripple probe measurement further, one can see that the sensitivity of the fast-measurement system starts where the ripple probe's sensitivity fades. It is important to note that the instability increases for longer time scales, so the part measured by the ripple probe but not seen by the fast-measurement system is more stable. This is again true for frequencies not measured by the high-voltage divider K35; here the fast-measurement system shows an overall higher stability. The fast instabilities measured by the fast-measurement system are far below KATRIN's stability requirement. Therefore, it is very well justified to have only the K35 measurement in place for continuous monitoring of the high voltage during neutrino mass measurements.

The deviation on averaging times > 10 s with the fast measurement system is slightly higher than for the measurement with the K35 only. At the time of the measurements with the fast measurement system,

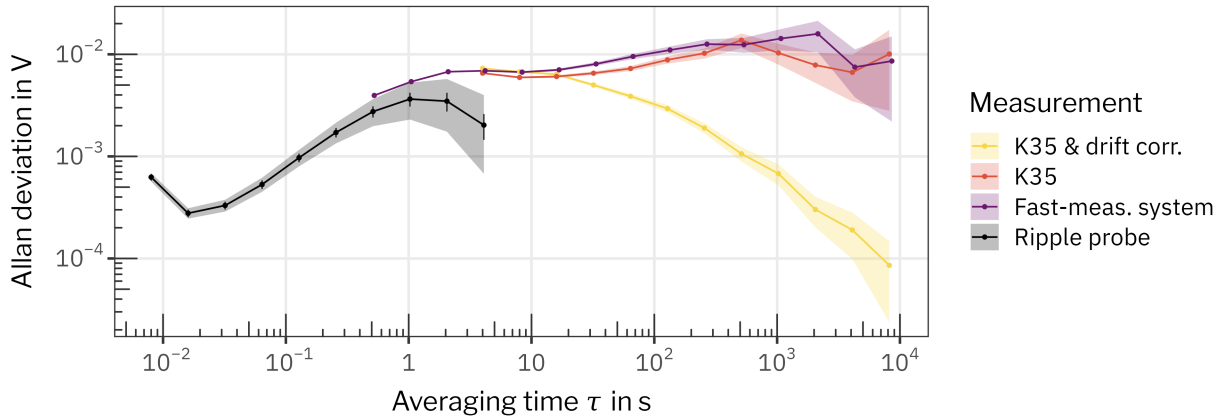

Figure 4.17 **Allan deviation.** At a retarding potential of –18.6 kV, the Allan deviation was determined for different measurement types. The DC drift correction of the post-regulation system was active for the data shown in yellow and inactive for the remaining cases. The readout rate is 1/2 Hz for the K35 voltmeter and 3 Hz for the fast-measurement system. For all three, the sample interval spans 11 h. For the ripple probe, the average Allan deviation over 1004 traces is plotted. Each trace is taken at a sample rate of 250 Hz over 33 s (the ripple probe is not limited to 250 Hz, cf. section 4.2.1).

The figure is adapted from [Rod+22], licensed under CC BY 4.0.

the auxiliary divider of the post-regulation was without any temperature stabilization inside the main spectrometer hall. This was improved at a later point and is in place for the K35 only measurements.

The measurements with the fast-measurement system and with the high-voltage divider K35 were both performed without the DC drift correction. The yellow curve in fig. 4.17 shows the performance with the DC drift correction. The DC drift correction removes the drifts on longer time scales (> minutes), as already visible in fig. 4.15.

4.4 Performance during neutrino mass measurements

The previous section has shown the stability of the high-voltage system over a wide range of time scales for a fixed retarding potential. During neutrino mass measurements, the retarding potential needs to be changed according to the measurement time distribution (MTD) An optimized MTD ensures that the measurement time is spent efficiently to determine the neutrino mass [Kle+19]. Throughout this section, one measurement of the tritium beta-decay spectrum where the voltage is changed according to the MTD is called a *run*. Each period of a run where the voltage stays unchanged is called a *sub-run*.

The performance reports for the measurement phases can be found here, here, and here.

For each measurement campaign a detailed investigation of the high-voltage system's performance has been conducted. For the first KATRIN neutrino mass measurement campaign (KNM1), the DC drift

correction was not yet implemented but was used for all later campaigns. Without the DC drift correction, the stability during a sub-run depends on its length [see figure 4 Kat21a], as expected from fig. 4.17. With the DC drift correction, this dependency vanishes.

Since the retarding potential is continuously monitored, it is always possible to map the rate measured at the detector to its corresponding retarding potential. However, all runs from one campaign, or from one period of the same conditions, need to be combined to perform the neutrino mass analysis and each retarding potential is an additional data point and with it an additional degree of freedom in the fit. Therefore, it is not only important to measure and stabilize the retarding potential, but it also needs to be set as precisely as possible. As described in section 4.2.2, the high-voltage control is optimized to ensure that the requested high-voltage setpoint is reached within ±20 mV.

In the case of KNM1, the setpoint reproducibility could be described by a Gaussian distribution with a standard deviation of 34(1) mV [cf. Kat21a]. The 34 mV correspond to the resolution of the post-regulation setpoint DAC (20 bit). The DC drift correction improves this and for later measurement camapaigns the setpoint can be reached with the same precision as its measurement by the high-voltage divider (K35/K65).

Since the campaigns KNM2-5 have a very similar performance, only the KNM5 campaign is shown here as an example. Detailed discussions for each campaign can be found in the sources listed above.

4.4.1 *Stability*

For the stability evaluation of the retarding potential during neutrino mass scans, it is convenient to calculate the standard deviation of the high voltage values U_i during each sub-run, with $i = 1, ..N$, and N the maximum numbers of voltages values during one sub-run:

$$\sigma = \sqrt{\frac{1}{N}\sum_i \left(U_i - \frac{1}{N}\sum_i U_i\right)^2}\,. \tag{4.19}$$

This value is already available in the *run summaries*.

For each neutrino mass run, the detector rates and selected sensor data, including the retarding potential, are combined in one file to unify the neutrino mass analysis. [Kat21c]

σ is independent of the retarding potential value, as visible in fig. 4.18, but it depends on the sub-run length. The average standard deviation is 11.5 mV with a spread of values within 23 mV. Shorter sub-runs have a wider spread compared to longer sub-runs (e.g. the spread is 7 mV for sub-runs longer than 5 minutes). At first glance this seems unintuitive and it is the direct opposite to the behavior during KNM1 without the DC drift correction. However, this comes from the optimization of waiting time after reaching a new voltage setpoint. As soon as the setpoint is reached within 20 mV, the sub-run is started and the DC drift correction forces the retarding potential slowly closer to the desired setpoint. For short sub-runs the linear drift of the voltage has a larger effect on the standard deviation during a sub-run than for longer sub-runs. Since it is still below 20 mV, it is not producing a significant bias on the neutrino mass and the waiting time can be saved.

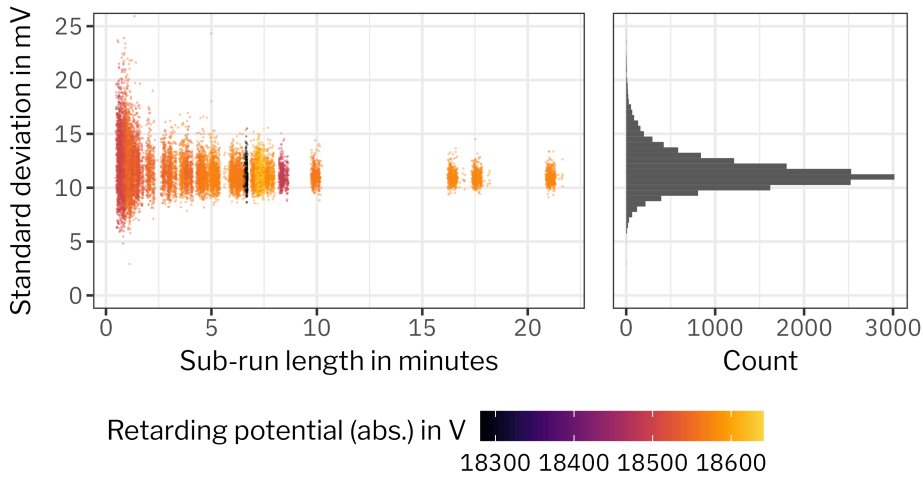

Figure 4.18 **Standard deviation for KNM5 sub-runs.** The standard deviation for each sub-run σ (4.19) is plotted against the length of the sub-run. The color corresponds to a setpoint for each sub-run. The sub-run length fluctuations are due to the dynamic adjustment of the sub-run boundaries which is intended to minimize the settling time (cf. section 4.2.2).

4.4.2 *Reproducibility*

The deviation of the mean voltage value from one single sub-run to the mean voltage value over all sub-runs of the same setpoint is called setpoint deviation here. For the combination of runs, a high reproducibility – a small setpoint deviation – is needed. Analogous to the standard deviation, the setpoint deviation is also independent of the retarding potential but depending on the sub-run length (see fig. A.22 in the appendix).

The current voltmeter calibration procedure is described in my master's thesis.

The reproducibility is influenced by the stability of the voltmeter. The voltmeter is calibrated regularly (2 times per week) and the voltage values used for the analysis are corrected by it, but calibration values are not included in the dynamic setpoint control logic. Resulting in a overlap of multiple Gaussian-like distributions for the setpoint deviation. For KNM5, two dominant distributions are visible.

The maximal spread of setpoint deviations is 69 mV. By excluding sub-runs shorter than 5 minutes, this is reduced to 19 mV. The standard deviation of the setpoint deviation is 6 mV.

4.4.3 *Settling time*

The time between sub-runs is evaluated to estimate the performance of the dynamic setpoint control logic. This duration is dominated by the change of the high voltage, other waiting times are negligible ($\mathcal{O}(1\,\mathrm{s})$) in comparison. It takes on average 23 s with a standard deviation of 12 s to change the high voltage. The settling time is independent of the voltage setpoint. An overview of the settling times for KNM5 sub-runs is shown in fig. A.23 in the appendix.

In fig. A.23 is a sharp maximum in the distribution at 7 s. For these

sub-runs, the logic started with the correct value for $M(U_0)$ (cf. section 4.2.2) and no iterative correction steps were needed. If the system changed (e.g. due to temperature changes) and $M(U_0)$ from the look-up table needs to be updated, the desired setpoint is not immediately reached and needs to be iteratively adjusted, leading to a distribution of different settling times.

4.5 Calibration of the high-voltage divider K35

The high-voltage dividers K35 [TMW09] and K65 [Bau+13] need to fulfill two essential requirements for successful neutrino mass measurements. Their scale factor needs to be stable over one measurement campaign, and constant over the voltage measurement interval ($\mathcal{O}(500\,\mathrm{V})$ at about −18 kV), both within 3 ppm. A third, more optional requirement, is to know the absolute scale factor value which gives access to high-accuracy electron spectroscopy. In chapter 5, a novel method is shown which removes the necessity for an absolute scale but where it is essential to know the linearity of the divider.

As shown in previous works [e.g. Thü07; Bau14; Res19], many different calibration techniques exist to prove that the dividers fulfill the requirements. Two of these methods, namely the *low-voltage calibration* [Bau14] and the *absolute calibration* [Res+19], have been established in the KATRIN main spectrometer building to enable in-situ calibration of both dividers during measurement breaks.

In this chapter, the recent low-voltage calibration results of the K35 are shown. Afterwards, the results from high-voltage calibrations, including the absolute calibration, for the first time applied to the K35, are presented. The chapter is focused on the K35 and the scale factor M_{1972} of its "1972:1" output, the one used during neutrino mass scans.

4.5.1 *Low-voltage calibration*

The reference divider is from the manufacturer Fluke and of type 752A

For the low-voltage calibration a self-calibrating divider is used as a reference. The reference divider can be used for voltages up to 1 kV and has two division ranges: 10:1 and 100:1. The divider is self-calibrated before each usage. The self-calibration procedure is based on the Wheatstone bridge. A stable voltage source of about 20 V (e.g. two 9-V batteries) is applied to the divider which is set to its *calibration mode* and a nullification is performed.

More details on the procedure can be found in the instruction manual provided by Fluke. Fluke specifies an accuracy of 0.5 ppm for the 100:1 output after calibration.

For the low-voltage calibration, a voltage is applied to both dividers, the one under test and the reference divider. At each divider, the output voltage is measured with a voltmeter. The scale factor for the divider under test M_{test} is then determined via

$$M_{\mathrm{test}} = M_{\mathrm{ref}} \frac{U_{\mathrm{ref}}}{U_{\mathrm{test}}} \,. \tag{4.20}$$

$M_{\mathrm{ref}} = 100$ is the scale factor of the reference divider and $U_{\mathrm{ref}}, U_{\mathrm{test}}$ are the voltages measured at the reference divider and the one under test respectively.

The voltmeters are calibrated beforehand with a stable voltage, for

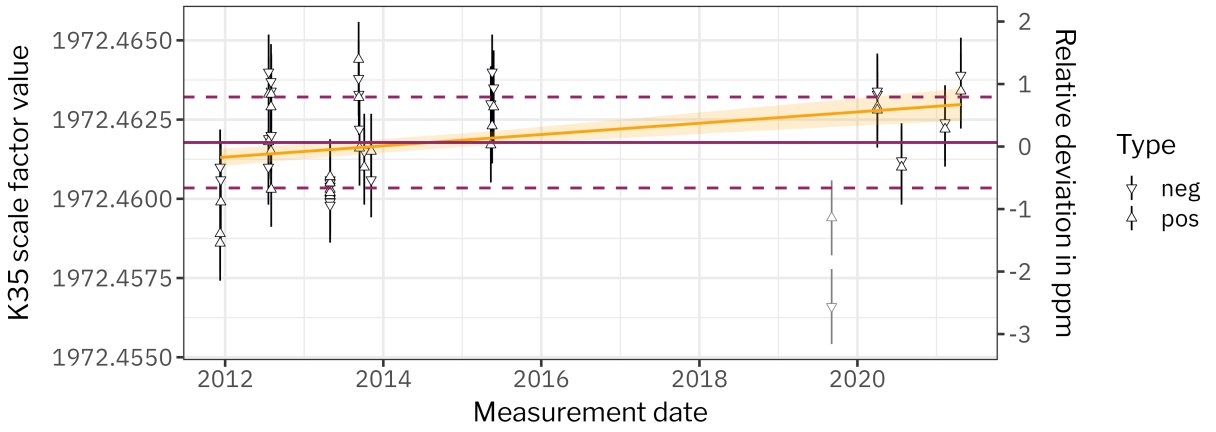

Figure 4.19 **Low-voltage calibration history of the high-voltage divider K35.** The timeline shows all available low-voltage calibration values of the 1972:1 output of the K35. The values dated earlier than 2019 are taken from [Bau14; Res19]. The different shapes indicate positive or negative test voltages. The two values colored in gray are excluded from further analysis. The purple line is the weighted mean with the dashed lines indicating the weighted standard deviation. The orange line is a linear fit to the data with a 1-σ uncertainty band.

example using a 10-V reference source. Since it is a relative measurement between both dividers, any stable voltage of about 10 V applied to both voltmeters simultaneously is sufficient; its absolute value does not need to be known.

A circuit diagram of the K35 is shown in fig. 2.6.

The calibration of the K35's 1972:1 output is performed in two steps. First the "100:1" output is calibrated against the reference divider. Afterwards, a voltage is applied at the 100:1 output and measured at the 1972:1 output (hereafter in this configuration referred to as "20:1" output) and calibratated against the reference divider. Combining the results of both gives M_{1972}.

For an additional check of systematic effects, the calibration is performed with both positive and negative test voltages. As shown in fig. 4.19, one measurement result shows a strong deviation between the scale factor resulting from a negative and from a positive test voltage. The mean value of both is an outlier compared to other calibration measurements. The value is kept to have a full history but is excluded from further analysis, since it is very probably caused by a faulty setup.

To describe the overall trend of the 1972:1 output, the measurement points were fitted by a linear function (cf. fig. 4.19). A linear function does not fit perfectly ($\chi_{\text{red}} = 1.3$) but better than a higher-degree polynomial. With a linear fit (increased errors for the values by $\sqrt{1.3}$ to artificially achieve $\chi_{\text{red}} = 1$) the drift is estimated as 0.09(4) ppm per year. The overall spread over the 10 years of measurement values is estimated by a weighted standard deviation to 0.7 ppm. The observed scale factor change over the years is well below the KATRIN requirement (3 ppm over 10 weeks) and almost not traceable within the uncertainty of the low-voltage calibration method.

The low-voltage calibration is a useful low-effort method to monitor the long-term behavior of a divider and to spot problems (cf. appendix A.2). However, it is not suitable to determine the scale factor of a divider under load (loads above 1 kV). Under load, the resistors heat up and their characteristics change. For the K35 and K65 divider this effect was minimized by a careful selection of paired resistors [cf. TMW09; Bau+13] but in order to have an absolute ppm-level calibration of the divider a calibration under load, a *high-voltage calibration*, is indispensable.

4.5.2 *High-voltage calibration*

The low-voltage calibration of the 20:1 output can be extended to a calibration under load. The desired load U_{load} is applied at the divider's main input and the voltage drop at the 100:1 output is adjusted with the calibrator. The voltage applied with the calibrator U_{cal} at the 100:1 output is measured with the reference divider, as done for the normal low-voltage calibration. U_{cal} is set coarsely (about 1×10^{-4} precision) to

$$U_{\text{cal}} = \frac{U_{\text{load}}}{M_{100}} \,. \tag{4.21}$$

The scale factor of the 100:1 output M_{100} is picked from the low-voltage calibration result.

Results of such a high-voltage calibration are shown in fig. 4.20. The measurements were repeated two times, for each one of them the reference divider was calibrated. One can see a difference between both measurement sets within the 0.5 ppm uncertainty for the reference divider. No dependency on the different loads (within 5 kV and 33 kV) is observed. In other words, the thermal load on the resistors above the 100:1 does not influence the resistors at the low-voltage 1972:1 output.

The calibration of the 100:1 output under load (up to 33 kV) with only a 1 kV reference divider is more difficult. In principle, with an open divider and access to all resistors, one could repeat the procedure as described for the 20:1 output above for each of the resistors above the 100:1 output. In the case of the K35 the procedure would need to be repeated at each of the 100 resistors (each with 1.84 MΩ cf. [TMW09]) or in case of the K65 at 165 resistors (each 880 kΩ cf. [Bau+13]). An enduring endeavor and not without risks due to the open divider.

A much more elegant and much more convenient method to calibrate the 100:1 output is the *absolute calibration method*. The method is introduced in [Res+19] and the results of applying the method to the K65 divider are presented. The setup described in this work was transferred to the KATRIN main spectrometer building, repeated for the K65 divider and performed for the first time for the K35 divider. After an introduction of the method along the description in [Res+19], the results for the K35 divider are presented here.

The absolute calibration method circumvents the need for a second high-precision reference divider by employing a differential measurement. An auxiliary divider with a scale factor similar to the one that is to be calibrated and with a proven short-term (about 10 minutes) stability is needed. The auxiliary divider's scale factor needs to be

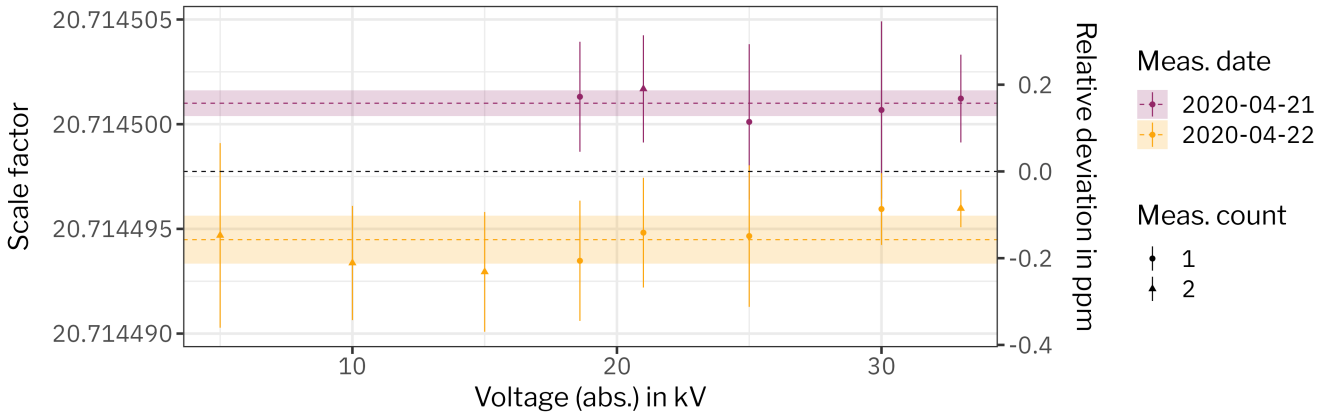

Figure 4.20 **Scale factor values for 20:1 at different loads.** As load, a negative voltage was applied to the divider. The measurement length for each point is on the order of 10 minutes. For some voltage points, two measurements have been performed. The colored dashed lines are the mean values of each respective set of measurements, and the shaded areas mark the standard deviation. $M_{20} = 20.714\,498(7)$ is determined from the mean value of both sets (black dashed line) and their difference is used as uncertainty.

known with a relative uncertainty of 1×10^{-4}.

The differential measurement is performed in two steps. In the first step, the ratio of the auxiliary divider's scale factor M_{aux} and the scale factor of the divider under test M_{test} is determined. For this, both dividers are set on a high voltage U_{load}. Depending on the size of U_{load}, the voltages at the 100:1 output of both dividers can be well above the 20-V range of the precision voltmeters. To stay within the 20-V range where the voltmeter can be calibrated with a 10-V reference source, a compensating voltage U_{comp} is applied between both voltmeters. The compensating voltage is supplied by a calibrator to have it as stable as possible. The measured ratio of both dividers is

A calibrator from the manufacturer Fluke and of type 5720A is used.

$$\mu = \frac{M_{\text{aux}}}{M_{\text{test}}} = \frac{U_{\text{test}} + U_{\text{comp}}}{U_{\text{aux}} + U_{\text{comp}}}\,. \tag{4.22}$$

By choosing the compensating voltage such that $U_{\text{aux}} \approx 0$, it follows

$$\mu \approx 1 + \frac{U_{\text{test}}}{U_{\text{comp}}}\,. \tag{4.23}$$

If both dividers have a similar 100:1 output, the absolute value of U_{comp} is of lesser importance since $U_{\text{test}} \ll U_{\text{comp}}$ and μ is approximately 1.

In the second step, an additional voltage U_{ref} is applied to the divider under test. Everything else is kept the same as during step one. With this, the change of M_{test} due to U_{ref}, more precisely the differential scale factor $M'_{\text{test}}(U_{\text{test}})$, is measured. Using μ determined in the first step, $M'_{\text{test}}(U_{\text{test}}))$ is defined as:

$$M'_{\text{test}}(U_{\text{test}}) = \frac{U_{\text{aux}} \cdot M_{\text{aux}} + U_{\text{ref}} \cdot M_{\text{ref}}}{U_{\text{test}} + (1-\mu)U_{\text{comp}}}\,. \tag{4.24}$$

In an ideal world, U_{ref} would be as small as possible to have the smallest amount of averaging in the differential. For the measurements, 1 kV is chosen for U_{ref}, resulting in a reasonable step size (not too many measurements to cover the dividers voltage range of up to 35 kV) and, more importantly, the 1 kV can be measured with the reference divider, providing the self-calibrated 100:1 output. The output voltage of about 10 V is measured with a voltmeter that is calibrated against a 10-V reference, tracing the calibration back to the Josephson standard.

The 10-V references are calibrated annually against a Josephson voltage standard (based on the Josephson effect), e.g. at the Physikalisch-Technische Bundesanstalt Braunschweig [Kat21c].

As visible in (4.24), as long as U_{aux} is small ($\mathcal{O}(1 \times 10^{-4})$), which is directly connected to μ (4.22) being close to 1, the influence of M_{aux} and U_{comp} on the resulting M'_{test} is small. The setup as used for [Res+19] had an auxiliary divider with a 100:1 output, perfectly matched to the G35 and K65 dividers that were calibrated with this setup. The "100:1" output of the K35 is 95:1 and therefore only close to 100:1.

To still use the same setup for the absolute calibration of the K35, two possible options were developed. For the first one, called here *method A*, an additional voltage is added between U_{comp} and the divider under test. A 10-V reference source was used. Due to the additional 10 V, U_{comp} can be chosen such that U_{aux} is $\mathcal{O}(1 \times 10^{-4})$.

As a second option, *method B*, the auxiliary divider was changed to have a 94:1 output. The auxiliary divider is a divider consisting of a series of Caddock resistors (thirty 20 MΩ resistors and six 1 MΩ resistors), resulting in a scale factor of $M_{\text{aux}} = 100$ [Res19]. After the first pair of 20 MΩ resistors, a cable is added to replace the normal feeder at the top of the resistor chain. With this modification, the scale factor is changed to $M_{\text{aux}} = 94$ and can be easily changed back to $M_{\text{aux}} = 100$ if needed.

Details on the hardware changes in Apr. 2020 are further documented in the electronic logbook.

The measurement results with methods A and B are plotted in fig. A.24 in the appendix. No significant difference between the two methods is visible. The scatter of multiple results within one method is larger than the difference between each method.

Important to note, the scatter of the individual measurements grows larger, with larger U_{test}. This is very probable due to the load dependency of the auxiliary divider. To compensate for possible drifts during the measurement, the μ measurement (the first step) is performed before and after step two and the average of both is used to determine M'_{test}. The whole sequence takes about 9 minutes.

Potential improvements for future measurements are: even shorter measurement intervals, a simple temperature stabilization of the divider, or much longer stabilization periods beforehand (here 1.5 h run-in time was spent for the 33 kV measurement) to allow the divider to heat up to equilibrium. The situation is worsened compared to the calibration with the K65 since the amount of resistors sharing the load is reduced by about 7 % for the adapted scale factor (method B).

Since the effect only starts at higher loads (about 20 kV), it might already be enough to cool the resistors with a stream of gas.

All measurements are combined by calculating the average over all measurements performed on one day and in one setup. The resulting averages are plotted in fig. 4.21 and fitted by [Res+19]:

$$\begin{aligned} f(U_{\text{test}}) &= M_{\text{test}}(U_{\text{test}})\Big|_{\text{lv}} + M'_{\text{test}}(U'_{\text{test}})\Big|_{\text{abs.cal.}} \\ &= \frac{1}{a' + b' U_{\text{test}}}\Big|_{\text{lv}} + \frac{1}{a' + 2b' U'_{\text{test}}}\Big|_{\text{abs.cal.}} . \end{aligned} \tag{4.25}$$

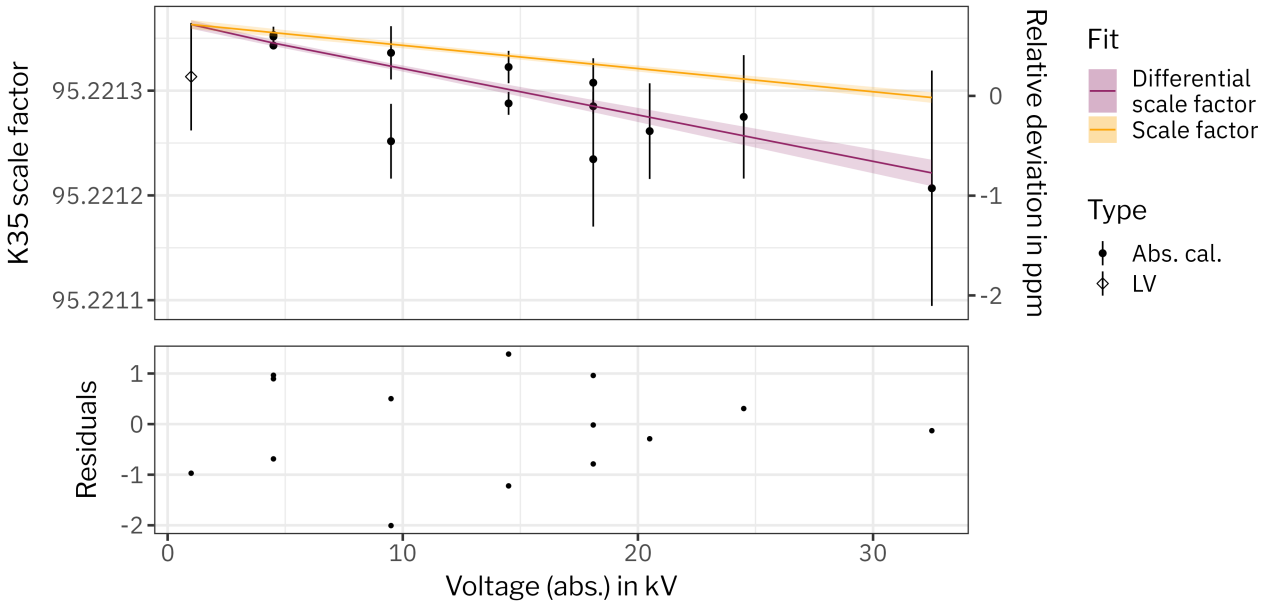

Figure 4.21 **Determination of the K35's voltage-dependent scale factor.** The differential scale factor M'_{test} (filled dots) and the low-voltage scale factor M_{test} (open diamond) is plotted against the voltage applied to the K35 (U'_{test} for M'_{test} and U_{test} for M_{test}). The data is fitted with $f(U_{\text{test}})$ (4.25) and the result for the differential scale factor $M'_{\text{test}}(U'_{\text{test}})$ is plotted in purple and for the scale factor $M_{\text{test}}(U_{\text{test}})$ in orange. The shaded area in orange and purple are the 1-σ error band of the fit. The fit results are $a' = 1.050\,184\,48(5) \times 10^{-2}$ $(1/a' = 95.221\,365\,3(5))$ and $b' = 2.4(2) \times 10^{-13}/\text{V}$ with $\chi_{\text{red}} = 1.048$.

The points from the low-voltage measurement are fitted by $M_{\text{test}}(U_{\text{test}})$ and the differential scale factor values from the absolute calibration are fitted by $M'_{\text{test}}(U'_{\text{test}})$. U'_{test} is the average U_{test} of the μ-measurement and the measurement with additional load (here 1 kV). Due to the K35's small voltage dependency (within 2 ppm over 33 kV), it is sufficient to use a polynomial of first degree to describe the temperature dependency of the resistors, analogously to the K65.

By multiplying the M_{20} result (constant, cf. fig. 4.20) and the result M_{95} from the absolute calibration method, the voltage-dependent M_{1972} is determined. Explicitly,

$$\begin{aligned} M_{1972}(U) = M_{95} \cdot M_{20} &= \frac{M_{20}}{a' + b' \cdot U} \\ &= \frac{1}{\frac{a'}{M_{20}} + \frac{b'}{M_{20}}} = \frac{1}{a + b \cdot U}\,. \end{aligned} \tag{4.26}$$

With the values for a', b' from the absolute calibration (cf. fig. 4.21) and M_{20} (cf. fig. 4.20) follows

$$a = 5.069\,804(2) \times 10^{-4}\,, \tag{4.27}$$

$$b = 1.2(1) \times 10^{-14}/\text{V}\,. \tag{4.28}$$

The M_{1972} result is plotted in fig. A.25 in the appendix. Evaluating (4.26) at $U = 18.6\,\mathrm{kV}$ and assuming the same systematic uncertainties as done in [Res+19] results in a scale factor value of

$$M(18.6\,\mathrm{kV}) = 1972.462(2)\,. \tag{4.29}$$

4.5.3 *Comparison with other calibration methods*

The result achieved with the calibrations described above can be compared to other calibrations performed with the K35. For example, it is possible to compare the results with the calibration of the 1972:1 scale factor at different loads at the PTB [TMW09]. As visible in fig. A.25 in the appendix, the measured voltage dependency of both methods is in agreement within the individual uncertainties.

For further comparisons, the focus is now at the most important load (around 18 kV) for neutrino mass measurements. All available results of the K35 at 18 kV are gathered and plotted in fig. 4.22. The results obtained with a high precision divider at the PTB as reference divider show, with exception for the outlier in 2006, an overall downwards drift. It is not clear what caused the drift (and the jump in 2006). In principle, the transport to the PTB could put mechanical strain on the resistor chain, leading to small changes visible in the calibration.

The result obtained with $^{83\mathrm{m}}$Kr has a significantly larger uncertainty but agrees within the uncertainty with the trend visible in the PTB results. The new value obtained by the absolute calibration fits within the uncertainties to the $^{83\mathrm{m}}$Kr result, but it does not fit to the downward trend. It fits very well to the very first measurement point and to the average over all measurements.

The low-voltage calibrations that started in 2012 have a drift in opposite direction and a smaller amplitude than the drift visible in the PTB results. The direction of the drift fits to the difference between the last PTB result and the value of the absolute calibration, but the amplitude (about 4.5 ppm) does not match. From a linear fit to the low-voltage results, a difference of about 0.6 ppm over the 7 years is expected which is a factor 6.5 smaller than the observed difference in the high-voltage results.

To further check the new absolute calibration result, the K65 was used to calibrate the K35. The procedure is called *cross calibration*. Two K65 scale factor values with a difference of 2.6 ppm were chosen for the analysis, one determined in May 2019, at the "original" absolute calibration setup in Münster, and one in October 2019, with the setup freshly installed in Karlsruhe. Inbetween both measurements the K65 was moved from Münster to Karlsruhe with an intermediate stop in Darmstadt. The new K35 absolute calibration value lies within the two values determined from the two different assumed K65 scale factors. Important to note, the two individual cross calibration measurements (one in September 2019, one in April 2020), are almost identical; both dividers stayed constant, or drifted the exact same amount in opposite direction.

More cross calibration measurements were performed, but are omitted in this overview plot due to the problems of the K65 stability after temperature gradients which has been discovered in 2021 (further de-

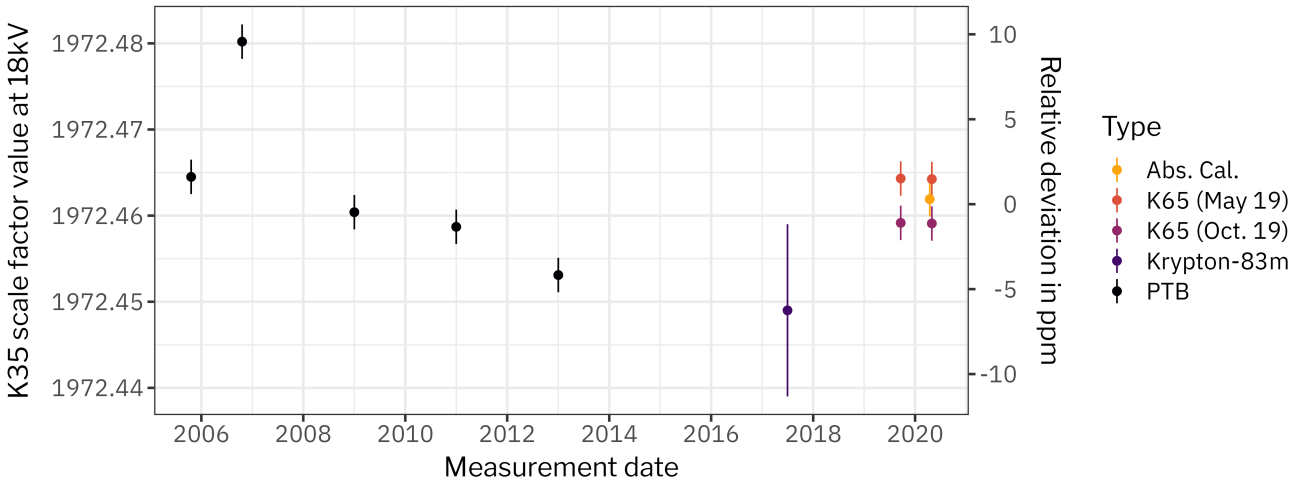

Figure 4.22 **High-voltage calibration history of the K35.** The timeline shows all available high-voltage calibration values of the K35's 1972:1 output. The values dated 2013 and earlier are taken from [Thü07; Bau14; Res19]. The ^{83m}Kr value in 2017 is taken from [Kat18a]. The values of type "K65" are calibrations of K35 using the K65 as a reference (with two different scale factor measurements: one measured in May 2019 and the other in October 2019).

tails in appendix A.2). During those cross calibration measurements, the K65 was the divider under test and the K35 was used as reference.

In order to investigate the influence of mechanical strain further, more in-situ calibration measurements are needed. In addition to repeating the absolute calibration method in the future, it should also be considered to use ^{83m}Kr measurements. Especially as soon as the novel method (presented in chapter 5) is applied and the transition energies are improved by an order of magnitude.

The calibration with ^{83m}Kr, also plotted in fig. 4.19, was performed by comparing two conversion lines from the same transition (K-32 and L_3-32) to avoid the large uncertainty (500 meV) on the transition energies. The uncertainty of this measurement is dominated by the binding energies. With the potential improvement on the transition energies, lines from the same sub-shell but different transitions (e.g.: L_3-32 and L_3-9.4) can be chosen. Also potential voltage dependency cross-checks by a combination of various different lines are possible.

In summary, future ^{83m}Kr calibration measurements can help to understand the observed differences within the different calibration methods.

4.6 Conclusion

Any instability of the retarding potential influences the transmission conditions for electrons inside KATRIN's main spectrometer. The effect on the neutrino mass can be estimated with a simple model of a

Gaussian broadening. A more detailed investigation was performed by employing simulations.

In the simulations, the electrons were tracked on their way through the spectrometer, allowing the injection of arbitrary time-dependent instabilities into the retarding potential. The biggest effect can be observed with fluctuations which occur during the time period in which the electrons pass through the spectrometer entrance, which is the location where the potential gradient is largest. One important result of the simulations is that the influence of a sinusoidal ripple for frequencies up to 10 MHz corresponds to a broadening of the transmission function equal to the density distribution of the sinusoidal. For frequencies above 10 MHz, the broadening decreases.

To minimize any broadening of the transmission function, especially from the 50 Hz power grid interference but also from power supply drifts or other interference sources, the post-regulation system is in place. The post-regulation system was integrated into the KATRIN control system for use in normal operation, for example during tritium electron spectroscopy or ^{83m}Kr conversion electron spectroscopy.

The DC drift correction path of the post-regulation system was added as an optional component. It improves the stability on longer time scales (> minutes) significantly. With active DC drift correction at voltages around 18.6 kV, the values vary within a Gaussian distribution with a standard deviation of 11 mV which corresponds to a stability on the sub-ppm level. The performance of the full post-regulation system was proven with independent methods, including ^{83m}Kr conversion electron measurements.

The sub-ppm precision stabilization is complemented with calibrations of the high-voltage dividers, providing ppm-scale trueness of the measurement chain. The absolute calibration method was assembled on site in the spectrometer building and adapted in such a way that it can also be applied to the K35 divider. With it, the K35's scale factor was determined with 1 ppm accuracy, and its voltage dependency was determined to be within 1 ppm across a 33-kV-wide range. In addition to the absolute calibration, low-voltage calibrations were performed and compared to previous measurements. The K35's low-voltage calibration history shows a weighted standard deviation of 0.7 ppm spanning over 10 years.

Overall, KATRIN's retarding potential has sub-ppm precision and ppm trueness on time scales from microseconds up to years. Such high accuracy is possible thanks to the unique combination of the post-regulation system and the precision high-voltage dividers with their dedicated calibrations.

„Na, Pippi, wieviel, glaubst du, daß 8 und 4 ist?“

„So ungefähr 67“, meinte Pippi.

„Aber nein“, sagte die Lehrerin, „8 und 4 ist 12.“

„Nein, meine kleine Alte, das geht zu weit“, sagte Pippi. „Eben erst hast du gesagt, 7 und 5 ist 12. Ordnung muß sein, selbst in einer Schule.“

Pippi Langstrumpf
Astrid Lindgren

5 Improving the energy scale calibration

The content in this chapter is based on the publication [Rod22], of which I am the sole author.

In the tritium spectrum fit of the neutrino mass analysis, the squared neutrino mass value and the effective endpoint are strongly correlated parameters (0.97 [Kat19]). Any unknown systematic leading to a shifted effective endpoint also biases the measured neutrino mass. For example, a Gaussian broadening of the energy scale of 60 meV would shift the measured squared neutrino mass value by $7 \times 10^{-3}\,\mathrm{eV}^2/c^4$, as introduced in chapter 4.

The steadiness of the fitted effective endpoint of the tritium spectrum is a good proxy for a stable energy scale (cf. [Kat21a]), but the absolute energy scale also needs to be known: As outlined in the work [OW08] and since implemented at KATRIN [Kat19], an important check for systematics is to translate the effective tritium endpoint value into the Q-value for comparison with independent measurements of the tritium–helium-3 mass difference [Str+14; Mye+15]. This cross-check is limited by the knowledge of the absolute energy scale. The method proposed here will significantly reduce the uncertainty in the absolute energy scale of KATRIN and thereby improve the ability to detect unknown systematics.

5.1 Energy scale calibration at KATRIN using $^{83\mathrm{m}}$Kr

For the absolute calibration of KATRIN's energy scale, monoenergetic conversion electrons from $^{83\mathrm{m}}$Kr are used as a reference.

$^{83\mathrm{m}}$Kr usually decays in a cascade of two transitions (32.2 keV, then 9.4 keV) to ^{83}Kr, or via the low-intensity 41.6-keV cross-over transition, as illustrated in fig. 5.1. These transitions can take place in the form of gamma emissions, or, more frequently, in the form of internal conversion electron emissions. The energy E released in each alternate

The 42-keV transition is highly suppressed and no precision spectroscopy of its conversion electrons has been performed yet. The electrons are however visible in the detector spectrum during routine $^{83\mathrm{m}}$Kr measurements at KATRIN. First mentioned by F. Fränkle and further presented by L. Thorne at a KATRIN collaboration meeting (Oct. 2017).

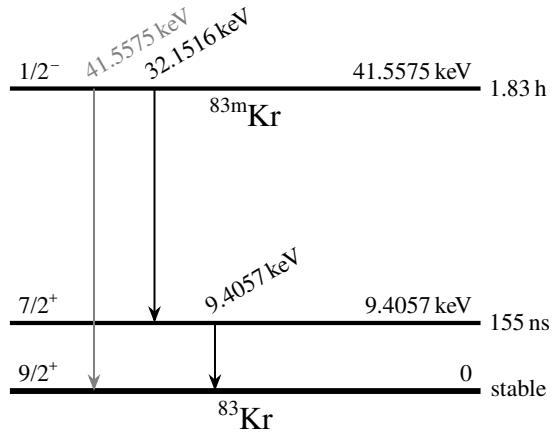

Figure 5.1 **Isomeric transitions of ^{83}Kr.** The values were taken from [Mcu15] and the low-intensity 41.6-keV cross-over transition was added. For each nuclear level, the spin-parity value, energy, and half-life are noted.

The figure is copied from [Rod22], licensed under CC BY 4.0.

process is

$$E = E_\gamma + E_{\gamma\,\mathrm{rec}} = E_\mathrm{ce} + E_\mathrm{bind} + E_\mathrm{rec}\,, \tag{5.1}$$

where E_γ denotes the energy of the emitted gamma ray, E_ce the kinetic energy of the conversion electron, and E_bind its binding energy. $E_{\gamma\,\mathrm{rec}}$ and E_rec are the recoil energies of the atom after emission of a gamma ray or a conversion electron, respectively. E is hereafter called simply the *transition energy*.

As follows from (5.1), the kinetic energy E_ce of a $^{83\mathrm{m}}$Kr conversion electron expressed in terms of the other energies is

$$\begin{aligned} E_\mathrm{ce} &= E_\gamma + E_{\gamma\,\mathrm{rec}} - E_\mathrm{bind} - E_\mathrm{rec} \\ &= \qquad\quad E - E_\mathrm{bind} - E_\mathrm{rec}\,. \end{aligned} \tag{5.2}$$

Values are available from literature for E_γ, $E_{\gamma\,\mathrm{rec}}$, E_bind, and E_rec (cf. [Vén+18]).

The $^{83\mathrm{m}}$Kr conversion electron energy E_ce can be measured at KATRIN. For this, a ^{83}Rb source emanating $^{83\mathrm{m}}$Kr (and ^{83}Kr) [Sen+18] is attached to the gas circulation sytem of the WGTS, transforming it into a gaseous krypton source (GKrS). Additionally, a condensed krypton source (CKrS) [Kat18b] is available, located between the transport and pumping section and the spectrometer section. The work [Kat20b] describes in detail how the position (i.e., energy) and width of the conversion electron line are determined by fitting the integrated spectrum. The line position in the measured spectrum deviates from the true value of E_ce by the shift $\Delta\Phi'$ of KATRIN's absolute energy scale at the time of the measurement.

5.1.1 *Shift of the energy scale*

There are many possible sources along the beamline that can impact the energy scale and contribute to the shift $\Delta\Phi'$. Most of them are

known very well, and methods exist to characterize them.

On the spectrometer side, the main spectrometer's work function Φ_{MS} and its retarding potential influence the energy scale. The work function can be measured with an electron gun [Beh16; Beh+17]. The retarding potential is kept stable within 2 ppm (2×10^{-6}) by the precision high-voltage setup [Rod+22]. The scale factor of the high-voltage dividers [TMW09; Bau+13] measuring the retarding potential U_{ret} is known from the absolute calibration [Res+19], with systematic uncertainties within 1 ppm. The retarding potential depression U_{dep} is known from simulations, with a possible systematic shift δU_{dep}.

The potential depression is the difference between the retarding voltage applied at the spectrometer vessel and the actual potential seen by the electrons inside the spectrometer.

On the source side, the energy scale is defined by the starting potential U_{start} of the electrons and their energy loss due to scattering inside the source. The work function of the WGTS, the work function of the rear wall and its bias voltage, and the plasma potential govern the starting potential. The stability and spatial distribution of the starting potential inside the WGTS are investigated with $^{83\mathrm{m}}$Kr measurements [Kat22]. The energy loss spectrum needs to be known precisely for measuring the continuous tritium spectrum and it is characterized with electron gun measurements [Kat21b]. For the monoenergetic conversion electron lines, the scattering process only reduces the intensity of the measured signal (the unscattered electrons), but does not change the measured line position.

The rear wall [Kat21c] is a gold coated disc at the far end of the WGTS which absorbs most of the tritium decay electrons which were not transmitted.

Considering all contributions and including U_{ret} and U_{dep} in the conversion electron spectrum fit leads to a measured line position of

$$\begin{aligned} E_{\mathrm{M}} = q \cdot (U_{\mathrm{ret}} - U_{\mathrm{dep}}) &= E_{\mathrm{ce}} + q \cdot \delta U_{\mathrm{dep}} + q \cdot U_{\mathrm{start}} + \Phi_{\mathrm{MS}} \\ &= E_{\mathrm{ce}} + \Delta\Phi' \,, \end{aligned} \tag{5.3}$$

where q is the charge of the electron and $\Delta\Phi'$ includes all unknowns $\delta U_{\mathrm{dep}}, \Phi_{\mathrm{MS}}$ and U_{start}. It should be noted that the particular sources of the individual shifts are not important for the conversion electron measurements. All of them combine into one effective shift of the measured line position relative to the actual value. An examplary conversion electron line measurement is shown in fig. 5.2.

Conversion electron spectra of the 32-keV transition are regularly measured at KATRIN and reveal the temporal variation of $\Delta\Phi'$. Additionally, by comparing the $^{83\mathrm{m}}$Kr line positions to the literature values, $\Delta\Phi'$ can be determined (cf. fig. 5.3) and with it KATRIN's absolute energy scale.

5.2 Novel method for determining the transition energies

When comparing the measured conversion electron lines to the literature, the dominant contributor of uncertainty is E_γ, which is known to 0.5 eV. KATRIN, meanwhile, has been shown to be able to perform electron spectroscopy with a precision of 0.025 eV [Kat20b], and future performance improvements are plausible. Despite its high resolution and the excellent linearity of its energy scale [Kat20b; Res+19], KATRIN's accuracy is limited by the uncertainty in $\Delta\Phi'$. The method

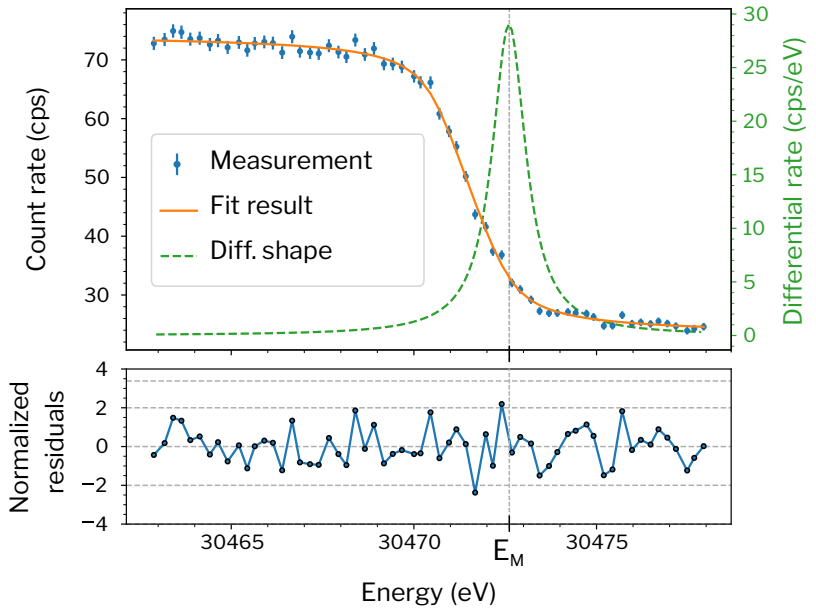

Figure 5.2 **Conversion electron line measurement at KATRIN.** The measurement points are the integral spectrum of a conversion electron line (L_3-32) measured at one detector pixel. The retarding potential depression U_{dep} is added to the retarding energy (x-axis). The energy distribution of the conversion electrons is described by a Lorentzian, folded with a Gaussian to account for Doppler broadening at a WGTS temperature of 100 K, resulting in a Voigt profile. The Voigt profile is folded with the transmission function (cf. section 2.1.4) and fitted to the data (orange line).

The plot is adapted from [Kat20b], licensed under CC BY 4.0.

presented here first removes this limitation so that the transition energies can then be determined with high accuracy.

5.2.1 *Leveraging the cross-over transition*

It is possible to determine $\Delta\Phi'$ *independently* of any transition energy literature value by measuring conversion electron lines from a set of three interconnected transitions: the 32-keV and 9-keV cascade transitions, as well as the corresponding 42-keV cross-over transition which can occur in their stead.

The transition energies $E(g)$ of each of the three transitions $g \in \{\tau_{32}, \tau_9, \tau_{42}\}$ relate to each other as

$$E(\tau_{42}) = E(\tau_{32}) + E(\tau_9)\,. \tag{5.4}$$

Generalizing and simplifying (5.2) and (5.3) leads to a measured line position

$$E_{\text{M}}(g, s) = E(g) - E_{\text{bind}}(s) - E_{\text{rec}}(g) + \Delta\Phi'\,, \tag{5.5}$$

with $s \in \{\text{K}, \text{L}_3, \text{N}_2, \ldots\}$ denoting the conversion electron's subshell.

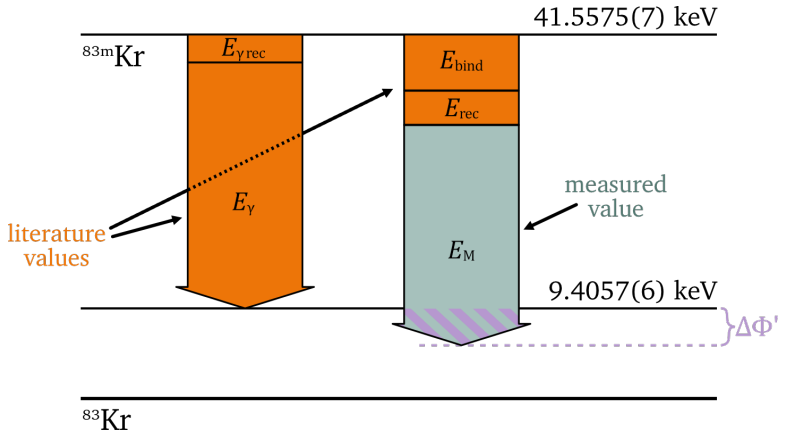

Figure 5.3 **Energy scale shift determination.** The diagram is loosely based on a transition diagram as shown in fig. 5.1 and illustrates how the shift of the energy scale is determined using a measurement of a ^{83m}Kr conversion electron line position E_M (5.3) and literature values for the gamma transition and the conversion electrons (5.2). The sum of the two energy components comprising the gamma emission case (left side) must be equal to the sum of the three components comprising the internal conversion case (right side). The difference when actually measured is the shift $\Delta\Phi'$. A 32-keV transition is shown here as an example, but the same is possible with a 9-keV transition.

Arbitrary subshells s_{32}, s_9, s_{42} can be chosen for the measurement of each respective transition. Inserting (5.5) into (5.4), the shift is then determined as

$$\begin{aligned}\Delta\Phi' = &- E_M(\tau_{42}, s_{42}) - E_{bind}(s_{42}) - E_{rec}(\tau_{42}) \\ &+ E_M(\tau_{32}, s_{32}) + E_{bind}(s_{32}) + E_{rec}(\tau_{32}) \\ &+ E_M(\tau_9, s_9) \quad + E_{bind}(s_9) \quad + E_{rec}(\tau_9) \quad .\end{aligned} \tag{5.6}$$

It is important to note that when determined in this way, $\Delta\Phi'$ does not depend on any transition energy E, and by extension does not depend on any gamma emission energy E_γ. In fig. 5.4, equations (5.4) to (5.6) are shown as a schematic.

For (5.6) to be valid, $\Delta\Phi'$ of course needs to be the same for all three measurements. A constant $\Delta\Phi'$ can be achieved by measuring under the same conditions along KATRIN's beamline. This effectively means measuring in direct succession to ensure unchanged source conditions. The retarding potential at the main spectrometer, meanwhile, necessarily changes as part of the measuring process. The absolute calibration method [Res+19] however characterizes the voltage dependency of the high-voltage divider measuring the retarding potential with a precision of 1 ppm. Furthermore, any possible systematic shift δU_{dep} of the main spectrometer field simulations to determine U_{dep} is independent of the voltage value. To summarize, $\Delta\Phi'$ is constant within an acceptable and known margin of error despite the varying retarding potential.

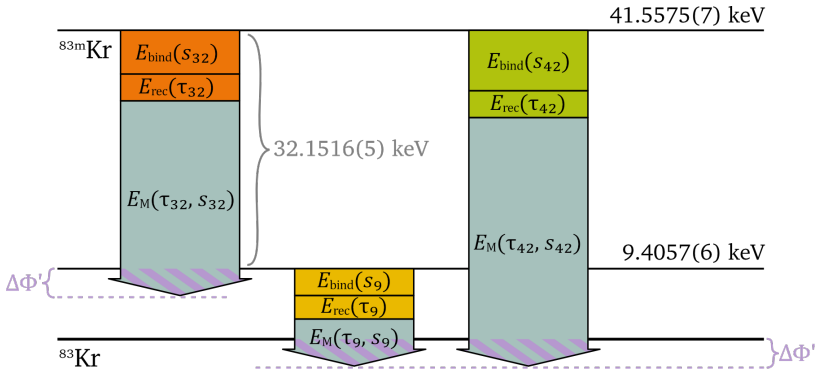

Figure 5.4 **Energy scale shift determination, improved.** With line position measurements from three interrelated transitions, $\Delta\Phi'$ can be determined without the use of gamma emission reference values, as shown in (5.6).

5.2.2 *Calculating the transition energies*

By solving each of the measurement series' instances of (5.5) for $E(g)$ and inserting $\Delta\Phi'$ as defined by (5.6), the transition energies can be determined:

$$\begin{aligned} E(g) &= E_M(g,s) + E_{bind}(s) + E_{rec}(g) - \Delta\Phi' \\ &= E_M(g,s) + E_{bind}(s) + E_{rec}(g) \\ &\quad + E_M(\tau_{42}, s_{42}) + E_{bind}(s_{42}) + E_{rec}(\tau_{42}) \\ &\quad - E_M(\tau_{32}, s_{32}) - E_{bind}(s_{32}) - E_{rec}(\tau_{32}) \\ &\quad - E_M(\tau_9, s_9) \quad - E_{bind}(s_9) \quad - E_{rec}(\tau_9) \ . \end{aligned} \tag{5.7}$$

The uncertainties in the recoil energies [Vén+18] are negligible here, leaving only the uncertainties in the electron's binding energies and those in the measured line positions. As can be seen in (5.7), using the same subshell for all measurements (i.e., $s_{32} = s_9 = s_{42}$) has the advantage of the binding energies canceling each other out, resulting in the simpler form

$$\begin{aligned} E(g) &= E_M(g,s) + E_{rec}(g) \\ &\quad + E_M(\tau_{42}, s_{42}) + E_{rec}(\tau_{42}) \\ &\quad - E_M(\tau_{32}, s_{32}) - E_{rec}(\tau_{32}) \\ &\quad - E_M(\tau_9, s_9) \quad - E_{rec}(\tau_9) \ . \end{aligned} \tag{5.8}$$

For an exemplary uncertainty estimation, let us assume a measurement series using exclusively electrons from the L_3 subshell. The L_3-32 line measurement is routine at KATRIN. The latest published result of the line position with the GKrS has a statistical uncertainty of 3 meV and a systematic uncertainty of 25 meV [Kat20b]. The L_3-9 measurement is not a routine measurement, and the L_3-42 line has yet to be measured at all. The challenges for both measurements are discussed in section 5.4. Assuming that the challenges are overcome, one could expect the same uncertainty as for the L_3-32 line measurement

Table 5.5 Selected energies of ^{83m}Kr decay. Energies (in eV) involved in ^{83m}Kr gamma decay and internal conversion for different transitions g and a selection of subshells s. Adapted from [Vén+18].

	E_γ	$E_{\gamma\,\mathrm{rec}}$		E_bind	E_rec		
					$g = \tau_{32}$	$g = \tau_9$	$g = \tau_{42}$
$g = \tau_{32}$	32 151.6(5)	0.0067	$s = \mathrm{K}$	14 327.26(4)	0.120	–	0.185
$g = \tau_9$	9405.7(6)	0.000 57	$s = \mathrm{L_3}$	1679.21(5)	0.207	0.051	0.274
			$s = \mathrm{N_2}$	14.67(1)	0.219	0.063	0.286
			$s = \mathrm{N_3}$	14.00(1)	0.219	0.063	0.286

(25 meV). Under this assumption, the energy of the 32-keV transition can be determined with an uncertainty of 35 meV, a considerable improvement over the 500 meV uncertainty in the current literature values (cf. table 5.5).

For the 9-keV transition, the expected uncertainty would be the same. Since the 42-keV transition is the sum of the other two transitions, the uncertainties of all three line positions contribute to $E(g)$ (5.8), leading to an uncertainty of 50 meV.

A proper uncertainty evaluation is of course only possible after the measurements have been performed. The values should be understood as an estimate of what may be achievable with this method.

5.3 Transferring the gains to routine calibrations

The higher-precision ^{83m}Kr transition energies can now serve as a better calibration reference for KATRIN's energy scale when using only a single ^{83m}Kr conversion electron line (cf. section 5.1.1, fig. 5.3).

One example is a simple one-hour measurement of the $\mathrm{L_3}$-32 line position. To match the conditions of the neutrino mass measurements as closely as possible, tritium and ^{83m}Kr should be circulated together inside the WGTS as was done in [Kat22; Mar+22]. With the $\mathrm{L_3}$-32 line position measurement, the shift can be determined with (5.5) as

$$\Delta\Phi' = E_\mathrm{M}(\tau_{32}, \mathrm{L_3}) - E(\tau_{32}) + E_\mathrm{bind}(\mathrm{L_3}) + E_\mathrm{rec}(\tau_{32})\,. \tag{5.9}$$

Following the assumption that all challenges described in section 5.4 are met to successfully determine $E(\tau_{32})$ with a precision of 35 meV (cf. section 5.2.2), the total uncertainty in $\Delta\Phi'$ would be 66 meV. Since the $\mathrm{L_3}$-32 line position measurements are performed regularly, any improvements can also be applied retroactively to $\Delta\Phi'$. With high source activity, the measurement of the $\mathrm{N_2N_3}$-32 doublet is also feasible, leading to an even smaller error in $\Delta\Phi'$ due to the smaller uncertainty in the binding energy (cf. table 5.5).

By measuring $\Delta\Phi'$ during a neutrino mass measurement campaign,

$\Delta\Phi'$ can be applied to the effective endpoint of tritium spectrum fits and translated into the measured Q-value.

To put the uncertainty of $\Delta\Phi'$ in perspective, the Q-value is known to 0.07 eV from external measurements [Mye+15] while the uncertainty is 0.6 eV in the most recent KATRIN publication [Kat22].

5.4 Challenges

An ideal measurement would use both the CKrS and the GKrS at the KATRIN beamline. Comparing the resulting transition energies can give access to hidden systematics. However, the 9-keV transition can be challenging to measure with the GKrS.

The first complication is that the conversion electron lines of the 9-keV transition are below the tritium endpoint. This complication is easy to solve by using helium as carrier gas, or circulating only krypton inside the source as was done in [Kat20b]. Then the background due to tritium is reduced to only residual tritium on the rear wall, which can be minimized by cleaning.

The second complication is that the 32-keV transition leaves the atom in a multiply-ionized state, and the 9-keV transition follows the 32-keV transition within the 155 ns half-life [Mcu15]. Due to the low ^{83m}Kr density inside the WGTS, the neutralization times are longer than the half-life. The multiply-ionized states shift the binding energies. Instead of one conversion electron line, multiple shifted lines are visible, with each corresponding to a charged state [DS90]. For a successful measurement, the charged states need to be identified. The work [Sei19] describes the first measurement of this kind at KATRIN. Inside the CKrS, the neutralization times are shorter than the half-life, thus no multiply-ionized states exist at the time of the 9-keV transition. Therefore, the observed conversion electron energy is not shifted.

For the CKrS, the binding energies of the different shells have an unknown shift due to condensed matter effects. Here it is vital that the three lines all come from the same subshell, as was done in (5.8), to cancel out the unknown binding energy.

Another challenge will be the measurement of the highly suppressed 42-keV transition. The expected intensity of the L_3-42 line is roughly 13 ppm of the L_3-32 line, and roughly 0.16 % of the N_3-32 line. However, the lack in intensity can be overcome by a high-luminosity source and an increase in measurement time. For example, successful high-intensity measurements of the N_2N_3-32 line doublet were already performed with a 10 GBq GKrS. The energetically higher lines from the 42-keV transition were clearly visible as background.

The intensity estimations were calculated by D. Vénos, based on the Weisskopf formula for the photon transition probability.

To measure the integrated spectrum of the L_3-42 line, a voltage of around −39.8 kV needs to be applied at the KATRIN spectrometer. During normal operation only voltages down to −35 kV are permitted. Several, but feasible, hardware changes are needed to operate the spectrometer at voltages down to −40 kV. The key to the precision high-voltage setup is the divider, and fortunately, one of the two available dividers is designed to measure voltages up to ±65 kV [Bau+13].

It is not possible to use the K-42 line with the CKrS since all measurements need to be from the same subshell, as explained earlier. The 9-keV transition is not possible for electrons from the K shell due to their binding energies of about 14 keV.

When using the GKrS, measuring the K-42 line at 27.2 keV instead is also a possibility. Since the spectrometer acts as a high pass filter, the signal would be lost in the background of the energetically higher lines (e.g. the L_3-32 at 30.5 keV has a roughly 4×10^4 higher intensity). Changing the magnetic fields to reduce the transmittance of electrons with high-surplus energy, or improving the energy resolution at the detector are possible solutions.

5.5 Conclusion

It has been shown that by measuring three distinct transitions of ^{83m}Kr, the shift $\Delta\Phi'$ of KATRIN's energy scale can be determined independently of the absolute transition energies. This allows the ^{83m}Kr transition energies with a precision improved over the current literature values to be determined. These higher-precision transition energy values translate directly into more precise single-line ^{83m}Kr calibration measurements at KATRIN, even retroactively.

6 Conclusion and outlook

Any measuring instrument needs proper calibration to characterize it and to validate its accuracy. Ideally, the instrument is tested against a well-known calibration source. Just like a voltmeter needs a voltage standard to be calibrated, an electron spectroscope needs an electron source for calibration. In the context of this thesis, a variety of calibration techniques for electron-energy related characteristics of KATRIN were used, further improved, and newly invented.

The e-gun, a mono-energetic electron source, was used to determine the loss of energy due to inelastic scattering of electrons on tritium inside the source. The minimal energy loss of an electron that is scattered on tritium is about 10 eV. In other words, the measured spectra from scans less than 10 eV deep consist entirely of unscattered electrons, making analysis straightforward. For scans deeper than that, like the scans 40 eV deep into the tritium spectrum for neutrino mass measurements, the energy loss is a necessary part of the analysis. The energy-loss function presented in this thesis is an in-situ measurement at the KATRIN beamline with significantly improved energy resolution compared to energy-loss functions measured at predecessor experiments.

One open question in the energy-loss function analysis is the slight deviation of the χ^2 value from 1.0 (1.08(2) for the fit on the differential data). The residuals in the region of the electronic excitations show small structures (within $2.5\,\sigma$). In the semi-empirical model, three Gaussians are used to describe a whole set of discrete excitation states. In the measurement, those discrete states are smeared by the energy resolution. The slight structures in the residuals might be a hint that the three Gaussians are not a sufficiently close approximation at the energy resolution achieved in the measurements. Future measurements with a new e-gun might shed light on this and clarify if it is a hidden systematic or a hint as to the limitations of the simplified model.

The e-gun is used not only to determine the energy loss but also to investigate the transmission condition inside the spectrometer. However, since the energy of the electrons emitted by the e-gun is known only relative to the retarding potential, the latter needs to be measured to determine the spectrometer's energy scale. Furthermore, it needs to be stabilized during measurements.

The post-regulation system does this stabilization. Within the scope of this thesis, the existing post-regulation system was integrated into the KATRIN control system and improved by integrating the precision high-voltage dividers into the regulation loop. Performance measurements demonstrate its sub-ppm precision on time scales from microseconds up to weeks. The high-voltage dividers' scale factors are calibrated with 1 ppm accuracy. Using the absolute calibration method, the voltage dependency of the high-voltage divider K35 was determined to be within 1 ppm across a 33-kV-wide range. Together with the low-voltage calibration, which is ideal for quick stability checks, on-site calibrations of the dividers during measurement breaks are now possible.

The calibration history of the K35 spans more than a decade already and includes multiple different calibration techniques. The low-voltage calibration results vary only slightly and have a weighted standard deviation of 0.8 ppm. In contrast, the high-voltage calibrations (including reference measurements to the PTB divider, calibration with ^{83m}Kr conversion electrons, and the absolute calibration) exhibit greater variation and there is also a notable divergence between the results from the different techniques. Even though the differences are negligible compared to the requirements needed for successful neutrino mass measurements with KATRIN, these observations highlight the importance of using a variety of different calibration techniques. Further measurements will likely be necessary to find a satisfactory explanation for the differences.

Still, even with a well-known and precisely calibrated retarding potential, the energy scale of the spectroscope is not completely defined. For a full characterization, a calibration with an electron source such as the isomer ^{83m}Kr is needed. While a naïve calibration with known ^{83m}Kr transition energy values from the literature would already be useful by itself, the proven linearity of KATRIN's energy scale presents an opportunity: By measuring conversion electrons from the 41.6-keV transition as well as from the corresponding cascade of a 32.2-keV and 9.4-keV transition, any absolute shift of the energy scale can be nullified, thus enabling precision beyond that of current literature values.

Not only the KATRIN experiment can benefit from better transition energy values, but any experiment using ^{83m}Kr for calibration and aiming for sub-eV precision. Further, other experiments performing electron spectroscopy (or gamma spectroscopy) could perform the proposed measurement pattern and determine the transition energies independently of their unique energy scale shifts. The single major requirement is, of course, a linear energy scale.

The results presented within this thesis demonstrate in three different ways KATRIN's ability to perform electron spectroscopy with sub-eV precision: First, with e-gun measurements. Second, with the stabilized retarding potential, whose calibration traces back to natural standards at metrology institutes. And third, with ^{83m}Kr as a nuclear standard which KATRIN has available from three different source types.

Appendix

A.1 Flight time simulation code

For fast simulations a C++ code is used to perform the calculations and the code is integrated in R code with the Rcpp interface. In the R code, not shown here, the input parameters are managed, for example fields, properties of the electrons (energy, angle), properties of the ripple, and also the output files. The calculations as described in section 4.1 are written in C++ and the essential part of the code is printed here.

```
#include <cmath>
#include "Rcpp.h"

using namespace Rcpp;

const double pi = 3.14159265358979323846264338327950288 4L;
const double c  = 299.792458;   // speed of light [m/us]
const double me = 510998.95000; // electron mass [eV/c^2]
const double qe = -1.0;         // electron charge [e]

constexpr double sq(double x) { return x * x; }

double
reciprocal_velocity(double Esource, // [eV]
                    double theta,   // [rad]
                    double delta,   // [eV]
                    double Bscale)  // [1]
{
    // energy at t=0 [eV]
    double Erel0 = Esource + me;

    // energy at z [eV]
    double Ekinz = Esource - delta;
    double Erelz = Ekinz + me;

    // squared momentum components times c^2 at z
    double perpendicular = (sq(Erel0) - sq(me)) * sq(sin(theta)) * Bscale;
    double parallel = sq(Erelz) - sq(me) - perpendicular;

```

```
30      // reciprocal velocity at z [us]
31      return Erelz / (sqrt(parallel) * c);
32  }
33
34  double
35  ripple(double tof,       // [us]
36         double freq,      // [Hz]
37         double amplitude) // [V]
38  {
39      return amplitude * sin(2.0 * pi * freq * tof * 0.000001);
40  }
41
42  double
43  ripple_step(double tof,       // [us]
44              double step,      // [us]
45              double amplitude) // [V]
46  {
47      if (tof < step)
48          return 0;
49      return amplitude;
50  }
51
52  // [[Rcpp::export]]
53  NumericMatrix
54  transmission_ripple_cpp(const NumericVector& Z,      // [m]
55                          const NumericVector& Uscale, // [1]
56                          const NumericVector& Bscale, // [1]
57                          double Uret,                 // [V]
58                          double Esource,              // [eV]
59                          double theta,                // [rad]
60                          double tof0,                 // [us]
61                          double freq,                 // [Hz]
62                          double amplitude)            // [V]
63  {
64      const int n = Z.size();
65      NumericMatrix result(n, 2);
66      double deltaE = result(0, 0) = 0;
67      double tof    = result(1, 0) = tof0;
68
69      result.attr("deltaE_ana") = NAN;
70      result.attr("transmission") = false;
71
72      for (int i = 1; i < n; i++) {
73          double rvel = (Z[i] - Z[i-1]) *
74              reciprocal_velocity(Esource, theta,
75                                  qe * Uret * Uscale[i] + deltaE, Bscale[i]);
76          if (std::isnan(rvel))
77              break;
78          tof += rvel;
79          result(i, 0) = tof;
80
81          deltaE += qe * (Uscale[i] - Uscale[i-1]) *
82              ripple(tof, freq, amplitude);
83          result(i, 1) = deltaE;
84
85          if (Z[i] == 0)
86              result.attr("deltaE_ana") = deltaE;
87
```

```
88          if (i == n - 1)
89              result.attr("transmission") = true;
90      }
91
92      result.attr("tof") = tof;
93
94      return result;
95  }
```

A.2 Temperature dependency of the high-voltage divider K65

During the fourth neutrino mass measurement campaign (KNM4) the temperature control of the K65 failed and the K65 divider cooled down and stayed at room temperature. During that time the K65 was used instead of the K35 to measure the retarding potential. To check the influence on the neutrino mass measurements, dedicated measurements to investigate the K65's temperature dependency were performed.

A full report about this is given in the internal electronic logbook entry.

During these measurements some unexpected instabilities of the K65 were discovered. This chapter summarizes the observations during the test measurements. Based on these results, the situation during KNM4 is evaluated and further possible steps on how to solve or to live with the observed issues in the future are discussed.

More details also here.

A.2.1 *First cross calibration with the K35*

The most convenient way to investigate the temperature dependency of the K65 is to determine the K65's scale factor at different temperatures with a cross calibration against the K35. On April 21, 2021, both dividers were attached to the same voltage source (−18.5 kV) and a voltmeter measures the voltage at the 2000:1 output of each divider. The temperature of the K35 is fixed at 25 °C during the complete measurement time. The temperature of the K65 is varied: First it is cooled down in one step to 15 °C and then in 1 °C steps heated up again to 25 °C. Important to note, during the measurement the regular measurement cables are not exchanged at the dividers, the only cabling changed for this measurement is the cabling for the high voltage feeding.

A.2.1.1 *Continuous measurement during cool-down*

During the cool-down from 25 °C to 15 °C the measurement was running continuously (shown in fig. A.1), allowing a continuous measurement of K65's scale factor. The K35 shows the normal run-in of the precision power supply at 18.5 kV. The K65 shows steps and spikes that are unusually large (up to 20 ppm peak-to-peak). The cabling was checked, including a short a voltmeter calibration, to exclude a problem with the cabling.

The spikes and high noise in the K65 readout can be directly connected to the K65 scale factor via

$$M_{\mathrm{K65}} = \frac{U_{\mathrm{K35}}}{U_{\mathrm{K65}}} \cdot M_{\mathrm{K35}} \,. \tag{1}$$

With $U_{\mathrm{K35,K65}}$ being the voltage readout at their voltmeter, corrected by voltmeter gain and offset. The scale factor is plotted in fig. A.2, focused on the more unstable periods. During the measurements the reasons for this behavior were unclear and the measurements were continued as planned, after checking the cabling for obvious mistakes.

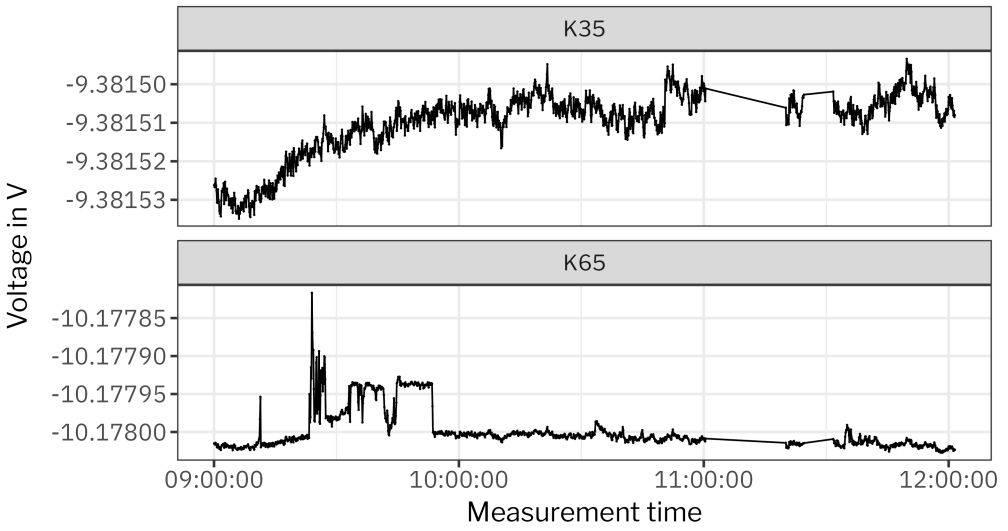

Figure A.1 **Voltmeter readout during cool-down of K65.** The plot shows the voltage at the 2000:1 output for the K35 (top panel) and for the K65 (lower panel) during the cool-down of the K65 from 25 °C down to 15 °C. During the break at 11:00 the voltmeters were calibrated and the cabling was checked.

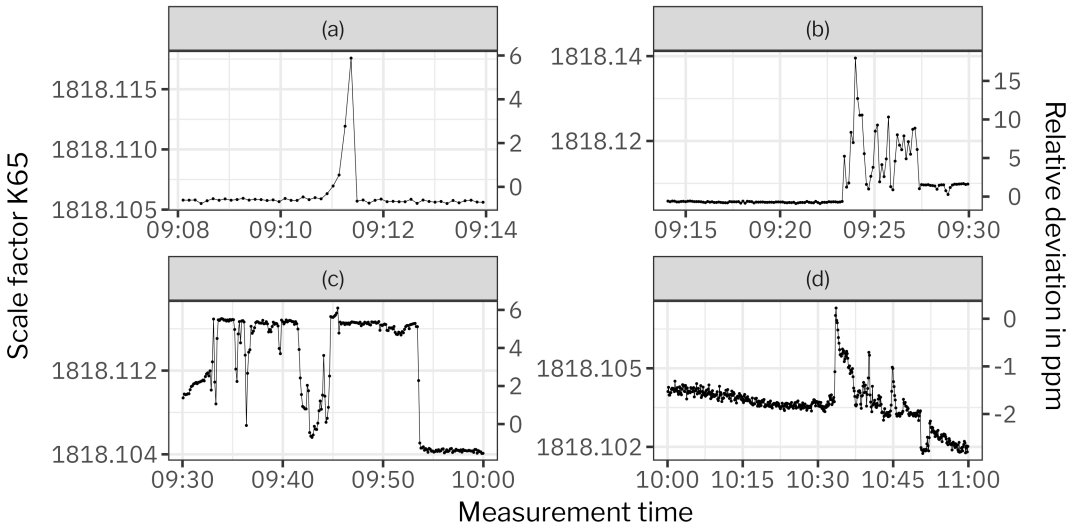

Figure A.2 **Scale factor of K65 during cool-down.** For better visibility the plot is divided up into different time periods. The right axis shows the deviation to the average scale factor over the whole dataset.

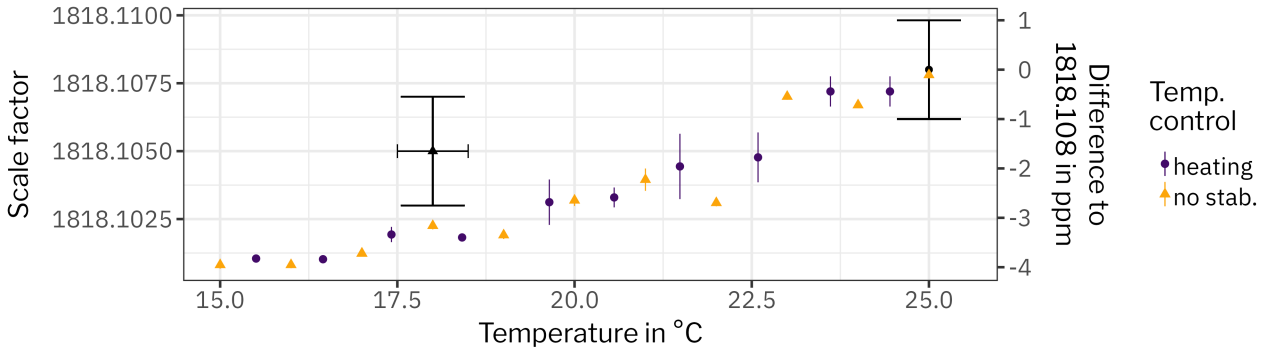

Figure A.3 **Scale factor of the K65 at different temperatures.** The triangle-shaped points are the mean scale factor during the time period without temperature stabilization, the filled circle during the heating periods. The line range represents the standard deviation. The black triangle with errorbars (including systematic uncertainties) is a cross-calibration result from January 5, 2021 without temperature stabilization. The black dot with errorbars (including systematic uncertainties) is the most-up-to-date scale factor value for the divider under nominal conditions at 25 °C. As described further in the text, the data shown here can not be used to characterize the "real" temperature dependency of the K65.

A.2.1.2 *Measurements during step-wise heating-up*

After the cool-down to 15 °C the divider is heated up again in 1 °C steps up to 25 °C. At each step, after some stabilization time, the temperature control is turned of by switching of the power supply for the temperature control and a measurement is performed. Depending on the temperature inside the divider relative to the 17 °C ambient temperature, the temperature changes during the measurement. The measurement length is adapted to keep the change smaller than 0.5 °C during one measurement.

Again instabilities are visible in the data. One instability is persistent over several minutes and rather large with 6 ppm peak-to-peak (similar to fig. A.2b). Another occurs at around 22 °C within 3 ppm peak-to-peak. Additionally, one build-up to about 6 ppm with a sharp decrease (similar to fig. A.2a) was observed.

Despite the instabilities, the data is further analyzed to extract a temperature dependent scale factor from the more stable periods. The result is shown in fig. A.3 and should be interpreted carefully. At first glance one could interpret this as linear with a slope of ≈ 0.4 ppm/K, but at 23 °C is a step. Similar to the one already observed during the cool-down (fig. A.2 at 09:28). In later measurements (discussed in the next sections) a similar step is also visible and can be connected to a kind of "relaxation" of the system.

The additional measurement point (black point in fig. A.3), is from a cross-calibration result on January 5, 2021 without temperature stabilization. Here the temperature stabilization was off since October 28, 2020, allowing the divider to get in equilibrium with the ambient

temperature (stable within 2 °C). At the time of the calibration the temperature readout was not active, but the temperature inside the divider can be approximated with the known ambient temperature together with old data to roughly (18 ± 0.5)°C. The error bars are a very coarse and conservative estimation of the systematic of the measurements method of about 1 ppm. Since this is a direct comparison measurement of the two dividers K35 and K65 the dominant systematic is the knowledge of the absolute scale factor value of the K35, which is only known to 1 ppm. The second systematic comes from the voltmeters, but with the regular calibration their properties are known to the sub-ppm level. For the direct comparison between the January and the April measurements the knowledge of the absolute K35 scale factor does not play any role, especially since we know from other measurements that the K35 is stable on the sub-ppm level per year (cf. section 4.5.1). Therefore the measurements are not compatible within their errors and the state of the K65 in January is different than in April.

The estimation is based on an average difference of the room temperature (measured by the K65 slow control) to the temperature inside the divider (mean of measurement on east and west side) of about 2.2 °C in November 2020. The average difference between the room temperature measurement and the temperature measurement at the detector platform is 0.3 °C in November. Using both on the 15.5 °C measured at the detector platform on January 5, 2021, leads to the estimated temperature of 18 °C inside the K65.

In addition to the disagreement to the measurement in January the temperature dependency shown in fig. A.3 is also in disagreement to previous characterization measurements [cf. Bau+13, table 2], showing a temperature dependency of less than 0.1 ppm/K.

Despite the problems in the temperature regions different to 25 °C, the last measurement points at 25° agree again with the normal value under nominal conditions (black line in fig. A.3). This is the first hint that the divider works normally under its nominal temperature, further investigations follow in the following sections.

A.2.2 *Low-voltage calibration*

To investigate the behavior further, more measurements were performed independent of the K35. Although the K35 is the ideal comparison, it was not available for long-term investigations due to ongoing measurements. Still, the low-voltage calibration method (cf. section 4.5.1) is sufficient for further investigations.

As a first step, a standard low-voltage calibration with both dividers was performed at nominal temperature. For both dividers the result is very compatible to the previous measurements.

For the 100:1 calibration measurement the cabling at both dividers was changed in comparison to the normal cable for the 2000:1 readout with a spare cable, but for both dividers (calibrated in succession) the same cable is used. The 20:1 calibration measurements are performed again with the same measurement cable that is used during normal mode.

A.2.2.1 *20:1 calibration at different temperatures*

After it was confirmed with the first step that the K65 behaves normally at 25 °C the divider was cooled down over the weekend by turning of the heating/cooling power supply. Everything else stayed the same.

During the cool-down, −184 V were applied to the 100:1 output and at the same time the divider was under load at −18.5 kV (20:1 calibration under load, cf. section 4.5.2). Quite different to the measurements

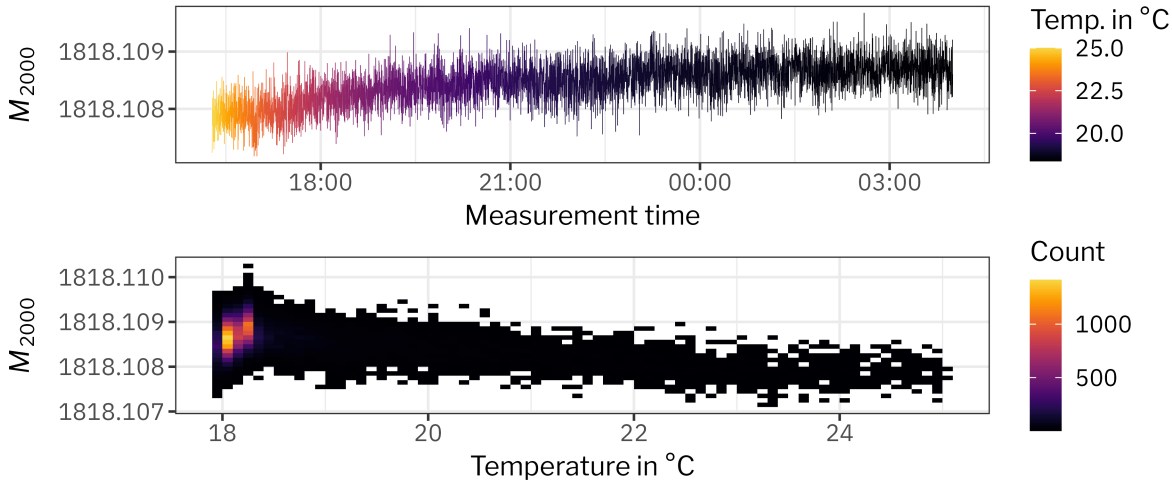

Figure A.4 ***M_{2000}* scale factor results during cool-down.** Results for the M_{2000} scale factor, measured with the 20:1 calibration method. The top panel shows only the first hours of measurements where the largest temperature change happened. The bottom panel shows the distribution of scale factor and temperature values across all available measurement data.

shown in the previous section the value is rather stable and only a very small temperature dependency is visible. The results are plotted in fig. A.4. To get the M_{2000} scale factor value the previously determined 100:1 value is used.

The measurements show that the resistors between the 100:1 output and the 2000:1 output have almost no temperature dependency and also do not show the same instabilities that were observed before. Also proofing that the measurement cable attached at the 2000:1 output is not responsible for the instabilities.

A.2.2.2 *100:1 calibration at different temperatures*

For further investigations, the low-voltage calibration of the 100:1 output was performed. −1 kV were applied with the calibrator at the K65 and the reference divider and both readout with two independent voltmeters. Since the focus of the measurements is on changes between different temperatures and less on absolute scale factor values, the reference divider was only calibrated once.

First the K65 was heated back to 25 °C (again instabilities visible, not shown here) and afterwards cooled down over night by turning of the heating/cooling power supply. The scale factor results from the cool-down from 25 °C over night is shown in fig. A.5. During the cool-down instabilities: spike and steps are visible, smaller and also slightly different from during the cross calibration with the K35 but still quite significant.

On the following measurement day, the divider was heated up to 22.5 °C with a roughly three hour period at fixed 20 °C. The measurement time with unstable periods are plotted in fig. A.6. During the first heating-up step the instabilities start almost directly after the start

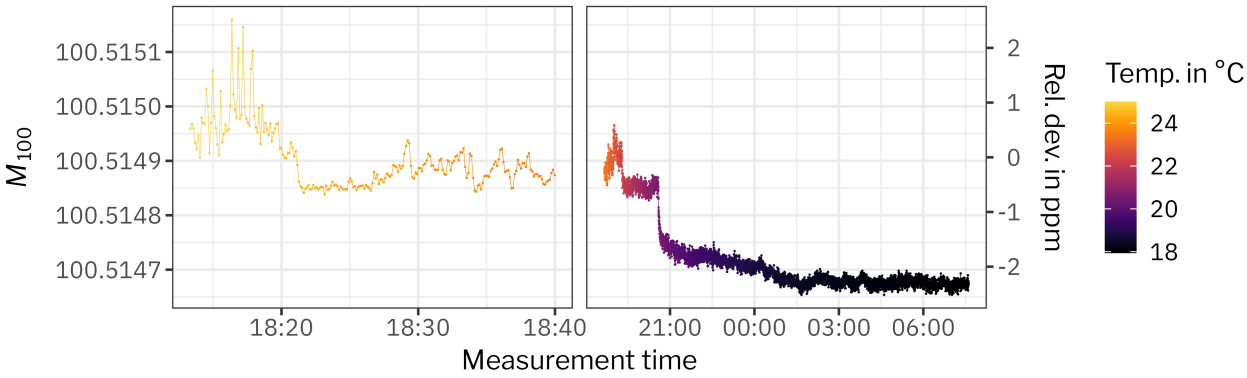

Figure A.5 ***M_{100}* scale factor results during cool-down.** The right axis shows the deviation to the average scale factor over the whole dataset.

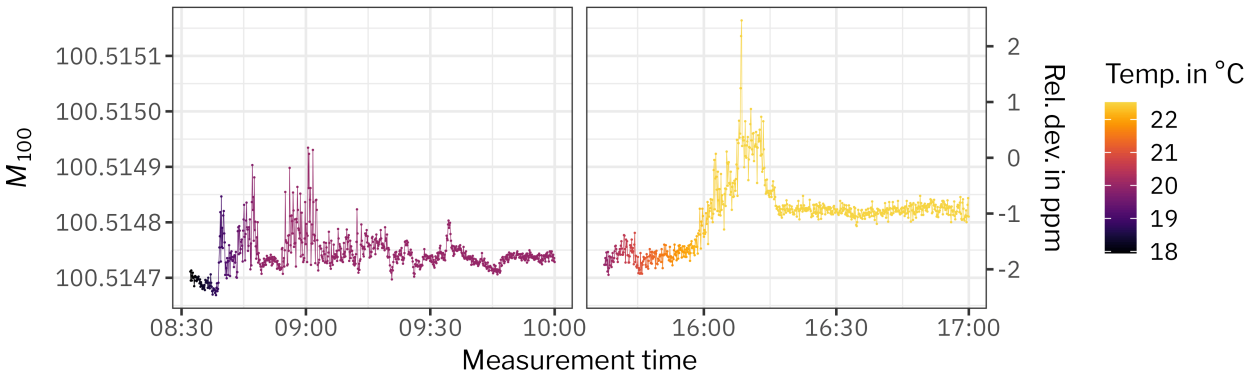

Figure A.6 ***M_{100}* scale factor results during step-wise heating-up.**

of the heating and are random spikes within ±1 ppm. During the second step, the instabilities (within ±2 ppm) start after the temperature is already reached and they stop after a build-up. In both cases, on the order of one hour after reaching the set value the K65 scale factor stabilized.

To investigate the stability while the divider is cooled down slowly, the PID controlled temperature stabilization was deactivated and the heating power supply was set to a fixed low value to slowly heat against the cool-down from the 17 °C ambient temperature. The measurement shown in fig. A.7 shows a slow build-up, starting at a temperature around 20.1 °C. The build-up evolves over a few hours and increases over time, up to an overall change of 150 ppm. The largest part of the build-up (approx. 100 ppm) happens within a few seconds, followed by an abrupt jump back. After the jump the scale factor value back to its previous value and stable. This build-up with a sharp fall-back was also seen during the cool-down during the cross calibration with the K35 divider but here it is roughly a factor 60 larger).

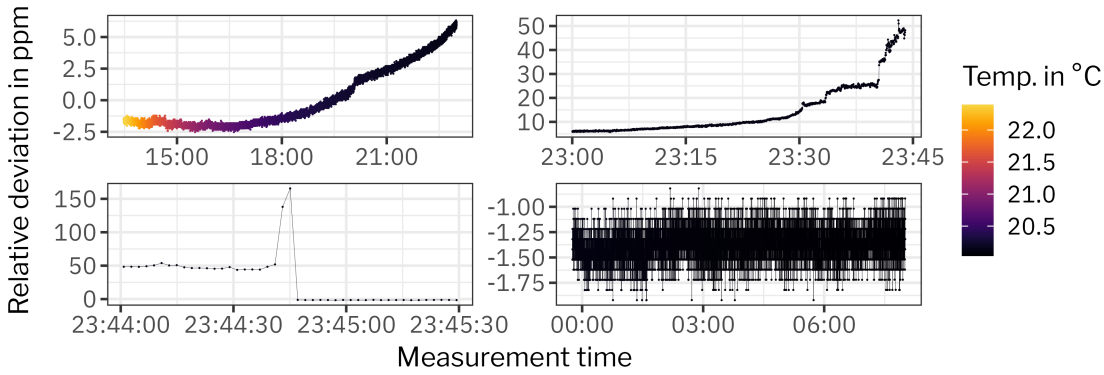

Figure A.7 **Relative M_{100} scale factor results during slow cool down.** The measurement is divided into four sections to highlight the different periods. The mean scale factor is calculated over the whole dataset and the relative deviation to the mean is plotted.

A.2.3 *Mechanical stability tests*

The behavior observed during the 100:1 measurements hint to a mechanical tense up during temperature gradients at the divider, introducing a changed conductivity that is visible in the change of the scale factor. If this is the case it should also be possible to trigger it mechanically.

To trigger it mechanically, the divider is rolled up a disc (two different discs were used, 3-mm and 5-mm thick) and then rolled down again. During all the tests the 100:1 scale factor of the divider is monitored with the low-voltage calibration. As a first test the divider was rolled up and down the disc at stable temperature of 25 °C, here the measured scale factor kept unchanged.

In the following tests the divider was cooled down to 20.5 °C and afterwards up again to 25 °C. During the cool-down it was possible to introduce a spike by moving the divider down from a disk. During the heating-up a small build-up was visible and by rolling down the divider it was stopped (together with introducing a spike).

The divider was kept on 25 °C over the weekend and the tests were repeated on Monday. To have a better prediction of the behavior, the divider was cooled down to 15 °C the same as during the cross calibration. During the cross calibration (cf. fig. A.2) a build-up with a spike was visible after about 10 minutes, and after about 23 minutes a general noisy behavior started.

Before the cool-down was started the divider was rolled up the disc again and no instabilities were observed. The scale factor during the cool-down is plotted in fig. A.8. After a few minutes a build-up started and the divider was rolled down the disc resulting in a spike and a recovered scale factor. Moving the divider up the disc again introduced a second, smaller spike. Later the general noisy behavior was visible and the divider was rolled down and the scale factor recovered again.

The tests show that the general behavior is reproducible and furthermore that it can be induced and stopped by a mechanical movement of the divider.

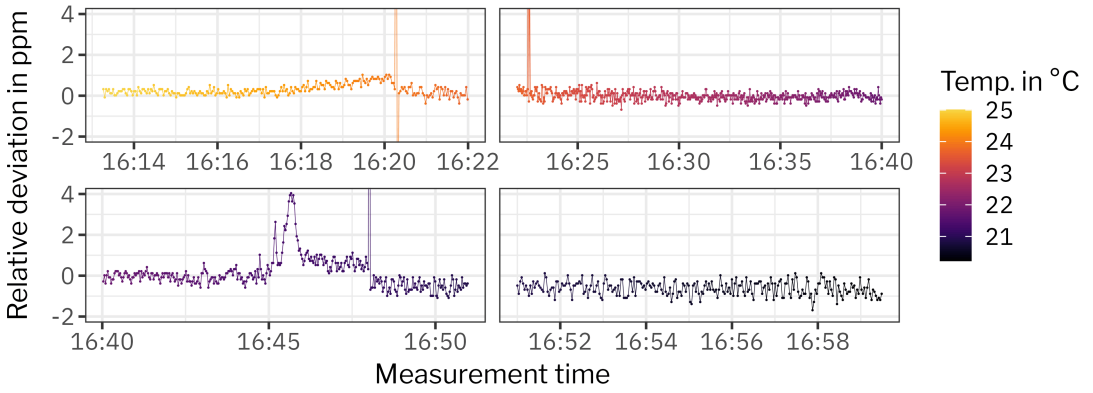

Figure A.8 **Scale factor during mechanical stability tests.** The measurement is divided into four sections to highlight the different periods. The mean scale factor (100:1) is calculated over the whole dataset and the relative deviation to the mean is plotted. The y-axis is limited, the first spike is about 30 ppm peak-to-peak, the second has an amplitude of about 10 ppm and the third about 20 ppm. At each spike the divider was moved: first rolled down, then up, then down again.

A.2.4 *Second cross calibration with the K35*

Roughly a month after the mechanic tests with the low-voltage calibration method, both dividers (K35 and K65) were available for more tests. The time was used to perform another cross calibration of K35 and K65. They differ from the previous ones in two important details: The K65 was before the measurements for one month fixed at 17 °C and a different voltmeter was used.

A.2.4.1 *Commissioning of Fluke 8588A*

This already occurred before, more details here.

The voltmeter used previously (a voltmeter of the type Fluke 8508A) was in an error state and not usable). To still have two voltmeters, a new one (of the type Fluke 8588A) was commissioned. For the following presented measurements the new Fluke 8588A was used to readout the K65.

One big advantage of the new voltmeter is the faster readout: instead of a 7.5-digit measurement every 2 s a measurement on the same level every 0.2 s is possible. To test the voltmeter, measurements with 10-V sources and long-time cross-calibration measurements at fixed temperature were performed. Later, also measurements with the K65 at nominal 25 °C yielded very comparable scale factor results to measurements with the voltmeters of the type Fluke 8508A.

A.2.4.2 *Measurements at fixed temperature*

As a first step, the K65 was cross-calibrated with the K35 at −18.5 kV. During this calibration the K65 was at 17 °C. The result is shown in fig. A.9. Averaging over the measurement leads to a scale factor for

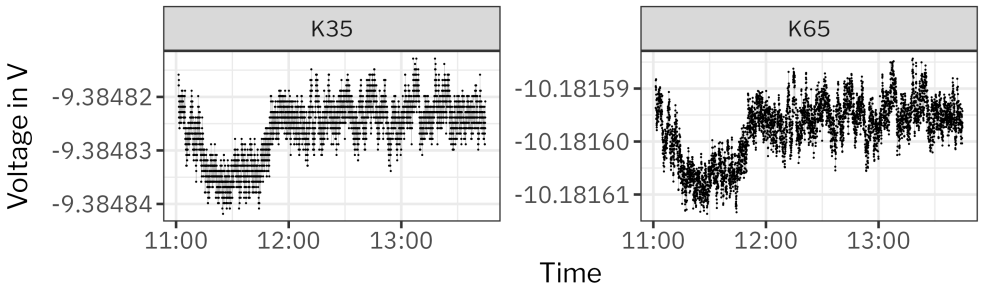

Figure A.9 **Voltmeter reading during cross calibration.** The K35 is read out with a Fluke 8508A and the K65 with the new Fluke 8588A.

the K65 of: 1818.1049, showing very good agreement to the 1818.1046 at around 18 °C (displayed in fig. A.3).

During a second measurement, the K65 was heated up to 25 °C over night. After the usual instabilities during the heating (see next section), the scale factor was again stable at 1818.1076, agreeing very well to previous scale factor measurements at 25 °C.

With the assumption that the new voltmeter meets its specifications – very well justified by the calibration and commissioning measurements of the new voltmeter – the K65 shows, as also shown during the low voltage calibration and the last cross calibration, very reproducible results at fixed and stable temperatures.

A.2.4.3 *Measurements at changing temperatures*

To further verify and reproduce the instabilities of the K65 with the cross calibration, the divider was heated up and cooled down again and the mechanical tests were repeated.

A key difference to the previous measurements shown in appendix A.2.1 is that this time the K65 was for a long time (1 month) at 17 °C, instead of its nominal 25 °C. The result is shown in fig. A.10. During the first heat up there are small and fast build-ups with spikes visible and also a larger overall build-up. In the second test (in-between the divider was cooled down), the slower overall build-up stopped suddenly. Although the behavior is quite similar, the amplitude of the effect is much lower than during the measurements one month earlier.

The K65 was temperature cycled several times and more instabilities were observed. It was also possible to repeat the mechanical stability tests. A subset of the measurements is shown in fig. A.11. The second and third plot in the lower part show two examples of the system reacting to the rolling down of the divider from the disc. In both cases the scale factor value jumps back afterwards and stays stable.

A.2.5 *Impact on neutrino mass measurements*

During KNM4 the power supply for the temperature control was separated from the mains supply and it was only noticed after a few weeks. The temperature inside the divider was continuously measured; it followed the ambient temperature and was on average at 20 °C.

More details here.

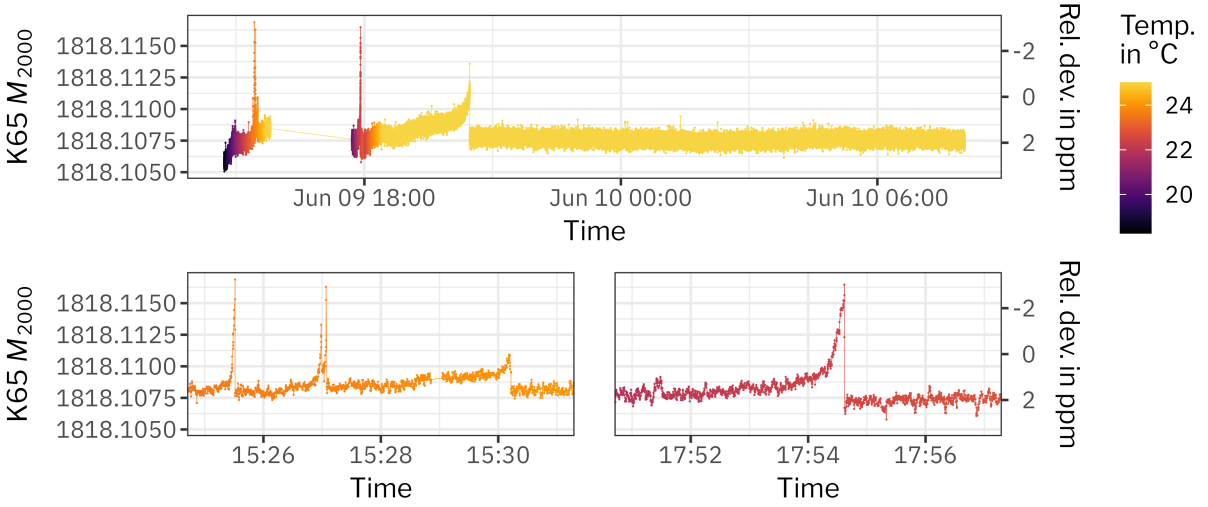

Figure A.10 **Scale factor of K65 during heat up.** M_{2000} is determined via the cross calibration with the K35. During the missing data points the K65 was cooled down.

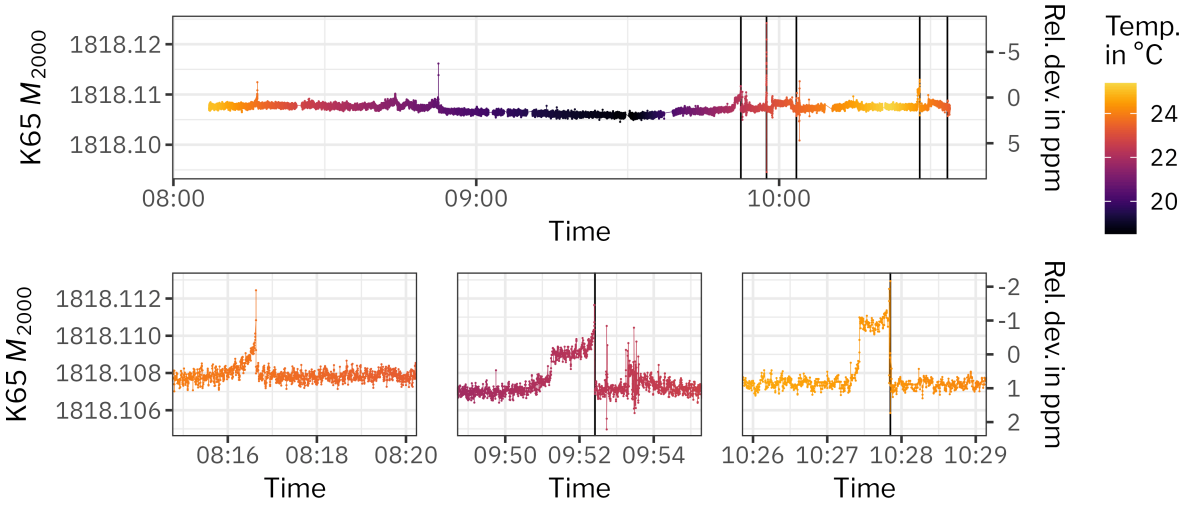

Figure A.11 **Scale factor of K65 during mechanical tests.** The black lines mark the times were the divider was rolled down the disc. Shortly afterwards it was always rolled up again, also visible as instability, but not marked in the plot. The three bottom panels show an exemplary zoom into regions with spikes. The gaps in the data are caused by some issues with the newly developed voltmeter readout.

At the beginning (during the fast drop down of the temperatures), fortunately no beta scans were running. The first beta scan started roughly 8 h after the stop of the temperature control. The measurements shown in the previous sections, for example in fig. A.5, indicate that at this point instabilities caused by the temperature decrease are already gone.

Based on multiple measurements it is safe to assume that as long as the temperature is stable the scale factor also stays stable. Except for a drop in temperature over 2 °C that recovered with a slow increase of 1 °C over one day, the temperature was stable during the beta scanning period.

Using the cross-calibration results at stable 25 °C and 17 °C (cf. appendix A.2.4) and assuming a linear temperature dependency a scale factor change of 0.19 ppm/°C can be estimated. The scale factor at 20 °C is estimated as 1818.106.

This is larger than the temperature dependency reported in [Bau+13] (< 0.1 ppm/K). The temperature dependency of the K35 was previously determined by a cross calibration with the K65 in June 2020 to be 0.5 ppm/°C. Also larger (and probably the opposite direction) than the −0.08 ppm/K reported in [TMW09]

Overall, the KNM4 beta scans are not critically affected by a 1-ppm step of the scale factor. With the very basic assumption of $\Delta m_\nu^2 = -2\sigma^2$ (very crude, since it is clearly a step and not a Gaussian broadening), the effect is on the order of $\Delta m_\nu^2 = 0.8 \times 10^{-3}\,\mathrm{eV}^2/\mathrm{c}^4$ and well within the uncertainty budget ($7.5 \times 10^{-3}\,\mathrm{eV}^2/c^4$, cf. chapter 4).

A.2.6 *Summary and next steps*

The measurements presented in this chapter indicate a stable scale factor of the K65 at its nominal operating temperature of 25 °C. All measurement campaigns (except for the time during KNM4) were performed with the K65 at 25 °C without abrupt temperature changes.

After the incident in KNM4, the temperature values are logged in ADEI and monitored (e.g. with manual checks during the voltmeter calibration) to recognize a potential future temperature problem earlier. However, to not introduce potential problems it is better to use the K35 as main divider and leave the K65 as fall back solution. Before using the K65, a check with a low-voltage or cross calibration is recommended.

On a more long-term view the real reason for these issues should be found and removed. Doing this requires opening the divider and checking all the connections of the resistor chain. In the best scenario one could already see/guess a cause by eye, maybe also by observing it during a temperature change (would require a temperature controlled room, or a web cam under the cover of the divider?).

One other and maybe more realistic possible procedure would be to find the connection causing this problem with an half-interval search where the voltage drop over a subset of the 165 880-kΩ resistors is measured during a temperature gradient (divider closed again). After eight steps ($\lceil \log_2(165) \rceil$) the problematic connection is found. If it is divided in the first step into one group of 101 and one of 64 resistors with a bit of luck only seven instead of eight steps are needed.

A.3 Supplemental figures and tables

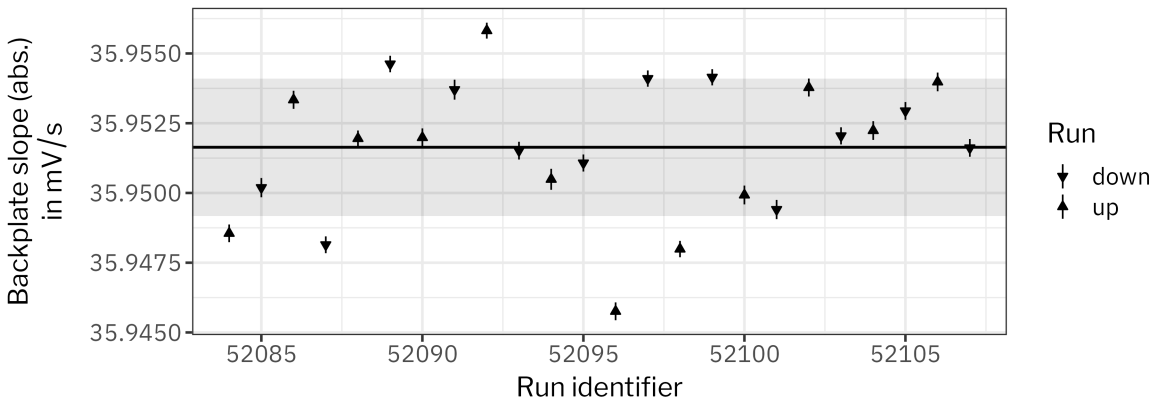

Figure A.12 **Voltage slopes at the photocathode during energy-loss measurements.** The voltage slope is determined by fitting a linear function to the measured voltage U_s at the backplate during each run. To avoid timing issues 50 s at the start and end of the run are excluded in the fit. The black line is the mean value and the gray shaded area, the standard deviation of all values. To show the slopes both for up and down runs in one plot, their absolute value is plotted. The slopes shown here are for the energy-loss measurement on tritium at 22 % $\rho_0 d$. The other measurements show a similar picture. The average voltage slope and standard deviation for all measurements can be found in table 3.5.

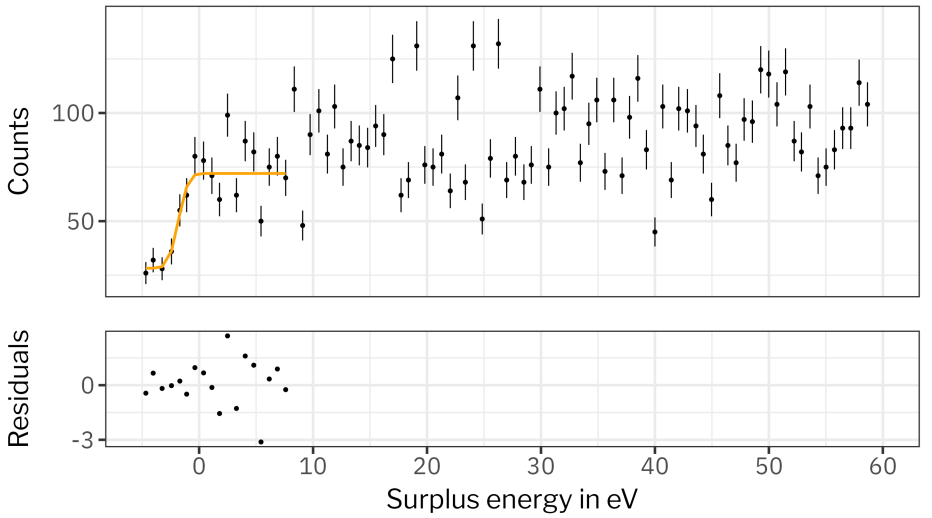

Figure A.13 **Measurement of the e-gun background.** The accumulated counts over three runs of e-gun background measurements. The measurement setup is similar to the standard energy-loss measurements but with the laser turned off. During the measurements the source was filled with tritium at about 22 % $\rho_0 d$. The surplus energy E'_s (3.12) on the x-axis is determined with a different procedure as normal energy-loss measurements. The orange line is an error function fit (3.13) with its residuals plotted below. The fit has a reduced χ^2 value of 2.0(4). The fit is only for $E'_s < 8$ eV, to only consider unscattered electrons. The fitted error function has a width of $\sigma = 0.7(4)$ eV and a position $\mu = -1.8(3)$ eV.

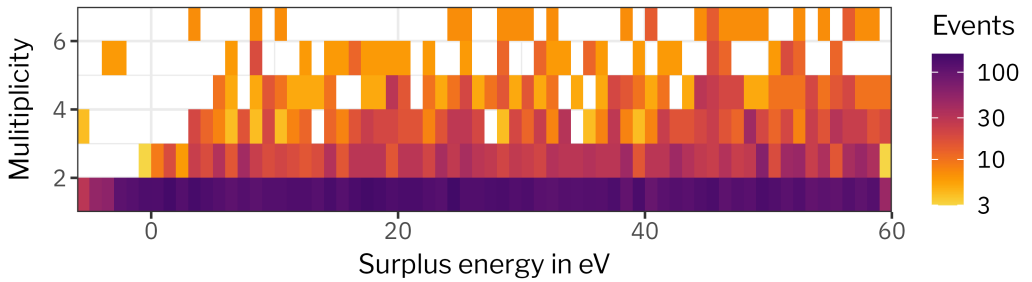

Figure A.14 **Multiplicity of events during a background run.** For each event recorded at the detector, its multiplicity is plotted against the surplus energy. The multiplicity for each event is determined via a pile-up reconstruction scheme.

Table A.15 **Best-fit parameters of the energy-loss fit.** The results for the parameters $\mathscr{P}$ of the least square minimization of tof-only fit (3.17) and the combined fit (3.21) are listed. All values are in eV, except the values for a_i which are in 1/eV. For the tof-only fit, $\chi^2 = 1.08(2)$ and for the combined fit $\chi^2 = 1.13(2)$. For the differential datasets, the indices relate to the column densities in the following way: $1\widehat{=}15\,\%$, $2\widehat{=}22\,\%$, $3\widehat{=}39\,\%$, and $4\widehat{=}84\,\%\ \rho_0 d$. For the integral datasets: $1\widehat{=}14\,\%$, $2\widehat{=}41\,\%$, and $3\widehat{=}86\,\%\ \rho_0 d$. The column density values are estimated from the mean scattering probabilities μ of the fit.

$\mathscr{P}$	tof-only	combined
m_1	11.921(8)	11.919(8)
m_2	12.805(2)	12.805(2)
m_3	14.958(4)	14.968(4)
σ_1	0.184(6)	0.184(7)
σ_2	0.468(2)	0.468(2)
σ_3	0.89(1)	0.90(1)
a_1	0.033(1)	0.033(1)
a_2	0.2979(8)	0.2957(6)
a_3	0.0764(4)	0.0758(3)
$\mu_{\text{int},1}$	-	0.2538(3)
$\mu_{\text{int},2}$	-	0.7452(3)
$\mu_{\text{int},3}$	-	1.5573(4)
$\mu_{\text{tof},1}$	0.270(4)	0.269(4)
$\mu_{\text{tof},2}$	0.406(5)	0.406(5)
$\mu_{\text{tof},3}$	0.718(5)	0.718(5)
$\mu_{\text{tof},4}$	1.521(5)	1.524(5)
$c_{\text{int},1}$	-	1.0075(2)
$c_{\text{int},2}$	-	1.0649(2)
$c_{\text{int},3}$	-	1.2351(4)
$c_{\text{tof},1}$	0.99(1)	0.99(1)
$c_{\text{tof},2}$	1.010(8)	1.013(8)
$c_{\text{tof},3}$	1.038(4)	1.041(4)
$c_{\text{tof},4}$	1.181(3)	1.186(3)
$b_{\text{int},1}$	-	0.000 29(3)
$b_{\text{int},2}$	-	0.000 63(4)
$b_{\text{int},3}$	-	0.0030(1)
$b_{\text{tof},1}$	0.000 17(2)	0.000 16(2)
$b_{\text{tof},2}$	0.000 41(4)	0.000 39(4)
$b_{\text{tof},3}$	0.000 63(5)	0.000 59(5)
$b_{\text{tof},4}$	0.001 85(1)	0.001 73(9)

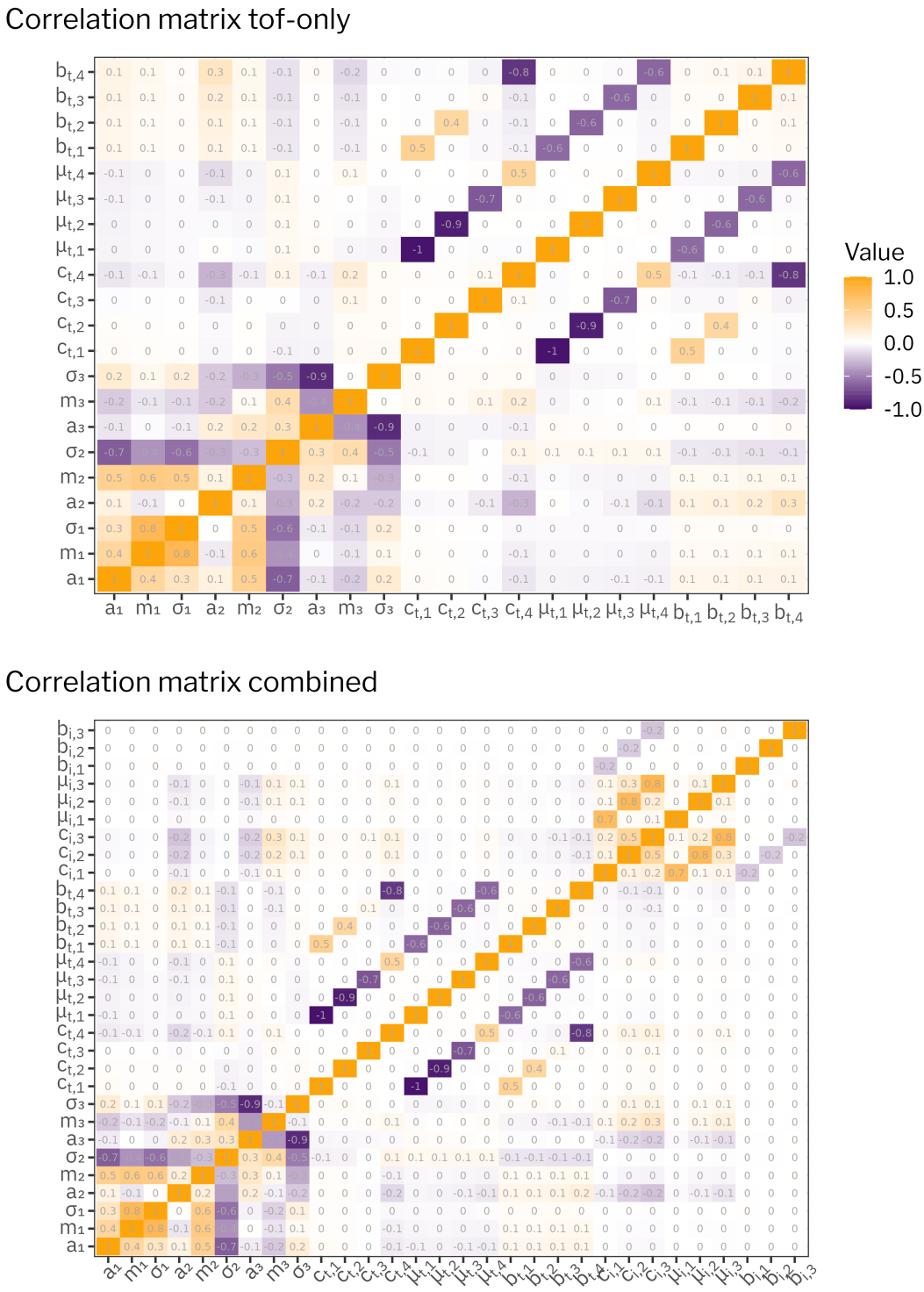

Figure A.16 **Correlation matrix of the energy-loss fit.** The color scale reflects the correlation value and is the same scale for both upper and lower plot. Here, "i" and "t" in the indices are shorthand for "int" and "tof" used everywhere else. The best fit parameters are listed in table A.15.

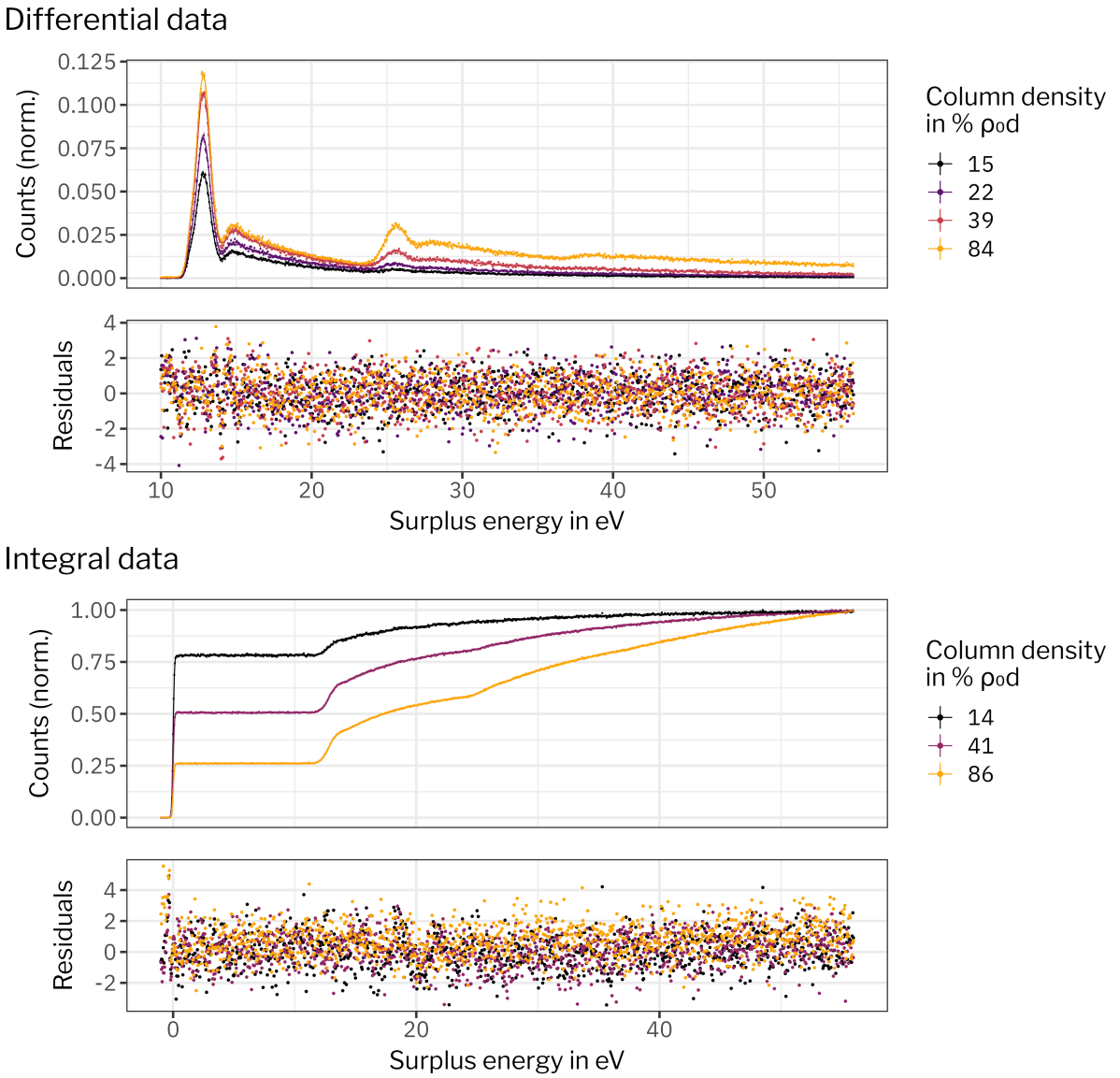

Figure A.17 **Combined fit result for the differential and integral data.** The measurement points and the resulting fit model (colored lines) are shown for all datasets that are used in the combined fit. The measured counts in the differential datasets are normalized by the area below all counts within −1 eV to 56 eV. In the integral datasets the counts are normalized by the count rate in the highest surplus energy bin. The residuals are normalized by the uncertainties of the observation. The best-fit parameters are listed in table A.15.

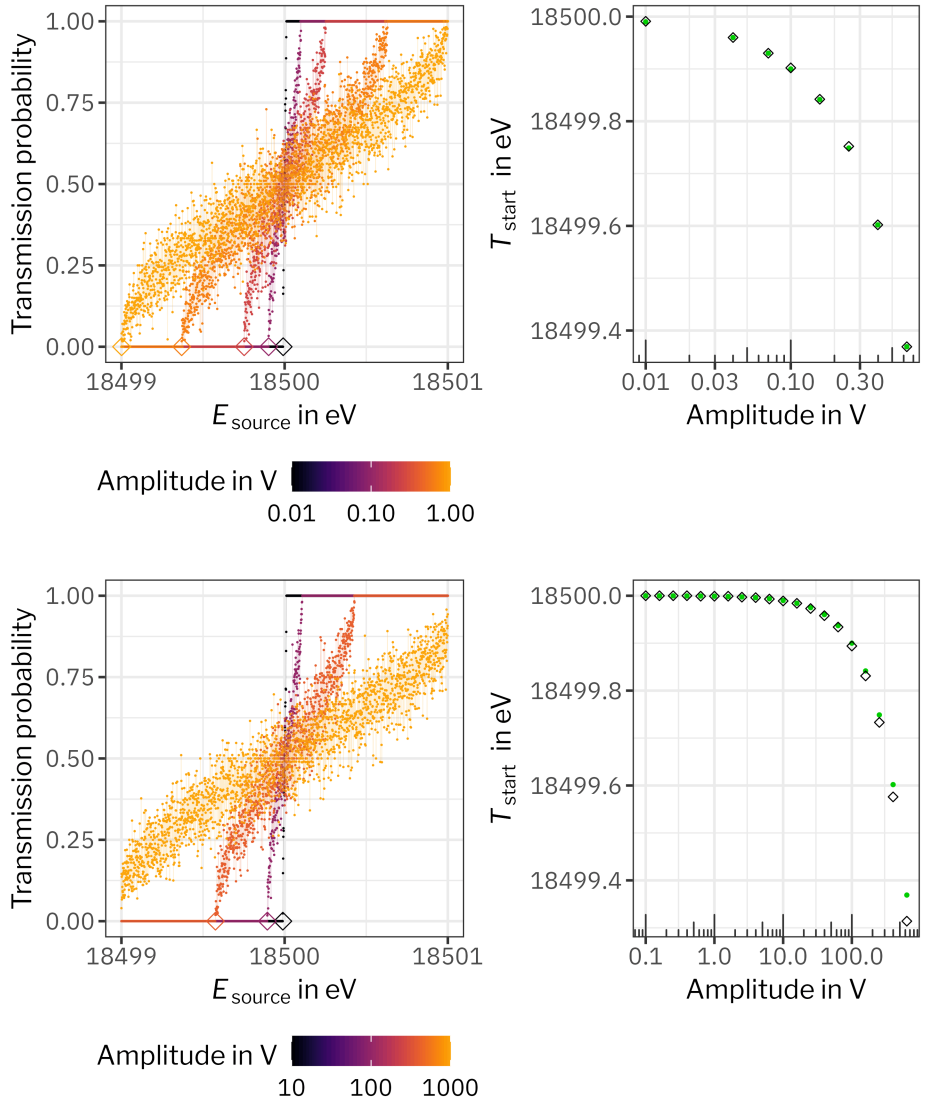

Figure A.18 **Transmission function for a sinusoidal ripple at various amplitudes.** $f_{\sin}(t)$ is used as time-dependent ripple in the simulation, with a fixed frequency of 50 Hz (top row) and 5×10^8 Hz (bottom row), at various amplitudes. For each of the two frequencies, 100 000 electrons are generated with $\theta = 0$, starting potential $E_{\text{source}} \in [18\,499\,\text{eV}, 18\,500\,\text{eV}]$, and randomized start times $t_{\text{start}} \in [0, 1/f]$. Their transmission probabilities are shown in the left column. In the right column, the black diamonds show T_{start} as a function of amplitude, where T_{start} is defined as the minimal E_{source} that is sufficient for the transmission of an electron (also indicated with diamonds in the left column). The green points in the upper right panel are equivalent to $U_0 - A$ and the ones in the lower right panel to $U_0 - A/1000$.

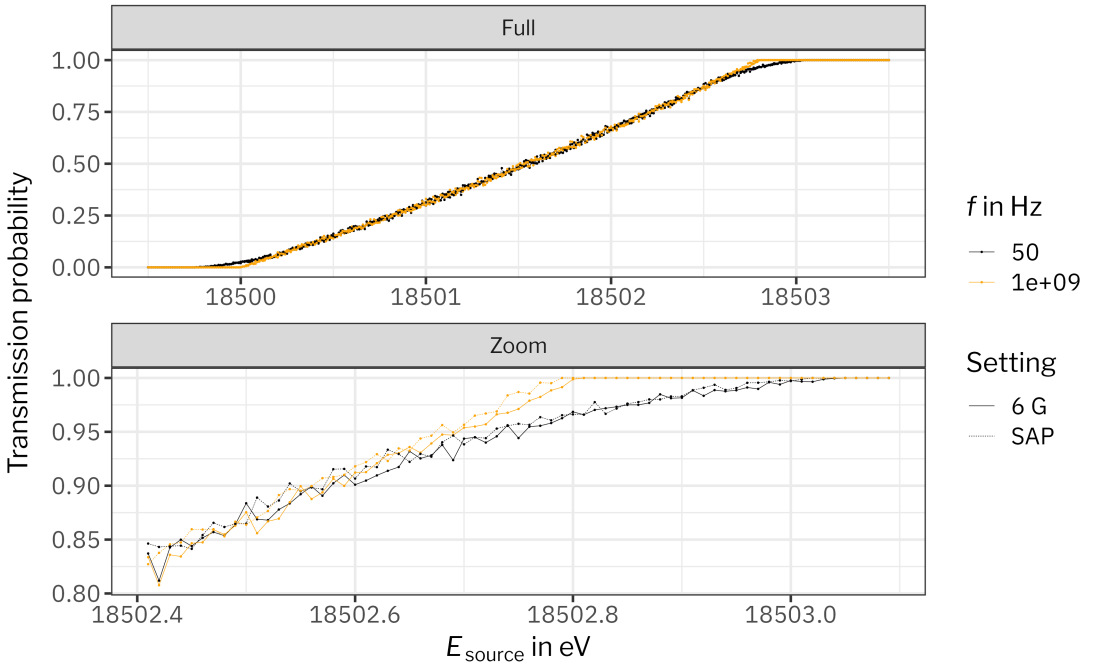

Figure A.19 **Broadening of the transmission function by a sinusoidal ripple.** For each setting (6 G / SAP), a simulation with 1×10^6 electrons is performed. The energies of the electron E_{source} are randomly sampled within $[18\,503.5\,\text{eV}, 18\,508.5\,\text{eV}]$. Their angles are picked from $\theta = \arccos(U(0,1) \cdot (1 - \cos(\theta_{\max})) + \cos(\theta_{\max}))$, here $U(0,1)$ is a uniform distribution within $[0,1]$ and $\theta_{\max} = \arcsin(\sqrt{\frac{B_{\text{source}}}{B_{\text{pinch}}}})$. The ripple $f_{\sin}(t)$ has a fixed amplitude at 0.25 V and the simulation is run for two different frequencies $f = 50\,\text{Hz}, 1\,\text{GHz}$.

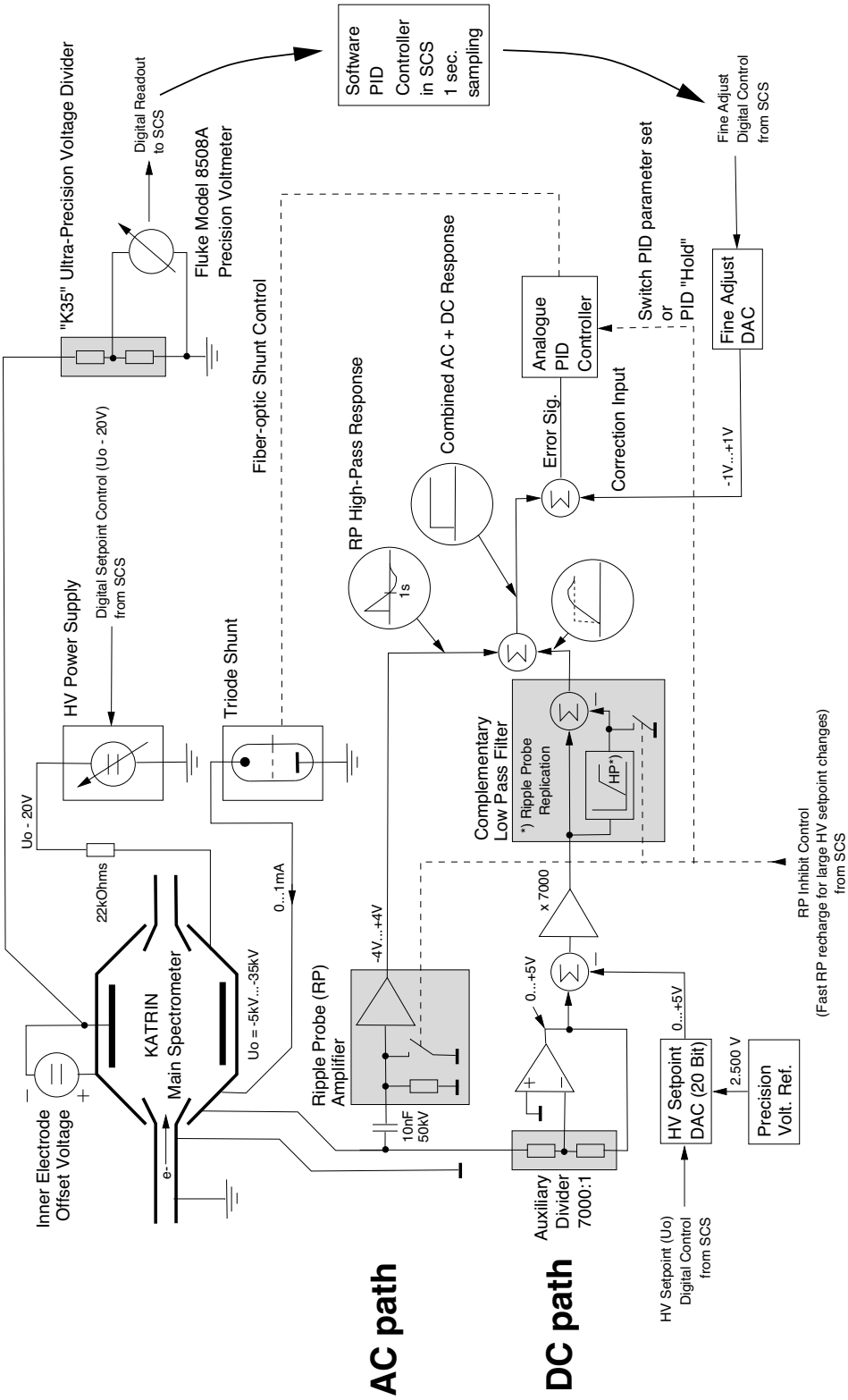

Figure A.20 **Block diagram of the post-regulation system.** A detailed block diagram of the post-regulation setup at KATRIN's main spectrometer.

The diagram was drawn by S. Wüstling and is published in [Rod+22], licensed under CC BY 4.0.

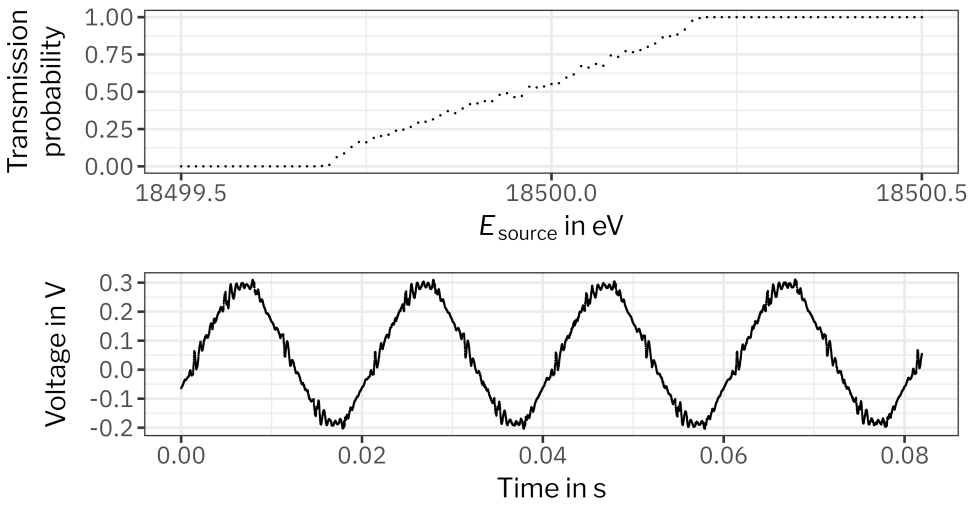

Figure A.21 **Broadening of the transmission function without post-regulation.** As time-dependent ripple for the simulation a ripple probe measurement (bottom panel) is used. 100 000 electrons with $\theta = 0°$, starting potential $E_{\text{source}} \in [18\,499.5\,\text{eV}, 18\,500.5\,\text{eV}]$, and randomized start times $t_{\text{start}} \in [0\,\text{s}, 0.08\,\text{s}]$ are generated. Their transmission probability is shown in the top panel.

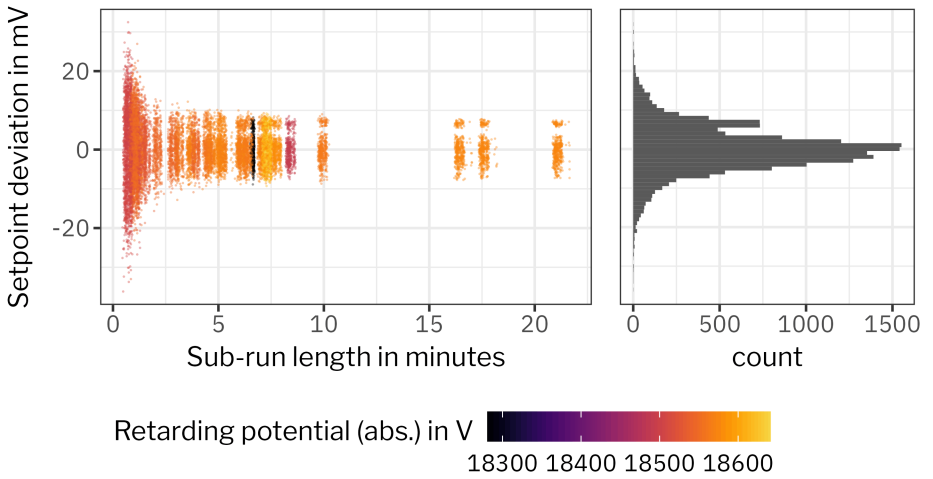

Figure A.22 **Reproducibility for KNM5 sub-runs.** The reproducibility is plotted against the length of a sub-run. The color corresponds to a setpoint for each sub-run. The scatter of the sub-run length is due to the dynamic adjustment of the sub-run boundaries to minimize the settling time (section 4.2.2).

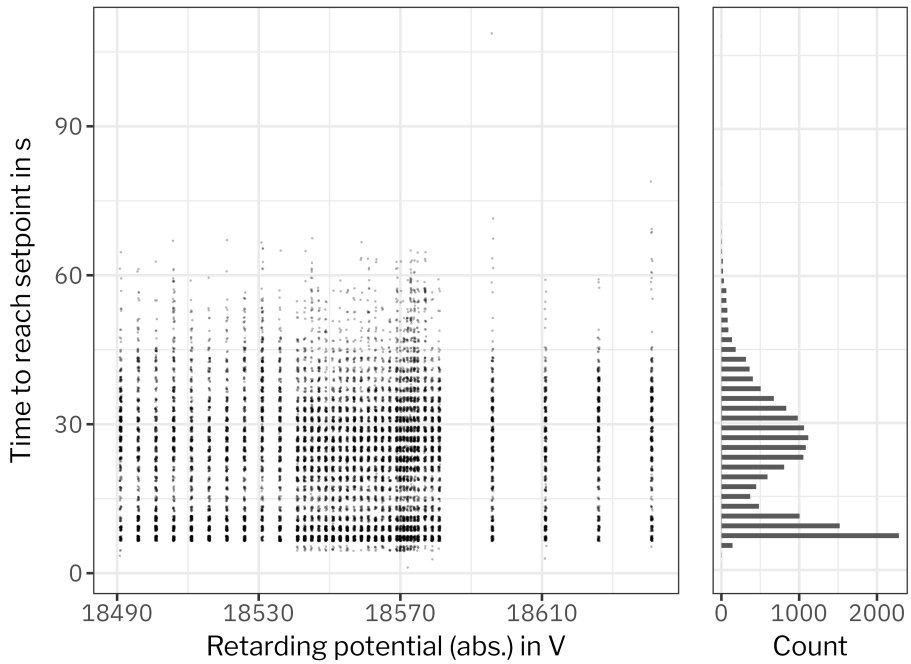

Figure A.23 **High voltage settling time for KNM5 sub-runs.** The time between sub-runs is plotted against the voltage setpoint for each sub-run. To improve visibility, the points are jittered along both axes and plotted with some transparency.

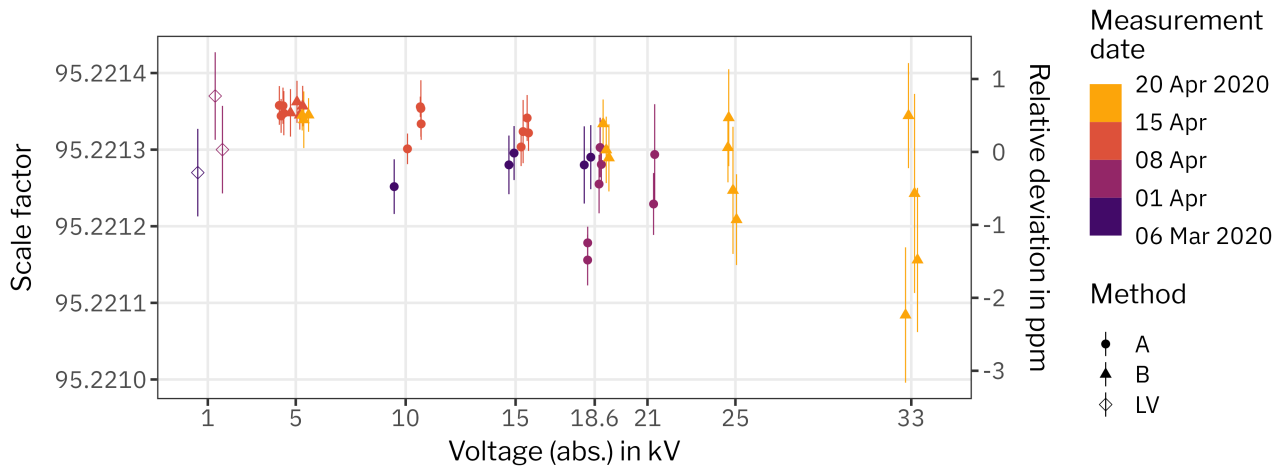

Figure A.24 **Differential scale factor of the K35.** The differential scale factor M'_{test} is plotted against the seven different voltages U_{test} applied to the K35 during the μ measurement. Additionally, the low-voltage calibration measurements at 1 kV are plotted. Some jitter is added to the horizontal positions for better visibility.

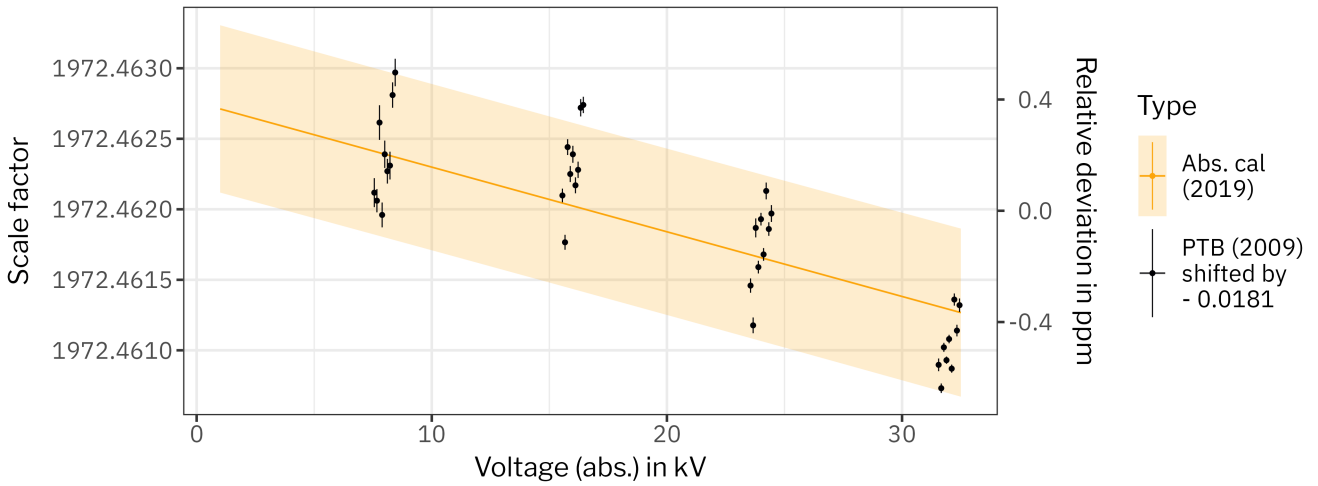

Figure A.25 **Voltage dependency of the K35's M_{1972} scale factor.** Comparison of the result obtained in 2019 with the absolute calibration method, as described in section 4.5.2 and a calibration at the Physikalisch Technische Bundesanstalt (PTB) in 2009, as published in [TMW09]. The absolute scale factor is different for both measurements. In order to compare the voltage dependency, the PTB result was shifted to match the 2019 result.

References

[Abd+17] D. N. Abdurashitov et al. “Electron scattering on hydrogen and deuterium molecules at 14–25 keV by the ‘Troitsk nu-mass’ experiment”. In: *Phys. Part. Nuclei Lett.* 14.6 (Nov. 2017), pp. 892–899. DOI: 10.1134/S1547477117060024.

[All66] D. W. Allan. “Statistics of atomic frequency standards”. In: *Proc. of the IEEE* 54.2 (Feb. 1966), pp. 221–230. DOI: 10.1109/PROC.1966.4634.

[Alp+15] B. Alpert et al. “HOLMES”. In: *Eur. Phys. J. C* 75, 112 (Mar. 2015). DOI: 10.1140/epjc/s10052-015-3329-5.

[Ams+15] J. F. Amsbaugh et al. “Focal-plane detector system for the KATRIN experiment”. In: *Nucl. Inst. and Meth. A* 778 (Apr. 2015), pp. 40–60. DOI: 10.1016/j.nima.2014.12.116.

[Ase+00] V. N. Aseev et al. “Energy loss of 18 keV electrons in gaseous T and quench condensed D films”. In: *Eur. Phys. J. D* 10.1 (Mar. 2000), pp. 39–52. DOI: 10.1007/s100530050525.

[Bab+12] M. Babutzka et al. “Monitoring of the operating parameters of the KATRIN windowless gaseous tritium source”. In: *New J. Phys.* 14, 103046 (Oct. 2012). DOI: 10.1088/1367-2630/14/10/103046.

[Bab14] M. Babutzka. “Design and development for the Rearsection of the KATRIN experiment”. PhD thesis. Karlsruhe Institute of Technology, 2014. DOI: 10.5445/IR/1000045598.

[Bah64a] J. N. Bahcall. “Solar neutrino cross sections and nuclear beta decay”. In: *Phys. Rev.* 135.1B (July 1964), B137–B146. DOI: 10.1103/PhysRev.135.B137.

[Bah64b] J. N. Bahcall. “Solar neutrinos. I. Theoretical”. In: *Phys. Rev. Lett.* 12.11 (Mar. 1964), pp. 300–302. DOI: 10.1103/PhysRevLett.12.300.

[Bar16] J. P. Barrett. “A spatially resolved study of the KATRIN main spectrometer using a novel fast multipole method”. PhD thesis. Massachusetts Institute of Technology, 2016. URL: https://dspace.mit.edu/handle/1721.1/114314.

[Bau14] S. Bauer. “Energy calibration and stability monitoring of the KATRIN experiment”. PhD thesis. University of Münster, 2014. URL: https://nbn-resolving.org/urn:nbn:de:hbz:6-04329567654.

[Bau+13] S. Bauer et al. “Next generation KATRIN high precision voltage divider for voltages up to 65 kV”. In: *J. Instrum.* 8, P10026 (Oct. 2013). DOI: 10.1088/1748-0221/8/10/P10026.

[BPT80] G. Beamson, H. Q. Porter, and D. W. Turner. “The collimating and magnifying properties of a superconducting field photoelectron spectrometer”. In: *J. Phys. E* 13.1 (Jan. 1980), p. 64. DOI: 10.1088/0022-3735/13/1/018.

[Bec96] H. Becquerel. “Sur les radiations émises par phosphorescence”. French. In: *C. R. Acad. Sci.* 122.8 (Feb. 1896), pp. 420–421. URL: https://gallica.bnf.fr/ark:/12148/bpt6k30780/f422.item.

[Beg+22] A. Beglarian et al. “Forward Beam Monitor for the KATRIN experiment”. In: *J. Instrum.* 17, T03002 (Mar. 2022). DOI: 10.1088/1748-0221/17/03/t03002.

[Beh16] J. Behrens. “Design and commissioning of a mono-energetic photoelectron source and active background reduction by magnetic pulse at the KATRIN spectrometers”. PhD thesis. University of Münster, 2016. URL: https://www.katrin.kit.edu/publikationen/phd_behrens.pdf.

[Beh+17] J. Behrens et al. “A pulsed, mono-energetic and angular-selective UV photoelectron source for the commissioning of the KATRIN experiment”. In: *Eur. Phys. J. C* 77, 410 (June 2017). DOI: 10.1140/epjc/s10052-017-4972-9.

[Bél+18] G. Bélanger, F. Boudjema, A. Goudelis, A. Pukhov, and B. Zaldívar. “micrOMEGAs5.0: Freeze-in”. In: *Comput. Phys. Commun.* 231 (Oct. 2018), pp. 173–186. DOI: 10.1016/j.cpc.2018.04.027.

[Bel+08] A. I. Belesev et al. “Investigation of space-charge effects in gaseous tritium as a source of distortions of the beta spectrum observed in the Troitsk neutrino-mass experiment”. In: *Phys. At. Nucl.* 71.3 (Mar. 2008), pp. 427–436. DOI: 10.1134/S1063778808030046.

[Blo22] F. Block. “Determination of electromagnetic fields and tritium column density for neutrino mass analysis with KATRIN”. PhD thesis. Karlsruhe Institute of Technology, 2022. DOI: 10.5445/IR/1000145073.

[Blo+13] A. Blondel et al. *Research proposal for an experiment to search for the decay $\mu \longrightarrow eee$*. Submitted to the Paul Scherrer Institute’s Research Committee for Particle Physics at the Ring Cyclotron. Jan. 2013. DOI: 10.48550/ARXIV.1301.6113.

[Boe+20] T. de Boer, M. Klasen, C. Rodenbeck, and S. Zeinstra. “Absolute neutrino mass as the missing link to the dark sector”. In: *Phys. Rev. D* 102, 051702 (Sept. 2020). DOI: 10.1103/PhysRevD.102.051702.

[Bon+99] J. Bonn, L. Bornschein, B. Degen, E. W. Otten, and C. Weinheimer. “A high resolution electrostatic time-of-flight spectrometer with adiabatic magnetic collimation”. In: *Nucl. Inst. and Meth. A* 421.1 (Jan. 1999), pp. 256–265. DOI: 10.1016/S0168-9002(98)01263-7.

[CI01] J. A. Casas and A. Ibarra. “Oscillating neutrinos and $\mu \longrightarrow e, \gamma$”. In: *Nucl. Phys. B* 618.1 (Dec. 2001), pp. 171–204. DOI: 10.1016/S0550-3213(01)00475-8.

[Cha14] J. Chadwick. “Intensitätsverteilung im magnetischen Spektrum der β-Strahlen von Radium B + C”. German. In: *Verh. Dtsch. Phys. Ges.* 2nd ser. 16 (Apr. 1914), pp. 383–391.

[Cha32] J. Chadwick. “Possible existence of a neutron”. In: *Nature* 129.3252 (Feb. 1932), p. 312. DOI: 10.1038/129312a0.

[Cle+98] B. T. Cleveland et al. “Measurement of the solar electron neutrino flux with the Homestake chlorine detector”. In: *Astrophys. J.* 496.1 (Mar. 1998), p. 505. DOI: 10.1086/305343.

[Cow+56] C. L. Cowan, F. Reines, F. B. Harrison, H. W. Kruse, and A. D. McGuire. “Detection of the free neutrino: A confirmation”. In: *Science* 124.3212 (July 1956), pp. 103–104. DOI: 10.1126/science.124.3212.103.

[CAC49] S. C. Curran, J. Angus, and A. L. Cockroft. “The beta-spectrum of tritium”. In: *Phys. Rev.* 76.6 (Sept. 1949), pp. 853–854. DOI: 10.1103/PhysRev.76.853.

[Dan+62] G. Danby, J.-M. Gaillard, K. Goulianos, L. M. Lederman, N. Mistry, M. Schwartz, and J. Steinberger. “Observation of high-energy neutrino reactions and the existence of two kinds of neutrinos”. In: *Phys. Rev. Lett.* 9.1 (July 1962), pp. 36–44. DOI: 10.1103/PhysRevLett.9.36.

[Dav64] R. Davis. “Solar neutrinos. II. Experimental”. In: *Phys. Rev. Lett.* 12.11 (Mar. 1964), pp. 303–305. DOI: 10.1103/PhysRevLett.12.303.

[DHH68] R. Davis, D. S. Harmer, and K. C. Hoffman. “Search for neutrinos from the sun”. In: *Phys. Rev. Lett.* 20.21 (May 1968), pp. 1205–1209. DOI: 10.1103/PhysRevLett.20.1205.

[DS90] D. J. Decman and W. Stoeffl. “Atomic electron binding energies of multiply charged krypton ions by internal-conversion-electron spectroscopy”. In: *Phys. Rev. Lett.* 64.23 (June 1990), pp. 2767–2770. DOI: 10.1103/PhysRevLett.64.2767.

[Dyb19] S. Dyba. “Background reduction by the inner wire electrode and set-up of the condensed krypton source at the neutrino mass experiment KATRIN”. PhD thesis. University of Münster, 2019. URL: https://nbn-resolving.org/urn:nbn:de:hbz:6-15149612886.

[EHM87] S. R. Elliott, A. A. Hahn, and M. K. Moe. “Direct evidence for two-neutrino double-beta decay in ^{82}Se”. In: *Phys. Rev. Lett.* 59.18 (Nov. 1987), pp. 2020–2023. DOI: 10.1103/PhysRevLett.59.2020.

[EWR27] C. D. Ellis, W. A. Wooster, and E. Rutherford. “The average energy of disintegration of radium E”. In: *Proc. R. Soc. A* 117.776 (Dec. 1927), pp. 109–123. DOI: 10.1098/rspa.1927.0168.

[EB64] F. Englert and R. Brout. “Broken symmetry and the mass of gauge vector mesons”. In: *Phys. Rev. Lett.* 13.9 (Aug. 1964), pp. 321–323. DOI: 10.1103/PhysRevLett.13.321.

[Erh+14] M. Erhard et al. “High-voltage monitoring with a solenoid retarding spectrometer at the KATRIN experiment”. In: *J. Instrum.* 9, P06022 (June 2014). DOI: 10.1088/1748-0221/9/06/P06022.

[Erh+18] M. Erhard et al. “Technical design and commissioning of the KATRIN large-volume air coil system”. In: *J. Instrum.* 13, P02003 (Feb. 2018). DOI: 10.1088/1748-0221/13/02/P02003.

[Est+20] I. Esteban, M. C. Gonzalez-Garcia, M. Maltoni, T. Schwetz, and A. Zhou. “The fate of hints: Updated global analysis of three-flavor neutrino oscillations”. In: *J. High Energy Phys.* 2020.9 (Sept. 2020), p. 178. DOI: 10.1007/JHEP09(2020)178.

[Fed19] M. Fedkevych. “Calibration and background reduction of the KATRIN experiment”. PhD thesis. University of Münster, 2019. URL: https://www.uni-muenster.de/imperia/md/content/physik_kp/agweinheimer/theses/diss_mariia_fedkevych.pdf.

[Fer34] E. Fermi. “Versuch einer Theorie der β-Strahlen. I”. German. In: *Z. Phys.* 88.3 (Mar. 1934), pp. 161–177. DOI: 10.1007/BF01351864.

[FGR21] J. A. Formaggio, A. L. C. de Gouvêa, and R. G. H. Robertson. “Direct measurements of neutrino mass”. In: *Phys. Rep.* 914 (June 2021), pp. 1–54. DOI: 10.1016/j.physrep.2021.02.002.

[Frä+11] F. M. Fränkle et al. “Radon induced background processes in the KATRIN pre-spectrometer”. In: *Astropart. Phys.* 35.3 (Oct. 2011), pp. 128–134. DOI: 10.1016/j.astropartphys.2011.06.009.

[Frä+22] F. M. Fränkle et al. “KATRIN background due to surface radioimpurities”. In: *Astropart. Phys.* 138, 102686 (2022). DOI: 10.1016/j.astropartphys.2022.102686.

[Fri+19] F. Friedel et al. “Time-dependent simulation of the flow reduction of D_2 and T_2 in the KATRIN experiment”. In: *Vacuum* 159 (Jan. 2019), pp. 161–172. DOI: 10.1016/j.vacuum.2018.10.002.

[Fri20] F. R. Friedel. “Ion and plasma systematics during the first KATRIN neutrino mass measurements”. PhD thesis. Karlsruhe Institute of Technology, 2020. DOI: 10.5445/IR/1000126837.

[Ful20] A. Fulst. “A novel quasi-differential method for MAC-E filters and determination and control of the electric potentials of the KATRIN experiment with a stabilized condensed krypton source and a UV illumination system”. PhD thesis. University of Münster, 2020.

[Ful+20] A. Fulst, A. Lokhov, M. Fedkevych, N. Steinbrink, and C. Weinheimer. “Time-focusing time-of-flight, a new method to turn a MAC-E-filter into a quasi-differential spectrometer”. In: *Eur. Phys. J. C* 80, 956 (Oct. 2020). DOI: 10.1140/epjc/s10052-020-08484-9.

[Fur+17] D. Furse et al. “Kassiopeia: A modern, extensible C++ particle tracking package”. In: *New J. Phys.* 19, 053012 (May 2017). DOI: 10.1088/1367-2630/aa6950.

[Gas+17] L. Gastaldo et al. “The electron capture in ^{163}Ho experiment – ECHo”. In: *Eur. Phys. J. ST* 226.8 (June 2017), pp. 1623–1694. DOI: 10.1140/epjst/e2017-70071-y.

[Gei64] J. Geiger. “Streuung von 25 keV-Elektronen an Gasen”. German. In: *Z. Phys.* 181.4 (Aug. 1964), pp. 413–425. DOI: 10.1007/BF01380873.

[GS69] J. Geiger and H. Schmoranzer. “Electronic and vibrational transition probabilities of isotopic hydrogen molecules H_2, HD, and D_2 based on electron energy loss spectra”. In: *J. Mol. Spectrosc.* 32.1 (Oct. 1969), pp. 39–53. DOI: 10.1016/0022-2852(69)90141-6.

[Ger20] M. Agostini et al. (GERDA collaboration). “Final results of GERDA on the search for neutrinoless double-β decay”. In: *Phys. Rev. Lett.* 125, 252502 (Dec. 2020). DOI: 10.1103/PhysRevLett.125.252502.

[Gla61] S. L. Glashow. “Partial-symmetries of weak interactions”. In: *Nucl. Phys.* 22.4 (Feb. 1961), pp. 579–588. DOI: 10.1016/0029-5582(61)90469-2.

[Goe35] M. Goeppert-Mayer. “Double beta-disintegration”. In: *Phys. Rev.* 48.6 (Sept. 1935), pp. 512–516. DOI: 10.1103/PhysRev.48.512.

[GGS58] M. Goldhaber, L. Grodzins, and A. W. Sunyar. “Helicity of neutrinos”. In: *Phys. Rev.* 109.3 (Feb. 1958), pp. 1015–1017. DOI: 10.1103/PhysRev.109.1015.

[Gri08] D. J. Griffiths. *Introduction to Elementary Particles*. 2nd ed. Wiley-VCH Verlag GmbH & Co. KGaA, 2008. ISBN: 978-3-527-40601-2.

[HP49] G. C. Hanna and B. Pontecorvo. “The β-spectrum of H^3”. In: *Phys. Rev.* 75.6 (Mar. 1949), pp. 983–984. DOI: 10.1103/PhysRev.75.983.3.

[Han+17] V. Hannen, I. Heese, C. Weinheimer, A. Sejersen Riis, and K. Valerius. “Deconvolution of the energy loss function of the KATRIN experiment”. In: *Astropart. Phys.* 89 (Mar. 2017), pp. 30–38. DOI: 10.1016/j.astropartphys.2017.01.010.

[HLS20] R. S. L. Hansen, M. Lindner, and O. Scholer. “Timing the neutrino signal of a galactic supernova”. In: *Phys. Rev. D* 101, 123018 (June 2020). DOI: 10.1103/PhysRevD.101.123018.

[Hig64] P. W. Higgs. “Broken symmetries and the masses of gauge bosons”. In: *Phys. Rev. Lett.* 13.16 (Oct. 1964), pp. 508–509. DOI: 10.1103/PhysRevLett.13.508.

[Hir+88] K. S. Hirata et al. “Experimental study of the atmospheric neutrino flux”. In: *Phys. Lett. B* 205.2 (Apr. 1988), pp. 416–420. DOI: 10.1016/0370-2693(88)91690-5.

[Hug10] K. Hugenberg. “An angular resolved pulsed UV LED photoelectron source for KATRIN”. In: *Prog. Part. Nucl. Phys.* 64.2 (Apr. 2010): *Neutrinos in Cosmology, in Astro, Particle and Nuclear Physics. International Workshop on Nuclear Physics, 31st course (ERICE 2009)*, pp. 288–290. DOI: 10.1016/j.ppnp.2009.12.031.

[Ino71] M. Inokuti. “Inelastic collisions of fast charged particles with atoms and molecules – the Bethe theory revisited”. In: *Rev. Mod. Phys.* 43.3 (July 1971), pp. 297–347. DOI: 10.1103/RevModPhys.43.297.

[Ino+81] M. Inokuti, J. L. Dehmer, T. Baer, and J. D. Hanson. “Oscillator-strength moments, stopping powers, and total inelastic-scattering cross sections of all atoms through strontium”. In: *Phys. Rev. A* 23.1 (Jan. 1981), pp. 95–109. DOI: 10.1103/PhysRevA.23.95.

[Kat05] J. Angrik et al. (KATRIN collaboration). *KATRIN Design Report 2004*. FZKA scientific report 7090. Feb. 2005. DOI: 10.5445/IR/270060419.

[Kat16] M. Arenz et al. (KATRIN collaboration). “Commissioning of the vacuum system of the KATRIN main spectrometer”. In: *J. Instrum.* 11, P04011 (Apr. 2016). DOI: 10.1088/1748-0221/11/04/P04011.

[Kat18a] M. Arenz et al. (KATRIN collaboration). “Calibration of high voltages at the ppm level by the difference of ^{83m}Kr conversion electron lines at the KATRIN experiment”. In: *Eur. Phys. J. C* 78, 368 (May 2018). DOI: 10.1140/epjc/s10052-018-5832-y.

[Kat18b] M. Arenz et al. (KATRIN collaboration). “First transmission of electrons and ions through the KATRIN beamline”. In: *J. Instrum.* 13, P04020 (Apr. 2018). DOI: 10.1088/1748-0221/13/04/P04020.

[Kat18c] M. Arenz et al. (KATRIN collaboration). “Reduction of stored-particle background by a magnetic pulse method at the KATRIN experiment”. In: *Eur. Phys. J. C* 78, 778 (Sept. 2018). DOI: 10.1140/epjc/s10052-018-6244-8.

[Kat18d] M. Arenz et al. (KATRIN collaboration). “The KATRIN superconducting magnets: Overview and first performance results”. In: *J. Instrum.* 13, T08005 (Aug. 2018). DOI: 10.1088/1748-0221/13/08/T08005.

[Kat19] M. Aker et al. (KATRIN collaboration). “Improved upper limit on the neutrino mass from a direct kinematic method by KATRIN”. In: *Phys. Rev. Lett.* 123, 221802 (Nov. 2019). DOI: 10.1103/PhysRevLett.123.221802.

[Kat20a] M. Aker et al. (KATRIN collaboration). “First operation of the KATRIN experiment with tritium”. In: *Eur. Phys. J. C* 80, 264 (Mar. 2020). DOI: 10.1140/epjc/s10052-020-7718-z.

[Kat20b] K. Altenmüller et al. (KATRIN collaboration). “High-resolution spectroscopy of gaseous ^{83m}Kr conversion electrons with the KATRIN experiment”. In: *J. Phys. G* 47, 065002 (May 2020). DOI: 10.1088/1361-6471/ab8480.

[Kat20c] M. Aker et al. (KATRIN collaboration). “Quantitative long-term monitoring of the circulating gases in the KATRIN experiment using Raman spectroscopy”. In: *Sensors* 20.17 (Aug. 2020). DOI: 10.3390/s20174827.

[Kat21a] M. Aker et al. (KATRIN collaboration). “Analysis methods for the first KATRIN neutrino-mass measurement”. In: *Phys. Rev. D* 104, 012005 (July 2021). DOI: 10.1103/PhysRevD.104.012005.

[Kat21b] M. Aker et al. (KATRIN collaboration). “Precision measurement of the electron energy-loss function in tritium and deuterium gas for the KATRIN experiment”. In: *Eur. Phys. J. C* 81, 579 (July 2021). DOI: 10.1140/epjc/s10052-021-09325-z.

[Kat21c] M. Aker et al. (KATRIN collaboration). “The design, construction, and commissioning of the KATRIN experiment”. In: *J. Instrum.* 16, T08015 (Aug. 2021). DOI: 10.1088/1748-0221/16/08/t08015.

[Kat22] M. Aker et al. (KATRIN collaboration). “Direct neutrino-mass measurement with sub-electronvolt sensitivity”. In: *Nat. Phys.* 18.2 (Feb. 2022), pp. 160–166. DOI: 10.1038/s41567-021-01463-1.

[Kay03] B. Kayser. “Neutrino mass, mixing, and flavor change”. In: *Neutrino Mass*. Ed. by G. Altarelli and K. Winter. Springer Tracts in Modern Physics 190. Springer, 2003, pp. 1–24. ISBN: 978-3-540-40328-9. DOI: 10.1007/b13585.

[Kaz+08] O. Kazachenko, B. Bornschein, N. Kernert, L. Doerr, M. Glugla, V. Weber, and D. Stern. “Tritium processing loop for KATRIN experiment”. In: *Fusion Sci. Technol.* 54.1 (July 2008): *Proceedings of the Eighth International Conference on Tritium Science and Technology; Rochester, New York, September 16–21, 2007*, pp. 67–70. DOI: 10.13182/FST08-A1766.

[Kib67] T. W. B. Kibble. “Symmetry breaking in non-abelian gauge theories”. In: *Phys. Rev.* 155.5 (Mar. 1967), pp. 1554–1561. DOI: 10.1103/PhysRev.155.1554.

[KR94] Y.-K. Kim and M. E. Rudd. “Binary-encounter-dipole model for electron-impact ionization”. In: *Phys. Rev. A* 50.5 (Nov. 1994), pp. 3954–3967. DOI: 10.1103/PhysRevA.50.3954.

[KSP00] Y.-K. Kim, J. P. Santos, and F. Parente. “Extension of the binary-encounter-dipole model to relativistic incident electrons”. In: *Phys. Rev. A* 62, 052710 (Oct. 2000). DOI: 10.1103/PhysRevA.62.052710.

[Kle+19] M. Kleesiek et al. “β-Decay Spectrum, response function and statistical model for neutrino mass measurements with the KATRIN experiment”. In: *Eur. Phys. J. C* 79, 204 (Mar. 2019). DOI: 10.1140/epjc/s10052-019-6686-7.

[Kle14] M. Kleesiek. “A data-analysis and sensitivity-optimization framework for the KATRIN experiment”. PhD thesis. Karlsruhe Institute of Technology, 2014. DOI: 10.5445/IR/1000043301.

[KLZ16] A. Gando et al. (KamLAND-Zen collaboration). “Search for Majorana neutrinos near the inverted mass hierarchy region with KamLAND-Zen”. In: *Phys. Rev. Lett.* 117, 082503 (Aug. 2016). DOI: 10.1103/PhysRevLett.117.082503.

[Kod+01] K. Kodama et al. “Observation of tau neutrino interactions”. In: *Phys. Lett. B* 504.3 (Apr. 2001), pp. 218–224. DOI: 10.1016/S0370-2693(01)00307-0.

[Kra+05] C. Kraus et al. “Final results from phase II of the Mainz neutrino mass search in tritium β decay”. In: *Eur. Phys. J. C* 40.4 (Apr. 2005), pp. 447–468. DOI: 10.1140/epjc/s2005-02139-7.

[Kra16] M. Kraus. “Energy-scale systematics at the KATRIN main spectrometer”. PhD thesis. Karlsruhe Institute of Technology, 2016. URL: https://nbn-resolving.org/urn:nbn:de:swb:90-544471.

[Kuc16] L. Kuckert. “The windowless gaseous tritium source of the KATRIN experiment – characterisation of gas dynamical and plasma properties”. PhD thesis. Karlsruhe Institute of Technology, 2016. DOI: 10.5445/IR/1000065077.

[Liu73] J. W. Liu. “Total inelastic cross section for collisions of H_2 with fast charged particles”. In: *Phys. Rev. A* 7.1 (Jan. 1973), pp. 103–109. DOI: 10.1103/PhysRevA.7.103.

[Liu87] J. W. Liu. “Total cross sections for high-energy electron scattering by H_2 ($^1\Sigma_g^+$), N_2 ($^1\Sigma_g^+$), and O_2 ($^3\Sigma_g^-$)”. In: *Phys. Rev. A* 35.2 (Jan. 1987), pp. 591–597. DOI: 10.1103/PhysRevA.35.591.

[Lob03] V. M. Lobashev. “The search for the neutrino mass by direct method in the tritium beta-decay and perspectives of study it in the project KATRIN”. In: *Nucl. Phys. A* 719 (May 2003), pp. C153–C160. DOI: 10.1016/S0375-9474(03)00985-0.

[LS85] V. M. Lobashev and P. E. Spivak. “A method for measuring the electron antineutrino rest mass”. In: *Nucl. Inst. and Meth. A* 240.2 (Oct. 1985), pp. 305–310. DOI: 10.1016/0168-9002(85)90640-0.

[Lok+22a] A. Lokhov et al. “Background reduction at the KATRIN experiment by the shifted analysing plane configuration”. In: *Eur. Phys. J. C* 82, 258 (Mar. 2022). DOI: 10.1140/epjc/s10052-022-10220-4.

[Lok+22b] A. Lokhov, S. Mertens, D. S. Parno, M. Schlösser, and K. Valerius. "Probing the neutrino-mass scale with the KATRIN experiment". In: *Annu. Rev. Nucl. Part. Sci.* 72.1 (July 2022), pp. 259–282. DOI: 10.1146/annurev-nucl-101920-113013.

[LL02] T. J. Loredo and D. Q. Lamb. "Bayesian analysis of neutrinos observed from supernova SN 1987A". In: *Phys. Rev. D* 65, 063002 (Feb. 2002). DOI: 10.1103/PhysRevD.65.063002.

[Ma98] E. Ma. "Pathways to naturally small neutrino masses". In: *Phys. Rev. Lett.* 81.6 (Aug. 1998), pp. 1171–1174. DOI: 10.1103/PhysRevLett.81.1171.

[Ma06] E. Ma. "Verifiable radiative seesaw mechanism of neutrino mass and dark matter". In: *Phys. Rev. D* 73, 077301 (Apr. 2006). DOI: 10.1103/PhysRevD.73.077301.

[Mac21] M. B. Machatschek. "A phenomenological theory of KATRIN source potential systematics and its application in krypton-83m calibration measurements". PhD thesis. Karlsruhe Institute of Technology, 2021. DOI: 10.5445/IR/1000132391.

[MNS62] Z. Maki, M. Nakagawa, and S. Sakata. "Remarks on the unified model of elementary particles". In: *Prog. Theor. Phys.* 28.5 (Nov. 1962), pp. 870–880. DOI: 10.1143/PTP.28.870.

[Mar+21] A. Marsteller et al. "Neutral tritium gas reduction in the KATRIN differential pumping sections". In: *Vacuum* 184, 109979 (Feb. 2021). DOI: 10.1016/j.vacuum.2020.109979.

[Mar+22] A. Marsteller et al. "Operation modes of the KATRIN experiment Tritium Loop System using ^{83m}Kr". In: *J. Instrum.* 17, P12010 (Dec. 2022). DOI: 10.1088/1748-0221/17/12/P12010.

[Mar20] A. C. Marsteller. "Characterization and optimization of the KATRIN tritium source". PhD thesis. Karlsruhe Institute of Technology, 2020. DOI: 10.5445/IR/1000127553.

[Mcu15] E. A. McCutchan. "Nuclear data sheets for A = 83". In: *Nucl. Data Sheets* 125 (2015), pp. 201–394. DOI: 10.1016/j.nds.2015.02.002.

[Meg16] A. M. Baldini et al. (MEG collaboration). "Search for the lepton flavour violating decay $\mu^+ \longrightarrow e^+\gamma$ with the full dataset of the MEG experiment". In: *Eur. Phys. J. C* 76, 434 (Aug. 2016). DOI: 10.1140/epjc/s10052-016-4271-x.

[MO30] L. Meitner and W. Orthmann. "Über eine absolute Bestimmung der Energie der primären β-Strahlen von Radium E". German. In: *Z. Phys.* 60.3 (Mar. 1930), pp. 143–155. DOI: 10.1007/BF01339819.

[MS86] S. P. Mikheyev and A. Y. Smirnov. "Resonant amplification of *ν* oscillations in matter and solar-neutrino spectroscopy". In: *Nuovo Cim. C* 9.1 (Jan. 1986), pp. 17–26. DOI: 10.1007/BF02508049.

[Mye+15] E. G. Myers, A. Wagner, H. Kracke, and B. A. Wesson. "Atomic masses of tritium and helium-3". In: *Phys. Rev. Lett.* 114, 013003 (Jan. 2015). DOI: 10.1103/PhysRevLett.114.013003.

[Nic19] L. Nickelson. *Electromagnetic Theory and Plasmonics for Engineers*. Springer Singapore, 2019. ISBN: 978-981-13-2350-8. DOI: 10.1007/978-981-13-2352-2.

[Nob15] Nobel Prize Outreach AB. *The Nobel Prize in Physics 2015*. Oct. 2015. URL: https://www.nobelprize.org/prizes/physics/2015/summary/ (visited on Feb. 7, 2023).

[Ost09] B. Ostrick. "Eine kondensierte ^{83m}Kr-Kalibrationsquelle für das KATRIN-Experiment". German. PhD thesis. University of Münster, 2009. URL: https://nbn-resolving.org/urn:nbn:de:hbz:6-91519454708.

[OW08] E. W. Otten and C. Weinheimer. "Neutrino mass limit from tritium β decay". In: *Rep. Prog. Phys.* 71, 086201 (July 2008). DOI: 10.1088/0034-4885/71/8/086201.

[Pan+91] N. Panagia, R. Gilmozzi, F. Macchetto, H.-M. Adorf, and R. Kirshner. "Properties of the SN 1987A circumstellar ring and the distance to the Large Magellanic Cloud". In: *Astrophys. J.* 380 (Oct. 1991), pp. L23–L26. DOI: 10.1086/186164.

[Pau30] W. Pauli. *Offener Brief an die Gruppe der Radioaktiven bei der Gauvereins-Tagung zu Tübingen*. German. Dec. 1930. URL: https://cds.cern.ch/record/83282/files/meitner_0393.pdf.

[PDG20] P. A. Zyla et al. (Particle Data Group). "Review of particle physics". In: *Prog. Theor. Exp. Phys.* 2020.8 (Aug. 2020). 083C01. DOI: 10.1093/ptep/ptaa104.

[PDG22] R. L. Workman et al. (Particle Data Group). "Review of particle physics". In: *Prog. Theor. Exp. Phys.* 2022.8 (Aug. 2022). 083C01. DOI: 10.1093/ptep/ptac097.

[Pic+92a] A. Picard et al. "A solenoid retarding spectrometer with high resolution and transmission for keV electrons". In: *Nucl. Inst. and Meth. B* 63.3 (Feb. 1992), pp. 345–358. DOI: 10.1016/0168-583X(92)95119-C.

[Pic+92b] A. Picard et al. "Precision measurement of the conversion electron spectrum of ^{83m}Kr with a solenoid retarding spectrometer". In: *Z. Phys. A* 342.1 (Mar. 1992), pp. 71–78. DOI: 10.1007/BF01294491.

[Pla20] N. Aghanim et al. (Planck collaboration). "Planck 2018 results. VI. Cosmological parameters". In: *Astron. Astrophys.* 641, A6 (Sept. 2020). DOI: 10.1051/0004-6361/201833910.

[Pon58] B. Pontecorvo. "Inverse beta processes and nonconservation of lepton charge". Trans. by A. Bincer. In: *Sov. Phys. JETP* 7 (July 1958), pp. 172–173. URL: http://jetp.ras.ru/cgi-bin/dn/e_007_01_0172.pdf. Trans. of "Обратные β-процессы и несохранение лептонного заряда". Russian. In: *Zh. Eksp. Teor. Fiz.* 34 (Jan. 1958), pp. 247–249.

[Pöp92] R. Pöpel. "The Josephson effect and voltage standards". In: *Metrologia* 29.2 (Jan. 1992), p. 153. DOI: 10.1088/0026-1394/29/2/005.

[PS12] W. Porod and F. Staub. "SPheno 3.1: Extensions including flavour, CP-phases and models beyond the MSSM". In: *Comput. Phys. Commun.* 183.11 (May 2012), pp. 2458–2469. DOI: 10.1016/j.cpc.2012.05.021.

[Pra11] M. Prall. “Background reduction of the KATRIN spectrometers: Transmission function of the pre-spectrometer and systematic test of the main-spectrometer wire electrode”. PhD thesis. University of Münster, 2011. URL: https://www.researchgate.net/publication/238418212.

[Pri06] M. Aoki et al. (PRISM/PRIME group). *An experimental search for a $\mu^- - e^-$ conversion at sensitivity of the order of 10^{-18} with a highly intense muon source: PRISM*. Letter of Intent. J-PARC, Apr. 2006. URL: https://j-parc.jp/researcher/Hadron/en/pac_0606/pdf/p20-Kuno.pdf.

[PSB15] F. Priester, M. Sturm, and B. Bornschein. “Commissioning and detailed results of KATRIN inner loop tritium processing system at Tritium Laboratory Karlsruhe”. In: *Vacuum* 116 (June 2015), pp. 42–47. DOI: 10.1016/j.vacuum.2015.02.030.

[Pro17] A. A. Esfahani et al. (Project 8 collaboration). “Determining the neutrino mass with cyclotron radiation emission spectroscopy—Project 8”. In: *J. Phys. G* 44, 054004 (Mar. 2017). DOI: 10.1088/1361-6471/aa5b4f.

[RC53a] F. Reines and C. L. Cowan. “A proposed experiment to detect the free neutrino”. In: *Phys. Rev.* 90.3 (May 1953), pp. 492–493. DOI: 10.1103/PhysRev.90.492.2.

[RC53b] F. Reines and C. L. Cowan. “Detection of the free neutrino”. In: *Phys. Rev.* 92.3 (Nov. 1953), pp. 830–831. DOI: 10.1103/PhysRev.92.830.

[Ren18] F. Renga. “The quest for $\mu \longrightarrow e\gamma$: Present and future”. In: *Hyperfine Interact.* 239.1 (Nov. 2018), p. 58. DOI: 10.1007/s10751-018-1534-y.

[Res19] O. Rest. “Precision high voltage at the KATRIN experiment and new methods for an absolute calibration at ppm-level for high-voltage dividers”. PhD thesis. University of Münster, 2019. URL: https://www.uni-muenster.de/imperia/md/content/physik_kp/agweinheimer/theses/diss-oliver_rest.pdf.

[Res+19] O. Rest et al. “A novel ppm-precise absolute calibration method for precision high-voltage dividers”. In: *Metrologia* 56, 045007 (July 2019). DOI: 10.1088/1681-7575/ab2997.

[Rie+19] A. G. Riess, S. Casertano, W. Yuan, L. M. Macri, and D. Scolnic. “Large Magellanic Cloud Cepheid standards provide a 1% foundation for the determination of the Hubble constant and stronger evidence for physics beyond ΛCDM”. In: *Astrophys. J.* 876.1, 85 (May 2019), p. 85. DOI: 10.3847/1538-4357/ab1422.

[Rob+91] R. G. H. Robertson, T. J. Bowles, G. J. Stephenson, D. L. Wark, J. F. Wilkerson, and D. A. Knapp. “Limit on $\bar{\nu}_e$ mass from observation of the β decay of molecular tritium”. In: *Phys. Rev. Lett.* 67.8 (Aug. 1991), pp. 957–960. DOI: 10.1103/PhysRevLett.67.957.

[RK88] R. G. H. Robertson and D. A. Knapp. “Direct measurements of neutrino mass”. In: *Annu. Rev. Nucl. Part. Sci.* 38.1 (Dec. 1988), pp. 185–215. DOI: 10.1146/annurev.ns.38.120188.001153.

[Rod22] C. Rodenbeck. “A method for determining the transition energies of ^{83m}Kr at the KATRIN experiment”. In: *Eur. Phys. J. C* 82, 700 (Aug. 2022). DOI: 10.1140/epjc/s10052-022-10667-5.

[Rod+22] C. Rodenbeck, S. Wüstling, S. Enomoto, J. Hartmann, O. Rest, T. Thümmler, and C. Weinheimer. “Wideband precision stabilization of the −18.6 kV retarding voltage for the KATRIN spectrometer”. In: *J. Instrum.* 17, P06003 (June 2022). DOI: 10.1088/1748-0221/17/06/p06003.

[Röl+13] M. Röllig et al. “Activity monitoring of a gaseous tritium source by beta induced X-ray spectrometry”. In: *Fusion Eng. Des.* 88.6–8 (Oct. 2013): *Proceedings of the 27th Symposium On Fusion Technology (SOFT-27); Liège, Belgium, September 24-28, 2012*, pp. 1263–1266. DOI: 10.1016/j.fusengdes.2012.11.001.

[Rut99] E. Rutherford. “Uranium radiation and the electrical conduction produced by it”. In: *Philos. Mag.* 5th ser. 47.284 (Jan. 1899), pp. 109–163. DOI: 10.1080/14786449908621245.

[Rut03] E. Rutherford. “The magnetic and electric deviation of the easily absorbed rays from radium”. In: *Philos. Mag.* 6th ser. 5.26 (Feb. 1903), pp. 177–187. DOI: 10.1080/14786440309462912.

[Sac20] R. Sack. “Measurement of the energy loss of 18.6 keV electrons on deuterium gas and determination of the tritium Q-value at the KATRIN experiment”. PhD thesis. University of Münster, 2020. URL: https://nbn-resolving.org/urn:nbn:de:hbz:6-59069498754.

[Sal68] A. Salam. “Weak and electromagnetic interactions”. In: *Elementary Particle Theory: Relativistic Groups and Analyticity*. Proceedings of the Eighth Nobel Symposium (Lerum, Sweden, May 19–25, 1968). Ed. by N. Svartholm. Almqvist & Wiksell, 1968, pp. 367–377.

[Sch21] L. Schimpf. “Characterisation of energy loss processes of 18.6 keV electrons inside the windowless tritium source of KATRIN”. PhD thesis. Karlsruhe Institute of Technology, 2021. DOI: 10.5445/IR/1000131810.

[Sei19] H. Seitz-Moskaliuk. “Characterisation of the KATRIN tritium source and evaluation of systematic effects”. PhD thesis. Karlsruhe Institute of Technology, 2019. DOI: 10.5445/IR/1000090748.

[Sen+18] J. Sentkerestiová, O. Dragoun, O. Lebeda, M. Ryšavý, M. Sturm, and D. Vénos. “Gaseous ^{83m}Kr generator for KATRIN”. In: *J. Instrum.* 13, P04018 (Apr. 2018). DOI: 10.1088/1748-0221/13/04/p04018.

[Sin88] U. Bellgardt et al. (SINDRUM collaboration). “Search for the decay $\mu^+ \longrightarrow e^+e^+e^-$”. In: *Nucl. Phys. B* 299.1 (Mar. 1988), pp. 1–6. DOI: 10.1016/0550-3213(88)90462-2.

[Sin93] C. Dohmen et al. (SINDRUM II collaboration). “Test of lepton-flavour conservation in $\mu \longrightarrow e$ conversion on titanium”. In: *Phys. Lett. B* 317.4 (Nov. 1993), pp. 631–636. DOI: 10.1016/0370-2693(93)91383-X.

[SK98a] Y. Fukuda et al. (Super-Kamiokande collaboration). “Evidence for oscillation of atmospheric neutrinos”. In: *Phys. Rev. Lett.* 81.8 (Aug. 1998), pp. 1562–1567. DOI: 10.1103/PhysRevLett.81.1562.

[SK98b] Y. Fukuda et al. (Super-Kamiokande collaboration). “Measurements of the solar neutrino flux from Super-Kamiokande’s first 300 days”. In: *Phys. Rev. Lett.* 81.6 (Aug. 1998), pp. 1158–1162. DOI: 10.1103/PhysRevLett.81.1158.

[Sle15] M. Slezák. “Monitoring of the energy scale in the KATRIN neutrino experiment”. PhD thesis. Charles University in Prague, 2015. URL: https://dspace.cuni.cz/handle/20.500.11956/77972.

[Sno02] Q. R. Ahmad et al. (SNO collaboration). “Direct evidence for neutrino flavor transformation from neutral-current interactions in the Sudbury Neutrino Observatory”. In: *Phys. Rev. Lett.* 89, 011301 (June 2002). DOI: 10.1103/PhysRevLett.89.011301.

[Ste+13] N. Steinbrink, V. Hannen, E. L. Martin, R. G. H. Robertson, M. Zacher, and C. Weinheimer. “Neutrino mass sensitivity by MAC-E-filter based time-of-flight spectroscopy with the example of KATRIN”. In: *New J. Phys.* 15, 113020 (Nov. 2013). DOI: 10.1088/1367-2630/15/11/113020.

[Ste17] N. M. N. Steinbrink. “Beyond-Standard Model neutrino physics sensitivity with KATRIN”. PhD thesis. University of Münster, 2017. URL: https://www.uni-muenster.de/imperia/md/content/physik_kp/agweinheimer/theses/diss-nicholas_steinbrink.pdf.

[Str+14] S. Streubel, T. Eronen, M. Höcker, J. Ketter, M. Schuh, R. S. Van Dyck, Jr., and K. Blaum. “Toward a more accurate Q value measurement of tritium: Status of THe-Trap”. In: *Appl. Phys. B* 114.1 (Jan. 2014), pp. 137–145. DOI: 10.1007/s00340-013-5669-x.

[Stu+10] M. Sturm, M. Schlösser, R. J. Lewis, B. Bornschein, G. Drexlin, and H. H. Telle. “Monitoring of all hydrogen isotopologues at Tritium Laboratory Karlsruhe using Raman spectroscopy”. In: *Laser Physics* 20.2 (Feb. 2010), pp. 493–507. DOI: 10.1134/S1054660X10030163.

[Tho13] M. Thomson. *Modern Particle Physics*. Cambridge University Press, 2013. ISBN: 978-1-107-03426-6.

[Thü07] T. Thümmler. “Präzisionsüberwachung und Kalibration der Hochspannung für das KATRIN-Experiment”. German. PhD thesis. University of Münster, 2007. URL: https://nbn-resolving.org/urn:nbn:de:hbz:6-16539562785.

[TMW09] T. Thümmler, R. Marx, and C. Weinheimer. “Precision high voltage divider for the KATRIN experiment”. In: *New J. Phys.* 11, 103007 (Oct. 2009). DOI: 10.1088/1367-2630/11/10/103007.

[Tro11] V. N. Aseev et al. (Troitsk collaboration). “Upper limit on the electron antineutrino mass from the Troitsk experiment”. In: *Phys. Rev. D* 84, 112003 (Dec. 2011). DOI: 10.1103/PhysRevD.84.112003.

[Val+09] K. Valerius et al. “A UV LED-based fast-pulsed photoelectron source for time-of-flight studies”. In: *New J. Phys.* 11, 063018 (June 2009). DOI: 10.1088/1367-2630/11/6/063018.

[Val+11] K. Valerius et al. “Prototype of an angular-selective photoelectron calibration source for the KATRIN experiment”. In: *J. Instrum.* 6, P01002 (Jan. 2011). DOI: 10.1088/1748-0221/6/01/P01002.

[Val10] K. Valerius. “The wire electrode system for the KATRIN main spectrometer”. In: *Prog. Part. Nucl. Phys.* 64.2 (Apr. 2010): *Neutrinos in Cosmology, in Astro, Particle and Nuclear Physics. International Workshop on Nuclear Physics, 31st course (ERICE 2009)*, pp. 291–293. DOI: 10.1016/j.ppnp.2009.12.032.

[Vel+19] C. Velte et al. “High-resolution and low-background ^{163}Ho spectrum: Interpretation of the resonance tails”. In: *Eur. Phys. J. C* 79, 1026 (Nov. 2019). DOI: 10.1140/epjc/s10052-019-7513-x.

[Vén+18] D. Vénos, J. Sentkerestiová, O. Dragoun, M. Slezák, M. Ryšavý, and A. Špalek. “Properties of ^{83m}Kr conversion electrons and their use in the KATRIN experiment”. In: *J. Instrum.* 13, T02012 (Feb. 2018). DOI: 10.1088/1748-0221/13/02/T02012.

[WJH99] P. Weck, B. Joulakian, and P. A. Hervieux. “Fivefold differential cross section of fast (e, $2e$) ionization of H_2, D_2, and T_2 by a Franck-Condon approach”. In: *Phys. Rev. A* 60.4 (Oct. 1999), pp. 3013–3019. DOI: 10.1103/PhysRevA.60.3013.

[Wei67] S. Weinberg. “A model of leptons”. In: *Phys. Rev. Lett.* 19.21 (Nov. 1967), pp. 1264–1266. DOI: 10.1103/PhysRevLett.19.1264.

[Wei79] S. Weinberg. “Baryon- and lepton-nonconserving processes”. In: *Phys. Rev. Lett.* 43.21 (Nov. 1979), pp. 1566–1570. DOI: 10.1103/PhysRevLett.43.1566.

[Wei35] C. F. v. Weizsäcker. “Zur Theorie der Kernmassen”. German. In: *Z. Phys.* 96.7 (July 1935), pp. 431–458. DOI: 10.1007/BF01337700.

[Wel+17] S. Welte, E. Fanghänel, S. Fischer, F. Kramer, T. L. Le, M. Sturm, and N. Tuchscherer. “Experimental performance test of key components of the KATRIN outer tritium loop”. In: *Fusion Sci. Technol.* 71.3 (Mar. 2017), pp. 316–320. DOI: 10.1080/15361055.2017.1291233.

[Wil09] W. Wilson. “On the absorption of homogeneous β-rays by matter, and on the variation of the absorption of the rays with velocity”. In: *Proc. R. Soc. A* 82.558 (Sept. 1909), pp. 612–628. DOI: 10.1098/rspa.1909.0067.

[Wol78] L. Wolfenstein. “Neutrino oscillations in matter”. In: *Phys. Rev. D* 17.9 (May 1978), pp. 2369–2374. DOI: 10.1103/PhysRevD.17.2369.

[Wu+57] C. S. Wu, E. Ambler, R. W. Hayward, D. D. Hoppes, and R. P. Hudson. “Experimental test of parity conservation in beta decay”. In: *Phys. Rev.* 105.4 (Feb. 1957), pp. 1413–1415. DOI: 10.1103/PhysRev.105.1413.

[Zac15] M. Zacher. “High-field electrodes design and an angular-selective photoelectron source for the KATRIN spectrometers”. PhD thesis. University of Münster, 2015.

[Zbo+13] M. Zbořil et al. “Ultra-stable implanted ^{83}Rb/^{83m}Kr electron sources for the energy scale monitoring in the KATRIN experiment”. In: *J. Instrum.* 8, P03009 (Mar. 2013). DOI: 10.1088/1748-0221/8/03/P03009.

[Zub20] K. Zuber. *Neutrino Physics*. 3rd ed. Series in High Energy Physics, Cosmology and Gravitation. CRC Press, 2020. ISBN: 978-1-138-71889-0. DOI: 10.1201/9781315195612.

List of figures

List of tables

Acknowledgments

I want to thank everyone who helped me during the course of this thesis. Since such a list can never be complete, I apologize in advance to everyone who should be in this list but is not. Feel free to contact me and complain about it. ☺

Zuallererst möchte ich mich bei Professor **Christian Weinheimer** bedanken. Nicht nur für die Ermöglichung der Doktorarbeit in diesen recht breit gefächerten Themen, sondern auch für die gute Betreuung. Neben seiner steten Hilfe auch den Blick über den Tellerrand zu schärfen, hat er auch tatkräftig bei Problemlösungen mitgeholfen. Um nur *eine* kleine Anekdote zu nennen: Er hat ein knapp 25 kg schweres Netzgerät spontan per Bahn von Münster nach Karlsruhe geschleppt und bei der Ansteuerung geholfen, damit wir den e-Gun-Beam finden konnten und die STS3a-Messphase vorangehen konnte. Das ist keine Selbstverständlichkeit.

Professor **Anton Andronic** möchte ich danken, dass er die Aufgabe des Zweitgutachters übernommen hat.

Professor **Michael Klasen und seiner gesamten Theoriegruppe** in Münster möchte ich für die spannenden zwei Monate danken, die ich dort verbringen durfte und während denen ich einmal wieder in die Arbeitsweise der Theorie schnuppern konnte.

Weiter möchte ich mich bei der **Arbeitsgruppe in Münster** bedanken. Immer wenn ich vor Ort war, aber auch von Karlsruhe aus, habe ich einen tollen kollegialen Zusammenhalt erlebt, in dem wir alle möglichen Dinge diskutieren, besprechen und gemeinsam lösen konnten.

Ebenfalls möchte ich mich bei der **Arbeitsgruppe in Karlsruhe** bedanken. Nicht nur durch die regelmäßigen gemeinsamen Mittagessen und Kaffeerunden, sondern auch durch die allgemein gute Atmosphäre auf dem Flur habe ich mich sehr wohlgefühlt.

Bei meinen neuen **Kollegen am TLK** möchte ich mich bedanken. Auch wenn ich die meiste Zeit nur im Zusammenschreibstress war, habt ihr mich direkt integriert und hattet immer ein offenes Ohr und Lösungen für Probleme aller Art.

Für die viele Hilfe zu organisatorischen Dingen möchte ich mich vorneweg bei **Michaela Erdmann** bedanken, nicht nur für das unermüdliche Weiterleiten der Post von Münster nach Karlsruhe, sondern dafür, dass Du bei jeglichen Problemen geholfen hast. Ebenso möchte ich **Marion Behechti** und **Eva Porter** danken.

Einen besonderen Dank möchte ich dem **Hochspannungsteam** aussprechen. Für die Einführung in die Kalibration und Hochspannung bei KATRIN allgemein möchte ich vor allem **Oliver** aber auch **Daniel** danken. Ganz besonders möchte ich mich bei **Thomas** und **Sascha** bedanken: Ihr beiden wart immer für mich da in Karlsruhe und wir konnten sowohl kleinere als auch größere Probleme immer gut besprechen, lösen und nebenbei die Hochspannung verbessern. Bei **Heike** möchte ich mich für die viele Unterstützung sowohl bei der Voltmeter- als auch Spannungsteilerkalibration bedanken. Du hast Struktur in unsere Kalibrationen gebracht.

Genauso möchte ich mich beim gesamten **e-Gun- und Eloss-Team** bedanken. Vorneweg bei **Lutz** und **Rudolf**; auch wenn die Messphasen oft sehr anstrengend waren, haben wir es zusammen gemeistert, die e-Gun erfolgreich durch KATRIN zu fädeln, Energieverlustmessungen aufzunehmen und zu analysieren und die e-Gun als Tool für viele Systematikuntersuchungen bereitzustellen. Zum e-Gun-/Eloss-Team

gehören auch noch **Philipp**, **Jan**, **Volker**, **Björn**, **Fabian** und **Sonja**. Danke, zusammen haben wir viele Probleme entdecken, meistern und lösen können!

Bei dem **Krypton-/Plasma-Team** möchte ich mich bedanken für die vielen spannenden gemeinsamen Messungen und Unterhaltungen im Kontrollraum, auch wenn wir uns manchmal um Messzeit „kloppen" mussten (e-Gun vs. Plasma und nur eine KATRIN-Beamline). Dazu gehören **Moritz M.**, **Fabian F.**, **Manuel** und **Magnus**. Genauso auch **Matthias** und **Benedikt**; die 40-kV-Messungen werden Euch sicher noch eine Weile auf Trab halten. ☺

Allen, mit denen ich im Kontrollraum spannende Zeiten verbracht habe, mit denen ich zusammen Messungen gerettet habe und die ich aber bis hier noch nicht erwähnt habe, möchte ich ebenfalls danken. Dazu zählen: **Alexander J.**, **Alexander M.**, **Alexander F.**, **Carsten**, **Dominic**, **Klaus S.**, **Leonard K.**, **Mariia**, **Max** und viele mehr. Ganz besonders hervorheben möchte ich **Florian F.**: von Dir konnte ich nicht nur sehr viel über ORCA lernen, Du warst auch sonst immer sehr hilfsbereit und hast mich auch bei ausgefalleneren Messideen tatkräftig unterstützt.

Alexey *and* **Sanshiro**, *I want to thank you both for the many hours in the control room and for the many discussions about all sorts of analyses, be it high voltage, energy loss, or any of the myriad other ones. I could always count on your help and on your insights.*

Für all den technischen Support möchte ich mich bei **Andreas Kopmann** und **Suren Chilingaryan** bedanken, ebenso bei **Tom Caldwell** (*Thank you for the great ORCA support!*). Ebenso bei **Thomas Höhn**: danke, dass Du unsere HV-Steuerung so gut wartest, erweiterst und zusammenhältst. Für den IT-Support und die spannenden Kaffeeraumdiskussionen möchte ich **Thomas C.** danken. **Armen**, Dir

möchte ich nicht nur für den Eiskonfekt während stressiger Messphasen danken, sondern vor allem: vielen Dank, dass Du immer bei allen möglichen Softwareproblemen sofort Zeit hattest und wir gemeinsam Lösungen finden konnten.

I would like to thank **Alan Poon** *for his book recommendations and other efforts to improve my written English.*

Für die spannenden und lehrreichen Diskussionen bei der Planung von diversen Messungen, aber vor allem für die Hilfe bei der Literaturrecherche für Energieverluste möchte ich mich bei **Ferenc** bedanken.

Klaus M., Dir möchte ich nicht nur für das strenge Einberufen des täglichen Elfuhrdreißig-Mittagessens, für die Kreuzworträtsel und philosophischen Diskussionen danken, sondern auch für Deinen Einsatz bei mechanischen Problemen aller Art. Besonders unsere Aktion, ein Fahrradschloss vorm Bahnhof unter polizeilicher Überwachung aufzuflexen, werde ich nicht so schnell vergessen.

Bei allen, die mich während der Schreibphase (und auch schon davor) zum Schreiben ermuntert haben, den aktuellen Schreibstatus abgefragt haben und interessiert zugehört haben, möchte ich mich bedanken. Vorneweg natürlich **Michael**, der als einer der Ersten damit angefangen und auch am wenigsten lockergelassen hat.

Allen, die diese Arbeit Korrektur gelesen haben und damit dazu beigetragen haben, ihr den nötigen Feinschliff zu geben, möchte ich danken. Dazu zählen **Thomas T.**, **Jan**, **Moritz**, **Alexey**, meine Schwester **Christine** und **Christopher**.

Ganz besonders aber möchte ich mich bei **meiner Familie** und bei **Christopher** bedanken. Eure stetige Unterstützung, das Aufbringen von Verständnis und Geduld vor allem in den stressigeren Phasen hat mich sehr gut über Wasser gehalten. Vielen lieben Dank!